ISSN 2525-2461

# Vietnam Journal of Science, Technology and Engineering

JUNE 2020 • VOLUME 62 NUMBER 2

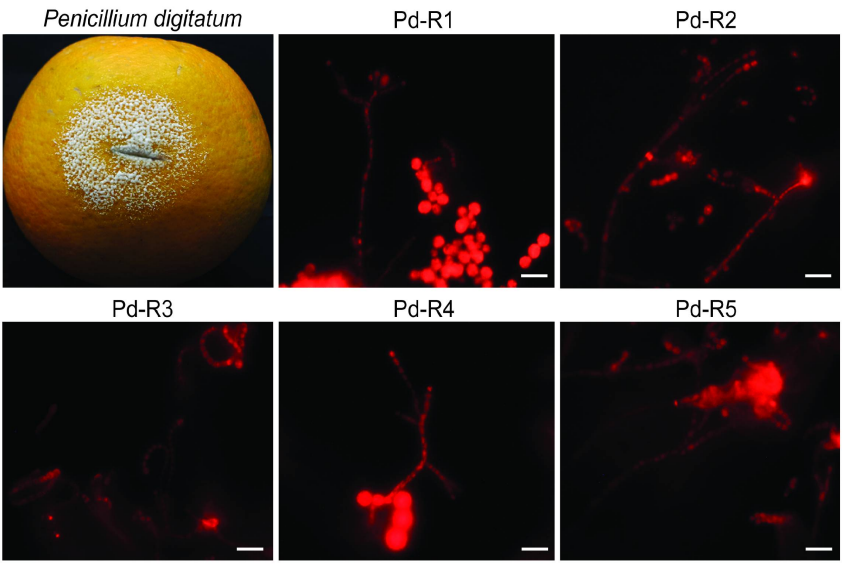


## Phleomycin resistance gene as a reliable selection marker for *Agrobacterium tumefaciens*-mediated transformation of the citrus postharvest pathogen *Penicillium digitatum*

VIETNAM JOURNAL OF SCIENCE, TECHNOLOGY AND ENGINEERING * JUNE 2020 * VOLUME 62 NUMBER 2
vietnamscience.vn

***Vietnam Journal of Science, Technology and Engineering (VJSTE)*** **is a quarterly double-blind peer-reviewed academic journal. VJSTE publishes research articles and review articles in all areas of science, technology and engineering with the focus on the life sciences and environmental sciences including the following topics:**

- **Agriculture**
- **Medicine**
- **Pharmacology**
- **Biology**
- **Biotechnology**
- **Ecology**
- **Climatology.**

## CLASSIFICATION SCHEME

1. **Mathematics and Computer Science**
   - 1.1. Mathematics
   - 1.2. Computer Science
   - 1.3. Computational Science
2. **Physical Sciences**
   - 2.1. Physics
   - 2.2. Chemistry
   - 2.3. Engineering
3. **Life Sciences**
   - 3.1. Agriculture
   - 3.2. Medicine
   - 3.3. Pharmacology
   - 3.4. Biology
   - 3.5. Biotechnology
4. **Geosciences**
   - 4.1. Geography
   - 4.2. Geology
   - 4.3. Geophysics
   - 4.4. Oceanography
5. **Environmental Sciences**
   - 5.1. Ecology
   - 5.2. Climatology

# CONTENTS

JUNE 2020 • VOLUME 62 NUMBER 2

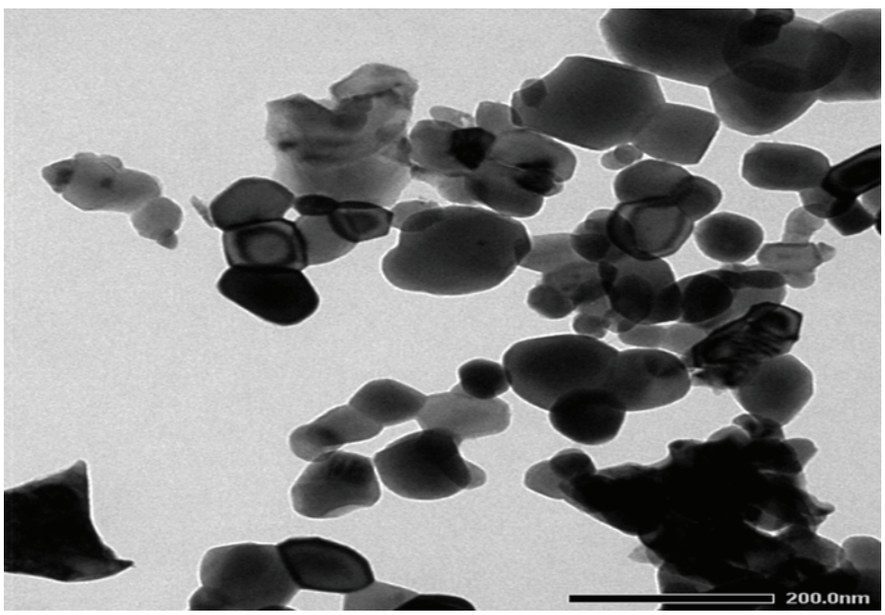


16

## PHYSICAL SCIENCES

# CONTENTS

JUNE 2020 • VOLUME 62 NUMBER 2

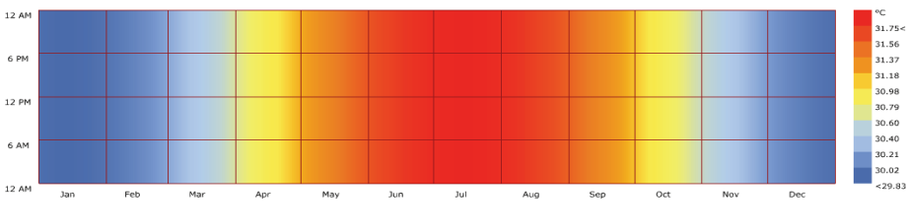


(A)

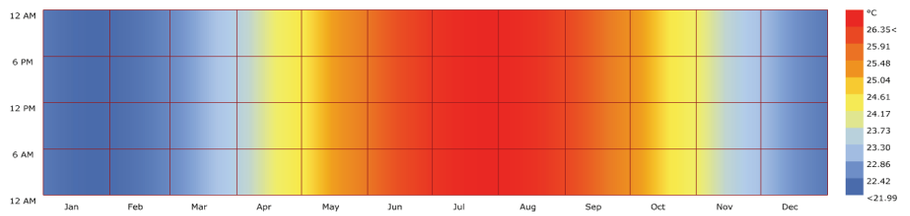


(B)

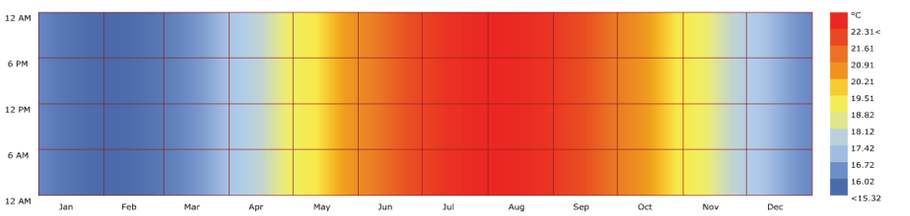


(C)

DOI: 10.31276/VJSTE.62(2).03-06



# Research and development of a luminance responsivity standard system at the Vietnam Metrology Institute

**Xuan Quan Cao*, Ngoc Dung Hoang, Hoang Luong Nguyen**

*Photometry and Radiometry Laboratory, Vietnam Metrology Institute*

Received 25 November 2019; accepted 10 March 2020

***Abstract:***

**The development of a luminance responsivity standard is central to the study of photometry and radiometry at the Vietnam Metrology Institute (VMI). Today, two methods are used to determine luminance responsivity. The first method uses an integrating sphere light source, also known as a luminous intensity standard lamp, and the second method compares the luminance responsivity value to that of a known standard photometer. Using these methods, it is possible to identify small uncertainties. In this work, we analysed the luminance responsivity standard system (model: VMI-PR-006) based on the national standard system of luminance (model: V11.04.18). This system was used to calibrate the luminance responsivity scale of standard photometer and luminance standard integrating sphere.**

**When using the national standard system (V11.04.18) to calibrate the luminance standard integrating sphere (model: LN3; S/N:05B840), an uncertainty of $U$=0.73% for $k$=2, where $k$ is the *, was found [1]. On the other hand, we calibrated the luminance responsivity scale of a standard photometer system (VMI-PR-006) based on the national standard system of luminance (V11.04.18) and compared it to the luminance responsivity scale calibrated at NMIA (National Measurement Institute Australia) with $E_n$=0.13<1, where $E_n$ is *. This standard system is used for the calibration and verification of measurement devices within the luminance measurement requirements specified by the Vietnam technical documents.**

***Keywords:*** **luminance meter, luminance responsivity scale (A/(cd/m²)), luminance standard integrating sphere source, photometry and radiometry.**

***Classification number:*** **2.1**

## Introduction

Luminance responsivity is a photometric quantity that realizes the brightness of a surface. Recently, a luminance responsivity scale has been presented [2, 3], which is based on a separate measurement of the spectral responsivity, as well as the distance and size of the aperture. The luminance responsivity value at the aperture plane of an integrating sphere is obtained from the measurements. In this work, we present our analysis of the unit of luminance responsivity.

This investigation, conducted at VMI, determines the unit of luminous intensity using a luminance integrating sphere source, a reference standard photometer, the distance and the size of the aperture, and a spectroradiometer. The method for determining the unit of luminance responsivity is comparable to that of the luminous intensity value. In addition, the area of the output aperture of the sphere must be known, as described in Refs. [2, 4, 5]. We present a newly developed method for separately measuring the spectral responsivity, the distance, and the size of aperture as described.

## Measurement setup and realization of unit

### *Measurement setup*

The measurement setup consisted of a reference standard photometer, a spectroradiometer, a luminance integrating sphere, and an optical bench. During the measurements, the integrating sphere, the reference standard photometer, and the spectroradiometer were placed on an optical bench.

The optical bench is shown in Fig. 1. The optical axis was determined by an alignment laser. The alignment laser is used to align and setup the luminance integrating sphere on the optical bench, where the optical axis is perpendicular to and passes through the centre point of the open aperture

*Corresponding author: Email: quancx@vmi.gov.vn.

of the luminance integrating sphere. The fixed location of the luminance integrating sphere determined the optical axis to be at a height of 55 cm above the surface of the optical bench. The optical axis was visualized by using a two-beam alignment laser positioned between the reference standard photometer and the integrating sphere.

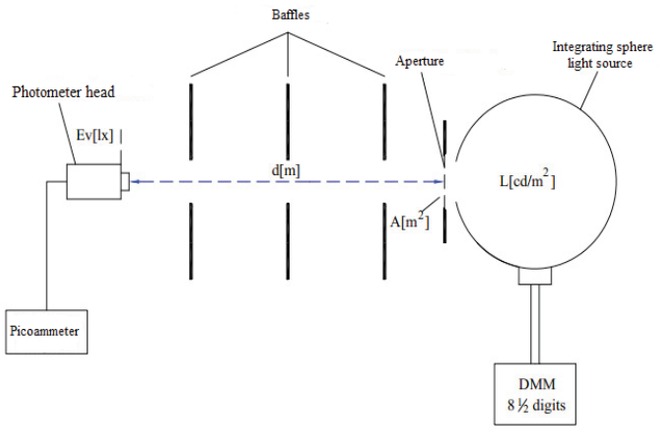


**Fig. 1. Principle of the measurement set-up for realization of the unit of luminance responsivity.**

The diameter of the aperture of the reference standard photometer was 30 mm. The photocurrent of the photometer was measured using a high precision picoammeter. The aperture diameter of the luminance integrating sphere was 70 mm. The luminance integrating sphere, which was coated with barium sulphate paint, was illuminated by a tungsten halogen lamp. The operating current of the lamp was chosen such that the correlated colour temperature of the source was 2856 K. The distances between the aperture plane of the integrating sphere and the reference standard photometer were measured by a length scale [3-6], in Fig. 2.

**Fig. 2. Photograph of the typical luminance measurement setup.**

The reference standard photometer was then moved to the appropriate measurement distance, which was determined by a length scale. The distance between the front surface of the aperture holder and the aperture plane of the integrating sphere source was measured mechanically.

***Luminance responsivity calibration***

The luminance responsivity of the reference standard photometer was determined from the measurement geometry and the illuminance measured with a reference standard photometer [4]. The luminance of the integrating sphere and luminance responsivity of the reference standard photometer were obtained from:

$$L_V = \frac{E_V \cdot D^2}{A_S} \quad (1)$$

where $L_V$ is the luminance, $E_V$ is the illuminance at the effective distance, $D$, between the aperture planes of the source and the standard photometer, and $A_S$ is the area of the light source aperture.

The luminance responsivity is obtained from:

$$S_L = \frac{S_V . A_S}{D^2} \quad (2)$$

where $S_L$ is the luminance responsivity in A (A/(cd/m$^2$)) and $S_V$ is the illuminance responsivity of reference photometer (A/lx). The effective distance, $D$, depends on the radius of the photometer aperture, $r_D$, the radius of the source, $r_S$, and the physical distance, $d$, between the two apertures according to the relation:

$$D = \sqrt{d^2 + r_D^2 + r_S^2} \quad (3)$$

Equation (3) is accurate within ±0.01% for distances that are at least one order of magnitude greater than the radii of the two apertures [4, 5].

The illuminance was measured at a distance greater than 2500 mm. The luminous intensity of the source was determined only at the luminance level and correlated colour temperature of 2856 K. The lower luminance levels were determined by measuring the changes in illuminance, with the photometer placed close to the aperture plane of the integrating sphere.

Because spatial uniformity is a crucial factor, we

investigated the non-uniformity of the output aperture of the integrating sphere. The non-uniformity of the integrating sphere is shown in Fig. 3.

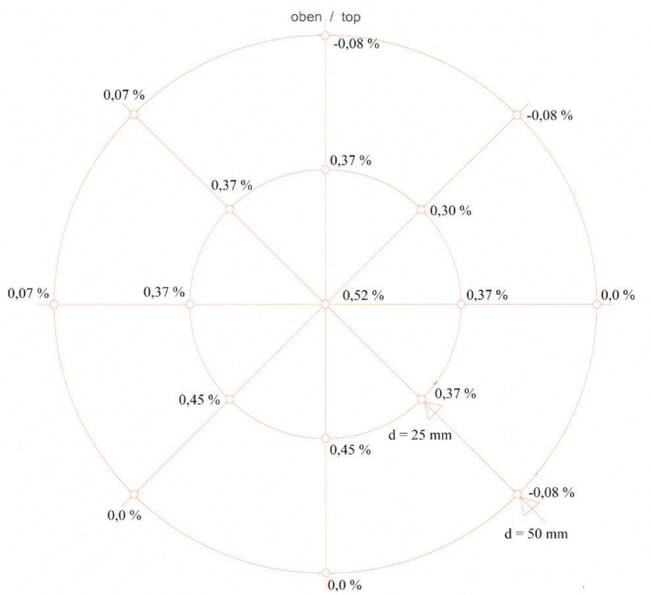


**Fig. 3. Non-uniformity of output aperture surface of the integrating sphere.**

The luminance of the integrating sphere and related analyses require corrections, thus, correction factors were calculated for all measurements. Calibration report data of the luminance used by the luminance responsivity of reference standard photometer is shown in Table 1.

**Table 1. Calibration report data of the luminance (cd/m²).**

| No. | Photocurrent values, nA | Standard illuminance values, $E_V$ (lx) | Calibrated luminance responsivity of reference standard photometer, $S_L$ (A/(cd/m²)) | Luminance of integrating sphere (LN3-05B840 at VMI, $L_v$ (cd/m²) |
|---|---|---|---|---|
| 1 | 63.184 | 4.090 | $4.819 \times 10^{-11}$ | 1311.1 |
| 2 | 63.187 | 4.090 | $4.819 \times 10^{-11}$ | 1311.2 |
| 3 | 63.182 | 4.089 | $4.819 \times 10^{-11}$ | 1311.1 |
| 4 | 63.185 | 4.090 | $4.819 \times 10^{-11}$ | 1311.2 |
| 5 | 63.184 | 4.090 | $4.819 \times 10^{-11}$ | 1311.1 |
| Avg. | 63.184 | 4.090 | $4.819 \times 10^{-11}$ | 1311.1 |

The luminance of integrating sphere measured at VMI (Vietnam) and PTB (Germany) are given in Table 2.

**Table 2. The luminance of integrating sphere measured at VMI (Vietnam) and PTB (Germany).**

| Luminance integrating sphere | Correlated colour temperature, K | Luminance of integrating sphere, $L_v$ (cd/m²) | | Absolute differences, $\Delta L_v$ |
|---|---|---|---|---|
| | | *VMI* | *PTB* | *(VMI/PTB) - 1* |
| LN3-LMT; 05B840 | 2856 | 1311.1 | 1311.3 | -0.00015 |

The maximum total luminance difference between the measurements at VMI and PTB, calculated as (VMI/PTB) - 1, of the integrating sphere was -0.00015, as seen in the Table 2.

The luminance responsivity of the reference standard photometer from the VMI and NMIA systems are given in Table 3.

**Table 3. Luminance responsivity of the reference standard photometer based on the national standard system.**

| Reference standard for luminance responsivity of photometer | Correlated colour temperature, K | Luminance responsivity of reference standard photometer, $S_L$ (A/(cd/m²)) | | Absolute differences, $\Delta S_L$ |
|---|---|---|---|---|
| | | *VMI* | *NMIA* | *(VMI/NMIA) - 1* |
| VMI.PR006 (VMI) | 2856 | $4.819 \times 10^{-11}$ | $4.827 \times 10^{-11}$ | 0.0017 |

The maximum luminance responsivity absolute difference between VMI and NMIA, (VMI/NMIA) - 1, of the reference standard photometer was 0.0017 as seen in Table 3.

## Uncertainty analysis

Table 4 presents the results of the uncertainty analyses for the determination of the unit of luminance responsivity. All known uncertainty components were included. Detailed uncertainty analyses for the realization of the unit of illuminance responsivity may be found in Refs. [6, 7].

**Table 4. The uncertainty analyses for the realization of the unit of luminance responsivity.**

| Components | Description | Rel. std. uncert., $u_i(x_i)$ | Prob. distrib. | Sens. coef., $c_i$ | Contrib. $c_i u_i(x_i)$, (%) | DoF |
|---|---|---|---|---|---|---|
| $u(S_v)$ | Uncertainty of reference standard photometer | 0.035 | Nor | 71 | 0.19 | ∞ |
| $u(y_L)$ | Standard uncertainty of the photocurrent measurement | 0.015 | t | 206 | 0.24 | 2385 |
| $u(y_L)_{rep}$ | Uncertainty in repeated measurements | 0.0030 | t | | | 4 |
| $u(y_L)_{res}$ | Uncertainty in the resolution | 0.000029 | Rect | | | ∞ |
| $u(y_L)_{inst}$ | Uncertainty of the picoammeter | 0.015 | Nor | | | ∞ |
| $u(d)$ | Standard uncertainty in the measurement distance | 0.0012 | t | 689 | 0.064 | 920 |
| $u(d)_{rep}$ | Uncertainty in repeated measurements | 0.00032 | t | | | 4 |
| $u(d)_{res}$ | Uncertainty in the resolution | 0.00029 | Rect | | | ∞ |
| $u(d)_{inst}$ | Uncertainty in instrument distance | 0.0012 | Nor | | | ∞ |
| $u(r_a)$ | Standard uncertainty in the open aperture of integrating sphere | $1.5x10^{-6}$ | t | 75806 | 0.01 | ∞ |
| $u(r_a)_{rep}$ | Uncertainty in repeated measurements | 0.00 | t | | | 4 |
| $u(r_a)_{res}$ | Uncertainty in the resolution | $2.9x10^{-9}$ | Rect | | | ∞ |
| $u(r_a)_{inst}$ | Uncertainty of the CMM | $1.5x10^{-6}$ | Nor | | | ∞ |
| $u(r_d)$ | Standard uncertainty in the diameter of reference photometer head | $1.5x10^{-6}$ | t | 3 | $3.3x10^{-7}$ | ∞ |
| $u(r_d)_{rep}$ | Uncertainty in repeat measurement | 0.00 | t | | | 4 |
| $u(r_d)_{res}$ | Uncertainty of the resolution | $2.9x10^{-9}$ | Rect | | | ∞ |
| $u(r_d)_{inst}$ | Uncertainty of the CMM | $1.5x10^{-6}$ | Nor | | | ∞ |
| $u(c_r)$ | Uncertainty of uncorrelated components | 0.0011 | t | 1319 | 0.11 | 938 |
| $u_{repro}$ | Standard uncertainty of the measurement reproducibility | 0.00044 | t | | | 24 |
| $u_{stablity}$ | Standard uncertainty of stability of the integrating sphere | 0.001 | Nor | | | ∞ |
| $u_{straylight}$ | Standard uncertainty of stray light | 0.024 | Nor | 1 | 0.024 | ∞ |
| $u(y_{SL})$ | Standard uncertainty of the photocurrent | 0.064 | t | 0.00076 | 0.1 | ∞ |
| $u_c$ | Combined uncertainty | | Nor | | 0.35 | 9586 |
| *U; k=2, P=95%* | Expanded uncertainty | | Nor | | 0.70 | |

## Conclusions

The luminance responsivity standard system was conducted by the Photometry and Radiometry Laboratory at the VMI and was used for the realization of the unit of luminance responsivity based on a separate measurement of the spectral responsivity, the distances, and the sizes of apertures as described above. The overall uncertainty related to this calibration was estimated to be 0.70% at k=2 at luminance level of 1300 cd/m$^2$.

This method is also capable of calibrating the transfer standard luminance meter and luminance light integrating source.

## ACKNOWLEDGEMENTS

This work is financially supported by VMI as a part of the research program No.1685/QD-TDC.

The authors declare that there is no conflict of interest regarding the publication of this article.

## REFERENCES

[1] Vietnam Metrology Institute (2018), *Realization of the Luminance Unit.*

[2] Alex Ryer, Ultraviolet Light, Visible Light (1997), *Light Measurement Handbook*.

[3] Casimer De Cusatis (1998), *Handbook of Applied Photometry.*

[4] Center for Temperature and Light, Division of Physical Metrology (Kriss), *Luminance Responsivity, Luminance Meter (CMC 1.6.0)*.

[5] Center for Temperature and Light, Division of Physical Metrology (Kriss), *Luminance, Tungsten - Based Source (CMC 1.5.1)*.

[6] Yuqin Zong, E. Maria, K. Nadal Benjamin, C. Tsai, Cameron Miller (2018), *Nist Measurement Services: Photometric Calibrations,* NIST Special Publication 250-95.

[7] Adam Mazikowski (2013), "Measurements of spectral spatial distribution of scattering materials for rear projection screens used in virtual reality systems", *Metrology and Measurement Systems*, **20(3)**, pp.443-452, DOI: https://doi.org/10.2478/mms-2013-0038.

DOI: 10.31276/VJSTE.62(2).07-11



# Simple systems to characterize wastewaters - the case of biomethane potential

**Jean-Luc Vasel[1*], Hung Viet Pham[2]**

[1]*EcoService Company, Libramont, Belgium*

[2]*Key Laboratory of Analytical Technology for Environmental Quality and Food Safety Control (KLATEFOS), University of Science, Vietnam National University, Hanoi, Vietnam*

Received 10 March 2020; accepted 21 May 2020

***Abstract:***

**When the design or operation of wastewater treatment plans is considered, it is important to measure the polluting loads to be treated. These loads are calculated as the product of a daily volume of liquid waste and the average concentration of the pollutant. Of course, to do this, the sample must correctly represent the liquid effluent. Extensive analytical equipment can be used to characterize the numerous compounds contained within wastewaters with high accuracy but cheap, simple, and even sometimes mobile equipment are mostly used for the daily operations of treatment plans. In this regard, we present the use of a pH-respirometer, based on manometric methods, to characterize wastewaters that will be treated by aerobic biological systems. Another type of biological treatment system is based on anaerobic processes when the effluents have a high content of biodegradable organic compounds. Anaerobic digestion is very attractive as it is possible to produce a valuable gas (biogas) out of the waste instead of consuming energy and oxygen to realize an aerobic treatment. In this paper, we will present the meaning of biochemical methane potential (BMP) curves and compare those curves to respirometric curves such as biological oxygen demand (BOD) tests.**

***Keywords:*** **anaerobic digestion, biogas, BMP, treatment, wastewater.**

***Classification number:*** **2.2**

## Introduction

Manometric methods, also called respirometers, have been used for decades to measure the main parameters defining the organic pollution of wastewaters, such as BOD (biochemical oxygen demand) or $COD_b$ (biodegradable chemical oxygen demand). In fact, BOD (or $COD_b$) are not compounds but properties of wastewater. For known compounds, the theoretical $COD_b$ can be calculated. For example, with an aerobic system and tertiary compounds (C, O, H):

$$C_nH_aO_b + \left(n + \frac{a}{4} - \frac{b}{2}\right)O_2 \longrightarrow nCO_2 + \frac{a}{2}H_2O \qquad (1)$$

It results that $COD_b$ will serve to evaluate the quantity of oxygen that is needed to totally oxidize the compound. This information is very important as it is estimated that 80% of the energy consumed in a wastewater treatment plant (WWTP) is related to the oxygen needed for the treatment. As oxidation is an electron transfer reaction, it is also possible to estimate the potential chemical energy associated with the compound. BOD aims at the quantification of the fraction of the COD that can be oxidized by biochemical processes, mainly as biological growth of aerobic bacteria.

If we combine oxidation and bacterial growth for a substrate such as glucose, one discovers a reaction as in Eq. (2):

$$24C_6H_{12}O_6 + (59+5x)O_2 + (17-x)NH_3 \longrightarrow (17-x)C_5H_7O_2 + (59+5x)CO_2 + (110+2x)H_2O \qquad (2)$$

with a value for $x$ between zero (growth) and 17 (full oxidation), the value $\frac{(17-x)\times M_{C_5H_7NO_2}}{24\times M_{C_6H_{12}O_6}}$ is known as the cell yield, $Y$, here expressed in g/g. From this equation, we see that even for a fully biodegradable compound such as glucose, the cell yield value depends on the degree of use/oxidation of the substrate. In a continuous system where the

*Corresponding author: Email: jlvasel@ulg.ac.be

biomass is known (and high) there will be nearly no biomass production ($x$=17) and the substrate is oxidized to provide energy to the bacteria. In the present case, the concept of feed/microorganism ratio (F/M) expressed in energy (of equivalent $O_2$) is equal to $\frac{24\times192}{160\times(17-x)}$.

When we measure BOD, we perform a batch test starting with a high F/M ratio and wait until the formed biomass is partly or totally degraded by the endogenous process under aerobic conditions. Those concepts can be associated with the classical growth curve of micro-organisms as shown in the following figure (Fig. 1).

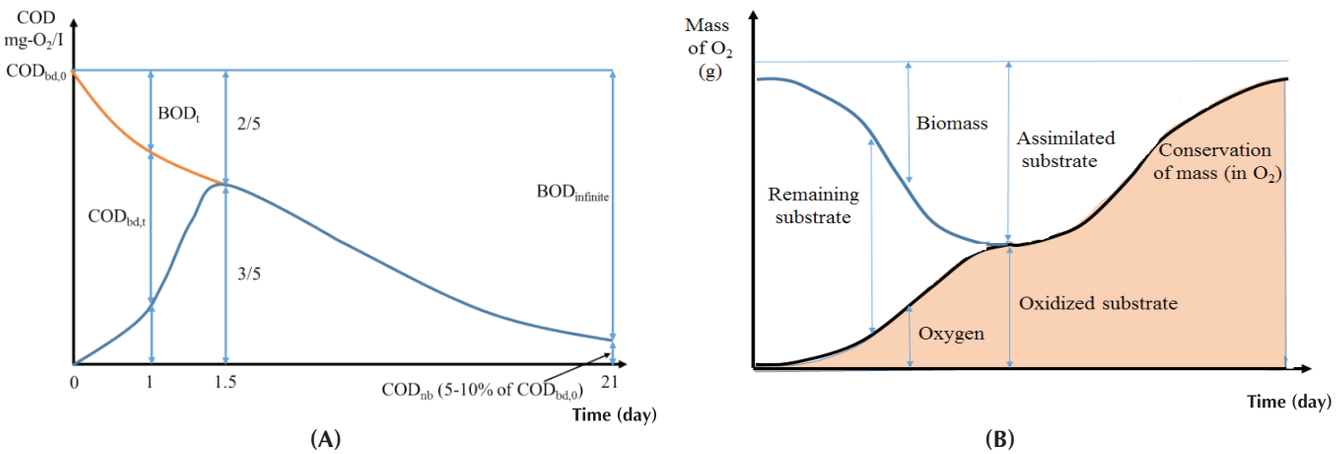


**Fig. 1. The relation between the growth curve and BOD test in terms of (A) COD and (B) mass of oxygen.**

In fact, when we perform a BOD test, we are measuring the cumulative oxygen consumption, which is the inverted part of the upper region of the graph. BMP tests have many similarities with BOD tests that will be described in the following paragraphs, but instead of a pressure decrease in the bottle due to the oxygen consumption, we observe a pressure increase due to biogas ($CO_2$ and $CH_4$) production. Holliger, et al. (2016) [1] recommend not to exceed 300 kPa in the bottle.

In this paper, the fundamental, as well as the applicability, of BMP tests in the characterization of wastewaters is presented.

## Materials and methods

BOD is usually measured in closed respirometers operating in batch mode. More precisely, it is a static gas, static liquid (GSS) type respirometer, which means that measurements are done in the gas phase (G) by manometric methods and liquid and gas are static (closed system). A mixing system, usually a magnet, is used to ensure that the liquid is mixed well and the equilibrium between gas and liquid phases is rapid.

BMP tests are usually done in GSS type bioreactors. Instead of measuring the consumption of a reactive ($O_2$) gas as in the BOD tests, the product of the serial reactions (biogas) is quantified in the BMP tests. As the quantity of expected biogas is much higher than the quantity of oxygen consumed, a pressure increase in the gas phase could have a negative effect on the metabolic activities, i.e. part of the biogas can be evacuated out of the bottle. If the biogas flows out of the bottle, we have a flowing gas, static liquid (GFS) system, which means that we need to measure the volume of collected gas (volumetric method) or the gas flow rate. Those methods must be combined with gas chromatography to measure the $CO_2/CH_4$ ratio, except if the $CO_2$ is adsorbed in a separate system and remaining $CH_4$ is measured subsequently.

Reliable and cheap sensors to measure gas flow rates over a very small range are not easy to find. For example, the measurement in the bioprocess control system is based on small volumetric equipment. Otherwise, storage can be done but the mass balance will be more complicated.

If the test is aiming at measuring the total production of methane (the energy-containing gas) a separation of $CO_2$ and $CH_4$ must be selected, most often using absorption of $CO_2$ in an alkaline solution. In the case of BOD, the quantity of $CO_2$ produced is small and can be neutralized in a small volume containing KOH directly integrated into the cap, which is not enough in the case of anaerobic systems.

Here, a simple concept of a BMP device that can

simultaneously measure biogas and $CH_4$ is demonstrated (Fig. 2). This system contains two bottles: the first bottle [bottle (1)] is an anaerobic reactor, in which the bacteria use organic compounds as food and release biogas; and the second [bottle (2)] is a $CO_2$-absorbed part that contains an alkaline solution, e.g. NaOH or KOH.

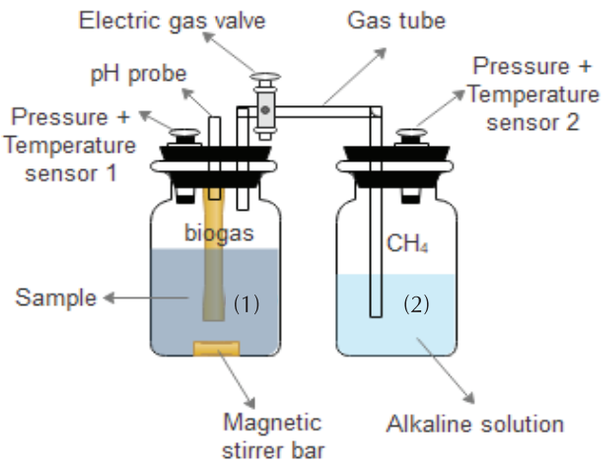


**Fig. 2. A simple concept of a BMP device.** Bottle (1) is the anaerobic reactor, and bottle (2) is the $CO_2$ absorbed part.

These bottles are connected by a gas tube. The movement of the gases between the two bottles is controlled by an electronic valve that is only opened when the pressure in bottle (1) is higher than a pre-set value, e.g. 1.2 bar. Then, the biogas will move through the gas pipe and be purged into the NaOH solution in bottle (2) to absorb all $CO_2$. The amount of gases could be calculated from the pressure and temperature data between valve opening times. To do that, each bottle is equipped with one pressure sensor and one temperature sensor.

Regarding the F/M ratio, it is quite different for aerobic and anaerobic measuring systems. In aerobic systems, we start with very high F/M ratios, but the kinetics are rapid and the $O_2$ consumption is fast. Usually, we consider that at the end of the test the final oxidation state is reached, including the oxidation of the synthetized biomass. The anaerobic metabolism is much slower and to reach a final stage within approximately the same period, it is necessary to start with a much lower F/M ratio. Often the inverse ratio, so-called ISR for inoculum-substrate ratio (expressed in g VS/g VS) is used in the BMP literature. Usually, tests are performed with an ISR in the range of 2 to 4. The BMP tests are performed at a loading rate of 20 to 60 g of total VS/l. If we take an average ISR ratio of 3, this will lead to a substrate loading rate of 5 to 15 g VS (substrate) per litre. If we compare with BOD tests, loading is less than 8 mg BOD/l in the case of the dilution method and in any case less than 2 g BOD/l for the manometric method.

In a closed anaerobic system, the electron quantity remains unchanged. Thus, the electrons (COD) contained in the substrate will be partly contained in the formed biomass and mostly in $CH_4$. As the yield factor, Y, is small in anaerobic systems, especially at a very small F/M ratio, we can assume that the final yield factor for $CH_4$ is close to 0.35 $Nm^3$ kg $COD^{-1}$ (degraded). Taking into account a usual F/M ratio of g COD/l, we should observe a biodegradable compound production of litres of methane at the end of the test. This means that the average volume of biogas should be around 500 ml at 35°C. Himanshu-Teagasc, et al. (2017) [2] compared manometric methods and automatic volumetric methods to measure the BMP.

Several norms, aimed at standardization of BMP tests, exist such as DIN 38414 TL8 (1985), ASTM D 5210 (1992), ASTM D 5511 (1994), ISO 11734 (1995), and ISO 15985 (2004) have been developed but various international efforts are still being made to harmonize the standards and to improve the accuracy of the method.

More details about the test methodology, including sample preparation, inoculum, number of replicates, blank assays, expression of the results and standard deviation, and criteria for the rejection of results can be found in Holliger, et al. [1].

## Resulfs and discussion

### *Applications of BMP tests*

We present some usual applications of BMP tests.

*Measurement of total quantity of biogas (methane) that can be produced from an effluent:* the BMP experimental curve has a pattern quite similar to a BOD curve (Fig. 3).

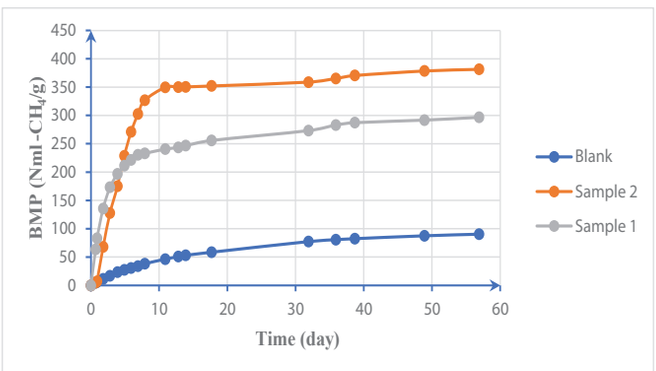


**Fig. 3. Example of the BMP curves in a set of BMP measurements with a sample of municipal solid waste (Sample 1) and cellulose (Sample 2).**

Consequently, similar equations can be used to describe the curve. One of those models may be written as:

$$BMP_t = BMP_{infinite}\left(1 - e^{-Kt}\right) \quad (3)$$

for which various fitting methods can be used. Such fittings will yield $BMP_{infinite}$ (which is the asymptote of the curve) and *K,* which is an apparent first-order kinetic coefficient; both useful information. Of course, the BMP of the blank (the seeming) must be deducted from the initial curve. More detailed methodology to fit these types of models, including sensitivity analysis, can be found in Da Silva, et al. (2018) [3].

If the elemental composition of the substrate is known, for example assuming the formula $C_nH_aO_bN_c$, the anaerobic degradation can be written as:

$$C_nH_aO_bN_c + \left(n - \frac{a}{4} - \frac{b}{2} + \frac{3c}{4}\right)H_2O \longrightarrow \left(\frac{n}{2} + \frac{a}{8} - \frac{b}{4} - \frac{3c}{8}\right)CH_4 + \left(\frac{n}{2} - \frac{a}{8} + \frac{b}{4} + \frac{3c}{8}\right)CO_2 + cNH_3 \quad (4)$$

If we consider the BMP as the volume of dry methane (at 273.15 K and 1 atm) per g of VS substrate, then the BMP value can be calculated as:

$$BMP = 22400 \times \frac{\left(\frac{n}{2} + \frac{a}{8} - \frac{b}{4} - \frac{3c}{8}\right)}{(12n + a + 16b + 14c)} \quad (5)$$

For an anaerobic system, the same tertiary compound as in Eq. 1 will be transformed into biogas as:

$$C_nH_aO_b + \left(n - \frac{a}{4} - \frac{b}{2}\right)H_2O \longrightarrow \left(\frac{n}{2} + \frac{a}{8} - \frac{b}{4}\right)CH_4 + \left(\frac{n}{2} - \frac{a}{8} + \frac{b}{4}\right)CO_2 \quad (6)$$

The molar ratio can be deducted from Eq. (6):

$$\frac{n_{CH_4}}{n_{CO_2}} = \frac{\left(\frac{n}{2} + \frac{a}{8} - \frac{b}{4}\right)}{\left(\frac{n}{2} - \frac{a}{8} + \frac{b}{4}\right)} = \frac{4n + a - 2b}{4n - a + 2b} \quad (7)$$

Thus, the $CH_4/CO_2$ ratio depends on *n*, *a*, and *b* values. For carbon (*n*=1), the ratio is equal to $\frac{4 + \frac{a}{n} - \frac{2b}{n}}{4 - \frac{a}{n} + \frac{2b}{n}}$. Moreover if we compare equation (6) to equation (1) we have $n_{CH_4} = \left(\frac{n}{2} + \frac{a}{8} - \frac{b}{4}\right) = \frac{n_{O_2}}{2} = COD$ (expressed in $\frac{1}{2}$ mol-$O_2$/l). The combination of both ratios yields *a* and *b* values.

In fact, biogas also contains some water. The BMP is defined as the quantity of dry methane that is produced by the degradation of 1 g of VS substrate. If the water vapor is not removed before analysis, then a correction can be made to calculate the contribution of water vapor in the biogas. Strömberg, et al. (2014) [4] suggested the following equation to calculate this contribution:

$$P_w = 10^{8.1962 - \frac{1730.63}{T - 39.724}} \quad (8)$$

with $P_w$ being the vapor pressure (mbar) and T in Kelvin.

*Distinguishing some fractions of the substrate (fractionation) in the conditions of the test:* Pearse, et al. [5] suggested some changes to the methodology to apply BMP tests to landfilled municipal solid wastes. To quantify the kinetic (and parameters) of the main processes, of course, the *K* value of Eq. (3) already provides an evaluation of an apparent first-order kinetic equation. But more sophisticated models can be used, as will be presented.

*Rapid evaluation of the effects of some operating parameters (pH, temperature, F/M ratio…) of substrates and co-substrates:* for example, Biswanath Sahaa, et al. (2018) [6] found an optimal F/M ratio of 2, which is rather high, to degrade Ageratum conyzoides. Hobbs, et al. (2018) [7] also tested the optimal ratio of inoculum and substrate for various food wastes using BMP tests and obtained an optimal F/M ratio of 1.42 g COD (substrate)/g VS (inoculum). Tan, et al. (2018) [8], using BMP tests, studied the inhibitory effect of ammonia and/or sulphide on the methane yield with acetate and propionate as a carbon source. Krause, et al. (2016) [9], studied the optimal ratio between waste and seeming and obtained, in this case, an optimum of 3 g COD/g VS. We can observe that those tests were performed at ISR values much lower than the recommended values for BMP tests. To test the optimal proportion of various substrates on the efficiency of a digester, BMP tests were performed by Grosser (2018) [10] that studied the optimal ratio between sewage sludge, organic fraction of municipal solid waste, and grease trap sludge, to increase methane production. Rodrigues, et al. (2019) [11] evaluated the effect of temperature and municipal waste particle size also using BMP tests.

### *Possible combinations of BMP tests with other tools*

Other developments can be considered as Fuzzy logic utilization to get more rapidly the results of the tests. Fuzzy logic is an interesting tool to predict the final values of BOD or BMP test using the time evolution of some parameters, without using sophisticated metabolic models.

*Using of databases to collect the results of BMP tests in order to provide preliminary estimates of biogas potential for many substrates, co-substrates, and their mixtures:* Holliger, et al. (2016) [1] recommend proceeding regularly at positive controls on the substrate whose BMP are well known, such as micro-crystalline cellulose or tributyrin, to check the equipment and quality of the seeming. Rodrigues, et al. (2019) [11] compared methods to estimate BMP results from some preliminary analyses (elemental analysis, organic fraction, COD or IR spectrum). Suitable results

could be obtained with multivariable regressions, especially if biodegradability (particularly lignin content) is taken into account. Edwiges, et al. (2018) [12] studied the BMP of various fruit and vegetable wastes and predicted the result using multiregressions. That work suggested that HCV (high calorific value) could be one interesting regression factor. To facilitate the development of such databases, such preliminary analyses should be done systematically.

*Combination of BMP test with dynamic mathematical models in order to fit some parameters of those models:* aerobic treatment processes have been described by mathematical models including stoichiometry and kinetics of the various biological processes. For example, the ASM (activated sludge models) of IWA can also be used to describe respirometers as aerobic bioreactors and use the models to quantify some characteristics of the substrate such as rapidly or slowly biodegradable fractions of a complex substrate. This is called fractionation of the substrates and this tool is now very useful in the field of modelling and control of bioreactors.

Similarly, mathematical models such as ADM1 (Anaerobic Digestion Model 1) have been developed to describe anaerobic bioreactors, but it seems that, so far, the link to describe the operation of BMP reactors has not been developed. In this case, the BMP system would be seen as a smart sensor system.

## Conclusions

BOD tests have been developed more than a century ago and used across many applications. The development of dynamic mathematical models to describe the behaviour of aerobic bioreactors yielded the development of various types of respirometers, including GSS-type ones such as BOD meters. Using these in combination with mathematical models to characterize some fractions of substrates and to fit parameters of the models, these respirometers can be called a smart sensor.

BMP tests were developed more recently, but the rapid development of anaerobic digesters to produce green energy should pave the way to the development of smart BMP sensors.

## ACKNOWLEDGEMENTS

This work was supported by Wallonie Bruxelles International (WBI) under project No. 15 and the Vietnam National University, Hanoi (VNU-Hanoi) under project code QG.17.18.

The authors declare that there is no conflict of interest regarding the publication of this article.

## REFERENCES

[1] C. Holliger, et al. (2016), "Towards a standardization of biomethane potential tests", *Water Science & Technology*, **74(11)**, pp.2515-2522.

[2] H. Himanshu-Teagasc, et al. (2017), "Factors controlling headspace pressure in a manual manometric BMP method can be used to produce a methane output comparable to AMPTS", *Bioresource Technology*, **238**, pp.633-642.

[3] Da Silva, et al. (2018), "Biochemical methane potential (BMP) tests: Reducing test time by early parameter estimation", *Waste Management*, **71(IV)**, pp.19-24.

[4] S. Strömberg, et al. (2014), "Towards eliminating systematic errors caused by the experimental conditions in Biochemical Methane Potential (BMP) tests", *Waste Management*, **34(11)**, pp.1939-1948.

[5] L.F. Pearse, et al. (2018), "Towards developing a representative biochemical methane potential (BMP) assay for landfilled municipal solid waste - a review", *Bioresource Technology*, **254**, pp.312-324.

[6] Biswanath Sahaa, et al. (2018), "Biochemical methane potential (BMP) test for Ageratum conyzoides to optimize ideal food to microorganism (F/M) ratio", *Journal of Environmental Chemical Engineering*, **6(4)**, pp.5135-5140.

[7] S.R. Hobbs, et al. (2018), "Enhancing anaerobic digestion of food waste through biochemical methane potential assays at different substrate: inoculum ratios", *Waste Management*, **71**, pp.612-617.

[8] L. Tan, et al. (2018), "Effects of ammonium and/or sulfide on methane production from acetate or propionate using biochemical methane potential tests", *J. Biosci. Bioeng.*, **127(3)**, pp.345-352.

[9] M.J. Krause, et al. (2016), "*Critical review of the methane generation potential of municipal solid waster", Critical Reviews in Environmental Science and Technology*, **46(13),** pp.1117-1182.

[10] A. Grosser (2018), "Determination of methane potential of mixtures composed of sewage sludge, organic fraction of municipal waste and grease trap sludge using biochemical methane potential assays. A comparison of BMP tests and semi-continuous trial results*", Energy*, **143**, pp.488-499.

[11] R.P. Rodrigues, et al. (2019), "Comparative analysis of methods and models for predicting biochemical methane potentiel of various organic substrates", *Science of the Total Environment*, **649**, pp.1599-1608.

[12] T. Edwiges, et al. (2018), "Influence of chemical composition biochemical methane potential of fruit and vegetable waste", *Waste Management*, **71(IV)**, pp.618-625.

DOI: 10.31276/VJSTE.62(2).12-18

# Fabrication of perovskite lanthanum orthoferrite as a photocatalyst for controlled atom transfer radical polymerization of methacrylate monomers toward an electrolyte material for lead acid batteries

**Huong Thi Le[1, 2], Tien Anh Nguyen[2], Thu Hoang Vo[1], Michał Michalak[3], Tam Hoang Luu[4], Ha Tran Nguyen[1, 4*]**

[1]*National Key Laboratory of Polymer and Composite Materials, University of Technology, Vietnam National University, Ho Chi Minh city, Vietnam*

[2]*Faculty of Chemistry, Ho Chi Minh city University of Education, Vietnam*

[3]*Centre of Polymer and Carbon Materials, Polish Academy of Sciences, Poland*

[4]*Faculty of Materials Technology, University of Technology, Vietnam National University, Ho Chi Minh city, Vietnam*

Received 10 January 2020; accepted 8 April 2020

***Abstract:***

**Lanthanum orthoferrite ($LaFeO_3$) photocatalysts were synthesized by a facile and cost-effective co-precipitation method via the hydrolysis of La (III) and Fe (III). The characteristics of $LaFeO_3$ were investigated through thermogravimetric analysis (TGA), X-ray diffraction (XRD), UV-Vis diffuse reflectance spectroscopy (DRS), vibrating sample magnetometry (VSM), and transmission electron microscopy (TEM). During the investigation of the applicability of $LaFeO_3$ as a photocatalyst for the atom transfer radical polymerization (ATRP) of methyl methacrylate monomer under UV irradiation, the obtained poly(methyl methacrylate) exhibited a high molecular weight and narrow polydispersity index. In addition, the $LaFeO_3$ can be recovered via application of a magnetic field and reused for the atom transfer radical polymerization process.**

***Keywords:*** **ATRP, lanthanum orthoferrite ($LaFeO_3$), methacrylate, photocatalysts.**

***Classification number:*** **2.2**

## Introduction

One of the most important achievements made by humanity in the 20th century is the development and application of powerful synthetic polymeric materials. Polymeric materials have since been widely used in daily life due to their superior mechanical properties, low cost, and variety of applications such as in chemicals, electricity, electronics, and biomedicine.

A polymer's properties depend on their molecular weight, multiple dispersion, and molecular structure; all of which determine its various applications. Further, these factors are influenced by the method of synthesis. ATRP is a process that allows control of the molecular weight according to the polymer's original design and multi-level narrow dispersion. ATRP is a useful and widely used method within a larger system of polymer-free polymerization methods. Traditional ATRP is advantageous because the method is cheap and easy to implement via readily available catalysts on the market. However, its weakness is the existence of a residual metal that is hard to remove or exclude from the product [1] . This factor limits the application of the polymer product in fields requiring a high level of cleanliness, such as medicine and biomedicine [2].

Because of this disadvantage existing in traditional ATRP, a method called Organocatalyzed atom transfer radical polymerization (O-ATRP) was created, which uses organic catalyst alternatives in place of the metal complex

*Corresponding author: Email: nguyentranha@hcmut.edu.vn

catalysts. The advantages of O-ATRP are the reliable control of the molecular weight and polymer dispersion variability, and the organic catalyst can be completely separated from the polymer product in a straightforward manner by centrifugation or precipitation in suitable solvent systems [3]. However, limitations of O-ATRP do exist, such as difficulty controlling high molecular weight products. So, the goal of this study is to find new photocatalysts that address the difficulty in controlling high molecular weight. In addition, such a well-controlled obtained polymer could be applied to electrolyte materials in rechargeable batteries.

In recent years, perovskite-type materials have been of great interest and importance because of their excellent potential as solid fuel [4], solid electrolytes, actuators, electromechanical devices, and transducers [5] due to their crystal structure, magnetism, electric conductivity, piezoelectric, electro-optic properties, and catalytic activity. However, studies about the photocatalytic performance of perovskites for the polymerization process have not yet been reported. The catalytic oxidation and surface electronic states of $LaFeO_3$ based on a typical $ABO_3$-type perovskite structure has been previously studied [6]. The excellent gas sensitivity and catalytic activity of $LaFeO_3$ has also been well investigated due to its high stability, non-toxicity, and small band gap energy [7]. In previous studies, $LaFeO_3$'s band gap was found to be in the range of 2.12 - 2.67 eV [6]. With this small band gap, $LaFeO_3$ has been used as a photocatalyst for the decomposition of water [8] and as a photocatalyst for the photochemical decomposition of some organic dyes under visible light irradiation [9]. In addition, $LaFeO_3$ has a magnetic nature [10] that allows straightforward recovery of the catalysts after the reaction.

While $LaFeO_3$ is a potential photocatalyst, there appears to be no other research in the world, to the best of the authors' knowledge, about the use of $LaFeO_3$ as a photocatalyst for the polymerization of free radicals.

## Materials and methods

### *Materials*

$La(NO_3)_3.6H_2O$, $Fe(NO_3)_3.9H_2O$, NaOH, methyl methacrylate (MMA), Tetrahydrofuran (THF), and Phenyl 2-bromo-2-methylpropanoate ($C_{10}H_{11}BrO_2$) were used in this work.

### *Instrumentation*

Thermal analysis of the sample was recorded on a DTG-60H (Japanese Shimadzu) at the Faculty of Chemistry, Ho Chi Minh city University of Education, in a dry air environment with a temperature rise of 10ºC/min and a maximum temperature of 1100ºC.

X-ray diffraction was measured on a D8 ADVANCE (Germany) at the National Key Laboratory of Polymer and Composite Materials, University of Technology, Vietnam National University, Ho Chi Minh city, with Cu-Kα radiation (λ=1.5406 Å), 2θ=10-80º, 0.03º measurement step, and dwell time every 1 s.

Microstructural and morphological images were taken by TEM on a JEOL-1400 (Japan) at the National Key Laboratory of Polymer and Composite Materials, University of Technology, Vietnam National University, Ho Chi Minh city.

The diffuse reflectance UV-Vis (DRS) of the material was determined by a JASCO 500 at the Institute of Applied Materials Science, which was fitted with a ISV-469 solid sample meter and using the $BaSO_4$ standard sample.

$^1$H-NMR spectra were recorded in deuterated chloroform ($CDCl_3$) with tetramethylsilane as an internal reference on a Bruker Avance 500 MHz NMR spectrometer.

The spectra from gel permeation chromatography (GPC) were recorded at the National Key Laboratory of Polymer and Composite Materials, University of Technology, Vietnam National University, Ho Chi Minh city, on a polymer PL-GPC 50.

### *Synthesis of lanthanum orthoferrite ($LaFeO_3$)*

$LaFeO_3$ nanomaterials were synthesized by slowly adding a small mixture of 1:1 $La(NO_3)_3.6H_2O$:$Fe(NO_3)_3.9H_2O$ into a cup of boiling water under constant magnetic stirring. After the salt mixture dissolved, boiling was continued for another 5-7 min, and then the mixture was allowed to cool. After slowly adding the NaOH solution to the mixture obtained above, excess NaOH was taken to collect the excess precipitates of the $La^{3+}$ and $Fe^{3+}$ cations (the filtered water was tested with a few drops of phenolphthalein). The precipitate was stirred on a stirrer for about 20 min, then filtered and washed several times with distilled water and dried naturally at room temperature for 3 d. After drying, the precipitate was finely ground and then heated under

air pressure from room temperature to several different temperatures to check the crystallization perfection and to create a homogenous phase of $LaFeO_3$. The heating rate was 10ºC/min.

### *General synthesis of polymers*

Polymer methyl methacrylate (PMMA) was synthesized via UV light-induced ATRP using a Phenyl 2-bromo-2-methylpropanoate (PhBMP) initiator and $LaFeO_3$ as the photocatalyst. In a typical experiment, 10.01 mg (41 µmol) of PhBMP initiator was placed in a 25 ml flask, and 1 ml of degassed THF was added by a syringe. The solution was stirred until it became a homogeneous solution. Then, the MMA monomer (0.44 ml, 4.1 mmol) and $LaFeO_3$ (1 mg, 0.4 µmol) were added separately. The mixture was degassed by three freeze-pump-thaw cycles. The solution was continuously stirred until it became homogeneous and placed in a UV-box (wavelength of 365 nm) for 24 h at room temperature. Finally, the resulted polymer solution was precipitated in cold methanol, followed by drying under vacuum, to give the desired product.

## Results and discussion

### *Structure and properties of $LaFeO_3$*

Figure 1 shows the DSC and TGA curves for the sample prepared by co-precipitation. A 19.16% weight loss of the entire sample can be seen during the heating process from room temperature to 1000°C. Many reactions are observed from the DrTGA curve, occurring from about 40ºC to 800ºC. All of these processes can be distinguished into three phases.

Phase 1 occurs from 40ºC to about 200ºC. In this phase, a weight loss of 8.344% took place, which corresponds to an endothermic peak in the DSC curve at 98.59ºC caused by surface desorption and dehydration [11]. The second phase of mass reduction occurred between 400ºC and 500ºC with a mass loss of 7.783%, which corresponds to an endothermic peak at 462.19ºC due to nitrate-based pyrolysis [12]. The third mass reduction phase, from 500ºC to 800ºC, includes the pyrolysis hydroxides of $La(OH)_3$, $Fe(OH)_3$, and base-carbonate salt pyrolysis of $La_2(CO_3)_{3-x}(OH)_{2x}$. The occurrence of base-carbonate salts in the precipitation after drying of rare earth element ions, especially $La^{3+}$, has been published in the research of Nagashima Kozo's group [13]. At 800ºC and upwards, the TG path is almost horizontal. From the thermal analysis scheme, the sample heating temperature is 900°C. Investigation of single-phase $LaFeO_3$ formation was analysed by X-ray diffraction. The results are shown in Fig. 2. The XRD diagram of $LaFeO_3$ was taken at 900ºC. The diagram shows only single-crystal phase peaks of the $LaFeO_3$ perovskite and no impurities peaks were

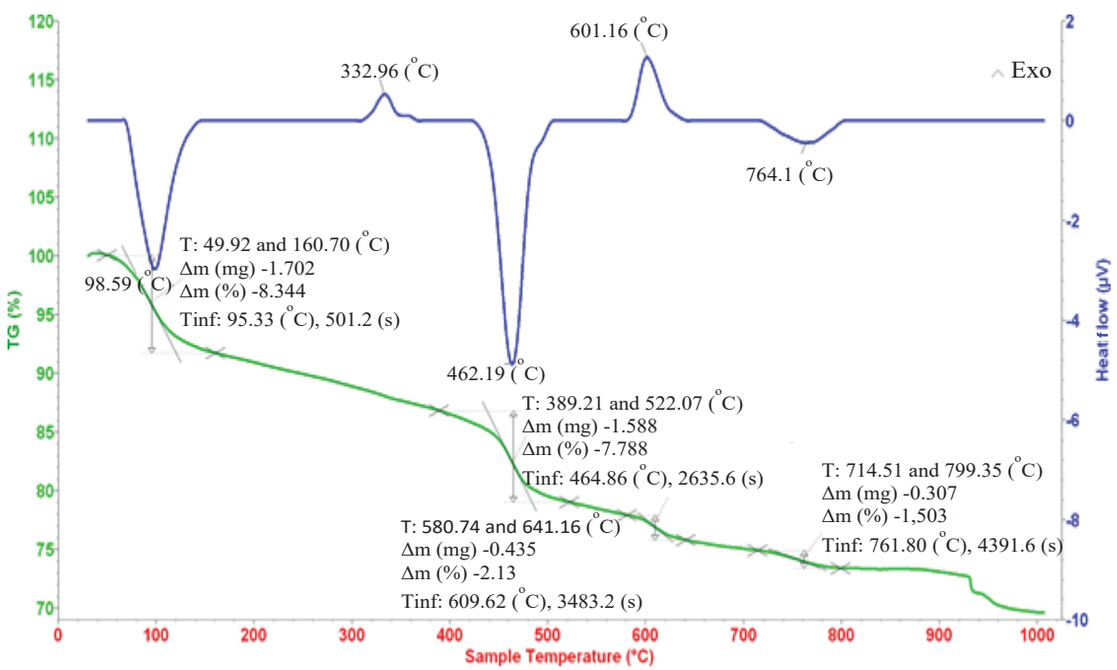


**Fig. 1. Thermal analysis diagram of $LaFeO_3$.**

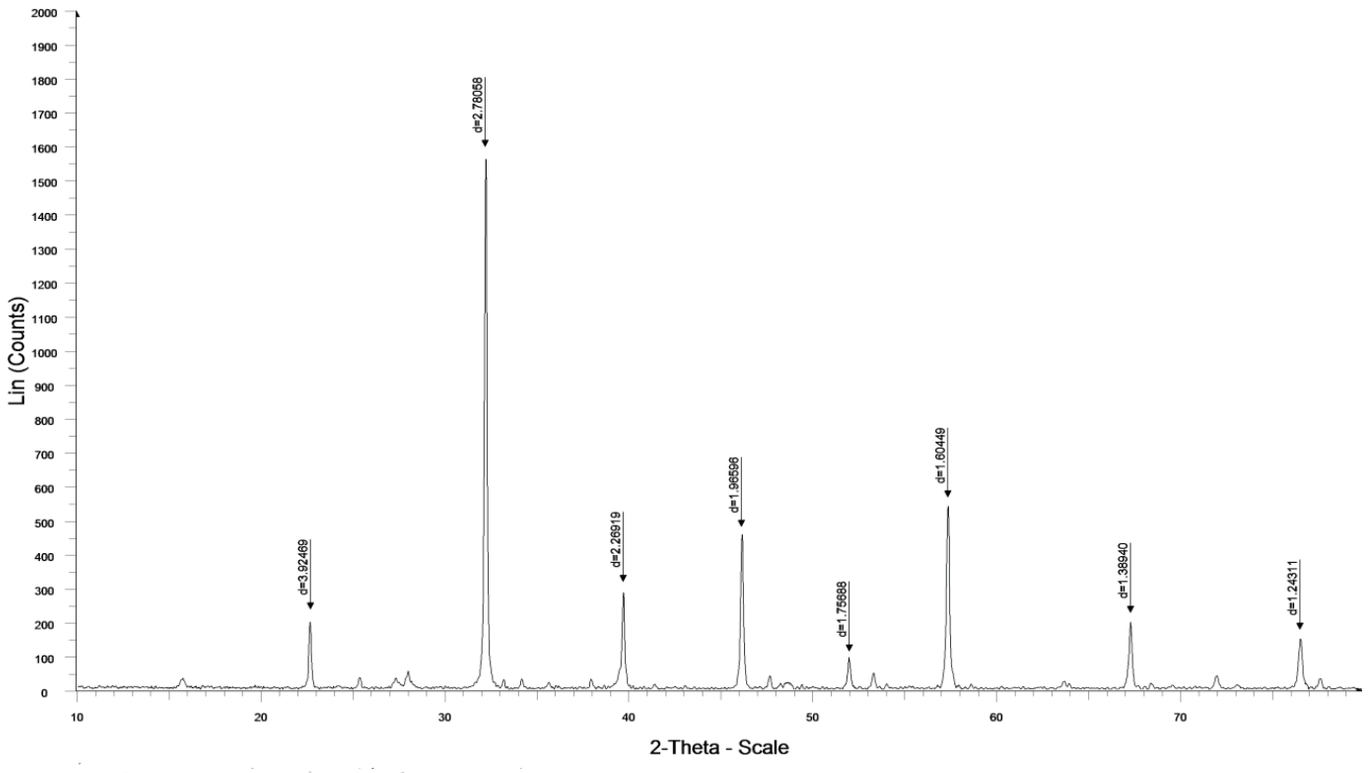


(A)

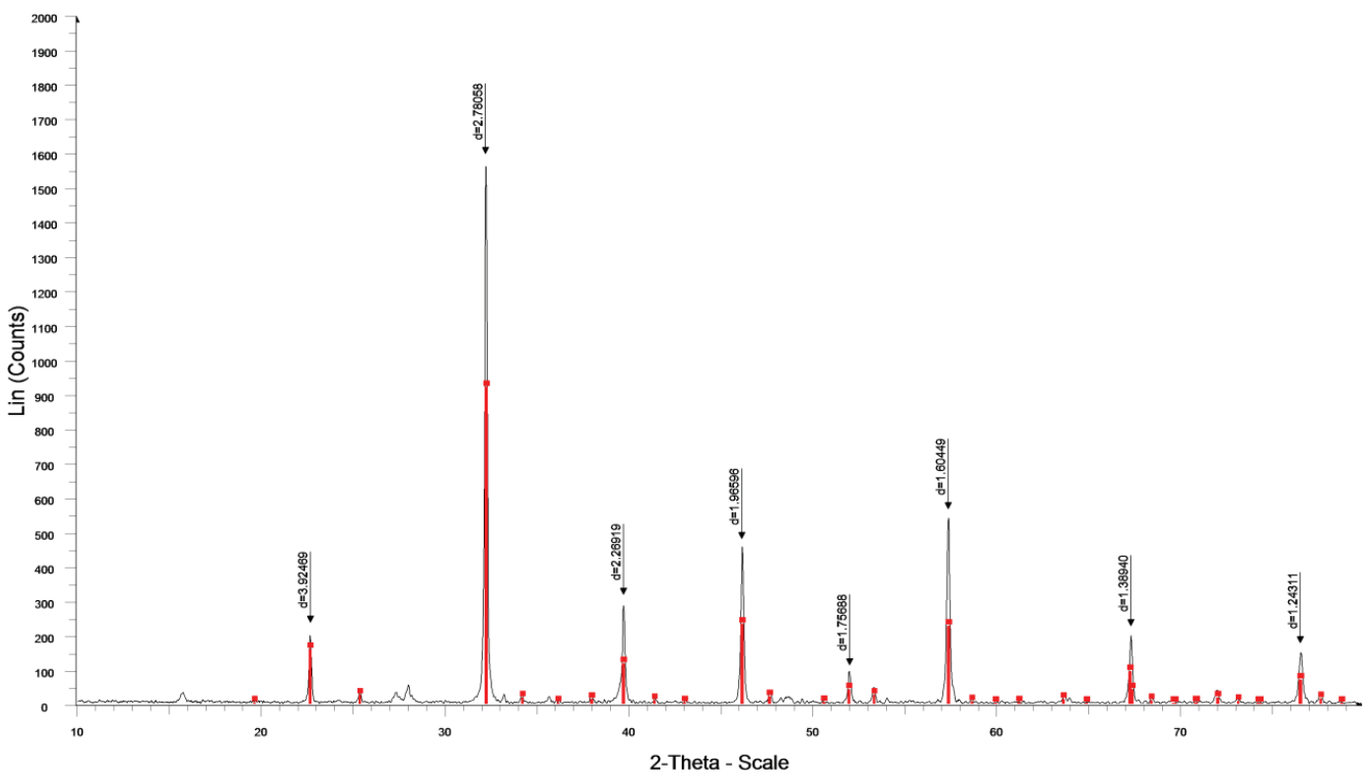


(B)

**Fig. 2. (A) XRD spectra of $LaFeO_3$ obtained at 900°C; (B) XRD spectrum of $LaFeO_3$ obtained overlapped with the standard spectrum.**

observed. The TEM results of the sample baked at 900°C showed $LaFeO_3$ nanoparticles have a spherical shape and are 50-70 nm in size (see Fig. 3).

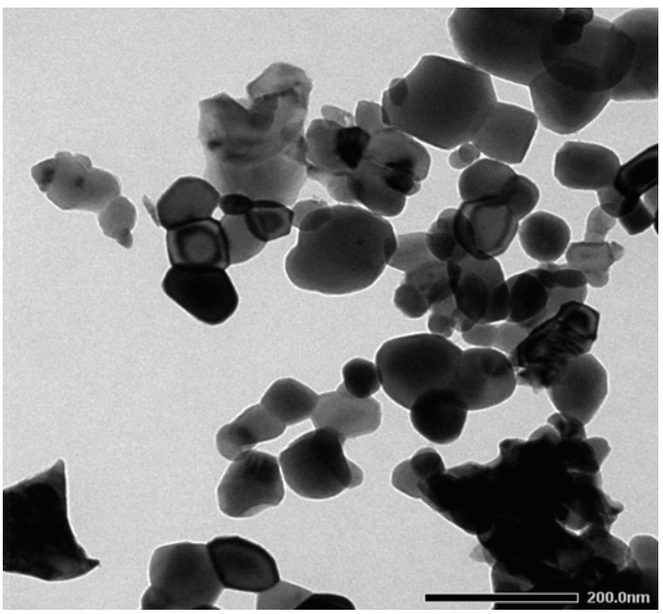


**Fig. 3. TEM image of $LaFeO_3$ prepared by the co-precipitation method, followed by calcination at 900°C.**

Figure 4 shows the magnetization curves of $LaFeO_3$ nanopowders measured at room temperature by VSM. The magnetic characteristics of $LaFeO_3$ nanomaterials samples at room temperature after calcination at 900°C show that the magnetic resistance (coercive field) value $H_C$=35.375 Oe, proving that the synthesized $LaFeO_3$ material is a soft magnetic material.

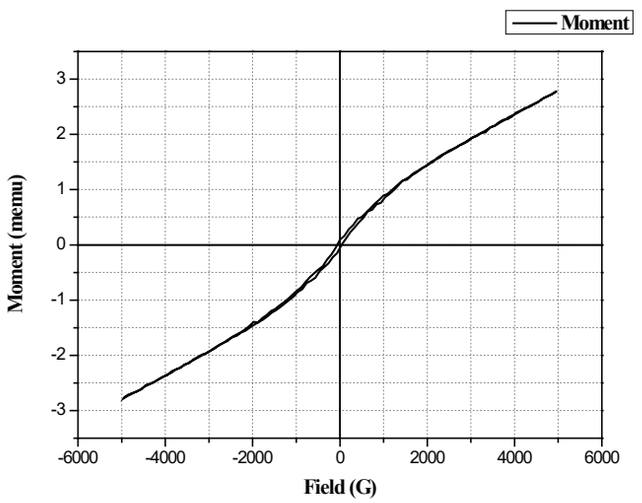


**Fig. 4. The room temperature hysteresis loop of $LaFeO_3$ after calcination at 900°C.**

The UV-Vis spectrum of the $LaFeO_3$ nanopowder is shown in Fig. 5. The UV-Vis results show that the catalyst can absorb spectral energy over a wide range between 350-800 nm and that $LaFeO_3$ absorbs maximum light at 411 nm with 93.63% absorption. These results prove that $LaFeO_3$ is a potential catalyst in the photocatalytic field.

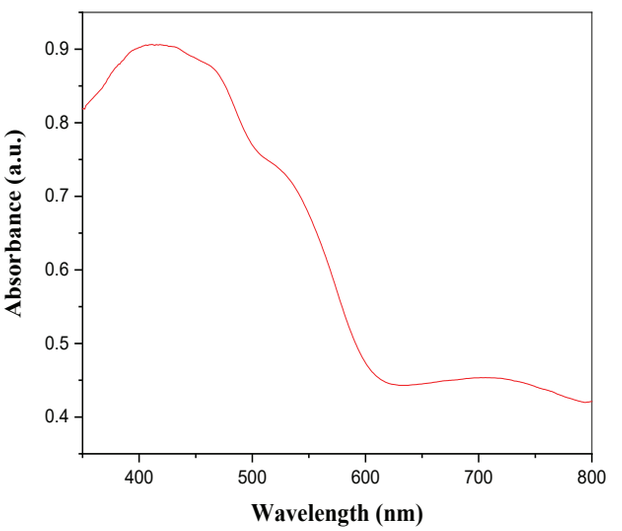


**Fig. 5. DR UV-Vis spectra of 900°C-activated $LaFeO_3$.**

A regression equation was established using the UV-Vis results of the ferrite perovskite $LaFeO_3$, with y=5.8361x-10.56 and a correlation coefficient $R^2$=0.9501. Based on the onset optical absorption (Fig. 6), the band gap of the $LaFeO_3$ material can be estimated to be about 1.809 eV.

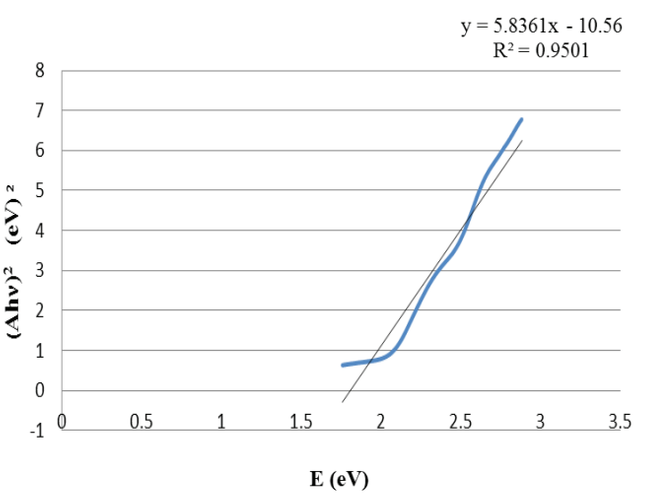


**Fig. 6. The regression equation from UV-Vis of the ferrite perovskite $LaFeO_3$.**

***Investigation of the possibility of polymerization of methyl methacrylate***

According to photocatalysts used in ATRP-based research from Hawker, Matyjaszewski, and Miyake, we used $LaFeO_3$ as the photocatalyst for ATRP of the MMA monomer. The ATRP of the MMA monomer involves photoexcitation of the $LaFeO_3$ catalyst to an excited state of $LaFeO_3$ under UV irradiation. The proposed mechanism of polymerization is illustrated in Fig. 7.

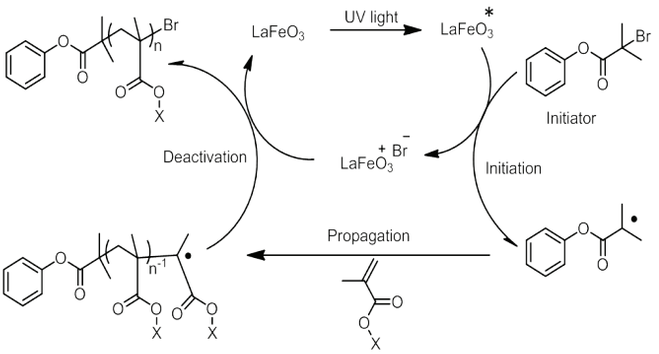


**Fig. 7. Proposed mechanism for ATRP using $LaFeO_3$.**

The obtained PMMA was characterized via $^1$H-NMR, as seen in Fig. 8, to determine its structure. The polymerization of MMA using the photocatalyst $LaFeO_3$ was carried out with the ratio [Monomer]:[Initiator]:[$LaFeO_3$]=100:1:0.1. The obtained polymer was precipitated in cold methanol and characterized by GPC to determine the average molecular weight. It should be noted that the molecular weight of the formed polymer is approximately equal to the designed molecular weight. The results of MMA polymerization using the $LaFeO_3$ catalyst are presented in Table 1.

**Table 1. Macromolecular characteristics of PMMA synthesized by ATRP using the $LaFeO_3$ catalyst.**

| [MMA]:[I]:[$LaFeO_3$] | $M_n$ (g/mol) | $M_w$ (g/mol) | Dispersity (PDI) |
|---|---|---|---|
| [100]:[1]:[0.1] | 35740 | 38200 | 1.09 |

## Conclusions

$LaFeO_3$ nanomaterials were synthesized by co-precipitation through the slow hydrolysis of $La^{3+}$ and $Fe^{3+}$ cations in boiling water with NaOH as the precipitating agent. $LaFeO_3$ nanomaterials formed after calcination and

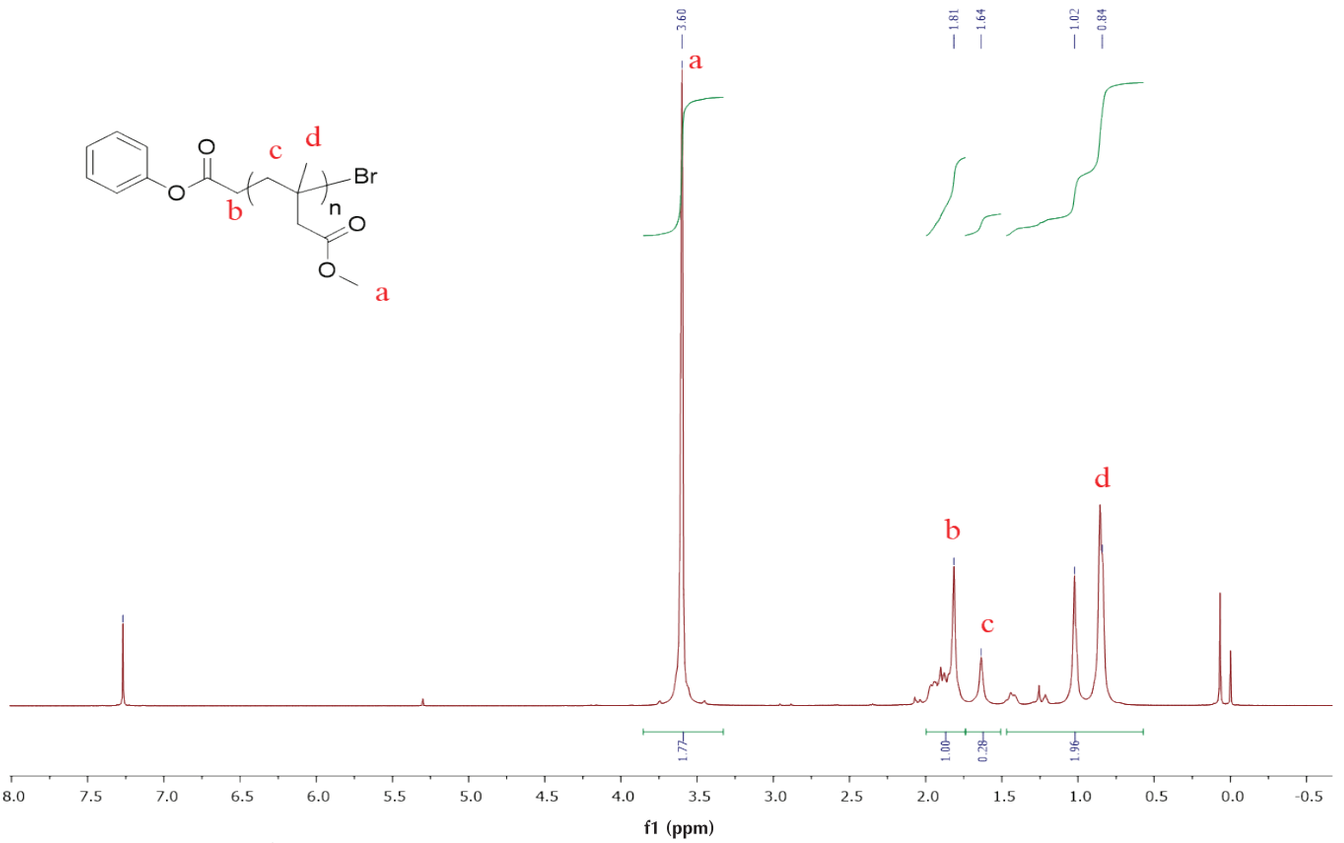


**Fig. 8. $^1$H-NMR spectra of PMMA.**

precipitation at 900°C with particle sizes of 50-70 nm. $LaFeO_3$ proved to be an efficient catalyst for ATRP, which produced polymethacrylates with a controlled molecular weight of 38200 g/mol, as well as a narrow polydispersity of 1.09 by UV irradiation. The obtained PMMA exhibited a high molecular weight and narrow polydispersity index. In addition, the $LaFeO_3$ was recovered via magnet field application and reused for the atom transfer radical polymerization process. Furthermore, the well-controlled PMMA could be investigated as a solid electrolyte material for rechargeable batteries in a prospective research study.

## ACKNOWLEDGEMENTS

This research is funded by University of Technology, Vietnam National University, Ho Chi Minh city, under grant number T-CNVL-2019-24.

The authors declare that there is no conflict of interest regarding the publication of this article.

## REFERENCES

[1] C. Cheng, E. Khoshdel, K.L. Wooley (2006), "Facile one-pot synthesis of brush polymers through tandem catalysis using Grubbs' catalyst for both ring-opening metathesis and atom transfer radical polymerizations", *Nano Lett.*, **6(8)**, pp.1741-1746.

[2] D.J. Siegwart, J.K. Oh, K. Matyjaszewski (2012), "ATRP in the design of functional materials for biomedical applications", *Prog. Polym. Sci.*, **37(1)**, pp.18-37.

[3] N.J. Treat, H. Sprafke, J.W. Kramer, P.G. Clark, B.E. Barton, J.R.D. Alaniz, B.P. Fors, C.J. Hawker (2014), "Metal-free atom transfer radical polymerization", *J. Am. Chem. Soc.*, **136(45)**, pp.16096-16101.

[4] F. Bidrawn, S. Lee, J.M. Vohs, R.J. Gorte (2008), "The effect of Ca, Sr, and Ba doping on the ionic conductivity and cathode performance of $LaFeO_3$", *J. Electrochem. Soc.*, **155(7)**, pp.660-665.

[5] X. Liu, H. Ji, Y. Gu, M. Xu (2006), "Preparation and acetone sensitive characteristics of nano-$LaFeO_3$ semiconductor thin films by polymerization complex method", *Mater. Sci. Eng. B Solid-State Mater. Adv. Technol.*, **133(1-3)**, pp.98-101.

[6] K.M. Parida, K.H. Reddy, S. Martha, D.P. Das, N. Biswal (2010), "Fabrication of nanocrystalline $LaFeO_3$: an efficient sol-gel auto-combustion assisted visible light responsive photocatalyst for water decomposition", *Int. J. Hydrogen Energy*, **35(22)**, pp.12161-12168.

[7] S. Li, L. Jing, W. Fu, L. Yang, B. Xin, H. Fu (2007), "Photoinduced charge property of nanosized perovskite-type $LaFeO_3$ and its relationships with photocatalytic activity under visible irradiation", *Mater. Res. Bull.*, **42(2)**, pp.203-212.

[8] S.N. Tijare, M.V. Joshi, P.S. Padole, P.A. Mangrulkar, S.S. Rayalu, N.K. Labhsetwar (2012), "Photocatalytic hydrogen generation through water splitting on nano-crystalline $LaFeO_3$ perovskite", *Int. J. Hydrogen Energy*, **37(13)**, pp.10451-10456.

[9] M. Ismael, M. Wark (2019), "Perovskite-type $LaFeO_3$: photoelectrochemical properties and photocatalytic degradation of organic pollutants under visible light irradiation", *Catalysts*, **9(4)**, DOI: 10.3390/catal9040342.

[10] N.A. Tien, P.P.H. Nhan (2016), "Synthesis of $LaFeO_3$ magnetic nanomaterials by co-precipitation method", *Journal of Science - Ho Chi Minh city University of Education*, **3(81)**, pp.5-11 (in Vietnamese).

[11] N.A. Tien, N.T.M. Thuy (2015), "Synthesis of $LaFeO_3$ magnetic nanomaterials by sol-gel method using albumen", *Vietnam Journal of Chemistry*, **43(1)**, pp.161-170 (in Vietnamese).

[12] D.T.A. Thu, H.T. Giang, D.H. Manh, N.N. Toan (2010), "Research on method to synsthesize $LaFeO_3$ gas-sensitive material by sol-gel method to create complex applications in alcohol vapor sensor", *VNU Journal of Science: Natural Sciences and Technology*, **26(1)**, pp.36-43 (in Vietnamese).

[13] K. Nagashima, H. Wakita, A. Mochizuki (1973), "The synthesis of crystalline rare earth carbonates", *Bulletin of the Chemical Society of Japan*, **46(1)**, pp.152-156.

DOI: 10.31276/VJSTE.62(2).19-23



# Removal of ammonia from anaerobic co-digestion effluent of organic fraction of food waste and domestic wastewater using air stripping process

**Lan Huong Nguyen[1], Hong Ha Bui[2*], Xuan Truong Nguyen[3]**

*[1]Ho Chi Minh city University of Food Industry*
*[2]Institute for Tropicalization and Environment*
*[3]Southern Education and Training Centre*

Received 12 August 2019; accepted 26 November 2019

***Abstract:***

**In this study, a continuous ammonium stripping lab-scale model of anaerobic co-digestion effluent from an organic fraction of food waste and domestic wastewater was used to investigate ammonium removal efficiency by air stripping. The effect of initial pH, liquid flow rate, and air-to-liquid ratio on the removal of ammonium from the effluent were examined in experiments. The operating parameters of the trials were established based on calculations from influent and effluent ammonia concentration and the theory of mass transfer. The results indicated that a pH value of 11, liquid flow of 0.25 l/min, and a ratio of air-to-liquid of 2925 gave a >90% ammonia removal efficiency and thus reached the allowable ammonia levels of wastewater discharged into receiving sources. The continuous stripping of nitrogen from anaerobic co-digestion of effluent had a huge significance in the removal of ammonium and recovery of ammonia gas , which aids in eutrophication prevention and fertilizer production.**

***Keywords:*** **air-to-liquid ratio, ammonia, anaerobic co-digestion, pH, stripping.**

***Classification number:*** **2.2**

## Introduction

For many years, anaerobic digestion has been widely applied to the treatment of wastewater with high biodegradable organic content like waste sludge, an organic fraction of solid waste, as well as to mixtures of wastewater and solid waste [1]. The anaerobic digestion process possesses advantages such as low sludge production, low energy consumption, and high potential recovery of biogases, which can be used for cooking and electricity. However, anaerobic effluent has a high ammonia concentration [1]. Further, ammonium is discharged into receiving bodies from various sources, namely fertilizer [2], landfill leachate [3], pig wastewater [4, 5], and especially in the effluent of an anaerobic co-digestion of a mixture of two or more solid wastes and wastewaters [6]. When discharged into receiving sources, ammonium causes eutrophication, dissolved oxygen depletion, and toxicity to aquatic organisms [7]. Additionally, the penetration of ammonia into ground water causes water contamination and is the cause of blue-skinned disease in children and pregnant women [7]. Because of the risks of untreated ammonia discharge, environmental regulations regarding the allowable limits of ammonia into receiving bodies are becoming more stringent across every country. In Vietnam, the maximum allowable limit of ammonium in drinking water is 3.0 mg/l [8].

Ammonia can be removed from wastewater by biological, chemical, and physicochemical technologies [2]. A biological treatment based on the combination of nitrification-denitrification processes by microorganisms is the most popular method of ammonia removal from wastewater due to low energy consumption, non-secondary pollutants, and non-chemical additives [8]. However, this method is very sensitive to loading shock and toxicity, and is not suitable for anaerobic effluent with low content of organic compounds [1, 9]. Beyond this, oxidation with

*Corresponding author: Email: buihonghavittep@yahoo.com

chlorine consumes chemicals and forms by-products [9]. Meanwhile, air stripping is a simple physical separation process using the contact of liquid and air in opposite directions in a tower filled with a different medium. Concentrated gaseous ammonia found in effluent can be recovered and adsorbed by strong acidic solutions ($H_2SO_4$) for the production of fertilizer [2, 9, 10]. The air stripping process is especially suitable for wastewater with high ammonium and low organic matter, such as the effluent from anaerobic co-digestion processes [6].

The aim of this study, thus, is to study ammonium removal efficiency by air stripping technology in a tower containing a medium of pall rings. The effect of the initial pH, liquid flow rate, and air-to-liquid ratio on ammonium removal are systematically investigated.

## Materials and methods

### *Materials*

*Wastewater:* influent wastewater for the air stripping model was taken from the effluent of the anaerobic co-digestion process in a membrane biological reactor (MF-AnCSTR and MF-UASB**),** which degrades a fraction of the organic food waste and domestic wastewater of an army billet based in Ho Chi Minh city, Vietnam. The characteristics of the influent wastewater from the air stripping process are presented in Table 1.

**Table 1. The characteristics of influent wastewater of air stripping model.**

| Parameter | Unit | Concentration | |
|---|---|---|---|
| | | ***MF-AnCSTR*** | ***MF-UASB*** |
| pH | - | 7.0±0.82 | 7.37±0.33 |
| $N\text{-}NH_4^+$ | mg/l | 150±12.09 | 152±13.45 |
| TN | mg/l | 163.90±17.04 | 171.34±24.08 |
| COD | mg/l | 81.02±2,50 | 85.02±2.76 |
| TSS | mg/l | 5.91±2.37 | 8.71±2.48 |

*Chemicals:* all chemicals used in this study were purchased from Merck. The acidic and alkaline solutions used to adjust the pH to desired values were prepared as follows: the 1 M NaOH solution was prepared by dissolving of 41.667 g NaOH in 1000 ml of deionized water. The 1 M $H_2SO_4$ solutions was diluted from 14 ml of concentrated 98% $H_2SO_4$ solution in 500 ml of deionized water. The 5 M $H_2SO_4$ solution was prepared by diluting 70 ml of concentrated 98% $H_2SO_4$ in 500 ml of deionized water. This acidic solution was used to neutralize the gaseous ammonia output of the air stripping model.

### *Experimental setup*

*The laboratory-scale air stripping system:* a plastic column (PAC) manufactured by the Binh Minh Company (Vietnam) was used for the design of the air stripping experiments. The column diameter and height was 11.4 cm and 130 cm, respectively. The column was filled with plastic spring carriers (size 2 cm x 3 cm) and the height of plastic carriers in the column was 75 cm. The air and liquid flows were continuously introduced into the air stripping column along the opposite direction of the carrier layer. The wastewater was adjusted to the desired pH and contained in 10-l tank. The wastewater was pumped at a pre-determined flow to the top of the column and was sprayed over the packing surface through a shower. The air was introduced into the bottom of the column by a fan with a capacity of 2.2 kW, the current strength of 7.8 A with a frequency of 50 Hz. The air was blown through the packing material. The ammonia containing output air was released at the top of the column and was adsorbed into a tank containing 5 M $H_2SO_4$. The scheme of the laboratory-scale ammonia stripping system is described in Fig. 1.

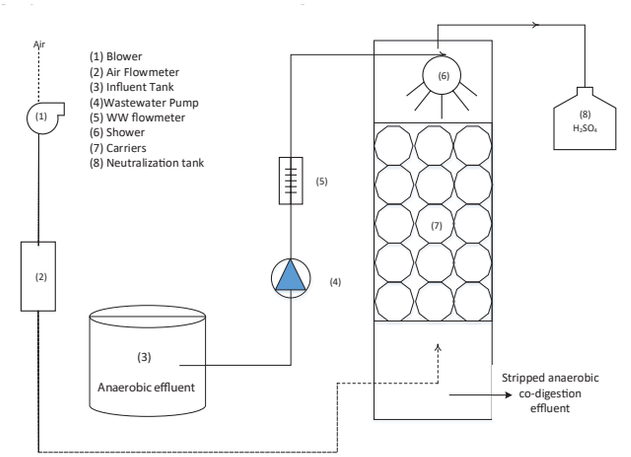


**Fig. 1. The scheme of the lab-scale ammonium stripping system for treatment of anaerobic co-digestion effluent.**

*Determination of parameters for design of the air stripping model:* the parameters of the air stripping model were calculated using mass transfer theory for the removal of $NH_4^+$-N (from 150 to 10 mg/l of QCVN 14:2008/BTNMT, column B) with 10 l volume of wastewater at 25±1°C.

The amount of air required to reduce the ammonia concentration from 150 to 10 mg/l in treated wastewater was calculated based on the text "Wastewater engineering: treatment and resource recovery" [11]. The parameters obtained for the design of the air stripping model are presented in Table 2.

**Table 2. The parameters for design the air stripping to treat ammonium in anaerobic effluent.**

| Parameter | Unit | Value |
|---|---|---|
| Provided air flow | l/min | 650 |
| Provided liquid flow | l/min | 50 |
| Air-to-liquid ratio | - | 2000-6000:1 |
| Diameter of column | mm | 114 |
| Height of packing | m | 0.75 |
| Height of column | m | 1.3 |
| Mass transfer coefficient | 1/s | 0.0125 |

The influent and effluent ammonia concentrations were determined according to the standard method by the APHA (American Public Health Association), AWWA (American Water Works Association), and WEF (Water Environment Federation) [12]. The pH was measured by a WTW pH meter 304.

*Operating condition:* the air stripping (AS) method used to treat the anaerobic co-digestion effluent was continuously operated to assess the effect of initial solution pH, liquid flow and air-to-liquid ratio on ammonium removal efficiency in anaerobic co-digestion effluent with packing column. The detailed operating conditions of the model were as follows:

The effect of solution pH on ammonia stripping was conducted by changing the pH values from 8 to 12 at an air flow rate of 650 l/min, wastewater volume of 10 l, and contact time of 25 min, under a constant influent ammonia concentration of 150±20 mg/l. The stripping process was examined over 15 experiments, where each of the 15 experiments were triplicated for each set of operating conditions.

The experiments used to evaluate the effect of the liquid flow on ammonia stripping were conducted by changing the influent liquid flow rate between 0.25 l/min, 0.5 l/min, 0.75 l/min, and 1.0 l/min at pH of 11 with air flow rate of 650 l/min, wastewater volume of 10 l and contact time of 25 min under a constant influent ammonia concentration of 150±20 mg/l. All the samples were analysed in triplicates.

The effect of the air-to-liquid ratio was conducted over 15 experiments, where each experiment was triplicated for each set of operating conditions. The air-to-liquid ratio was varied from 0, 2084, 2260, 2632, and 2925 at a pH of 11 with an air flow of 650 l/min, wastewater volume of 10 l and contact time of 25 min with influent ammonia concentration of 150±20 mg/l.

## Results and discussion

### *Effect of pH on ammonia stripping*

The pH solution was chosen based on the theory of air stripping by George Tchobanoglous, et al. (2014) [11]. The effect of initial pH on ammonia stripping is presented in Fig. 2.

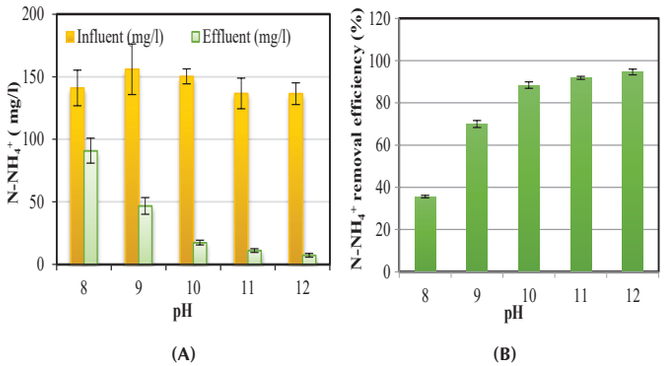


**Fig. 2. (A)The influent and effluent ammonium and (B) ammonium removal efficiency at various initial pH values.**

Figure 2 indicates that effluent ammonium decreased when pH was increased from 8 to 12. The removal efficiency of ammonium reached 35.64±0.75, 70.02±1.67, 88.39±1.54, 91.87±0.68, and 94.61±1.35% corresponding to a pH of 8, 9, 10, 11, and 12, respectively. At pH 11 a high removal efficiency was found and reached QCVN 14:2008/BTNMT. Thus, a pH of 11 was chosen for the next experiments.

It can be seen that the pH value had the most significant effect on the conversion efficiency of $N\text{-}NH_4^+$ into gaseous $N\text{-}NH_3$. A low efficiency of 35.64±0.75% was obtained at pH 8. The removal efficiency quickly rose to 91.87±0.68% and 94.61±1.35% at pH 11 and 12, respectively, corresponding with a $N\text{-}NH_4^+$ concentration of effluent of 11.12±1.46 mg/l and 7.30±1.52 mg/l, respectively, which reached the permitted standard discharge amounts for receiving sources. This result agrees with research conducted by Guštin and Marinšek-Logar (2011) [6]. That study reached its highest ammonia removal efficiency of anaerobic digestion effluent at a pH between 10.5-11.

### *Effect of contact time on ammonia stripping*

The change of ammonium as a function of contact time is demonstrated in Fig. 3. It can be seen from Fig. 3 that the ammonium removal efficiency at an initial pH of 8 did not change with contact time. However, the removal efficiency of $N\text{-}NH_4^+$ gradually increased at pH of 11 with increasing contact time until it became constant at 25 min.

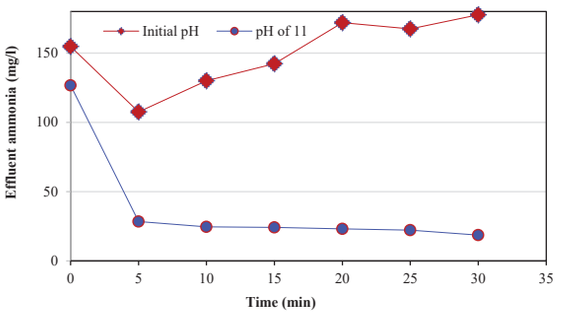


**Fig. 3. Contact time dependence of ammonium concentration at initial pH and pH of 11.**

Figure 3 also indicates that the contact time had an insignificant effect on ammonia removal efficiency. The N-$NH_4^+$ concentration reached 156.68, 29.51, 23.75, 17.12, 14.64, and 12.02 mg/l, respectively, at contact times of 0, 5, 10, 15, 20, and 25 min. The ammonia removal efficiency reached its maximum at a contact time of 25 min and pH of 11, and met the allowable limit of N-$NH_4^+$ (QCVN 14:2008/BTNMT, column B). Thus, a pH of 11 and contact time of 25 min was chosen for the next experiments.

### *Effect of liquid flow rate on ammonia stripping*

The influent and effluent ammonium concentration and removal efficiency of the air stripping system are presented in Fig. 4. Fig. 4A illustrates that effluent ammonium increased when the liquid flow rate increased. The effluent ammonium was 6.38±0.77, 11.12±1.46, 30.51±6.16, and 40.25±3.84 mg/l corresponding to a liquid flow rate of 0.25, 0.5, 0.75, and 1.0 l/min, respectively. Fig. 4B shows a N-$NH_4^+$ removal efficiency of 95.80, 91.87, 81.81, and 72.59% when the liquid flow rate increased from 0.25 to 1.0 l/min, respectively.

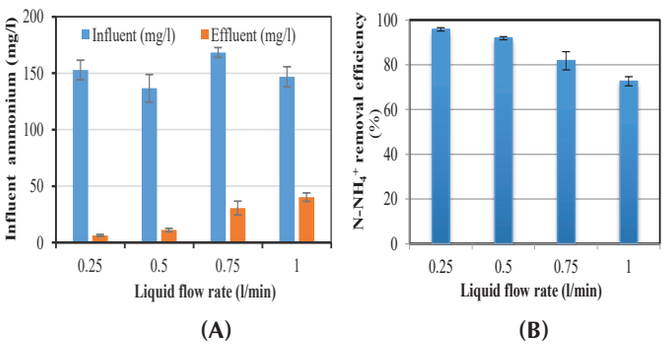


**Fig. 4. (A) The influent and effluent ammonium and (B) ammonium removal efficiency at various of liquid flow rates.**

The removal efficiency decreased from 95.80 to 72.59% when the flow rate ($Q_L$) increased from 0.25 to 1.0 l/min. These results may be due to the decrease in liquid hydraulic retention time and stripping factor, resulting in a decrease in removal efficiency for air stripping [2]. The results were similar to the results obtained by Yuan, et al. (2016) [9] when using a rotating packed bed to strip ammonia from ammonia-rich wastewater.

### *Effect of air-to-liquid ratio on ammonia stripping*

Figure 5 shows the effect of the air-to-liquid ratio ($Q_G/Q_L$) (from 0 to 2925) on ammonia stripping. As illustrated in Fig. 5, $Q_G/Q_L$ had a significant effect on ammonia removal efficiency. The removal efficiencies obtained were 24.38±2.96, 71.51±0.53, 88.00±0.68, 95.80±0.75, and 97.08±0.34% at $Q_G/Q_L$ values of 0, 2086, 2260, 2633, and 2925, respectively. The removal efficiency reached a maximum at $Q_G/Q_L$ of 2925. The results showed that with increasing $Q_G/Q_L$, the removal efficiency also increased.

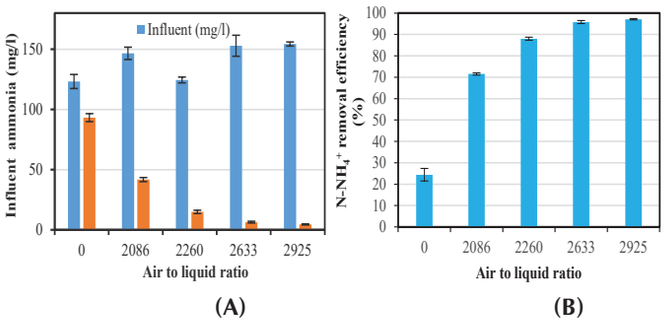


**Fig. 5. (A) The influent and effluent ammonium and (B) ammonium removal efficiency at various air-to-liquid ratios.**

A higher air-to-liquid ratio enhances the gas flow leading to a reduction in mass transfer resistance and, thus, a promotion ammonia stripping efficiency [13]. Moreover, the ammonia stripping efficiency increase due to increasing $Q_G/Q_L$ was found using the same volume of wastewater, 10 l, placed in a separate area, and under a fixed liquid flow rate of 0.25 l/min. At a higher air flow rate, a higher velocity is produced that breaks down the liquid-gas interface and easily pushes out the ammonia gas from the wastewater [9].

## Conclusions

The lab-scale air stripping system used in these experiments has successfully removed ammonium from anaerobic co-digestion effluent. The results indicated that the initial pH of wastewater had the most significant effect on ammonia stripping efficiency. A pH value of 11 gave the highest ammonia removal efficiency. Similarly, a higher air-to-liquid ratio increased the ammonia removal efficiency due to a reduction in the mass transfer resistance between the liquid-gas interface. This study has huge significance in the removal of ammonia from ammonia-rich wastewaters and anaerobic co-digestion effluent, and contributes to the

prevention of eutrophication and promotes environmental protection. The gaseous ammonia obtained from the stripping effluent can be recovered to produce fertilizer for agriculture. Thus, this study has opened up new prospects for the protection of the environment and nutrient recovery from wastewater.

## ACKNOWLEDGEMENTS

This research is funded by Ho Chi Minh city University of Food Industry under grant number 84/HD-DCT.

The authors declare that there is no conflict of interest regarding the publication of this article.

## REFERENCES

[1] C. Bougrier, J.P. Delgenes, H. Carrere (2006), "Combination of thermal treatments and anaerobic digestion to reduce sewage sludge quantity and improve biogas yield", *Environmental Protection*, **84**, pp.280-284.

[2] M-H. Yuan, Y-H. Chen, J-Y. Tsai, C-Y. Chang (2016a), "Removal of ammonia from wastewater by air stripping process in laboratory and pilot scales using a rotating packed bed at ambient temperature", *Journal of the Taiwan Institute of Chemical Engineers*, **60**, pp.488-495.

[3] K-C. Cheung, L-M. Chu, M-H. Wong (1997), "Ammonia stripping as a pretreatment for landfill leachate", *Water Air Soil Pollution*, **94**, pp.209-216.

[4] P-H. Liao, A. Chen, K-V. Lo (1995), "Removal of nitrogen from swine manure wastewaters by ammonia stripping", *Bioresource Technology*, **54**, pp.17-20.

[5] M. Laureni, J. Palatsi, M. Llovera, A. Bonmati (2013), "Influence of pig slurry characteristics on ammonia stripping efficiencies and quality of the recovered ammoniumsulfate solution", *Journal Chemistry Technology Biotechnology*, **88**, pp.1654-1662.

[6] S. Guštin, R. Marinšek-Logar (2011), "Effect of pH, temperature and air flow rate on the continuous ammonia stripping of the anaerobic digestion effluent", *Process Safety and Environmental Protection*, **89**, pp.61-66.

[7] L.J. Ding, X.L. An, S. Li, G.L. Zhang, Y.G. Zhu (2014), "Nitrogen loss through anaerobic ammonium oxidation coupled to iron reduction from paddy soils in a chronosequence", *Environmental Science Technology*, **48**, pp.10641-10647.

[8] QCVN 01:2009/BYT, *National Technical Regulation on Drinking Water Quality*.

[9] M-H. Yuan, Y-H. Chen, J-Y. Tsai, C-Y. Chang (2016b), "Ammonia removal from ammonia-rich wastewater by air stripping using a rotating packed bed", *Process Safety and Environment Protection*, **102**, pp.777-785.

[10] N. Değermenci, O-N. Ata, E. Yildız (2012), "Ammonia removal by air stripping in a semi-batch jet loop reactor", *Journal of Industrial and Engineering Chemistry*, **18**, pp.399-404.

[11] George Tchobanoglous, et al. (2014), *Wastewater Engineering: Treatment and Resource Recovery*, McGraw-Hill: ISBN 0073401188.

[12] APHA (American Public Health Association), AWWA (American Water Works Association) and WEF (Water Environment Federation) (1998), *Standard Methods for the Examination of Water and Wastewater*, 20th ed., Washington D.C.

[13] X. Quan, F. Wang, Q. Zhao, T. Zhao, J. Xiang (2009), "Air stripping of ammonia in water-sparged aerocyclone reactor", *Journal of Hazardous Material*, **170**, pp.983-988.

DOI: 10.31276/VJSTE.62(2).24-29

# Prediction of inhibition constants of (*R*)-3-amidinophenylalanine inhibitors toward factor Xa by 2D-QSAR model

**Thi Bich Van Pham[1], Minh Hao Hoang[2*]**

[1]*Department of Chemistry, Faculty of Sciences, Nong Lam University, Ho Chi Minh city*

[2]*Department of Chemical Technology, Faculty of Chemical and Food Technology, Ho Chi Minh city University of Technology and Education*

Received 9 September 2019; accepted 2 December 2019

***Abstract:***

**A coagulation cascade forms through proteolytic reactions and involves different factors. There are two coagulation pathways, including intrinsic and extrinsic mechanisms, which converge by the formation of factor Xa. Factor Xa plays a crucial role in the formation of the complex with factor Va in the presence of calcium ions and phospholipids. This complex converts prothrombin to thrombin, which leads to the formation of a very strong fibrin clot. Much effort has been devoted to the efficient interference of this enzyme cascade by the inhibition of factor Xa due to its important effect. (*R*)-3-amidinophenylalanine inhibitors are known inhibitors of factor Xa reported so far. In the present work, a two-dimensional quantitative structure activity relationship (2D-QSAR) was performed on 50 (*R*)-3-amidinophenylalanine inhibitors (the training set) with respect to their $pK_i$ values toward factor Xa, where $pK_i$=-log$K_i$, and $K_i$ is the inhibition constant, to develop a mathematical model that depends on the physicochemical properties of the inhibitors. Partial least squares regression (PLSR) was used to yield a QSAR model containing molecular descriptors that significantly contribute to $pK_i$ values. The statistically significant parameters of the model, such as squared correlation coefficient, $R^2$=0.834, root mean square error, RMSE=0.210, cross-validated $Q^2_{cv}$=0.789, and cross-validated $RMSE_{cv}$=0.237, were obtained for the training set. The developed 2D-QSAR model was applied to predict the $pK_i$ values of the 62 inhibitors. Furthermore, the reliability of the model was also confirmed via statistically significant parameters obtained from validation on an external set.**

***Keywords:*** **coagulation cascade, descriptors, factor Xa, (*R*)-3-amidinophenylalanine inhibitors, 2D-QSAR.**

***Classification number:*** **2.2**

## Introduction

Blood coagulation can be a beneficial response of human body that decreases the amount of bleeding by forming blood clots. These clots play an important role in the sealing of blood vessels to prevent injury from excessive bleeding. However, blood clots can become harmful when they gather together into a compact mass. The presence of large blood clots can cause congestion of blood flow to the body's organs. As a consequence, the supply of oxygen to the organs, especially the brain or heart, is restricted. This leads to a stroke or heart attack. There are two mechanisms leading to coagulation: the contact activation (intrinsic) and tissue factor (extrinsic) pathways [1]. In general, these two pathways occur over several consecutive steps leading to an activation of factor X to factor Xa ("a" activated). Therefore, factor Xa is located at the junction between these two coagulation pathways. In the extrinsic mechanism, factor Xa and factor Va form a complex in the presence of calcium ions and phospholipids. This complex then converts prothrombin to thrombin, which leads to the formation of a very strong fibrin clot [2, 3]. An abnormal clot that forms in a vein may result in pain and swelling, and in many cases, this clot can cause disability and death.

*Corresponding author: Email: haohm@hcmute.edu.vn

Due to the pivotal role of factor Xa to fibrin formation, several great efforts have been made to suppress the coagulation cascade by inhibition of this enzyme. A number of series of novel inhibitors toward factor Xa have been discovered such as mono-benzamidine, non-benzamidine, and diamidino derivatives. These inhibitors have displayed high affinities in *in vitro* and *in vivo* experiments [4]. (*R*)-3-amidinophenylalanine inhibitors were found to represent promising new selective inhibitors of factor Xa due to their hydrophobic interactions with factor Xa [5, 6].

Many drug molecules are enzyme inhibitors and their inhibitory activity is characterised by the inhibition constant, $K_i$. When an enzyme (E) binds to an inhibitor (I) to form an enzyme-inhibitor complex (EI), E + I $\leftrightarrow$ EI, where $K_i$ is defined as an equilibrium constant such that $K_i$=[EI]/[E][I], where [E], [I], and [EI] are the equilibrium concentrations of the enzyme, inhibitor, and enzyme-inhibitor complex [7]. A high $K_i$ value ensures that a drug will have high inhibitory activity.

The two-dimensional quantitative structure-activity relationship (2D-QSAR) has seen wide application in the field of medicinal chemistry for many years. This method presents a quantitative relationship between the chemical response (inhibitory activity/toxicity/binding affinity) of a molecule and its physicochemical properties via a mathematical equation [8]. The QSAR method helps to screen new drug candidates, thus avoiding costly trial and error experiments in synthesis and biological screening. In the present attempt, we developed a mathematical model that provided a quantitative relationship of the binding affinity (e.g., $pK_i$) of (*R*)-3-amidinophenylalanine inhibitors toward factor Xa, a crucial enzyme in the clotting cascade. The quantitative relationship was presented by a mathematically linear equation that depends on molecular physicochemical properties (descriptors) of (*R*)-3-amidinophenylalanine inhibitors. The developed 2D-QSAR model was applied to predict the $K_i$ values of 62 inhibitors.

## Methodology

Structures of (*R*)-3-amidinophenylalanine inhibitors and their experimental $pK_i$=-log$K_i$ values were obtained from the literature [9] (Table 1). Chemical structures were drawn and optimized energy in Molecular Operating Environment (MOE) 2008.10. In order to develop a 2D-QSAR model, a training set including 50 (*R*)-3-amidinophenylalanine inhibitors was randomly chosen in MOE 2008.10. The remaining inhibitors (12 molecules) were used as a testing (external) set. One hundred and eighty-four (184) two-dimensional (2D) descriptors were numerically calculated by MOE software. By using Rapidminer 5.0, the descriptors showing zero value, low correlation with binding affinity (<0.07), and high intercorrelation themselves (>0.9) were removed to select the most significant descriptors for the 2D-QSAR model. In addition, Weka 3.6 software, QuaSAR-Contigency, and Principle Components in MOE 2008.10 were also employed to select the best descriptors to establish the QSAR model. Then, partial least squares regression was used to develop a mathematical equation.

## Results

### *2D-QSAR model*

Descriptors are the physicochemical properties of each molecule that characterize its chemical structure and they take on numerical values [8]. After the irrelevant descriptors were omitted, PLSR was employed to develop a mathematical QSAR model that describes a quantitative relationship between the descriptors of (*R*)-3-amidinophenylalanine inhibitors with their $pK_i$ values. The estimated QSAR model is shown below:

$$pK_i = 3.73958 - 1.14732 \times b\_ar + 0.56128 \times PEOE\_VSA\_POS + 1.16326 \times SlogP\_VSA6 + 2.08858 \times SMR\_VSA5$$

where b_ar is the number of aromatic bonds, PEOE_VSA_POS is the total positive van der Waals surface area, SlogP_VSA is the logarithm of the *n*-octanol/water partition coefficient, and SMR_VSA is the molecular refractivity. The training set was randomly selected from 62 inhibitors to develop the 2D-QSAR model. The model with statistically significant parameters was chosen as the best model. Several training sets were used to develop the 2D-QSAR models. Unfortunately, they gave statistically insignificant $R^2$, RMSE, $Q^2_{cv}$, and $RMSE_{cv}$ values. Therefore, those models were not selected for further analysis.

**Table 1. Chemical structures of 62 (*R*)-3-amidinophenylalanine inhibitors with respect to their experimental (Exp) $pK_i$ values.** The predicted (Pre) $pK_i$ values of 62 inhibitors calculated from the 2D-QSAR equation were also added.

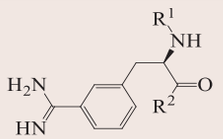

(*R*)-3-amidinophenylalanine inhibitors

| N⁰ | R¹ | R² | Exp $pK_i$ | Pred $pK_i$ | N⁰ | R¹ | R² | Exp $pK_i$ | Pred $pK_i$ |
|---|---|---|---|---|---|---|---|---|---|
| 1 | 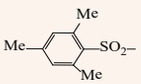 | —NHMe | 3.194 | 3.638 | 32 | 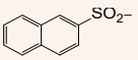 |  | 4.886 | 4.689 |
| 2 | 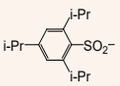 |  | 5.824 | 5.494 | 33 | 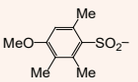 | —NHMe | 3.721 | 3.670 |
| 3 | 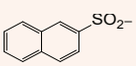 |  | 4.456 | 4.280 | 34 | 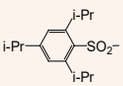 | 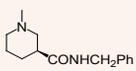 | 5.602 | 5.909 |
| 4 | 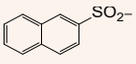 |  | 4.337 | 4.554 | 35 | 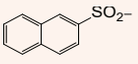 |  | 4.658 | 4.724 |
| 5 | 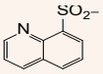 | 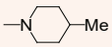 | 3.745 | 4.243 | 36 | 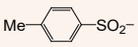 |  | 4.119 | 4.176 |
| 6 | 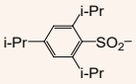 | —NHMe | 4.959 | 4.979 | 37 | 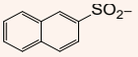 | 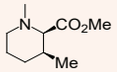 | 4.444 | 4.461 |
| 7 | 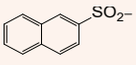 | 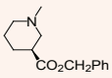 | 5.066 | 4.898 | 38 | 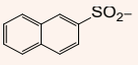 | 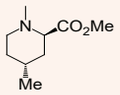 | 4.237 | 4.461 |
| 8 | 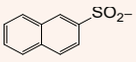 |  | 3.886 | 4.270 | 39 | 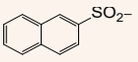 |  | 4.319 | 4.272 |
| 9 | 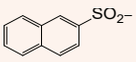 |  | 4.42 | 4.422 | 40 | 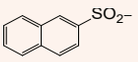 | 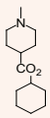 | 5.119 | 5.126 |
| 10 | 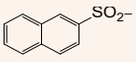 |  | 4.367 | 4.467 | 41 | 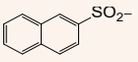 | 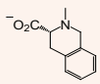 | 4.382 | 4.454 |
| 11 | 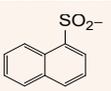 |  | 4.77 | 4.386 | 42 |  |  | 4.886 | 5.345 |
| 12 |  |  | 4.523 | 4.272 | 43 |  |  | 4.387 | 4.196 |
| 13 |  |  | 4.796 | 4.606 | 44 |  |  | 3.921 | 3.969 |
| 14 |  |  | 4.119 | 4.484 | 45 |  |  | 5.114 | 5.048 |

| | | | | | | | | | | |
|---|---|---|---|---|---|---|---|---|---|---|
| 15 | 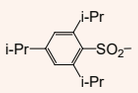 | 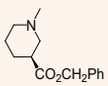 | 6.046 | 5.908 | 46 | 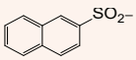 | 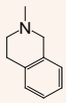 | 4.745 | 4.453 |
| 16 | 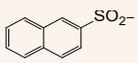 | 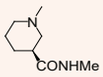 | 4.481 | 4.484 | 47 | 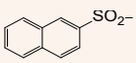 | 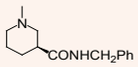 | 4.77 | 4.899 |
| 17 | 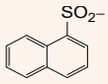 |  | 4.377 | 4.293 | 48 | 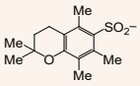 |  | 4.097 | 4.161 |
| 18 | 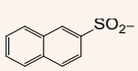 |  | 4.363 | 4.335 | 49 | 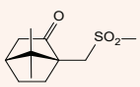 |  | 4.854 | 4.560 |
| 19 | 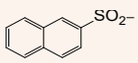 |  | 4.357 | 4.335 | 50 |  |  | 3.638 | 3.869 |
| 20 | 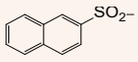 |  | 4.569 | 4.486 | 51* | 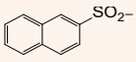 | 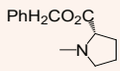 | 4.699 | 4.833 |
| 21 | 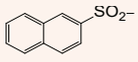 | 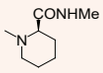 | 4.244 | 4.571 | 52* | 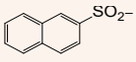 |  | 4.658 | 4.992 |
| 22 | 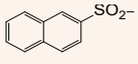 |  | 4.62 | 4.428 | 53* | 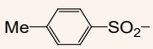 |  | 4.398 | 3.877 |
| 23 | 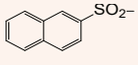 |  | 4.569 | 4.616 | 54* | 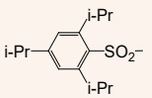 |  | 5.699 | 5.338 |
| 24 | 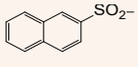 |  | 4.42 | 4.421 | 55* | 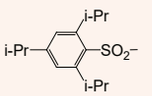 |  | 5.585 | 5.476 |
| 25 |  |  | 4.745 | 4.467 | 56* |  |  | 4.000 | 4.029 |
| 26 |  |  | 3.959 | 4.402 | 57* |  |  | 4.721 | 4.363 |
| 27 |  |  | 4.585 | 4.572 | 58* |  |  | 4.194 | 4.070 |
| 28 |  |  | 4.268 | 4.315 | 59* |  |  | 5.131 | 5.278 |
| 29 |  |  | 4.125 | 4.101 | 60* |  |  | 4.387 | 4.328 |
| 30 |  |  | 4.114 | 4.272 | 61* |  |  | 5.092 | 4.898 |
| 31 |  |  | 4.076 | 4.135 | 62* |  |  | 4.284 | 4.036 |

*Testing set.

### *Statistical parameters*

The statistical parameters, such as $R^2$ and RMSE, are important parameters for the selection of the best 2D-QSAR model. A model was chosen with the greatest $R^2$ (>0.5), while RMSE value must be below 0.5 [8, 10]. The significant values of $R^2$, RMSE, $Q^2_{cv}$, and $RMSE_{cv}$ reflect the reliability of the QSAR model. The obtained values are shown in Table 2.

**Table 2. The statistical parameters of the established 2D-QSAR model.**

| | Training set | Cross-validation | Testing set | Total set |
|---|---|---|---|---|
| $N^0$ | 50 | 50 | 12 | 62 |
| $R^2$ | 0.834 | | 0.934 | 0.814 |
| $Q^2_{cv}$ | | 0.789 | | |
| RMSE | 0.210 | 0.237 | 0.132 | 0.227 |

### *Experimental $pK_i$ vs. predicted $pK_i$*

The $pK_i$ values of the 62 inhibitors were predicted by using the established 2D-QSAR model. The relationship between the experimental $pK_i$ and predicted $pK_i$ is presented in Fig. 1. The fitting equation is given in the top of the Fig. 1.

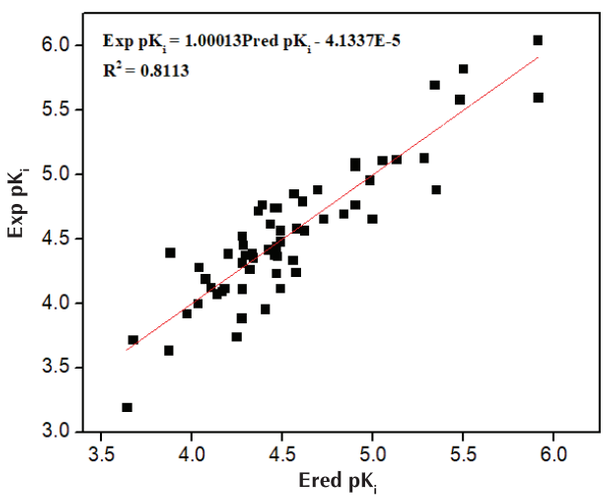


**Fig. 1. The plot shows the relationship between the experimental $pK_i$ and predicted $pK_i$.**

## Discussion

### *Subdata set selection to establish a 2D-QSAR model*

A data set of 88 inhibitors with respect to their experimental $pK_i$ values was firstly used to perform a QSAR study. As presented in the methodology section, the training set (80%) was selected through their assigned random values (sorted in descending order). After removing the irrelevant descriptors from 184 2D-descriptors, the QSAR model was built. If the first model possessed statistically significant parameters of $R^2$ and RMSE, the model was used for cross-validations, and if the parameters of $Q^2_{cv}$, $RMSE_{cv}$ were acceptable, the model was applied to the total set and testing set. Note that the values of $R^2$, RMSE, and $Q^2_{cv}$, are dependent on which of the compounds were used in the training set. Therefore, if these values were not statistically satisfied, the first model would not be used further. Consequently, random values of each molecule in 88 inhibitors would be re-calculated and sorted again to select a new training set (the calculation was randomly done by MOE). Then, a second attempt at 2D-QSAR modelling was established based on the new descriptors. This procedure was repeated 8-10 times for the first dataset containing 88 inhibitors and if the validation parameters of $R^2$, RMSE, and $Q^2_{cv}$ were not statistically significant, the other solutions were taken into account. The reasons behind the statistically insignificant values are the irrelevant selection of descriptors and/or the interfering compounds. Thus, the interfering molecules should be considered. The Z-score values were obtained after cross-validation and the compound outliers to the fit were omitted. As a result, the number of inhibitors will be less. As mentioned earlier, the selection of training and testing sets was random and tthe same procedure was performed to get the statistical parameters. If the results were unacceptable, more interfering molecules were screened via the Z-score until the statistically desired values were obtained from a certain subset of the data. Fortunately, data consisting of 62 inhibitors gave statistically significant parameters for validation.

### *Molecular descriptors*

According to the established equation, $pK_i$ depends on four 2D-descriptors consisting of the number of aromatic bonds, the total positive van der Waals surface area, the logarithm of the *n*-octanol/water partition coefficient, and the molecular refractivity. In comparison with the results discussed in Ref. [9], the model gave more 2D-descriptors and thus may potentially be used in experimental studies. Five 3D-physicochemical properties including steric, electrostatic, hydrophobic, and hydrogen-bond donor and acceptor factors play crucial roles in the binding affinities of inhibitors toward factor Xa [9]. Here, the SlogP descriptor ($P=C_{n\text{-octanol}}/C_{water}$; where $C_{n\text{-octanol}}$ and $C_{water}$ are the concentrations of a solute in the lipid phase (*n*-octanol) and in the aqueous phase (water), respectively) relating to the absorption, transport, and excretion of drugs, i.e., the relative affinity for an aqueous (hydrophilic) or lipid (hydrophobic) medium, is present and contributes to $pK_i$. This could mean that the descriptor reflecting the hydrophobicity of the inhibitors is indispensable to the binding affinities toward factor Xa in 2D and 3D-QSAR studies. From the present results, the 2D-descriptors of b_ar, PEOE_VSA_POS, and SMR_VSA were found to contribute to $pK_i$. This result is helpful for further studies where these 2D-descriptors are not readily applicable. SMR_VSA5 and SlogP_VSA6 are descriptors based on the approximate accessible van der

Waals surface area (VSA), which is the surface area of a biomolecule that is accessible to a solvent, in unit of Å$^2$. Each atom has an accessible van der Waals surface area, $\nu_i$, along with an atomic property, $L_i$. This property is in a specified range (a, b) and contributes to the descriptor. Thus, the SlogP_VSA6 is the sum of the $\nu_i$ from all atoms such that the $L_i$ value of each atom, *i*, is in the range of (0.20, 0.25] [11]. The $L_i$ contributes to the descriptor logP. The SMR_VSA5 refers to the sum of $\nu_i$ of all atoms such that the $L_i$ value of each atom, *i*, is in the range of (0.44, 0.485) [12]. This $L_i$ contributes to the descriptor the molecular refractivity (MR). The PEOE_VSA_POS denotes the sum of the van der Waals surface area of atom *i*, $v_i$, such that the partial charge of atom *i*, $q_i$, is non-negative. The atomic partial charges were calculated by partial equalization of orbital electronegativities (PEOE), in which charge is transferred between bonded atoms until equilibrium [13]. Descriptors using PEOE charges are prefixed with PEOE_. The positive coefficient signs of the descriptors represent a linear relationship between $pK_i$ and the descriptors, i.e., the increase of these descriptors induces an increase in $pK_i$ values (i.e., binding affinity decreases) while the negative coefficients imply an increase in binding affinity when the value of that descriptor increases.

The reliability of the developed model was evaluated via internal (cross), external, and total validations. The model gave statistically significant parameters for the external (12 inhibitors) and total (62 inhibitors) validations. The cross-validated squared correlation coefficient was $Q^2_{cv}$=0.789 and $R^2$=0.814, both of which are greater than 0.5. The RMSE values were lower than 0.5. These values confirmed the goodness of fit of the QSAR model. The model was also employed to predict the $pK_i$ values of 62 inhibitors (Table 1).

By plotting the experimental $pK_i$ vs. predicted $pK_i$, a linear correlation between experimental $pK_i$ and predicted values was found. This linear relationship indicated that the model has a good predictive ability. Note that, the regression line was described as y=ax+b instead of y=x to simply illustrate a linear trend between the experimental $pK_i$ vs. predicted $pK_i$, i.e., the experimentally large/small $pK_i$ value (low/high activity) of one compound, the predicted value should be also large/small.

## Conclusions

A 2D-QSAR model was established from 50 (*R*)-3-amidinophenylalanine inhibitors. The number of aromatic bonds, the positive van der Waals surface area, the logarithm of the *n*-octanol/water partition coefficients, and the molecular refractivity are crucial descriptors that contribute to $pK_i$ values. The results demonstrated that the hydrophobicity, which has been reported in 3D-QSAR studies, plays a pivotal role on the affinities of inhibitors toward factor Xa. The model in this work gave significantly statistical parameters. The $pK_i$ values of all inhibitors were predicted by employing the established 2D-QSAR model and there was a linear relationship between the experimental and predicted $pK_i$ values. These results indicate the reliability of the model and could be helpful to develop drug candidates based on (*R*)-3-amidinophenylalanine derivatives.

## ACKNOWLEDGEMENTS

The authors are thankful to Ho Chi Minh city University of Technology and Education for supporting websites to download the scientific articles.

The authors declare that there is no conflict of interest regarding the publication of this article.

## REFERENCES

[1] E.W. Davie, K. Fujikawa, W. Kisiels (1991), "The coagulation cascade: initiation, maintenance, and regulation", *Biochemistry*, **30(43)**, pp.10364-10370.

[2] R.G. MacFarlane (1964), "An enzyme cascade in the blood clotting mechanism, and its function as a biochemical amplifier", *Nature*, **202**, pp.498-499.

[3] E.W. Davie, O.D. Ratnoff (1964), "Waterfall sequence for intrinsic blood clotting", *Science*, **145(3638)**, pp.1310-1312.

[4] B.Y. Zhu, R.M. Scarborough (2000), "Factor Xa inhibitors: recent advances in anticoagulant agents", *Annual Reports in Medicinal Chemistry*, **35**, pp.83-102.

[5] M.M. Mueller, S. Sperl, J. Stürzebecher, W. Bode, L. Moroder (2002), "(*R*)-3-amidinophenylalanine-derived inhibitors of factor Xa with a novel active-site binding mode", *Biological Chemistry*, **383(7-8)**, pp.1185-1191.

[6] S. Sperl, A. Bergner, J. Stürzebecher, V. Magdolen, W. Bode, L. Moroder (2000), "Urethanyl-3-amidinophenylalanine derivatives as inhibitors of factor Xa. X-ray crystal structure of a trypsin/inhibitor complex and modeling studies", *Biological Chemistry*, **381(4)**, pp.321-329.

[7] M. Dixon (1953), "The determination of enzyme inhibitor constants", *Biochemical Journal*, **55(1)**, pp.170-171.

[8] K. Roy, S. Kar, R.N. Das (2015), *Understanding the Basics of QSAR for Applications in Pharmaceutical Sciences and Risk Assessment*, Elsevier.

[9] M. Böhm, J. Stürzebecher, G. Klebe (1999), "Three-dimensional quantitative structure-activity relationship analyses using comparative molecular field analysis and comparative molecular similarity indices analysis to elucidate selectivity differences of inhibitors binding to trypsin, thrombin, and factor Xa", *Journal of Medicinal Chemistry*, **42(3)**, pp.458-477.

[10] R. Veerasamy1, H. Rajak, A. Jain, S. Sivadasan, C.P. Varghese, R.K. Agrawal (2011), "Validation of QSAR models - strategies and importance", *International Journal of Drug Design and Discovery*, **2(3)**, pp.511-519.

[11] C. Hansch, A. Leo, D. Hoekman (1995), *Exploring QSAR Vol. 2: Hydrophobic, Electronic and Steric Constants*, Washington.

[12] S.A. Wildman, G.M. Crippen (1999), "Prediction of physiochemical parameters by atomic contributions", *Journal of Chemical Information and Computer Sciences*, **39(5)**, pp.868-873.

[13] J. Gasteiger, M. Marsili (1980), "Iterative partial equalization of orbital electronegativity - a rapid access to atomic charges", *Tetrahedron*, **36(22)**, pp.3219-3228.

DOI: 10.31276/VJSTE.62(2).30-33

# Chemical constituents from ethyl acetate extract of the leaves of *Rourea harmandiana* Pierre

**Ngoc Thuc Dinh[1*], The Minh Do[1], Xuan Luong Ngo[1], Huan Trinh Thi[1], Huong Nguyen Thi[1], Ha Mai Vu Thi[1], Ngoc Mai Nguyen Thi[1], Thi Kim Oanh Vu[2]**

*[1]Hong Duc University*
*[2]Institute of Marine Biochemistry, VAST*

Received 15 April 2020; accepted 4 June 2020

***Abstract:***

***Rourea harmandiana* Pierre is a species which belongs to the family of Connaraceae. This plant is found abundantly in central of Vietnam (Thua Thien - Hue, Da Nang). Chemical study on the ethyl acetate extract of *Rourea harmandiana* leaves has led to the isolation of four compounds including vomifoliol (1), boscialin (2), abscisic acid (3) and *p*-coumaric acid (4). The structures of these compounds have been identified by NMR, MS spectroscopic data and comparison with the reported literature. These compounds were isolated from *Rourea harmandiana* species as well as from the genus *Rourea* for the first time.**

***Keywords:*** **abscisic acid, boscialin, *p*-coumaric acid, *Rourea harmandiana*, vomifoliol.**

***Classification number:*** **2.2**

## Introduction

*Rourea harmandiana* Pierre. is a climbing plant of the *Rourea* genus, that belongs to the Connaraceae family. This plant, which is one of 7 Rourea species found in Vietnam, is distributed in Hai Van mountain areas [1]. *Rourea* species have been used in traditional medicine to treat rheumatism, diabetes, dysentery and to promote wound healing [2]. Several classes of natural compounds such as flavonoids, triterpenoids, coumarins, quinones have been isolated from *Rourea* plants. The isolated compounds and *Rourea* plant extracts have been tested for several biological properties such as antibacterial, anti-inflammatory, antioxidant and anti-diabetic activities, and have shown positive results [3, 4].

In the biological screening program of Vietnamese plants, the MeOH extracts of *Rourea oligophlebia* and *R. harmandianan* showed good antibacterial activity against several microbial strains. We have reported the chemical study of *Rourea oligophlebia* species collected in Ben En national park, Thanh Hoa province [5]. In continuation of our search for bioactive compounds from *Rourea* species in Vietnam, four compounds including vomifoliol (**1**), boscialin (**2**), abscisic acid (**3**) and *p*-coumaric acid (**4**) were isolated from the ethyl acetate extract of the leaves of *R. harmadiana*. Their chemical structures were elucidated by different spectroscopic methods. This is the first study of the *R. harmandiana*. These compounds were firstly isolated from this species as well as from the genus *Rourea*.

## Experimental

### *Plant materials*

The leaves of *R. harmandiana* were collected at Phu Loc district, Thua Thien - Hue province, Vietnam in October

*Corresponding author: Email: dinhngocthuc@hdu.edu.vn

2010. The plant sample was identified by Dr. Nguyen The Cuong, Institute of Ecological and Biological Resources, VAST. A voucher specimen (VN-2149) was provided to the Institute of Ecological and Biological Resources.

***General procedures***

The $^{1}$H-NMR (500 MHz) and $^{13}$C-NMR (125 MHz) spectra were recorded by a Bruker AM500 FT-NMR spectrometer (Institute of Chemistry, VAST) using TMS as an internal standard. The electrospray ionization mass spectra (ESI-MS) were obtained on an Agilent 1260 series single quadrupole LC/MS system. Column chromatography (CC) was performed on silica gel (Merck, 230-400 mesh), reversed-phase silica gel (YMC, RP-18) or Sephadex LH-20 (Sigma). Thin layer chromatography used precoated silica gel plates (Merck 60 $F_{254}$). Compounds were visualized by spraying with 10% sulfuric acid. The optical rotations were measured on the JASCO P-2000 Polarimeter (Institute of Marine Biochemistry, VAST).

***Extraction and isolation of compounds*** (Fig. 1)

The leaves of *R. harmandiana* were dried in the shade and crushed into a powder. The dried leaves powder (2.0 kg) was extracted with MeOH at room temperature for 24 hours (10 l × 3 times). The extracts were combined and concentrated under reduced pressure to obtain MeOH residues. MeOH residue was suspended with 1 l of distilled water, and extracted with ethyl acetate (500 ml × 3 times). After removal of the organic solvent, ethyl acetate residue (44 g) was obtained.

The ethyl acetate residue was subjected to a silica gel column chromatography (CC) and eluted with a gradient solvent of *n*-hexane/acetone (0-100% acetone) to afford 13 fractions (E1-E13). The E7 fraction (4.1 g) was purified on a silica gel CC using dichloromethane/ethyl acetate (19/1) as eluant to afford 10 sub-fractions denoted as E7.1-E7.10. The E7.7 sub-fraction (210 mg) was separated on silica gel CC and eluted with dichloromethane/acetone (9/1) to obtain **1** (3.2 mg). The sub-fraction E7.10 (324 mg) was purified on a reversed-phase silica gel CC, and eluted with MeOH/water (3/1) to give **2** (4.2 mg), and **3** (3.7 mg). The E8 fraction (2.5 g) was fractionated on a Sephadex LH-20 CC using dichloromethane/MeOH (1/4) as eluant to give 3 sub-fractions denoted as E8.1-E8.3. The sub-fraction E8.3 (371 mg) was purified on a reversed-phase silica gel CC, and eluted with acetone/water (1/3) to give **4** (7.1 mg).

*Vomifoliol (1):* colorless oil; $[\alpha]^{25}_{D}$ + 190$^{o}$ (*c* 0.13, MeOH); ESI-MS *m/z*: 225 $[M+H]^{+}$. $^{1}$H-NMR (500 MHz, $CD_3OD$): $\delta_H$ (ppm) 5.89 (1H, m, H-5), 5.83 (1H, m, H-8), 5.80 (1H, m, H-7), 4,34 (1H, m, H-9), 2.53 (1H, d, *J*=17 Hz, H-3), 2.18 (1H, d, *J*=17 Hz, H-3), 1.94 (3H, s, H-13), 1.26 (3H, d, *J*=6.5 Hz, H-10), 1.06 (3H, s, H-11), 1.04 (3H, s, H-12). $^{13}$C-NMR (125 MHz, $CD_3OD$): $\delta_C$ (ppm) 201.2 (C-4), 167.4 (C-6), 136.9 (C-8), 130.1 (C-7), 127.1 (C-5), 79.9 (C-1), 68.7 (C-9), 50.7 (C-3), 42.4 (C-2), 24.5 (C-11), 23.8 (C-10), 23.4 (C-12), 19.5 (C-13).

*Boscialin (2):* white solid, $[\alpha]^{25}_{D}$ -17$^{o}$ (*c* 0.12, MeOH); ESI-MS *m/z*: 229 $[M+H]^{+}$. $^{1}$H-NMR (500 MHz, $CD_3OD$): $\delta_H$ (ppm) 6.90 (1H, d, *J*=16 Hz, H-7), 6.37 (1H, d, *J*=16 Hz, H-8), 3.85 (1H, m, H-4), 2.29 (3H, s, H-10), 2.11 (1H, m, H-6), 1.75-1.67 (2H, m, H-3 and H-5), 1.46-1.38 (2H, m, H-3 and H-5), 1.06 (3H, s, H-11), 0.88 (3H, s, H-12), 0.83 (3H, d, *J*=7 Hz, H-13). $^{13}$C-NMR (125 MHz, $CD_3OD$): $\delta_C$ (ppm) 201.2 (C-9), 154.3 (C-7), 131.6 (C-8), 78.9 (C-1), 67.2 (C-4), 45.7 (C-3), 40.9 (C-2), 39.5 (C-5), 35.3 (C-6), 27.4 (C-10), 25.9 (C-11), 25.1 (C-12), 16.4 (C-13).

*Abscisic acid (3):* white solid, $[\alpha]^{25}_{D}$ + 225$^{o}$ (*c* 0.13, MeOH); ESI-MS *m/z*: 265 $[M+H]^{+}$. $^{1}$H-NMR (500 MHz, $CD_3OD$): $\delta_H$ (ppm) 7.78 (1H, d, *J*=16 Hz, H-8), 6.23 (1H, d, *J*=16 Hz, H-7), 5.94 (1H, s, H-5), 5.78 (1H, s, H-10), 2.54 (1H, d, *J*=17 Hz, H-3), 2.19 (1H, d, *J*=17 Hz, H-3), 2.05 (3H, s, H-12), 1.95 (3H, s, H-15), 1.08 (3H, s, H-13), 1.05 (3H, s, H-14). $^{13}$C-NMR (125 MHz, $CD_3OD$): $\delta_C$ (ppm) 201.0 (C-4), 170.5 (C-11), 166.6 (C-9), 150.1 (C-6), 137.5 (C-7), 129.6 (C-8), 127.5 (C-5), 120.5 (C-11), 80.6 (C-1), 50.7 (C-3), 42.8 (C-2), 24.6 (C-12), 23.5 (C-14), 21.1 (C-15), 19.6 (C-13).

*p-coumaric acid (4):* white solid. ESI-MS *m/z*: 265 $[M+H]^{+}$. $^{1}$H-NMR (500 MHz, $CD_3OD$): $\delta_H$ (ppm) **7**.62 (1H, d, *J*=16.0 Hz, H-7), 7.45 (1H, d, *J*=8.5 Hz, H-2 and H-6), 6.82 (2H, d, *J*=8.5 Hz, H-3 and H-5), 6.29 (1H, d, J=16.5 Hz, H-8). $^{13}$C-NMR (125 MHz, $CD_3OD$): $\delta_C$ (ppm) 171.0 (C-9), 161.0 (C-4), 146.6 (C-7) 131.0 (C-2 and C-6), 127.2 (C-1), 116.7 (C-3 and C-5), 115.6 (C-8).

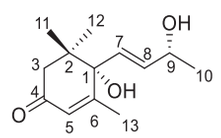

**Vomifoliol (1)**

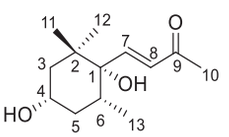

**Boscialin (2)**

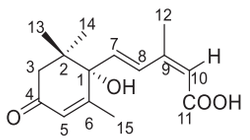

**Abscisic acid (3)**

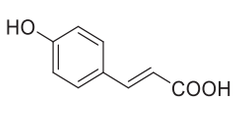

***p*-coumaric acid (4)**

**Fig. 1. Chemical structures of isolated compounds 1-4.**

## Results and discussion

### *Vomifoliol (1)*

Compound 1 was obtained as colorless oil. The ESI-MS showed a *quasi*-molecular ion peak *m/z* 225 $[M+H]^+$, that suggests the molecular formula of **1** is $C_{13}H_{20}O_3$ (M=224). The $^1H$ and $^{13}C$-NMR spectra showed typical signals of a megastigman compound. The $^1H$ NMR spectrum shown three olefinic protons at $\delta_H$ 5.89 (1H, m, H-5), 5.83 (1H, m, H-8), and 5.80 (1H, m, H-7); an oxymethine group signal at $\delta_H$ 4.34 (1H, m, H-9) and signals of 4 methyl groups including 3 singlets at $\delta_H$ 1.94 (3H, s, H-13), 1.06 (3H, s, H-11) and 1.04 (3H, s, H-12), and a doublet at $\delta_H$ 1.26 (3H, d, *J*=6.5 Hz, H-10). The $^{13}C$-NMR spectrum displayed 13 carbon signals including a carbonyl group at $\delta_C$ 201.2 (C-4), 4 olefinic carbons at $\delta_C$ 167.4 (C-6), 136.9 (C-8), 130.1 (C-7), and 127.1 (C-5), 2 oxygen-bonded carbons at $\delta_C$ 79.9 (C-1) and 68.7 (C-9) and 4 methyl groups at $\delta_C$ 24.5 (C-11), 23.8 (C-10), 23.4 (C-12) and 19.5 (C-13). From the MS, NMR spectra together with optical rotation value [6], **1** was determined as vomifoliol. The analytical NMR data of **1** are in accordance with those of a previous report [7].

### *Boscialin (2)*

Compound **2** was obtained as a white solid. The ESI-MS showed a *pseudo*-molecular ion peak *m/z* 227 $[M+H]^+$, combined with the NMR spectra, that suggests the molecular formula of **2** is $C_{13}H_{22}O_3$ (M=226). The NMR data of **2** also exhibited the signals of a megastigman compound with signals of four methyl groups including three singlets at $\delta_H$ 2.29 (3H, s, H-10), 1.06 (3H, s, H-11) and 0.88 (3H, s, H-12) and a doublet at $\delta_H$ 0.83 (3H, d, *J*=7 Hz, H-13); an oxymethine signal at $\delta_H$ 3.85 (1H, m, H-4) and 2 *trans*-olefinic protons at $\delta_H$ 6.90 (1H, d, *J*=16 Hz, H-7) and 6.37 (1H, d, *J*=16 Hz, H-8). The singlet of methyl group at $\delta_H$ 2.29 (3H, s, H-10) suggested that a ketone group was positioned at C-9. Similar to **1**, the $^{13}C$-NMR spectrum also gave signals of 13 carbons including a carbonyl group at $\delta_C$ 201.2 (C-9), two olefinic carbons at $\delta_C$ 154.3 (C-7) and 131.6 (C-8), two oxygen-bonded signals at $\delta_C$ 78.9 (C-1) and 67.2 (C-4) and 4 methyl groups at $\delta_C$ 27.4 (C-10), 25.9 (C-11), 25.1 (C-12) and 16.4 (C-13). Based on the NMR spectral data analysis above, along with comparison of the optical rotation, **2** was identified as boscialin [8].

### *Abscisic acid (3)*

Compound **3** was isolated from ethyl acetate extract as a white solid. The ESI-MS showed a *quasi*-molecular ion peak *m/z* 265 $[M+H]^+$, that corresponds to a molecular formula of $C_{15}H_{20}O_4$ (M=264). The $^1H$-NMR spectrum displayed proton signals similar to those of **1**. On the spectrum, there appeared signals of two olefinic protons in *trans* form at $\delta_H$ 7.78 (1H, d, *J*=16 Hz, H-8) and 6.23 (1H, d, *J*=16 Hz, H-7) and two other singlet olefinic protons at $\delta_H$ 5.94 (1H, s, H-5) and 5.78 (1H, s, H-10). Different from compound **1**, four methyl groups of **3** appeared as four singlets at $\delta_H$ 2.05 (3H, s, H-12), 1.95 (3H, s, H-15), 1.08 (3H, s, H-13) and 1.05 (3H, s, H-14). The $^{13}C$-NMR spectrum gave of 15 carbon signals including a carbonyl group at $\delta_C$ 201.0 (C-4), a carboxylic group at $\delta_C$ 170.5 (C-11); six olefinic carbons at $\delta_C$ 166.6 (C-9), 150.1 (C-6), 137.5 (C-7), 129.6 (C-8), 127.5 (C-5) and 120.5 (C-11), an oxygen-bonded carbon at $\delta_C$ 80.6 (C-1) and four methyl groups at $\delta_C$ 24.6 (C-12), 23.5 (C-14), 21.1 (C-15) and 19.6 (C-13). From the analysis of the spectral data above, combined with previous literature [9], compound **3** was identified as abscisic acid.

### *p-coumaric acid (4)*

Compound **4** was isolated as a white solid. The ESI-MS showed a *quasi*-molecular ion peak *m/z* 165 $[M+H]^+$, that corresponds to a molecular formula of $C_9H_8O_3$ (M=164). The $^1H$-NMR spectrum showed signals of an $A_2B_2$ system at $\delta_H$ 7.45 (1H, d, *J*=8.5 Hz, H-2 and H-6) and 6.82 (2H, d, *J*=8.5 Hz, H-3 and H-5). In addition, signals of 2 *trans*-olefinic protons were observed at $\delta_H$ **7**.62 (1H, d, *J*=16.0 Hz, H-7) and 6.29 (1H, d, J=16.5 Hz, H-8). The $^{13}C$-NMR spectrum revealed 9 carbon signals including a carboxylic acid at $\delta_C$ 171.0 (C-9), and 8 olefinic carbon signals at $\delta_C$ 161.0 (C-4), 146.6 (C-7), 131.0 (C-2 and C-6), 127.2 (C-1), 116.7 (C-3 and C-5), and 115.6 (C-8). Therefore, **4** was elucidated as *p*-coumaric acid. The NMR data of **4** are in agreement with those of a previous study [10].

These compounds **1-4** were the first chemical substances discovered from *R. harmandiana* as well as from the genus *Rourea*. Especially, in the previous studies of *Rourea* species, only one megastigman compound dihydrovomifoliol-9-β-D-glucopyranoside was discovered from *R. minor* [11]. Vomifoliol (**1**) showed antimicrobial against *Aspergillus niger* and *Fusarium oxysporum* strains with MIC values of 100 and 50 µg/ml, respetively [6]. Boscialin (**2**) revealed activity against various strains including *Corynebacterium minutissimum*, *Candida albicans*, against *Trypanosoma brucei rhodesiens*e and also revealed cytotoxicity against HT-29 human cancer cell [12]. Abscisic acid (**3**) exhibited antibacterial activity against *Helicobacter pylori* [13] and antifungal activity. Compound **4** demonstrates an antibacterial activity against three Gram-positive bacteria (*Streptococcus pneumonia*, *Staphylococcus aureus* and *Bacillus subtilis*; all $MIC_{50}$=20 µg/ml) and three Gram-negative bacteria (*Escherichia coli*, $MIC_{50}$=80 µg/ml; *Shigella dysenteriae*, $MIC_{50}$=10 µg/ ml; and *Salmonella typhimurium*, $MIC_{50}$=20 µg/ml) [14]. The antibacterial activity of the isolated compounds **1-4** possibly made contributions to

antibacterial activity of the MeOH extract of *R. harmandiana* leaves.

## Conclusions

From the ethyl acetate extract of *R. harmandiana* leaves, four compounds were isolated and identified as vomifoliol (**1**), boscialin (**2**), abscisic acid (**3**) and *p*-coumaric acid (**4**). This is the first study about *R. harmandiana* in the world. These compounds were firstly discovered from *R. harmandiana* as well as from the *Rourea* genus.

## ACKNOWLEDGEMENTS

This research is funded by Vietnam National Foundation for Science and Technology Development (NAFOSTED) under grant number 104.01-2018.08.

The authors declare that there is no conflict of interest regarding the publication of this article.

## REFERENCES

[1] Pham Hoang Ho (2003), *Vietnamese Plants*, Youth Publishing House, Ho Chi Minh City, **1**, pp.758-760.

[2] Vo Van Chi (2012), *Dictionary of Vietnamese Medicinal Plants*, Medical Publishing House, **1**, pp.1206-1207.

[3] C.P. Osman, Z. Zahari, M.I. Adenan, R.M. Zohdi (2019), "A review on traditional uses, phytochemistry, and pharmacology of the genus *Rourea*", *Journal of Applied Pharmaceutical Science*, **9(9)**, pp.125-131.

[4] H.N. Ngoc, S. Löffler, D.T. Nghiem, T.L.G. Pham, H. Stuppner, M. Ganzera (2019), "Phytochemical study of *Rourea minor* stems and the analysis of therein contained Bergenin and Catechin derivatives by capillary electrophoresis", *Microchemical Journal*, **149**, DOI: 10.1016/j.microc.2019.104063.

[5] Dinh Ngoc Thuc, Do Van Duc, Le Nguyen Thanh (2018), "Chemical constituents from the leaves of *Rourea oligophlebia* Merr.", *Vietnam Pharmaceutical Journal*, **520(59)**, pp.33-36.

[6] Y. Yamano, M. Ito (2005), "Synthesis of optically active vomifoliol and roseoside stereoisomers", *Chemical and Pharmaceutical Bulletin*, **53(5)**, pp.541-546.

[7] P.T.T. Huong, N. Van Thanh, C.N. Diep, N.P. Thao, N.X. Cuong, N.H. Nam, C.V. Minh (2015), "Antimicrobial compounds from *Rhizophora stylosa*", *Vietnam Journal of Science and Technology*, **53(2)**, pp.205-210.

[8] N. Pauli, U. Séquin, A. Walter (1990), "Boscialin and boscialin 4′-O-glucoside, two new compounds isolated from the leaves of *Boscia salicifolia* Oliv", *Helvetica Chimica Acta*, **73(3)**, pp.578-582.

[9] F. Ferreres, P. Andrade, F.A. Tomás-Barberán (1996), "Natural occurrence of abscisic acid in heather honey and floral nectar", *Journal of Agricultural and Food Chemistry*, **44(8)**, pp.2053-2056.

[10] S.Y. Lee, et al. (2010), "A new phenylpropane glycoside from the rhizome of *Sparganium stoloniferum*", *Archives of Pharmacal Research*, **33(4)**, pp.515-521.

[11] Z.D. He, et al. (2006), "Rourinoside and rouremin, antimalarial constituents from *Rourea minor*", *Phytochemistry*, **67(13)**, pp.1378-1384.

[12] J. Busch, et al. (1998), "Total synthesis and biological activities of (+)-and (−)-boscialin and their 1 '-epimers", *Journal of Natural Products*, **61(5)**, pp.591-597.

[13] S. Kim, et al. (2017), "Isolation of abscisic acid from Korean acacia honey with anti-Helicobacter pylori activity", *Pharmacognosy Magazine*, **13**, Suppl. 2, pp.S170-S173.

[14] K. Pei, et al. (2016), "*p*-Coumaric acid and its conjugates: dietary sources, pharmacokinetic properties and biological activities", *Journal of the Science of Food and Agriculture*, **96(9)**, pp.2952-2962.

DOI: 10.31276/VJSTE.62(2).34-37

# Synthesis of sulfonylurea derivatives and their α-glucosidase inhibitory activity

**Thi Thoi Bui[1*], Dai Quang Ngo[2], Van Loc Tran[3]**

*[1]Vietnam Institute of Industrial Chemistry*
*[2]Vietnam National Chemical Group*
*[3]Institute of Chemistry, VAST*

Received 16 September 2019; accepted 12 December 2019

***Abstract:***

**The paper describes the preparation of new sulfonylurea derivatives from sulfonyl carbamate 6 with amino derivatives. The process for synthesis of the key compound 6 included three steps starting from compound 6-chloronicotinic acid 1, which are readily available chemicals. The compound 1 in the presence of triethylamine in anhydrous acetone solvent and ethyl chloroformate to obtain 6-chloronicotinic (ethyl carbonic) anhydride compound 3. The compound 3 were subsequently reacted with compound 4 to obtain compounds 5. The sulfonamides 5 was refluxed with ethyl chloroformate in present anhydrous potassium carbonate in dry acetone to obtain the key compounds 6. The total yield of the key intermediate compound 6 is about 81.35%, related to the starting materials. Finally, three sulfonylurea derivatives 7a-c were synthesized by condensation of 6 with various of amines in toluene. Their structures have been determined by IR, MS and $^{1}H$ and $^{13}C$ NMR spectroscopic methods, and their α-glucosidase inhibitory activity have been evaluated.**

***Keywords:*** **6-chloronicotinic acid, sulfonyl carbamate, sulfonylurea derivatives.**

***Classification number:*** **2.2**

## Introduction

Sulfonylurea derivatives are oral hypoglycemic agents used for the treatment of type II diabeties for almost eight decades [1]. These drugs act by releasing insulin from the β cells of the pancreas [2]. Along with antidiabetic activity, large numbers of sulfonylurea derivatives also exhibit a wide range of biological activity [3] such as diuretic, histamine H3 receptor antagonist, antimalarial, anticancer, and anti-inflammatory activity.

The common synthesis method of sulfonylurea derivatives is the treatment of sulfonamide with an appropriate isocyanate in the presence of a base [4]. Scheme 1 describes the synthetic route of Glipizide, Glibenclamide. The various substituted carboxylic acids were treated with 2-phenethylamine in presence of ethyl chloroformate and triethylamine in anhydrous acetone to provide the corresponding amide. The corresponding sulfonamide derivatives were prepared by reaction of 4 (see Scheme 1) with chlorosulfonation and trapped by ammoniac solution, followed by reaction with isocyanates to obtain the desired product [5].

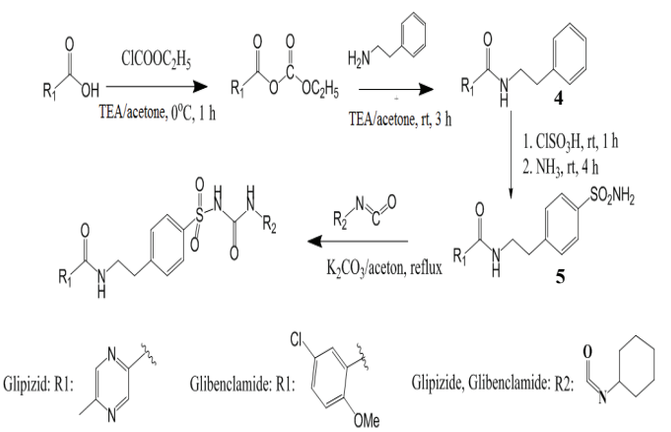


**Scheme 1. The synthetic route of Glipizide, Glibenclamide.**

*Corresponding author: Email: thoibt@gmail.com

In the present paper, we report the synthesis details of new sulfonylurea derivatives. As depicted in Scheme 2 [6], compound 6-chloronicotinic acid **1** was treated with TEA and ethyl chloroformate in anhydrous acetone followed by an addition of commercially available 4-(2-aminoethyl) benzenesulfoamide to provide the product **5** (91.2%). The sulfonamide **5** was subsequently refluxed with ethyl chloroformate in the presence of anhydrous potassium carbonate to yield intermediate compound **6** (89.2%). Next, sulfonylurea derivatives **7a-c** were synthesized by the condensation of **6** with various of amines in toluene (Scheme 2). The overall yield of each compound was above 62%. The structures of the synthesized compounds were assigned on the analysis of mass spectrometry (MS) and $^{1}H$ and $^{13}C$ nuclear magnetic resonance (NMR) data. All synthesized compounds were evaluated for α-glucosidase inhibitor activity.

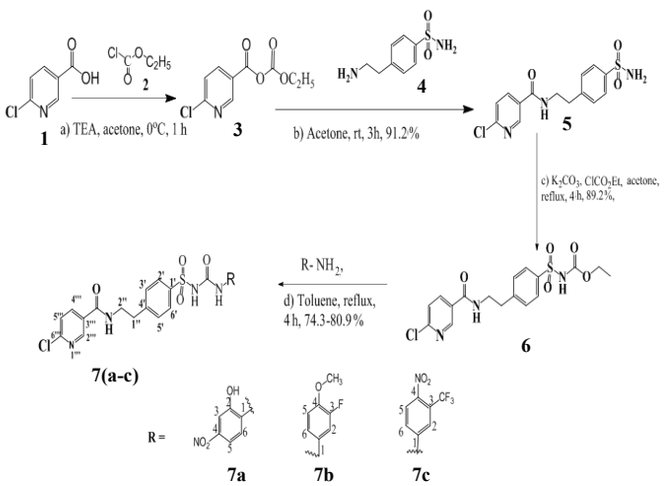


**Scheme 2. Synthesis 7(a-c) novel sunlfonylureas compounds.**

## Experimental

### *Materials and methods*

Reagents were purchased from Aldrich and Merck with analytical grade and used without further purification. Solvents for column chromatography were distilled before use. Melting points (°C) were determined on a Thermo Mel-temp 3.0 (USA). IR spectra were recorded on an IMPACT 410 Nicolet spectrometer. Electrospray ionization mass spectrometry (ESI-MS) spectra were measured on an 1100 Agilent LC/MS ion trap. NMR spectra ($^{1}H$, $^{13}C$) were recorded on a Bruker Avance 500 MHz with tetramethylsilane (TMS) as the internal standard for $^{1}H$ and solvent signal for $^{13}C$. Thin-layer chromatography was performed on a pre-coated silica gel 60 F254 (Merck) and visualized under UV light ($\lambda_{max}$ 254 nm) and stained with a solution of 1% (v/v) vanillin in $H_2SO_4$. Column chromatography was performed on silica gel 300-400 mesh (Merck).

### *Procedure for the preparation of 6-Chloro-N-(4-sulfamoylphenethyl)nicotinamide (5)*

To a stirred solution of 6-chloronicotinic acid (0.01 mol) in anhydrous acetone (50 ml) and triethylamine (1.42 ml, 0.01 mol) at 0°C, ethyl chloroformate (0.97 ml, 0.01 mol) was added dropwise and the reaction was further stirred for 60 min. After 15 min, a solution of 4-(2-aminoethyl)-benzenesulfonamide (2.0 g, 0.01 mol) and triethylamine (1.42 ml, 0.01 mol) in anhydrous acetone was added. The resulting mixture was stirred for 3 h at room temperature. Acetone was then removed, and the residue was acidified with 5% HCl to pH≈5. The white solid was collected and washed with distilled water. Pure product was obtained by recrystallization from ethanol.

Yield: 91.20% - white powder, m.p. 236-238°C. -IR (KBr): ν=3378 (NH), 1637 (CO-amid), 1587 (C=C-aromatic), 1320 and 1158 (O=S=O) $cm^{-1}$. - $^{1}H$ NMR (500 MHz, DMSO-$d_6$, 25°C, TMS): δ=8.84 (1H, br s, CONH), 8.78 (1H, s, H-2'''), 8.19 (1H, d, *J*=8.0 Hz, H-4'''), 7.75 (2H, d, *J*=8.0 Hz, H-2', H-6'), 7.64 (1H, d, *J*=8.0 Hz, H-5'''), 7.43 (2H, d, *J*=8 Hz, H-3', H-5'), 7.28 (2H, s, $SO_2NH_2$), 3.54 (2H, q, *J*=7.0 Hz, H-2''), 2.93 (2H, t, *J*=7.0 Hz, H-1''). - $^{13}C$ NMR (125 MHz, DMSO-$d_6$, 25°C, TMS): δ=164.42 (CONH), 152.47, 148.98, 143.9, 142.21, 138.78, 129.59, 129.49 (2C), 126.05 (2C), 124.48, 40.84, 34.89.

### *Procedure for the preparation of Ethyl-((4-(2-(6-chloronicotinamido)ethyl)phenyl) sulfonyl) carbamate (6)*

6-Chloro-N-(4-sulfamoylphenethyl)nicotinamide **5** (0.01 mol) were mixed with a solution of ethyl chloroformate (1.23 ml, 0.013 mol) and anhydrous potassium carbonate (2.0 g, 0.014 mmol) in dry acetone (300 ml). The reaction was refluxed for 4h and acetone was removed under reduced pressure. The residue was suspended in 100 ml water and neutralized with 1% HCl. The white solid was filtered and washed with distilled water to obtain the desired product.

Yield: 89.20% - white powder, m.p. 159-160°C. - $^{1}H$ NMR (500 MHz, DMSO-$d_6$, 25°C, TMS): δ=11.90 (1H, s, $SO_2NH$), 8.83 (1H, t, *J*=5.5 Hz, CONH), 8.76 (1H, d, *J*=2.0 Hz, H-2'''), 8.18 (1H, dd, *J*=2.0, 8.5 Hz, H-4'''), 7.82 (2H, d, *J*=8.0 Hz, H-2', H-6'), 7.63 (1H, d, *J*=8.0 Hz, H-5'''), 7.50 (2H, d, *J*=8.0 Hz, H-3', H-5'), 4.00 (2H, q, *J*=7.0 Hz, $CH_2$-carbamate), 3.55 (2H, q, *J*=7.0 Hz, H-2''), 2.96 (2H, t, *J*=7.0 Hz, H-1''), 1.08 (3H, t, *J*=7.0 Hz, $CH_3$). - $^{13}C$ NMR (125 MHz, DMSO-$d_6$, 25°C, TMS): δ=163.69 (CONH), 152.46 (CONH), 151.02, 148.79, 145.79, 143.51, 138.45, 137.13, 129.13 (2C), 125.69 (2C), 124.1, 56.00 ($CH_2$ carbamate), 40.45, 34.64, 18.51 ($CH_3$).

***General procedure for the preparation of sulfonylurea derivatives (7a-c)***

Ethyl-((4-(2-(6-chloronicotinamido)ethyl)phenyl) sulfonyl) carbamate (6) (0.01 mol) and appropriate amines (0.011 mol) in toluene was refluxed for 4 h and then allowed cool to room temperature. The solid was filtered, washed with water and recrystallized in ethanol.

*6-Chloro-N-(4-(N-((2-hydroxy-4-nitrophenyl) carbamoyl)sulfamoyl)phenethyl)nico - tinamide (7a):* yield 74.90% - white powder, m.p. 170-172°C**.** - MS ((-)-ESI): *m/z* (%)=520 (100). $[M-H]^-$. - IR (KBr): ν=3399 (OH), 3342 (NH), 1655 (C=O, amide), 1538 (C=C-aromatic), 1153 (C-N), 1425 and 1268 ($NO_2$) 1327 and 1185 (O=S=O) $cm^{-1}$. - $^1H$ NMR (500 MHz, DMSO-$d_6$, 25°C, TMS): δ=8.84 (1H, t, *J*=5.5 Hz, CONH), 8.78 (1H, d, *J*=2.0 Hz, H-2'''), 8.25 (1H, s, CONH), 8.18 (1H, dd, *J*=2.5, 7.5 Hz, H-4'''), 7.75-7.71 (3H, m, H-6, H-2', H-6'), 7.60 (1H, d, *J*=8.0 Hz, H-5'''), 7.59 (1H, dd, *J*=2.5, 9.0 Hz, H-5), 7.49 (1H, d, *J*=2.5 Hz, H-3), 7.27 (1H, d, *J*=8.0 Hz, H-3', H-5'), 3.52 (2H, q, *J*=6.5 Hz, H-2''), 2.88 (2H, t, *J*=7.5 Hz, H-1''). - $^{13}C$ NMR (125 MHz, DMSO-$d_6$, 25°C, TMS): δ=163.7 (CONH), 152.39 (CONH), 148.81 (2C), 143.92, 141.32, 138.44 (2C), 137.25, 129.4, 127.98 (2C), 126.75 (2C), 124.05 (2C), 117.15, 115.55, 110.13, 40.63, 34.62.

*6-Chloro-N-(4-(N-((4-nitro-3-(trifluoromethyl)phenyl) carbamoyl)sulfamoyl)phene - thyl)-nicotinamide 7b):* yield 74.30% - white powder, m.p 221-222°C. - MS ((-)-ESI): *m/z* (%) = 570 (20). $[M-H]^-$. - IR (KBr): ν=3421 (NH), 1635 (C=O, amide), 1569 (C=C-aromatic), 1141 (C-N), 1458 ($NO_2$), 1348 and 1153 (O=S=O) $cm^{-1}$. - $^1H$ NMR (500 MHz, DMSO-$d_6$, 25°C, TMS): δ=9.73 (1H, br s, $SO_2NH$), 8.81 (1H, br s, CONH), 8.75 (1H, br s, H-2'''), 8.16 (1H, d, *J*=6.5 Hz, H-4'''), 8.12 (1H, d, *J*=8.5 Hz, H-5), Hz, 8.01 (1H, br s, H-2), 7.91 (2H, d, *J*=7.0 Hz, H-2', H-6'), 7.81 (1H, d, *J*=7.5 Hz, H-6), 7.60 (1H, d, *J*=8.0 Hz, H -5'''), 7.51 (2H, d, *J*=7.0 Hz, H-3', H-5'), 3.55 (2H, d, *J*=5.5 Hz, H-2''), 2.96 (2H, s, H-1''). - $^{13}C$ NMR (125 MHz, DMSO-$d_6$, 25°C, TMS): δ=163.67 (CONH), 154.29, 152.43 (CONH), 148.76, 143.48, 142.09, 138.42, 133.74, 129.58, 129.33, 129.09 (2C), 127.51, 125.66 (2C), 124.15, 124.06, 123.54, 114.43, 111.67 ($CF_3$), 40.42, 34.54.

*2-(2-(6-Chloronicotinamido)ethyl)-5-(N-((3-fluoro-4-methoxyphenyl)carbamoyl)-sulfamoyl)-benzene-1-ylium (7c):* yield 80.90% - white powder, m.p 209-211°C. - MS ((-)-ESI): *m/z* (%) = 505 (100). $[M-H]^-$. - IR (KBr): ν=3409 (NH), 1673 (C=O, amide), 1539 (C=C-aromatic), 1246 (C-O), 1355 and 1170 (O=S=O) $cm^{-1}$. - $^1H$ NMR (500 MHz, DMSO-$d_6$, 25°C, TMS): δ=8.82-8.77 (3H, m, CONH, H-5''', H-2'''), 8.17 (1H, dd, *J*=2.5, 8.5 Hz, H-4'''), 7.88 (2H, d, *J*=8.5 Hz, H-2', H-6'), 7.59 (1H, d, *J*=8.5 Hz, H-5), 7.49 (2H, d, *J*=8.5 Hz, H-3', H-5'), 7.27 (1H, dd, *J*=2.0, 14.0 Hz, H-6), 7.07-7,01 (2H, m, H-2, CONH), 3.77 (3H, s, $OCH_3$), 3.57-3.53 (2H, m, H-2''), 2.95 (2H, t, *J*=7.5 Hz, H-1''). - $^{13}C$ NMR (125 MHz, DMSO-$d_6$, 25°C, TMS): δ=163.75 (CONH), 163.71 (CONH), 152.43, 148.77, 145.13, 143.50, 142.09, 138.45, 129.39 (2C), 129.12, 127.46 (2C), 125.68, 124.10, 124.05, 116.14, 115.15, 114.15, 56.18 ($OCH_3$), 40.00, 34.65.

## Resutls and discussion

***Chemistry***

The synthetic routes of three new *sulfonylurea derivatives* compounds are shown in Schemes 2. 6-Chloronicotinic acid was treated with ethyl chloroformate in the presence of triethylamine in anhydrous acetone solvent and to furnish 6-Chloronicotinic (ethyl carbonic) anhydride compound **3** [7]. Compound **3** was subsequently reacted with 4-(2-aminoethyl) benzenesulfonamide **4** to obtain compounds 6-chloro-N-(4-sulfamoylphenethyl) nicotinamide **5**. Refluxing of sulfonamide **5** with ethyl chloroformate in present anhydrous potassium carbonate in dry acetone obtain compound **6**. Finally, sulfonylurea derivatives **7 (a-c)** were synthesized by a reaction of **6** with various amines in toluene. The use of toluene as a solvent gives the highest product yield when compared to other solvents such as dioxane or DMF. The structures of the products were confirmed by means of $^1H$ and $^{13}C$ NMR. The $^1H$ NMR spectrum of compound **5** indicated the presence of three aromatic protons of the pyridine ring at $\delta_H$ 8.78 (1H, s, H-2'''), 8.19 (1H, d, *J*=8.0 Hz, H-4'''), 7.64 (1H, d, *J*=8.0 Hz, H-5'''). The appearance of the NH protons at $\delta_H$ 8.84 (1H, br s), 7.28 (2H, s, $SO_2NH_2$) in the $^1H$ NMR spectrum of compound **5** confirmed the formation of amide products. Furthermore, the $^1H$ NMR spectrum showed signals for benzene protons at $\delta_H$ 7.75 (2H, d, *J*=8.0 Hz, H-2', H-6'), 7.43 (2H, d, *J*=8 Hz, H-3', H-5') and the methylene protons at $\delta_H$ 3.54 (2H, q, *J*=7.0 Hz, H-2''), 2.93 (2H, t, *J*=7.0 Hz, H-1'') ppm. The $^{13}C$ NMR spectra of 5 was in good agreement with the structure assigned. The $^{13}C$ NMR spectra exhibited signals at $\delta_C$ 164,42 assignable to the amide moiety (CONH). The key intermediate **6** was characterized by $^1H$ NMR spectra which exhibited additional signals at $\delta_H$ 4.00 (2H, q, *J*=7.0 Hz, $CH_2$-carbamate) and $\delta_H$ 1.08 (3H, t, *J*=7.0 Hz, $CH_3$), corresponding to the ethyl ester group. The $^{13}C$ NMR spectra exhibited additional signals at $\delta_C$ 152.46 (CONH), $\delta_C$ 56.00 ($CH_2$ carbamate), and $\delta_C$ 18.51 ($CH_3$) assignable to the carbamate moiety ($NHCOOCH_2CH_3$). The $^1H$ NMR spectra of the sulfonylurea derivatives **(7a-c)** indicated the presence of two broad singlets appearing at $\delta_H$ 8.25 **(7a)**, $\delta_H$ 8.81 **(7b)**, $\delta_H$ 8.82 **(7c)**, for the NH proton of the urea moiety. Moreover, the disappearance of the ethyl ester protons and the presence of aromatic protons at $\delta_H$ 7.01-8.12 clearly confirmed the formation of urea derivatives. The $^{13}C$ NMR spectra of urea derivatives showed a frequency signal range observed at 152.39, 152.43, and 163.71 ppm assignable to the carbonyl carbon between the two NH groups of the urea

of compounds **7a**, **7b**, and **7c**, respectively.

***α-glucosidase inhibitory activity***

Three compounds were evaluated for their ability to inhibit α-glucosidase**.** Acarbose was used as standard compound and glipizide was also tested to compare with the synthesized derivatives. Compound **7c** showed moderate activity with an $IC_{50}$ value of 329.62 µM, similar to glipizide, while compounds **7a-b** have no α-glucosidase inhibitor activity (Table 1).

**Table 1. The α-glucosidase inhibitor activity of compounds 7(a-c).**

| Compounds | α-glucosidase inhibitory activity $IC_{50}$ (µM) |
|---|---|
| Acarbose control | 268.29 |
| Glipizide | 300.47 |
| 7a | >492.39 |
| 7b | >447.62 |
| 7c | 329.62 |

## Conclusions

We have successfully synthesized **t**hree new sulfonylurea derivatives. The structures of products were confirmed by means of $^{1}H$ and $^{13}C$ NMR. $^{1}H$ NMR spectrum. Newly synthesized sulfonylurea derivative **7c** exhibited promising α-glucosidase inhibitory activity, similar to that of a glipizide agent.

The authors declare that there is no conflict of interest regarding the publication of this article.

## REFERENCES

[1] R. Levine (1984), "Sulfonylureas: background and development of the field", *Diabetes Care*, **7(1)**, pp.3-7.

[2] S. Seino (2012), "Cell signalling in insulin secretion: the molecular targets of ATP, cAMP and sulfonylurea", *Diabetologia*, **55(8)**, pp.2096-2108.

[3] S. Sen, Ruchika, D. Kumar, T.S. Easwari, S. Gohri (2016), "Therapeutic aspects of sulfonylureas: a brief review", *Journal of Chemical and Pharmaceutical Research*, **8(12)**, pp.121-130.

[4] WO 2001005354 A2 (2001), https://patents.google.com/patent/WO2001005354A2/sv.

[5] Thi Thoi Bui, Dai Quang Ngo, Van Loc Tran, Van Chien Tran, Thi Phuong Thao Tran (2016), "Synthesis of glipizide for the treatment of type 2 diabetes", *Vietnam Journal of Chemistry*, **54(6e2)**, pp.233-236.

[6] I.G. Rathish, et al. (2009), "Synthesis and blood glucose lowering effect of novel pyridazinone substituted benzenesulfonylurea derivatives", *European Journal of Medicinal Chemistry*, **44(8)**, pp.2673-2678.

[7] Ho Sik Rho, Heung Soo Baek, Duck Hee Kim, Ih Seop Chang (2006), "A convenient method for the preparation of alkanolamides", *Bull. Korean Chem. Soc*., **27(4)**, DOI: 10.5012/bkcs.2006.27.4.584.

DOI: 10.31276/VJSTE.62(2).38-40

# Synthesis of a novel polymer via the coupling reaction of cyanuric chloride and a di-amine

**Hung Quang Pham[1, 2], Thuy Thu Truong[2], Duc-Anh Song Nguyen[1, 2], Le-Thu Thi Nguyen[2*]**

*[1]National Key Laboratory of Polymer and Composite Materials, University of Technology, Vietnam National University, Ho Chi Minh city*

*[2]Faculty of Materials Technology, University of Technology, Vietnam National University, Ho Chi Minh city*

Received 3 January 2020; accepted 6 March 2020

***Abstract:***

**Polymers containing hydrogen bonds are of great significance as they have the potential to strengthen the mechanical properties of a material through non-covalent crosslinking, which is the basis for paint and self-healing materials. In this work we describe a method to obtain a novel polymer via the coupling reaction of cyanuric chloride and a di-amine. We investigate the reaction conditions to optimise the polymerization yield and molecular weight polydispersity. The polymerization process was characterised by gel permeation chromatography (GPC), nuclear magnetic resonance spectroscopy (NMR), and attenuated total reflection Fourier-transform infrared (ATR FT-IR) spectrometry.**

***Keywords:*** **cyanuric chloride, di-amine, hydrogen bond, triazine.**

***Classification number:*** **2.2**

## Introduction

There is a growing interest in synthetic polymers with strong non-covalent crosslinking that induces ionic, π-π stacking, and hydrogen bonding. This type of polymer is applied across many fields from paint to recycled and self-healing materials. In this article, we synthesised a polymer with hydrogen interaction by cyanuric chloride and amine. The attractive interaction between a high-electron-density atom and an electron-deficient hydrogen gives rise to hydrogen bonding [1, 2]. A hydrogen bond forms when an electron is moved from a proton acceptor (such as N, F, O atoms) to a proton donor molecule (i.e. electron-deficient hydrogen). Although hydrogen bonds are weaker than polar and covalent bonds, they are stronger than the van der Waals forces [3]. Thus, one can use hydrogen bonding to effectively enhance the mechanical properties of a material.

Polymerization of cyanuric chloride with a di-amine is used to introduce a triazine ring and NH group to the polymer backbone. Hydrogen interactions can form between the proton-acceptor of the triazine ring and the proton-donor of the NH group. This hydrogen bond in the triazine ring is popularly used. When the coupling reaction of cyanuric chloride with the di-amine occurs, the obtained polymer backbone has one nitrogen atom acceptor and two amino hydrogen donors next to each other. This structure can form a stronger hydrogen bond [4]. Therefore, the triazine ring is introduced into the polymer chain using a coupling reaction to cyanuric chloride.

Cyanuric chloride is known as a multifunctional reactive dye and can be completely controlled by temperature. The chlorine atoms of cyanuric chloride are easily replaced by other nucleophilic agents in the presence of a hydrochloride electron acceptor. The chlorine substitution is temperature controlled step by step, has been observed to follow an empirical rule: mono chlorine replacement occurs at a temperature of 0°C or lower, di-chlorine at room temperature, and tri-chlorine at temperatures above 60°C [5].

This synthetic process is an easy polymerization technique to create triazine-based polymers with hydrogen bonding interactions. Moreover, the reaction of cyanuric chloride with a di-amine is efficient and gives a high yield.

## Materials and methods

### *Materials*

The polypropylene oxide di-amine (PPO di-amine) was purchased from Sigma Aldrich with molecular weight of 2000 g/mol, cyanuric chloride (99%) and N,N-Diisopropylethylamine (DIPEA, 99%) were bought from Sigma Aldrich and the solvents were received from Fisher Chemicals.

*Corresponding author: Email: nguyenthilethu@hcmut.edu.vn

### *Characterisation*

Proton nuclear magnetic resonance ($^1$H NMR) spectra were measured at 300 MHz using a Bruker Avance 300 with deuterated acetone ($C_3D_6O$) and tetramethylsilane internal reference. Attenuated total reflection Fourier-transform infrared (ATR FT-IR) spectra of the polymers were measured at 4 $cm^{-1}$ resolution using an FT-IR Tensor 27 spectrometer with a diamond/ZnSe element combined with a Pike MIRacle ATR accessory. Gel permeation chromatography was recorded on a Polymer PL-GPC 50 gel permeation chromatograph system with a refractive index (RI) detector. Chloroform was used as the eluent and the flow rate was 1.0 ml/min. Polystyrene standards were used for the calculation of the molecular weight and molecular weight distribution.

### *Synthesis of polymer triazine*

Cyanuric chloride 1.0 g (5.42 mmol) was added to 27.1 ml of the tetrahydrofuran solvent in a two-neck flask. Polypropylene oxide di-amines 2.3 g (5.42 mmol) and N,N-diisopropylethylamine 2.1 ml (1.5 g, 11.93 mmol) was then added to the flask. The reaction was kept under constant stirring for 24 h at room temperature. Then, the solid was removed by filtration and the polymer, in liquid form, was collected.

## Results and discussion

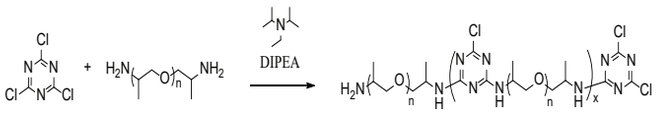


**Scheme 1. Synthesis of polymer triazine.**

The polymerization process described in Scheme 1 is the reaction of the primary amine with cyanuric chloride. At room temperature, the first and second reactive positions on cyanuric chloride react, while a temperature of 60°C or higher is needed to activate the third reactive site [6]. The above polymerization process was maintained at room temperature so that the polymer backbone was extended instead of forming a network. The molecular weight of the polymer was observed by the GPC curve in Fig. 1, where the number averaged molecular weight ($M_n$) is approximated at 11090, the molecular weight ($M_w$) is approximated at 15160, and the high PDI ($M_w/M_n$=1.36) is likely due to the coupling reaction, since the number of repetitions of the unit in the polymer cannot be controlled.

The polymer triazine was synthesised with the catalyst DIPEA as shown in Scheme 1, so that the peak at 1.4 ppm for the $CH_3$ group in DIPEA appeared in the $^1$H NMR spectrum of the polymer, as seen in Fig. 2. The disappearance of the $NH_2$ group in the $^1$H NMR spectrum of polypropylene oxide di-amines (2.6-3 ppm, Fig. 3) can be observed, which indicates that all $NH_2$ groups reacted with the cyanuric chloride. The appearance of peak d (6.3-6.7 ppm, Fig. 2) corresponding to the NH groups were created.

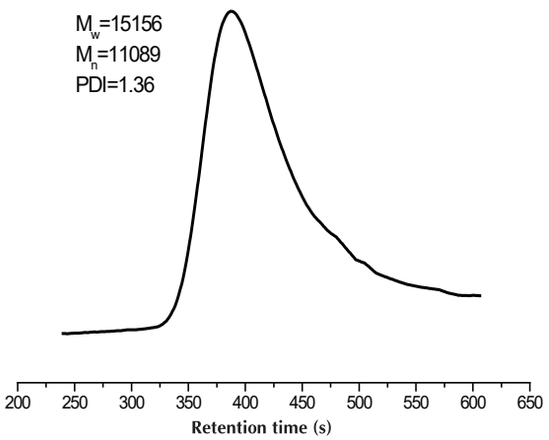


**Fig. 1. GPC of polymer triazine.**

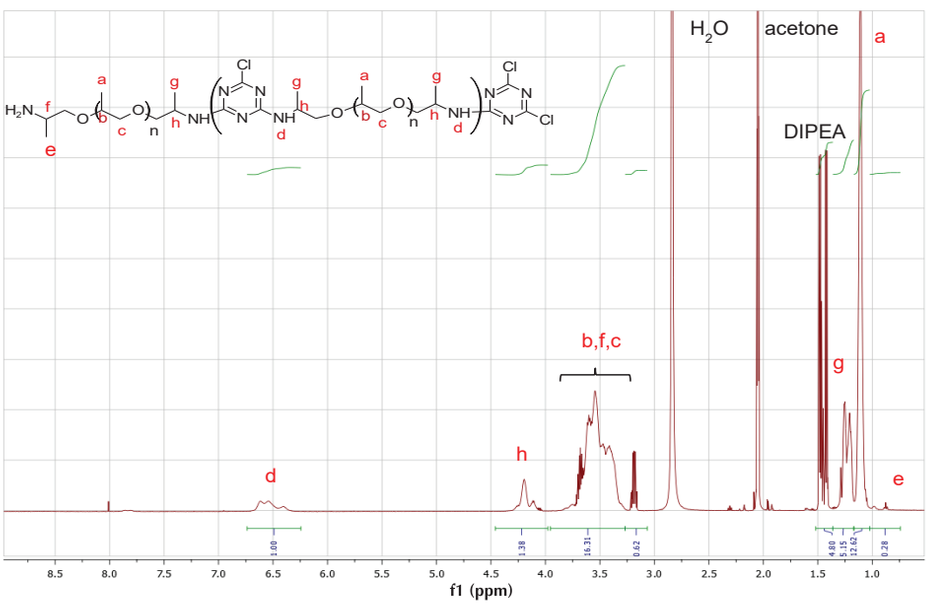


**Fig. 2. $^1$H NMR spectrum of polymer triazine in acetone.**

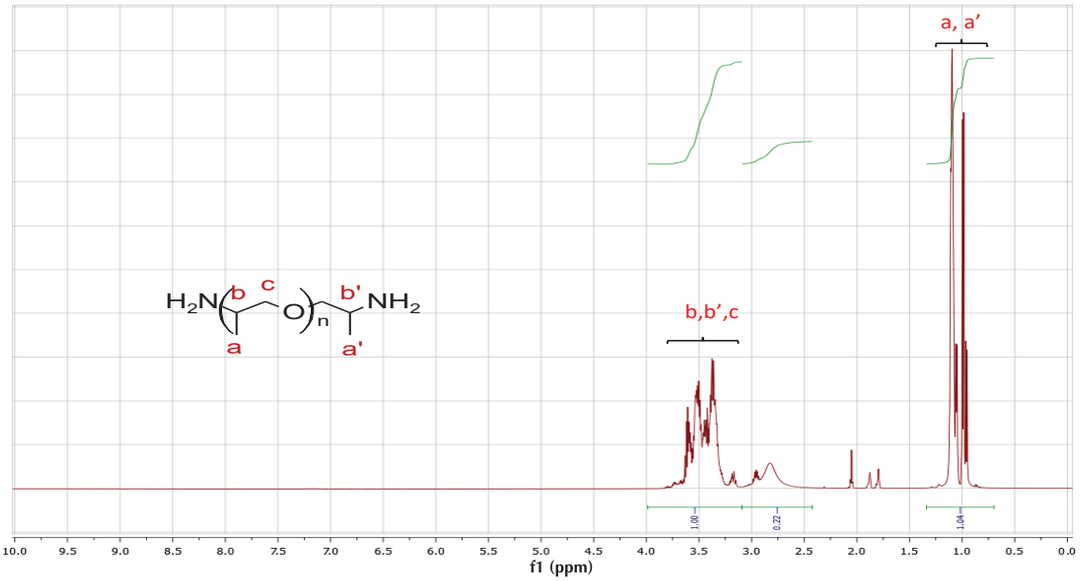


**Fig. 3. $^1$H NMR spectrum of polypropylene oxide di-amines in $CDCl_3$.**

From the FT-IR spectra of cyanuric chloride, polypropylene oxide di-amines, and the polymer in Fig. 4, the characteristic absorption bands of cyanuric chloride at 1171 and 1265 cm$^{-1}$ assigned to the triazine stretch [7] and the bands at 844 cm$^{-1}$ corresponds the C-Cl stretch vibrational absorption [8] can be observed. After the coupling reaction, the band for the C-Cl stretch at 844 cm$^{-1}$ in FT-IR spectrum of polymer disappeared. The appearance of the peak at 1571 cm$^{-1}$ was due to N-H secondary amine in reaction.

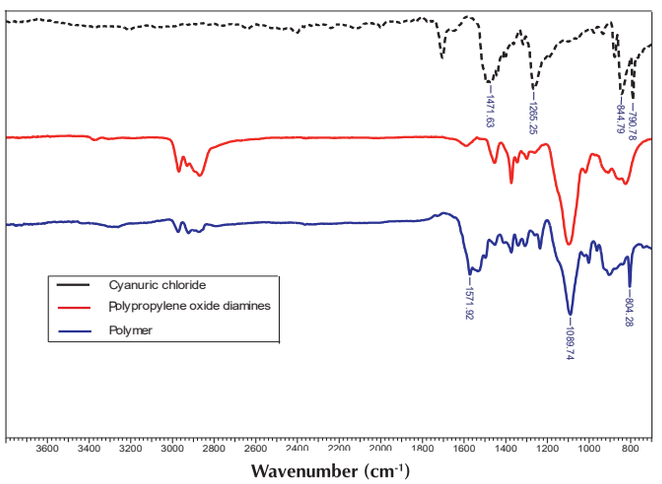


**Fig. 4. ATR FT-IR spectra of cyanuric chloride, polypropylene oxide di-amines and polymer triazine after synthesis.**

## Conclusions

In conclusion, the triazine-based polymer capable of hydrogen interaction was successfully synthesised by the coupling reaction of cyanuric chloride with a di-amine. The structure of the polymer and the appearance of hydrogen bonding were clarified by ATR FT-IR and $^1$H NMR. Moreover, the modification processes to attach more proton donors and acceptors are currently under further study.

## ACKNOWLEDGEMENTS

This research is funded by Vietnam National Foundation for Science and Technology Development (NAFOSTED) under grant number 104.02-2019.13.

The authors declare that there is no conflict of interest regarding the publication of this article.

## REFERENCES

[1] Desiraju, R. Gautam, Thomas Steiner (2001), *The Weak Hydrogen Bond: In Structural Chemistry and Biology*, International Union of Crystal, Oxford Science Publication.

[2] Thomas Steiner (2001), "Competition of hydrogen-bond acceptors for the strong carboxyl donor", *Acta Crystallographica Section B: Structural Science*, **57(1)**, pp.103-106.

[3] Y. He, B. Zhu, and Y. Inoue (2004), "Hydrogen bonds in polymer blends", *Progress in Polymer Science*, **29(10)**, pp.1021-1051.

[4] Highfill, L. Melissa, et al. (2002), "Superstructural variety from an alkylated triazine: formation of one-dimensional hydrogen-bonded arrays or cyclic rosettes", *Crystal Growth & Design*, **2(1)**, pp.15-20.

[5] G. Blotny (2006), "Recent applications of 2,4,6-trichloro-1,3,5-triazine and its derivatives in organic synthesis", *Tetrahedron*, **62(41)**, pp.9507-9522.

[6] Thurston, T. Jack, et al. (1951), "Cyanuric chloride derivatives. I. Aminochloro-s-triazines", *Journal of the American Chemical Society*, **73(7)**, pp.2981-2983.

[7] D.M. Thomas, et al. (1970), "Single-crystal infrared and raman spectra of cyanuric chloride", *The Journal of Chemical Physics*, **53(9)**, pp.3698-3709.

[8] Q. Liao, et al. (2007), "Surface-enhanced Raman scattering and DFT computational studies of a cyanuric chloride derivative", *Vibrational Spectroscopy*, **44(2)**, pp.351-356.

DOI: 10.31276/VJSTE.62(2).41-47



# Evaluation of groundwater quality for domestic purposes and human health risk assessment for arsenic and manganese exposure in Cu Chi district, Ho Chi Minh city, Vietnam

**Ha Lan Nguyen, Viet Ky Nguyen, Van Ngo Dau, Thi Phi Oanh Tran***

*University of Technology, Vietnam National University, Ho Chi Minh city*

Received 3 February 2020; accepted 29 May 2020

***Abstract:***

**Water is extremely important to all life currently, the Cu Chi district has been provided with one hundred percent clean water. However, due to long-standing habits and easy extraction, citizens are still using groundwater daily for water consumption and cooking.**

**Therefore, in this study, the use of groundwater from the middle-upper Pleistocene aquifer in the Cu Chi district of Ho Chi Minh city, for domestic and drinking purposes was investigated. In terms of pH and Fe, $NH_4^+$, $NO_3^-$, As and Mn content, data were collected from central water supply stations under the operation of the Centre for Rural Water Supply and Sanitation (CERWASS). Furthermore, samples collected from 94 households and water supply stations were also evaluated for groundwater quality via pH and Fe, As, Hg, Cd, Pb, $Cr^{6+}$ and $CN^-$ concentration. On the other hand, a human health risk assessment for carcinogenic substances (As) and non-carcinogenic substances (Mn) was performed by a variety of assessments including the susceptibility to contamination according to the DRASTIC index, which weights water risks by applying a semi-quantitative model. Because pollution is inevitable with today's modernization and industrialization, these research results contribute to management and control measures deeply needed to achieve and maintain a safe water supply, thereby ensuring the health and safety for the communities in the Cu Chi district.**

***Keywords:*** **domestic water, groundwater pollution, middle-upper Pleistocene aquifer, risk assessment.**

***Classification number:*** **2.2**

## Introduction

This study investigated the current situation of groundwater use for domestic purposes and consumption. The research team collected data from several centralized water supply stations operated by the CERWASS. The team also conducted surveys and took water samples from 94 households and water supply stations. The evaluation of groundwater quality and its suitability for domestic use was also conducted. The results showed that in terms of raw water quality, most of the samples had low iron (Fe) concentration and pH value. All samples met the National Technical Regulation on Groundwater Quality (QCVN 09-MT:2015/BTMNT). The results showed that, although the assessed risks were minimal, management and control measures are still needed to achieve a safe and sustainable water supply.

In terms of risk assessments, the research team conducted a variety of evaluations: (1) an assessment of the susceptibility to contamination according to the DRASTIC index, (2) an assessment of the water risks by applying a semi-quantitative model, and (3) an assessment of human health risks for both As and Mn. These findings showed that, although the risks were small, management and control measures are sorely needed to achieve a safe water supply as well as to ensure the health and safety of the communities in the area.

## Materials and methods

### *Sampling*

The research team collected data from seven water supply stations in the Cu Chi district to assess the groundwater contamination. In order to evaluate raw water quality and assess human health risks of ingestion exposure, water samples were collected and the concentration of heavy metals (Mn and As) from household wells at different depths (-18 to -72 m) within the Upper- and Middle-Upper Pleistocene aquifers were analysed.

*Corresponding author: Email: tranthiphioanh@gmail.com

Within the studied region, 94 groundwater samples were collected between November 15, 2019 and November 31, 2019 from household wells located in 17 communes of Cu Chi district, Ho Chi Minh city. The number of samples and their locations are shown below in Figs. 1 and 2.

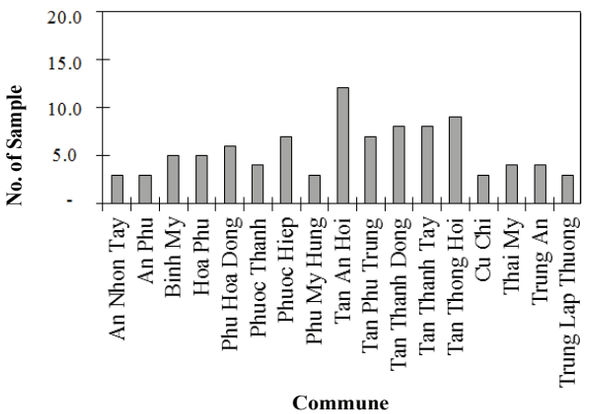


**Fig. 1. Diagram showing the number of drilled wells in aquifers at different locations.**

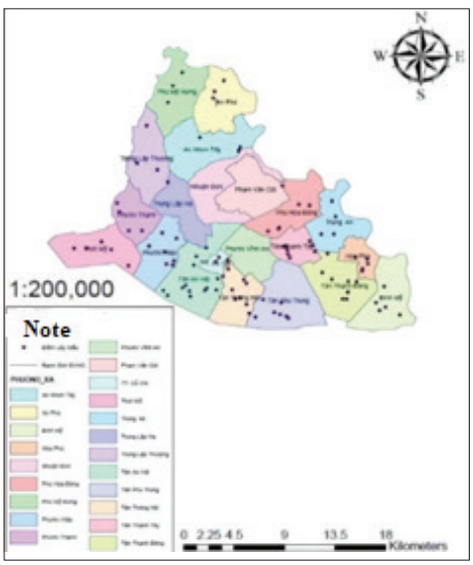


**Fig. 2. Sampling locations.**

### *Indicators and analytical procedure*

The indicators are the total concentration of Mn and As. The sampling method was followed in accordance with the National Standard TCVN 6663-11:2011 (ISO 5667-11:2009) [1]. Sample storage and handling followed the procedure in the National Standard TCVN 6663-11:2008 (ISO 5667-3:2003).

The analysis was conducted according to the Standard Methods for the Examination of Water and Wastewater, 22nd ALPHA, 2012, and the current National Standards. Experiments and analyses were carried out at the Centre of Analytical Services and Experimentation (CASE), Ho Chi Minh city. Measurements were performed by inductively coupled plasma optical emission spectrometry (ICP - OES) and ammonium ($NH_4^+$), nitrate ($NO_3^-$), and nitrite ($NO_2^-$) were inferred from nitrogen concentration (see Table 1).

**Table 1. Summary of analytical methods.**

| No | Indicators | Unit | Methods | Equipment | Accuracy |
|---|---|---|---|---|---|
| 1 | pH | - | TCVN 6492-2011 | | |
| 2 | Total iron | mg/l | TCVN 6177:1996 | ICP – MS/MS | ±0.01 |
| 3 | Manganese | mg/l | SMEWW 3113B:2012 | ICP – MS/MS | ±0.01 |
| 4 | Aluminium | mg/l | SMEWW3111B:2012 | ICP – MS/MS | ±0.01 |
| 5 | Copper | mg/l | SMEWW3111B:2012 | ICP – MS/MS | ±0.01 |
| 6 | Lead | mg/l | SMEWW3113B:2012 | ICP – MS/MS | ±0.01 |
| 7 | Total arsenic | mg/l | SMEWW 3114B:2012 | ICP – MS/MS | ±0.01 |
| 8 | Cadmium | mg/l | SMEWW 3113B:2012 | ICP – MS/MS | ±0.01 |
| 9 | Nitrate | mg/l | SMEWW 4500-$NO_3^-$.E:2017 | DR 5000 | ±0.001 |
| 10 | Nitrite | mg/l | SMEWW 4500-$NO_2^-$.B:2017 | DR 5000 | ±0.001 |
| 11 | Ammonium | mg/l | SMEWW 4500-$NH_4^+$.B&F:2017 | DR 5000 | ±0.001 |

### *Evaluation methods*

*Assessment of the groundwater vulnerability to contamination:*

The quality of raw water sources in water supply stations was assessed according to the National Standard QCVN 09:2008/BTNMT: National Technical Regulation on Groundwater Quality issued by the Ministry of Natural Resources and Environment.

The quality of treated water is assessed according to the National Standard QCVN 01-1:2018/BYT: National Technical Regulation on Domestic Water Quality issued by the Ministry of Health.

The DRASTIC index (DI) model was used to evaluate the groundwater contamination potential to organic pollution at seven water supply stations. The acronym DRASTIC stands for the seven parameters specific to the water source: the depth to groundwater (D), net recharge of groundwater (R), aquifer media (A), soil media (S), topography (T), impact of the vadose zone media (I), and the hydraulic conductivity of aquifers (C). The vulnerability of groundwater to contamination [2, 3] is as follows:

$$DI = 5D + 4R + 3A + 2S + 1T + 5I + 3C$$

where D: depth (m); R: recharge (mm); A: aquifer; S: soil; T: topography (%); I: impact of vadose zone; and C: conductivity (m/day). The rating scale for groundwater vulnerability is given in Table 2.

**Table 2. A rating scale for the groundwater vulnerability to contamination.**

| No | Rating | Vulnerability category |
|---|---|---|
| 1 | <120 | Very low |
| 2 | 120-139 | Low |
| 3 | 140-159 | Moderate |
| 4 | 160-179 | Moderately high |
| 5 | 180-199 | High |
| 6 | >199 | Very high |

*Water risk assessment by semi-quantitative model:*

The risk assessment of raw water quality was calculated based on the risk quotient (RQ) formula as follows [4]:

RQ = MEC(PEC)/PNEC

where RQ: risk quotient; MEC: measured environmental concentration (mg/l); PEC: predicted environmental concentration (mg/l); and PNEC: predicted-no-effect concentration (mg/l). The risk level rating is classified in Table 3.

**Table 3. Classifications for RQ value.**

| Rating | Low | Moderate | High |
|---|---|---|---|
| RQ value | 0.01-0.1 | 0.1-1 | ≥1 |

*Human health risk (HHR) assessment* [4, 5]:

HHR may be assessed in relation to the potential exposure to toxic substances. The HHR assessment for chemical exposure is usually characterized by the carcinogenic health risks from potential exposure to As and non-carcinogenic health risks from potential exposure to Mn.

*Carcinogenic risk assessment:*

The method used to estimate the likelihood of a person contracting cancer as a result of exposure to toxic substances in groundwater continuously over the assumption of an average 60-year lifetime can be estimated using the following relationship:

$$RISH_{water} = SF_o \times C_w \times 0.149$$

where $SF_0$: the cancer potency slope factor for water ingestion (l/mg/kg-day) and $C_w$: the chemical concentration of chemical in water (mg/l).

*Non-carcinogenic risk assessment:*

The method used to calculate the probability that a receptor will experience health problems when continuously exposed to a chemical constituent associated with water ingestion over an average 60-year lifetime is presented in reduced form as follows:

$$HAZARD_{water} = \frac{1}{RfD_o} \times C_w \times 0.0639$$

where $RfD_0$: reference dose for ingestion route (mg/kg-day) and $C_w$: the chemical concentration of chemical in water (mg/l).

The non-carcinogenic risk associated with potential exposure to a chemical constituent in groundwater can be evaluated in Table 4.

**Table 4. The classifications of non-carcinogenic risk assessment results.**

| Value | $RISH_{water}$ $>10^{-4}$ | $10^{-6}< RISH_{water} <10^{-4}$ | $RISH_{water} < 10^{-6}$ | $HAZARD_{water}$ <1 | $HAZARD_{water}$ >1 |
|---|---|---|---|---|---|
| Risk presumptions | High risk, unacceptable | Moderate risk* | Low risk, insignificant, acceptable | Acceptable risk | Unacceptable risk |

*Risks may or may not exist, and these decisions should be based on further analysis.

## Results and discussion

***Assessment of the vulnerability of groundwater to contamination***

The results of Fe content and corresponding pH in samples from the water supply stations tested in the Cu Chi district are shown in Table 5 and Fig. 3.

**Table 5. Total Fe concentration and pH.**

| No | Station | pH | Total Fe (mg/l) |
|---|---|---|---|
| 1 | An Nhon Tay | 6.15 | 0.0516 |
| 2 | Binh My | 5.42 | 0.0888 |
| 3 | Pham Van Coi | 5.25 | 0.0312 |
| 4 | Phuoc Thanh | 4.96 | 0.0156 |
| 5 | Thai My | 6.08 | 1.7448 |
| 6 | Trung An | 5.78 | 0.0468 |
| 7 | Trung Lap Ha | 5.55 | 0.0624 |

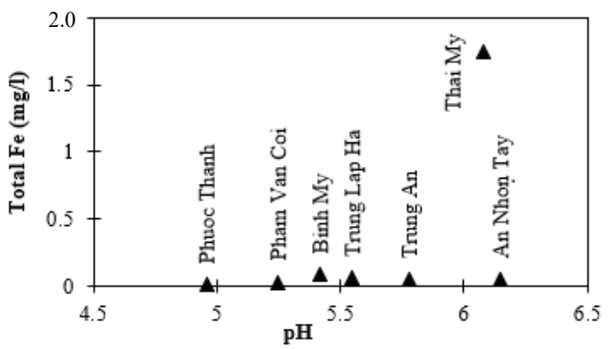


**Fig. 3. Total Fe concentration and pH at water supply stations.**

In general, the groundwater samples from the water supply stations in the Cu Chi district have a small (almost insignificant) trace of Fe that is widely distributed in the groundwater from the Pleistocene aquifer with a total Fe concentration <0,3 mg/l, particularly at the Thai My station. All samples had low pH values that ranged from 4.96 to

6.15. However, most of them had measured values between a pH level 5.0 and 5.5.

The analysis of the results of ammonium ($NH_4^+$), nitrite ($NO_2^-$), and nitrate ($NO_3^-$) content are shown in Table 6 and Figs. 4 to 6.

**Table 6. Ammonium, nitrite, and nitrate concentration at water supply stations.**

| No | Station | Concentration (mg/l) | | |
|---|---|---|---|---|
| | | $NH_4^+$ | $NO_2^-$ | $NO_3^-$ |
| | | *<0.1* | *<1* | *<15* |
| 1 | An Nhon Tay | 0.05 | 0.0041 | 1.6 |
| 2 | Binh My | 0.07 | 0.0037 | 2.5145 |
| 3 | Pham Van Coi | 0.1 | 0.0047 | 28.1254 |
| 4 | Phuoc Thanh | 0.09 | 0.0039 | 4.4115 |
| 5 | Thai My | 0.27 | 0.0067 | 2.0522 |
| 6 | Trung An | 0.12 | 0.0047 | 3.2737 |
| 7 | Trung Lap Ha | 0.07 | 0.0043 | 24.723 |

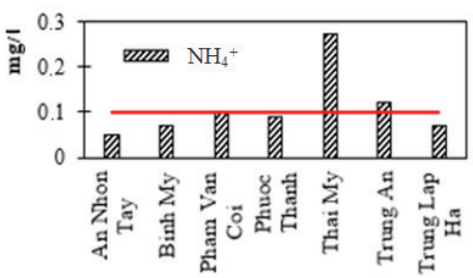


**Fig. 4. $NH_4^+$-N concentration at water supply stations.**

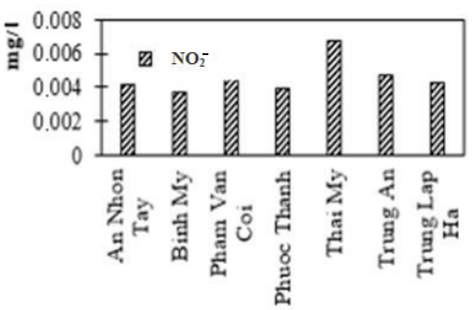


**Fig. 5. $NO_2^-$-N concentration at water supply stations.**

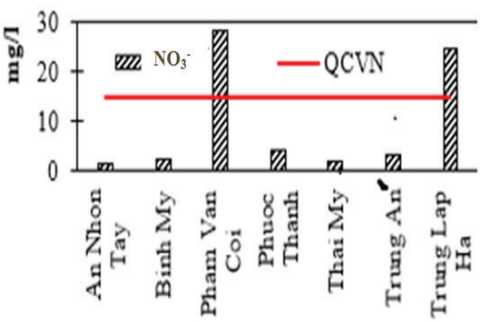


**Fig. 6. $NO_3^-$ concentration at water supply stations.**

Most of the samples showed the presence of $NH_4^+$ and $NO_3^-$ but $NO_2^-$ was almost absent. Thus, this region was previously contaminated for a long time but now the contamination has been temporarily reduced, which explains the absence of $NO_2^-$. However, groundwater contamination has recently increased and continued to spread through this region.

From analysis of the results, a sharp increase in $NH_4^+$ was observed from the samples taken from Pham Van Coi and Thai My stations. Because the location of the Pham Van Coi station is near the city's cemetery and the Thai My station is close to the Tan Hiep landfill, the risk of contamination from groundwater in these areas is inevitable.

The results of groundwater vulnerability to contamination at the seven water supply stations in the Cu Chi district are shown in Table 7.

**Table 7. DRASTIC index of 7 water supply stations in Cu Chi district.**

| No | Station | D | R | A | S | T | I | C | DRASTIC | Risk to contamination |
|---|---|---|---|---|---|---|---|---|---|---|
| 1 | An Nhon Tay | 1 | 9 | 8 | 5 | 10 | 1 | 4 | 102 | Very low |
| 2 | Binh My | 1 | 9 | 6 | 1 | 10 | 1 | 1 | 79 | Very low |
| 3 | Pham Van Coi | 5 | 9 | 8 | 6 | 10 | 1 | 1 | 115 | Very low |
| 4 | Phuoc Thanh | 5 | 9 | 7 | 6 | 10 | 1 | 4 | 121 | Low |
| 5 | Thai My | 1 | 9 | 8 | 1 | 10 | 8 | 4 | 129 | Low |
| 6 | Trung An | 1 | 9 | 8 | 1 | 10 | 1 | 4 | 94 | Very low |
| 7 | Trung Lap Ha | 1 | 9 | 8 | 5 | 10 | 1 | 4 | 102 | Very low |

The above results of the DI show that the majority of the currently exploited groundwater sources in the area are of very low vulnerability to pollution, but it is necessary to have control measures and close monitoring of groundwater quality in this area to prevent future contamination.

In term of the water quality after treatment at water supply stations, the analysis results of Mn, Hg, $Cr^{6+}$, and $CN^-$ met the standard limits in QCVN 01-1:2018/BYT for domestic water quality (Table 8).

**Table 8. Analysis results of water quality after treatment at water supply stations.**

| No | Station | Mn (mg/l) | Hg (ppb) | $Cr^{6+}$(mg/l) | $CN^-$(mg/l) |
|---|---|---|---|---|---|
| 1 | An Nhon Tay | ND | 0.0180 | ND | ND |
| 2 | Binh My | 0.0684 | 0.0174 | ND | ND |
| 3 | Pham Van Coi | ND | 0.0141 | ND | ND |
| 4 | Phuoc Thanh | 0.0036 | 0.0257 | ND | ND |
| 5 | Thai My | 0.3492 | 0.0175 | ND | ND |
| 6 | Trung An | ND | 0.0203 | ND | ND |
| 7 | Trung Lap Ha | 0.06 | 0.0146 | ND | ND |

ND: no data.

***Risk assessment by semi-quantitative model***

The RQ is calculated with PNEC based on QCVN 01-1:2018/BYT and MEC max measured from sampled wells at 94 households in Cu Chi district, Ho Chi Minh city. The results are shown in Tables 9 and 10 below.

**Table 9. MEC max at 94 households in Cu Chi district, Ho Chi Minh city.**

| Depth | pH | Fe (ppm) | Mn (ppm) | Al (ppm) | As (ppm) | Cu (ppm) | Pb (ppm) | Cd (ppm) |
|---|---|---|---|---|---|---|---|---|
| -18 | 4.7 | 0.00003 | 0.00008 | 0.00013 | 0.00003 | ND | 0.00175 | 0.00002 |
| -19 | 4.6 | 0.00015 | 0.00003 | 0.00012 | 0.00005 | 0.00001 | 0.01121 | 0.00002 |
| -20 | 5.5 | 0.00010 | 0.00004 | 0.00015 | 0.00237 | ND | 0.00066 | 0.00001 |
| -22 | 4.5 | 0.00017 | 0.00009 | 0.00014 | 0.00004 | 0.00001 | 0.00294 | 0.00003 |
| -24 | 4.9 | 0.00003 | 0.00006 | 0.00020 | 0.00001 | ND | 0.00033 | ND |
| -25 | 4.9 | 0.00006 | 0.00019 | 0.00005 | 0.00002 | ND | 0.00310 | 0.00009 |
| -26 | 4.5 | 0.00003 | 0.00004 | 0.00057 | 0.00025 | ND | 0.01413 | ND |
| -27 | 4.5 | 0.00002 | 0.00001 | 0.00001 | 0.00000 | ND | ND | ND |
| -28 | 4.6 | 0.00003 | 0.00008 | 0.00028 | 0.00004 | ND | 0.00453 | 0.00001 |
| -30 | 4.7 | 0.00019 | 0.00012 | 0.00007 | 0.00003 | ND | 0.00122 | 0.00001 |
| -32 | 5.0 | 0.00004 | 0.00004 | 0.00002 | ND | ND | 0.02686 | 0.00006 |
| -34 | 4.5 | 0.00002 | 0.00002 | 0.00029 | ND | ND | 0.00460 | ND |
| -35 | 4.5 | 0.00005 | 0.00005 | 0.00066 | 0.00015 | ND | 0.00594 | ND |
| -36 | 4.3 | 0.00003 | 0.00017 | 0.00007 | ND | ND | ND | ND |
| -40 | 4.7 | 0.00012 | 0.00139 | 0.00010 | 0.00002 | 0.00001 | 0.00199 | 0.00011 |
| -42 | 5.2 | 0.00059 | 0.00003 | 0.00001 | ND | 0.00002 | 0.00204 | ND |
| -45 | 4.6 | 0.00003 | 0.00003 | 0.00006 | ND | 0.00003 | 0.00441 | ND |
| -50 | 5.5 | 0.00050 | 0.00001 | 0.00002 | 0.00016 | ND | 0.00021 | 0.00001 |
| -55 | 4.9 | 0.00002 | ND | 0.00003 | ND | ND | 0.00030 | ND |
| -57 | 5.2 | 0.00007 | 0.00004 | 0.00001 | ND | ND | 0.00026 | ND |
| -60 | 6.2 | 0.00030 | 0.00003 | 0.00002 | 0.00009 | ND | 0.00021 | ND |
| -70 | 6.7 | 0.00011 | ND | 0.00002 | 0.00194 | ND | 0.00202 | 0.00004 |
| -72 | 5.1 | 0.00104 | 0.00008 | 0.00001 | 0.00027 | ND | 0.00020 | ND |
| QCVN 01-1:2018/BYT | 7.5 | 0.3 | 0.1 | 0.2 | 0.01 | 1.0 | 0.01 | 0.03 |

**Table 10. RQ of raw water at 94 households in Cu Chi district, Ho Chi Minh city.**

| Depth | pH | Fe | Mn | Al | As | Cu | Pb | Cd |
|---|---|---|---|---|---|---|---|---|
| -18 | 0.64855 | 0.00011 | 0.00076 | 0.00066 | 0.00280 | - | 0.17480 | 0.00533 |
| -19 | 0.63448 | 0.00050 | 0.00025 | 0.00060 | 0.00500 | 0.00001 | 1.12050 | 0.00500 |
| -20 | 0.75517 | 0.00034 | 0.00040 | 0.00073 | 0.23725 | - | 0.06575 | 0.00167 |
| -22 | 0.62586 | 0.00056 | 0.00085 | 0.00071 | 0.00413 | 0.00001 | 0.29438 | 0.00833 |
| -24 | 0.67034 | 0.00011 | 0.00056 | 0.00099 | 0.00120 | - | 0.03320 | - |
| -25 | 0.68244 | 0.00020 | 0.00190 | 0.00023 | 0.00223 | - | 0.31008 | 0.02846 |
| -26 | 0.62069 | 0.00010 | 0.00040 | 0.00285 | 0.02500 | - | 1.41300 | - |
| -27 | 0.62069 | 0.00007 | 0.00010 | 0.00005 | - | - | - | - |
| -28 | 0.63845 | 0.00011 | 0.00075 | 0.00141 | 0.00375 | - | 0.45300 | 0.00208 |
| -30 | 0.65147 | 0.00063 | 0.00119 | 0.00034 | 0.00281 | - | 0.12225 | 0.00292 |
| -32 | 0.68345 | 0.00013 | 0.00040 | 0.00010 | - | - | 2.68600 | 0.01833 |
| -34 | 0.62069 | 0.00007 | 0.00020 | 0.00145 | - | - | 0.46000 | - |
| -35 | 0.62069 | 0.00015 | 0.00050 | 0.00330 | 0.01500 | - | 0.59350 | - |
| -36 | 0.59310 | 0.00010 | 0.00170 | 0.00035 | - | - | - | - |
| -40 | 0.64138 | 0.00041 | 0.01392 | 0.00048 | 0.00183 | 0.00001 | 0.19917 | 0.03611 |
| -42 | 0.71724 | 0.00197 | 0.00030 | 0.00005 | - | 0.00002 | 0.20400 | - |
| -45 | 0.62897 | 0.00008 | 0.00025 | 0.00030 | - | 0.00003 | 0.44050 | - |
| -50 | 0.75241 | 0.00166 | 0.00008 | 0.00009 | 0.01600 | - | 0.02125 | 0.00333 |
| -55 | 0.67862 | 0.00007 | - | 0.00015 | - | - | 0.03000 | - |
| -57 | 0.71034 | 0.00023 | 0.00040 | 0.00005 | - | - | 0.02600 | - |
| -60 | 0.85977 | 0.00099 | 0.00033 | 0.00010 | 0.00933 | - | 0.02067 | - |
| -70 | 0.92414 | 0.00037 | - | 0.00010 | 0.19400 | - | 0.20200 | 0.01333 |
| -72 | 0.70345 | 0.00347 | 0.00080 | 0.00005 | 0.02700 | - | 0.02000 | - |

In the above results, most of the estimated RQ of heavy metals Fe, Mn, As, Al, Cu, and Cd suggest that the environmental risk is very low (RQ<0,01) for all sampling depths. However, As was identified as posing a low risk at depths of -26 m, -35 m, -50 m, and -72 m (0.01<RQ<0.1) and moderate risk at depths of -20 m and -70 m (0.1<RQ<1.0).

In addition, the Pb concentration had a RQ value less than 0.01 at depths of -20 m, -24 m, -55 m, -57 m, -60 m, and -72 m, which indicate very low risk. At depths of -18 m, -22 m, -25 m, -28 m, -30 m, -34 m, -35 m, -50 m, RQ values were within the range of 0.01 and 0.1, which show low risk. At depths of -19 m, - 26 m, -32 m, -40 m, -42 m, -45 m, and -70 m, RQ was in the range of 0.1 and 1.0, which is evaluated as showing moderate risk. At depths of -19 m, -26 m, -32 m, RQ was greater than 1, which is high risk.

The results revealed that the assessment in raw water use related to heavy metal contamination showed low risk, but this does not guarantee health safety for the long-term use of this water without proper treatment.

**Table 11. Risk quotient for carcinogenic to As.**

| Depth | As (ppm) | Carcinogenic risk |
|---|---|---|
| -18 | 0.00003 | 0.00001 |
| -19 | 0.00005 | 0.00001 |
| -20 | 0.00237 | 0.00062 |
| -22 | 0.00004 | 0.00001 |
| -24 | 0.00001 | 0.00000 |
| -25 | 0.00002 | 0.00001 |
| -26 | 0.00025 | 0.00007 |
| -27 | 0.00000 | 0.00000 |
| -28 | 0.00004 | 0.00001 |
| -30 | 0.00003 | 0.00001 |
| -32 | ND | - |
| -34 | ND | - |
| -35 | 0.00015 | 0.00004 |
| -36 | ND | - |
| -40 | 0.00002 | 0.00000 |
| -42 | ND | - |
| -45 | ND | - |
| -50 | 0.00016 | 0.00004 |
| -55 | ND | - |
| -57 | ND | - |
| -60 | 0.00009 | 0.00002 |
| -70 | 0.00194 | 0.00051 |
| -72 | 0.00027 | 0.00007 |

***Health risk assessment***

Carcinogenic risks of the potential exposure to As were estimated for 94 groundwater samples collected from household wells in Cu Chi district, Ho Chi Minh city are shown in Table 11. The non-carcinogenic risks of Mn related to the daily use of groundwater from the 94 households in Cu Chi district, Ho Chi Minh city are shown in Table 12.

**Table 12. Risk quotient for non-carcinogenic to Mn.**

| Depth | Mn (ppm) | Carcinogenic risk |
|---|---|---|
| -18 | 0.00008 | 0.00097128 |
| -19 | 0.00003 | 0.0003195 |
| -20 | 0.00004 | 0.0005112 |
| -22 | 0.00009 | 0.0010863 |
| -24 | 0.00006 | 0.00071568 |
| -25 | 0.00019 | 0.0024282 |
| -26 | 0.00004 | 0.0005112 |
| -27 | 0.00001 | 0.0001278 |
| -28 | 0.00008 | 0.0009585 |
| -30 | 0.00012 | 0.001517625 |
| -32 | 0.00004 | 0.0005112 |
| -34 | 0.00002 | 0.0002556 |
| -35 | 0.00005 | 0.000639 |
| -36 | 0.00017 | 0.0021726 |
| -40 | 0.00139 | 0.0177855 |
| -42 | 0.00003 | 0.0003834 |
| -45 | 0.00003 | 0.0003195 |
| -50 | 0.00001 | 0.00009585 |
| -55 | ND | - |
| -57 | 0.00004 | 0.0005112 |
| -60 | 0.00003 | 0.000426 |
| -70 | ND | - |
| -72 | 0.00008 | 0.0010224 |

Based on the results from the water quality analysis and cancer risk assessment, the groundwater across the 94 households in Cu Chi district had an acceptable quality and As poses no carcinogenic risk or any serious health concerns to the local residents.

The assessment results indicate that the non-carcinogenic risk of Mn through ingestion shows no adverse health effects. Setting priorities of risks from chemical constituent contamination in groundwater according to the semi-quantitative model is shown in the Table 13.

**Table 13. The priority risks according to semi-quantitative model.**

| No. | Chemical constituent | Risk level |
|---|---|---|
| 1 | Mn | No |
| 2 | As | No |

While the above discussion describes that priority risks are currently non-existent, such risks will eventually become unavoidable in the future at the current rate of industrialization and modernization. The situations of using water from rudimentary treatment procedures or its direct use from sources do not guarantee human health and safety in the future. Therefore, it is necessary to continue to study appropriate mitigation and preventive measures.

## Conclusions

The analysis results of pH and total Fe content at 7 water supply stations in the Cu Chi district are very low and ranged within 4.96-6.15, and 0.0156-1.7448, respectively. The $NO_2^-$ parameters have all met the standard limits as given in QCVN 09:2008/BTNMT. On the other hand, the $NH_4^+$ and $NO_3^-$ content of the water from the Pham Van Coi and Thai My stations exceeded the permitted standard. Because the Pham Van Coi station is located near the city's cemetery and the Thai My station is close to the Tan Hiep landfill, the risk of contamination is inevitable.

After surveying and assessing the vulnerability of groundwater to contamination at seven water supply stations across the Cu Chi district, the water supply shows a high unlikeliness of being contaminated.

However, recent studies indicate that, groundwater reserves and its quality are decreasing due to contamination from surface water and unreasonable exploitation. Therefore, it is necessary to have control measures in place and to continue close monitoring of groundwater quality in this area to prevent future contamination. In addition, greater investment in the construction of underground water treatment systems after exploitation is necessary. The analysis of the concentrations of Fe, As, Mn, Pb, Cd, Hg, $Cr^{6+}$, and $CN^-$ have met the standard limits in QCVN 01-1:2018/BYT for domestic water quality after treatment at the surveyed water supply stations.

Analysis of the well water from 94 households in the Cu Chi district found that the environmental risk related to heavy metal contamination was not high. However, at certain depths, the RQ coefficient for Pb and As was generally high. Hence, the data showed that the groundwater across the 94 households in the Cu Chi district has acceptable quality and As levels in the water poses no carcinogenic risk or any serious health concerns to local residents.

However, in the future, contamination risks will eventually become unavoidable at the current rate of industrialization and modernization. The water condition from rudimentary treatment procedures or any direct use from natural sources do not guarantee human health and safety in the future. Therefore, it is essential to further study appropriate mitigation and preventive measures.

The results of this work are a premise for management as well as further research of the mitigation and prevention of water contamination.

## ACKNOWLEDGEMENTS

The authors wish to thank the Ministry of Education and Training of Vietnam, B2019.SPD.05 Project, for their financial support of this work.

The authors declare that there is no conflict of interest regarding the publication of this article.

## REFERENCES

[1] Ministry of Science and Technology (2011), *Vietnam Standard 6663-11:2011, ISO 5667-11:2009: Water Quality - Sampling_Chapter 11: Guidelines for Sampling Groundwater*.

[2] Viet Ky Nguyen, Duc Chan Ngo, Tran Vuong Bui, Van Chung Tran, Van Vinh Hoang (2006), *Exploitation and Conservation of Groundwater*, Vietnam National University, Ho Chi Minh city Publisher.

[3] WHO-Sawaco (2007), *Training Material for Safe Water Supply Plan.*

[4] L.T.H. Tran (2008), *Health and Ecological Risk Assessment*, Science and Technique Publisher.

[5] Annette Davison and Deere (2007), *Manual for Safe Water Supply Plan*.

DOI: 10.31276/VJSTE.62(2).48-55

# Optimization of culture conditions of iron-enriched biomass of *Saccharomyces pastorianus* by response surface methodology

**Pham Quynh Nhu, Tran Thanh Uyen, Phan Minh Vuong, Phan Thanh Thao***

*Institute of Chemical Technology, Vietnam Academy of Science and Technology (VAST)*

Received 4 February 2020; accepted 20 May 2020

***Abstract:***

**Yeast biomass enriched with iron is used in a profound and safe treatment for anaemia. In this work, response surface methodology (RSM) was used to survey the response of culture conditions (temperature, degrees brix, time, and initial iron concentration) to the bioaccumulation of ferric ion ($Fe^{3+}$) in yeast (*Saccharomyces pastorianus*). On the other hand, the Box-Behnken design was used to determine the optimum conditions of 24°C, 13°Bx of the culture solid content for 49 h incubation and 656 ppm of initial iron concentration. The total $Fe^{3+}$ content in the biomass was significantly affected by the culture temperature and degrees brix ($p<0.0001$). Under optimum conditions, the maximum level of Fe (III) ions in the dry cell weight of *S. pastorianus* was 16.82±0.65 mg/g. The results from statistical analysis showed that the model was significant ($p<0.0001$) and adequate.**

***Keywords:*** **Box-Behnken, Fe (III) citrate, optimization, response surface methodology, *Saccharomyces pastorianus*.**

***Classification numbers:*** **2.2, 3.5**

## Introduction

Iron is known to be an essential micronutrient for all living organisms as it takes part in biochemical functions such as oxygen transportation, molecules storage, and enzyme catalysation, which require the redox reaction for the generation of energy, metabolism, and immune systems [1]. Iron deficiency (ID) and iron deficiency anaemia (IDA) are popularly considered as nutritional problems.

The most extensive cure for ID and IDA is oral iron medication. The most prescribed iron supplement contains ferrous salts that have quite low bioavailability rates [2]. Therefore, it is necessary to investigate the bioavailability and safest form of iron and identify the optimal length of treatment to supply enough iron for the body's needs.

An interest in the methods of the production of microelements such as enriched yeast has increased dramatically in recent years to produce products to prevent trace element deficiencies that are non-toxic, have high availability, are easy to digest, and are easily absorbed by the human body. The ability to bio-absorb metal elements turns yeast into a host for many mineral supplements. Recently, *Saccharomyces cerevisiae* yeast cells have been used to survey metal transportation and accumulation. Under proper conditions, *S. cerevisiae* can absorb a considerable quantity of trace elements including iron, zinc, copper, manganese, and selenium, which can be synthesized into organic compounds [3-5].

*Saccharomyces pastorianus* is a key component to the fermentation of lager beer and grows facultatively in popular media. As a successful combination of a variety of Saccharomyces strains, *S. pastorianus's* ability of bio-absorption and conversion of iron in media are as high as that of *S. cerevisae*. Ferric citrate pentahydrate

*Corresponding author: Email: phanthao60@gmail.com

($C_6H_5FeO_7.5H_2O$) is chosen to regulate the blood levels of iron because of insignificant harmful effects of gastric acidity to the yeast growth [6].

Response surface methodology (RSM) is a collection of mathematical and statistical techniques that is useful for designing experiments, establishing models, and analysing the effects of several independent factors [6]. RSM assists in the limitation of the number of experimental trials needed to evaluate multiple factors and their interactions. RSM is based on the fit of empirical models to experimental data obtained in relation to the experimental design, which leads to the employment of polynomial functions to express the system as an equation and to display experimental conditions until its optimization [7]. Researchers can use RSM to study responses related to several variables. The results of the interaction between levels of variables are the key to adjusting the factors to achieve the optimum condition. The result of analysis of the RSM's statistical data can predict the values of a given response with any combination of factors. Response surface methodology is chosen to aid this study based on the advantages of narrowing down the number of experimental runs and surveying the connection between responses and variables. The Box-Behnken technique allows the user to set the number of levels as well as factors related to experiment to create an ideal model. The Box-Behnken design (BBD) is proven to be the most popular technique to optimize processes thanks to the availability of the theory and fundamentals of BBD [6, 8]. BBD is designed for four-variable optimization with 27 experimental runs (3 central points) [7]. To compare with other designs only using one factor, it is noted that BBD can assist researchers in the study of an extensive number of variables over a small number of experimental runs because of its efficiency and economy, thereby reducing the quantity of experimental runs, reagents, samples, and effort to determine the optimal conditions for bio-absorption. Further, BBD improves the statistical interpretation and demonstration of the interaction between variables.

The present study focuses on optimising the amount of *Saccharomyces pastorianus* biomass cultivated in control and experimental media enriched with iron under culture operating parameters (e.g. temperature, culture solid content (degrees brix), incubation time, and initial iron concentration) for producing a yeast biomass with high iron content. Then, RSM is employed with a four-variable, three-level BBD to investigate the affinities between the absorption variables and the content of Fe (III) ions in dry cell weight (mg Fe per g dry cell weight). Through that process, the optimal cultivation parameters for the highest content of Fe (III) ions in the biomass were determined. The optimum absorption conditions can be used for the development of iron-enriched *S. pastorianus* for human and animal health on both laboratory and industrial scales in pharmaceutical and functional food production.

## Materials and methods

### *Microorganism and media*

*S. pastorianus* was obtained from the Research Institute of Brewing and Malting (Czech Republic) under freeze drying condition. It was then reactivated and cultured in a sterilized medium to obtain $10^8$ CFU/ml. The pale malt obtained from the Barrett Burston Malting Co. Pty. Ltd. (Australia) contained 10.2% of protein and 178 mg/l of beta-glucan. Based on the beer production process of Beer & Malt Manufacturing, the 20°Bx malt wort was produced following the procedure of Esslinger [3]. The degrees of brix were adjusted in various levels depending on the experimental plan.

### *Chemicals and apparatus*

Iron (III) citrate pentahydrate ($C_6H_5FeO_7.5H_2O$) and other chemicals used for analytical grade were purchased from Merck (Millipore, USA). Hydroxylamine hydrochloride ($NH_2OH.HCl$), sodium acetate ($CH_3COONa$), and 1,10 - phenanthroline was also obtained from Sigma-Aldrich Co. (USA) as a calibration standard for UV-Vis analysis. To obtain a stock Fe (III) citrate solution of 10000 ppm Fe, 60 g of $C_6H_5FeO_7.5H_2O$ was dissolved in 1 litre of deionized water at pH 4.0. The stock solution was further diluted to obtain the desired initial concentrations, from 500 to 1000 mg/l, which were sterilized (120°C, 10 min).

### *Fermentation experiments*

Culturing experiments were run in triplicate in 250 ml Erlenmeyer flasks by using the malt media to optimize cultivation conditions. The 250 ml Erlenmeyer flasks containing 200 ml of wort medium were inoculated with 10% (v/v) of a previously prepared yeast sample. Fe (III) citrate pentahydrate salt ($C_6H_5FeO_7.5H_2O$) was added to the medium at the initial concentrations of 500-1000 ppm in the preliminary studies. The cultures were aerobically incubated on a rotary shaker at 400 rpm. The samples were withdrawn at regular intervals and analysed to determine the dry cell weight (g/l) and Fe (III) ions uptake (mg/g).

### *Determination of iron absorption*

The incorporation of $Fe^{3+}$ into the yeast cells was determined by two steps using the chemical method of cell lysis. Firstly, to remove the free $Fe^{3+}$ ions bound to the cell surface and iron precipitation, the biomass was washed with deionized water and then filtrated by vacuum filter. Secondly, 1 g of the filtrate was digested using $HNO_3$ 65% for 30 min and heated to 150°C to release the intercellular iron. The iron content in the yeast cells was analysed using a UV-Vis spectrophotometer. The standard curve was prepared with samples obtained by the dilution of the standard solutions (1000 ppm) with deionized water.

### *Dry cell weight measurement*

For measurement of the dry cell weight, 200 ml of culture after planned fermentation was centrifuged at 3000 rpm for 5 min and washed twice with deionized water. The biomass was freeze dried and weighed to determine the dry cell weight.

### *Experimental design*

The Box-Behnken design provides the quantity of experimental runs following this equation:

$$N = 2k^2 - 2k + cp \quad (1)$$

where k is the factor number and cp is the replicate number of the central point. In RSM, the collected data from variables is of practical use for solving equations and for concluding the optimum condition. To be more specific, an empirical second order polynomial model is fitted to the data for analysis of the variables as shown in Eq. 2:

$$Y = \beta_0 + \sum_{i=1}^{k} B_i X_1 + \sum_{i=1}^{k} B_{ii} X^2 + \sum_{i=1}^{k} \sum_{j=i+1}^{k} B_{ij} X_i X_j \quad (2)$$

where $\beta_o$ is a constant, $B_i$ the linear coefficient, $B_{ii}$ the quadratic coefficient, and $B_{ij}$ is the cross-product coefficient. The variables $X_i$ and $X_j$ are levels of the independent variables while $k$ equals the number of the tested factors ($k$=4). The optimal culture conditions for the Fe (III) ions in dry cell weight (Y) were determined using RSM to study the effects of culture parameters on the accumulation yields of the final biomass and intercellular iron content in yeast cells.

A summary of the temperature, degrees brix, incubation duration, and initial Fe (III) ions concentration of the 27 experiments is shown in Table 1.

**Table 1. Experimental independent variables.**

| Factor | Units | Levels and range (coded) | | |
|---|---|---|---|---|
| | | -1 | 0 | +1 |
| Temperature | °C | 20 | 26 | 32 |
| Degrees brix | °Bx | 12 | 14 | 16 |
| Incubation time | hour | 24 | 48 | 72 |
| Initial Fe (III) ions concentration | ppm | 500 | 750 | 1000 |

### *Model fitting and statistical analysis*

The experimental data was analysed by using Design Expert software version 11 (Stat-Ease, Inc., Minneapolis MN, USA) for regression analysis and statistical significance of the derived equation. A design of 27 experiments was formulated from four factors ($2^4$), three replicates at the central points, and the three levels are used in experiment based on the order of Eq. 2. The results of the equation and of the response surface plots help to optimize reasonable values. The adequacy of the fitted model was counted using the lack of fit, the coefficient of determination ($R^2$), and the statistical significances of all terms in the polynomial model by an F-test from ANOVA at a probability (p) of 0.001, 0.01, or 0.05, then calculating the determined coefficients to achieve curve maps from the regression models.

## Results and discussion

The results obtained from experiment (Table 2) showed the effects of temperature, incubated time, degrees brix, and initial iron (III) concentration on the accumulation of Fe in yeast biomass. The second-order polynomial equation presented the connection between the variables and responses and the optimum conditions of the process were obtained from the model by fitting the equation with coefficients. Table 3 showed the results of the ANOVA with regression model. A probability value smaller than 0.05 indicated that the model terms are significant. An insignificant value of "lack of fit" showed the validity of the quadratic model for accumulation by *S. pastorianus*. Equation 3 lists the final empirical formula model for the amount of Fe (III) ions in dry cells weight in terms of coded factors:

$$\text{Iron (III) ions in dry cells weight (mg/g)} = +15.68 - 1.80A - 2.71B + 0.33C - 0.589D + 1.76AB - 0.703AC - 0.810AD - 0.490BC + 0.775BD + 1.95CD - 2.51A^2 - 3.63B^2 - 4.44C^2 - 0.879D^2 \quad (3)$$

where A, B, C and D are the coded terms for temperature, degrees brix, time and initial Fe (III) concentration.

**Table 2. Comparison of experimental and predicted values on Fe (III) ions in dry cell weight (mg/g).**

| Std order | Independent variables | | | | Fe (III) ions in dry cell weight (mg/g)* | |
|---|---|---|---|---|---|---|
| | Temp (°C) | Degrees brix (°Bx) | Time (h) | Initial iron (III) centration (ppm) | Experimental value | Predicted value |
| 1 | 20 | 12 | 48 | 750 | 15.89 | 15.82 |
| 2 | 32 | 12 | 48 | 750 | 9.05 | 8.69 |
| 3 | 20 | 16 | 48 | 750 | 6.78 | 6.88 |
| 4 | 32 | 16 | 48 | 750 | 6.98 | 6.80 |
| 5 | 26 | 14 | 24 | 500 | 12.21 | 12.58 |
| 6 | 26 | 14 | 72 | 500 | 9.51 | 9.33 |
| 7 | 26 | 14 | 24 | 1000 | 7.57 | 7.49 |
| 8 | 26 | 14 | 72 | 1000 | 12.68 | 12.06 |
| 9 | 20 | 14 | 48 | 500 | 13.51 | 13.88 |
| 10 | 32 | 14 | 48 | 500 | 12.15 | 11.89 |
| 11 | 20 | 14 | 48 | 1000 | 14.02 | 14.32 |
| 12 | 32 | 14 | 48 | 1000 | 9.42 | 9.10 |
| 13 | 26 | 12 | 24 | 750 | 9.23 | 9.50 |
| 14 | 26 | 16 | 24 | 750 | 5.52 | 5.07 |
| 15 | 26 | 12 | 72 | 750 | 10.65 | 11.14 |
| 16 | 26 | 16 | 72 | 750 | 4.98 | 4.75 |
| 17 | 20 | 14 | 24 | 750 | 10.01 | 9.50 |
| 18 | 32 | 14 | 24 | 750 | 6.91 | 7.31 |
| 19 | 20 | 14 | 72 | 750 | 11.75 | 11.57 |
| 20 | 32 | 14 | 72 | 750 | 5.84 | 6.56 |
| 21 | 26 | 12 | 48 | 500 | 15.67 | 15.25 |
| 22 | 26 | 16 | 48 | 500 | 8.15 | 8.28 |
| 23 | 26 | 12 | 48 | 1000 | 12.43 | 12.52 |
| 24 | 26 | 16 | 48 | 1000 | 8.01 | 8.65 |
| Repeated runs | | | | | | |
| 25 | 26 | 14 | 48 | 750 | 16.04 | 15.68 |
| 26 | 26 | 14 | 48 | 750 | 16.02 | 15.68 |
| 27 | 26 | 14 | 48 | 750 | 14.98 | 15.68 |

*Average value of triplicate experiments.

**Table 3. Analysis of variance (ANOVA) for Fe (III) ions in dry cell weight (mg/g).**

| Source | Sum of squares | Degree of freedom | Mean square | F-value | p-value | Comment |
|---|---|---|---|---|---|---|
| Model | 312.44 | 14 | 22.32 | 66.52 | <0.0001 | |
| A-Temperature | 38.92 | 1 | 38.92 | 116.00 | <0.0001 | |
| B-Degrees brix | 88.02 | 1 | 88.02 | 262.37 | <0.0001 | |
| C-Incubation time | 1.31 | 1 | 1.31 | 3.90 | 0.0719 | |
| D-Initial Fe concentration | 4.17 | 1 | 4.17 | 12.42 | 0.0042 | |
| AB | 12.39 | 1 | 12.39 | 36.93 | <0.0001 | |
| AC | 1.97 | 1 | 1.97 | 5.88 | 0.0320 | |
| AD | 2.62 | 1 | 2.62 | 7.82 | 0.0161 | |
| BC | 0.9604 | 1 | 0.9604 | 2.86 | 0.1164 | significant |
| BD | 2.40 | 1 | 2.40 | 7.16 | 0.0202 | |
| CD | 15.25 | 1 | 15.25 | 45.45 | <0.0001 | |
| $A^2$ | 33.50 | 1 | 33.50 | 99.86 | <0.0001 | |
| $B^2$ | 70.18 | 1 | 70.18 | 209.19 | <0.0001 | |
| $C^2$ | 105.02 | 1 | 105.02 | 313.05 | <0.0001 | |
| $D^2$ | 4.12 | 1 | 4.12 | 12.28 | 0.0044 | |
| Residual | 4.03 | 12 | 0.3355 | | | |
| Lack of fit | 3.29 | 10 | 0.3291 | 0.8952 | 0.6352 | not significant |
| Pure error | 0.7352 | 2 | 0.3676 | | | |
| Cor total | 316.46 | 26 | | | | |
| $R^2$=0.9873, $R^2$ adj=0.9724; C.V%=5.47; Adeq precision=25.639 | | | | | | |

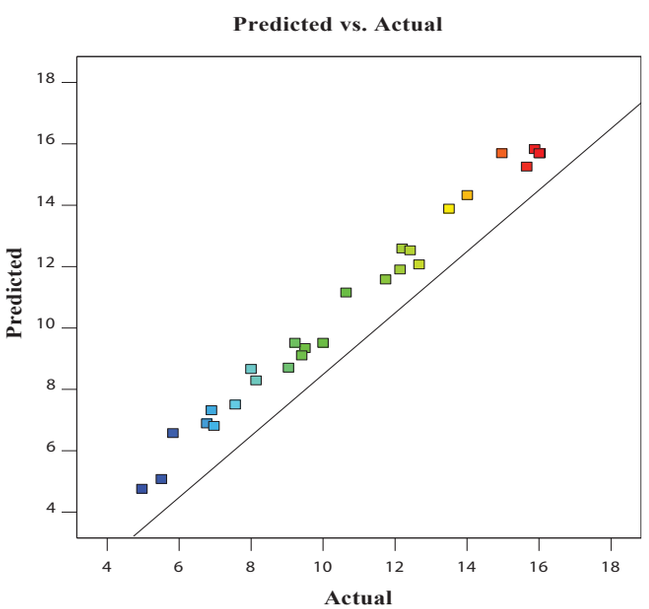


**Fig. 1. Plot of experimental versus predicted values of Fe (III) ions amounts per dry cell weight of *S. pastorianus*.**

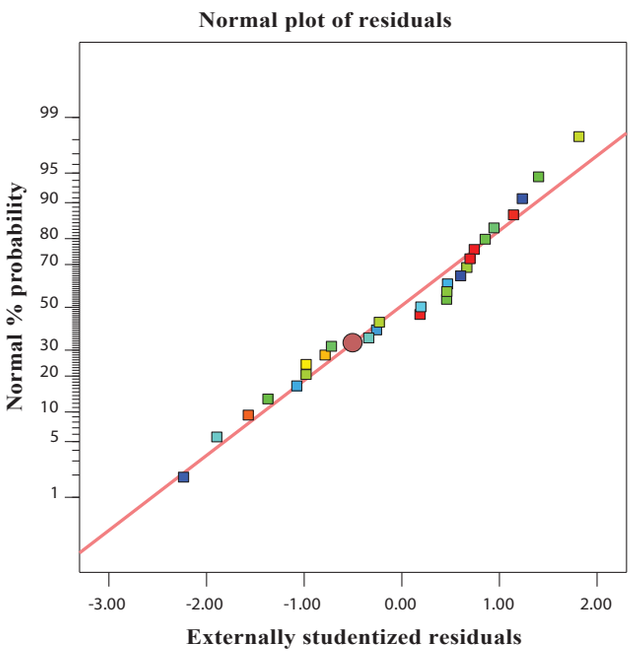


**Fig. 2. Plot of experimental residual versus predicted values of Fe (III) ions amounts per dry cell weight of S. *pastorianus.***

The results from ANOVA (Table 3) also identified that the second-order polynomial model of Eq. 3 for accumulation yields of Fe (III) ions was statistically significant and adequate to represent the actual relationship between responses and the variables, with a small probability value ($p<0.0001$) and satisfactory coefficient of determination ($R^2=0.9873$). The R-squared ($R^2$) and adjusted R-squared ($R^2$adj) coefficients of this model are 0.9873 and 0.9724, respectively, which are close to 1.0. This indicates a good fit of the model with the experimental data. Moreover, the resemblance between the $R^2$ and adjusted $R^2$ reveals the ability of the model to anticipate the results of the optimization. The F-values of 66.52, together with $p<0.0001$ for the Fe (III) ions in dry cells weight, and insignificant p-value for "lack of fit" as 0.6352 for the accumulation of Fe (III) ions yield, indicated that the model adequately fit the experimental data. Furthermore, the normal probability plot and predicted versus actual plot are presented in Figs. 1 and 2. The examination of the presumption of homogeneity is conducted by using the residuals. In particular, the studentized residuals are plotted against the probability values. The model's suitability level for the present research is indicated by the data in regard to either side of the zero line, which is spread out in a homogeneous manner.

Additionally, the predicted versus actual plots were delineated between predicted and actual response parameter values. These diagnostic plots were made in order to investigate the goodness of fit of the proposed model. The predicted $R^2$ (0.9349) shows an appropriate harmony between the value predicted by the model and the actual data. Moreover, the absence of trends in the plot of studentized residual versus the values predicted by the model shows that the variances in the data are acceptable and no outliers are present in the experiments (Fig. 2). Fig. 1 shows that the predicted versus actual plot revealed a highly linear trend through the origin, which signified that the experimentally observed values of Fe(III) ions in dry cell weight were in close agreement with predicted values. From Table 3, the overall effects of the four manipulated variables on the response revealed that the temperature and degrees brix ($p<0.0001$) were important factors for the accumulation of Fe (III) ions in dry *S. pastorianus* cells.

### *Response surface analysis*

Using surface response plots of the polynomial model, the relationships between the culture conditions and the response could be better understood by holding two variables constant at its central level and studying the relationship between the other two variables in the experimental range under investigation. To express the effects of any independent variable on the absorption of Fe (III) ions, three-dimensional surface plots were generated according to Eq. 3. On the basis of a quadratic polynomial of the response surface methodology, the effect of interacting variables, i.e., temperature (14-32$^o$C), incubated time (24-72 h), degrees brix (12-16$^o$Bx) and initial iron (III) concentration (500-1000 ppm) on the accumulation of Fe (III) were analysed.

The information obtained from the experiments showed that the range of ferric ions in dry weight was 5.52 to 16.04 (mg/g). The lack of fit F-value of 0.8952 suggested that the lack of fit is not significant, which presents acceptability of the model. Furthermore, the relative standard deviation (RSD) or C.V.% of 5.47 indicates the accuracy and repeatability of the model. Eventually, in this study, the modified quadratic polynomial equation is an appropriate model to explain the level of ferric ion amounts entrapped in *S. pastorianus* cells. The regression analysis report for the modified quadratic model showed that linear, squared, and interaction coefficients are significant ($p<0.05$) except for one linear interaction (Table 3). It is reported that the

coefficients of the three factors (temperature, degrees brix, and initial iron concentration) are negative, whereas positive coefficients were obtained for the factor of incubated time. The negative coefficient of the three factors on response implies that lowering these factors causes higher iron content in dry cell weight, which affects the number of cellular active sites available to uptake as well as metal speciation.

In Fig. 3, the relationship between the initial iron concentration and three remaining parameters was investigated. This plot shows that the interaction between initial iron concentration and temperature, degrees brix, and time is insignificant. The effect of initial iron concentration as a significant factor is relatively lower than that of the other variables. Previous studies [9] supposed that fermentation temperature had a close relationship with the growth of yeast and Fe (III) ions was a biomass-related product. The temperature disturbs the physical or chemical structure of the channels, which could either enhance or decline the amount of metal bioaccumulation sites. Besides, the malt solution obtained not only contains mainly carbohydrates (glucose, fructose, sucrose, maltose, maltotriose, and non-fermentable dextrins) but also many other molecular compounds such as nitrogenous materials and other constituents too numerous to mention [10]. Consequently, the higher the wort gravity, the smaller the impact on the bioaccumulation and biomass production because a great amount of large molecular compounds present in the malt wort is capable of binding ions, which lowers their bioavailability [3, 11]. The metabolism of Saccharomyces strains relies on glucose as the key source of energy and through fermentation the cells uptake glucose along with trace elements, which is iron in this work, to produce ethanol or pyruvate. Furthermore, the growth behavior of *S. pastorianus* has not been shown to be significantly different from other strains of Saccharomyces while its metabolism requires a fixed amount of iron for the citric acid cycle and respiratory chain. The iron concentration suitable for *S. cerevisiae* is reported to be between 5 ppm to 1500 ppm. In this work, we choose 1000 ppm Fe supplemented in the form of $C_6H_5FeO_7.5H_2O$ to study for *S. pastorianus*. The results of this work point out that supplementation of malt media with $Fe^{3+}$ has a significant influence on the bioaccumulation rate and brewing yeast growth. Iron at higher, semi-toxic levels (above 750 ppm) act as a stressing agent and cause growth inhibition as the decrease of Fe

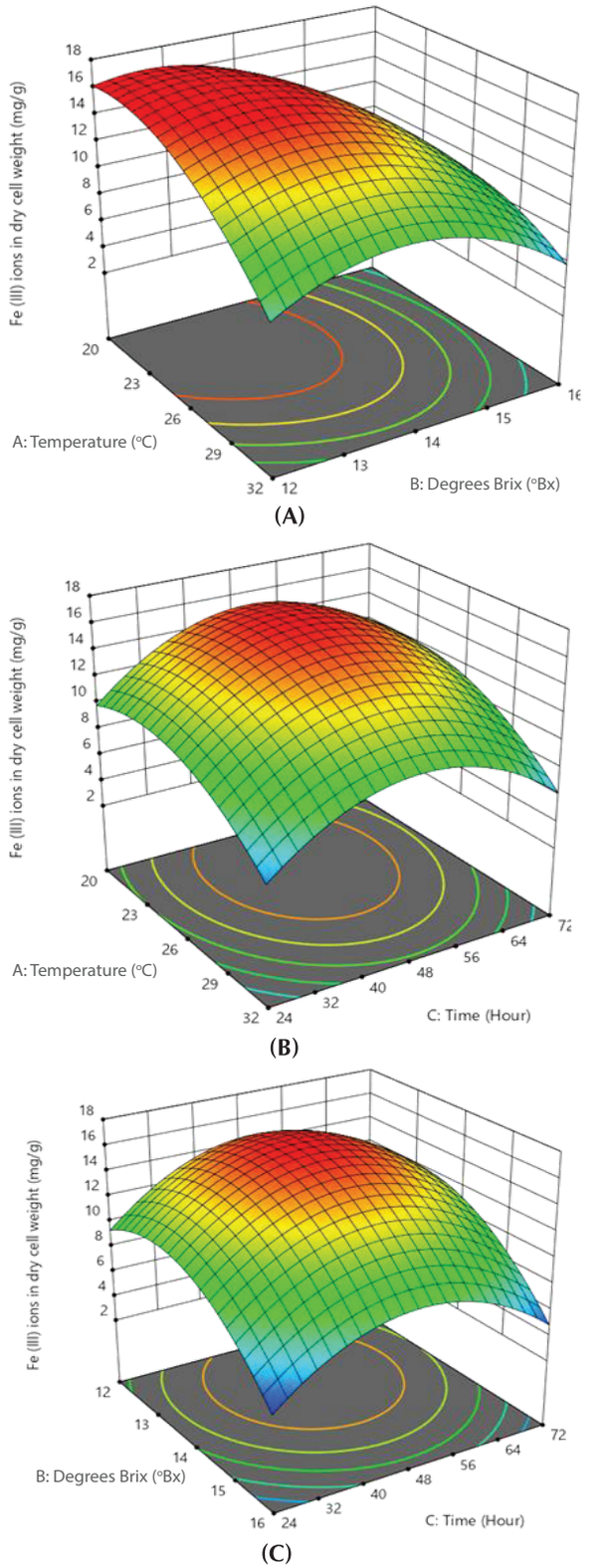


**Fig. 3. Response surface plot indicating the effect of (A) temperature (°C) and degrees brix (°Bx), (B) temperature (°C) and incubated time (hour), (C) degrees brix (°Bx) and incubated time (h) interaction on Fe (III) ions amount per dry cell weight of *S. pastorianus*.**

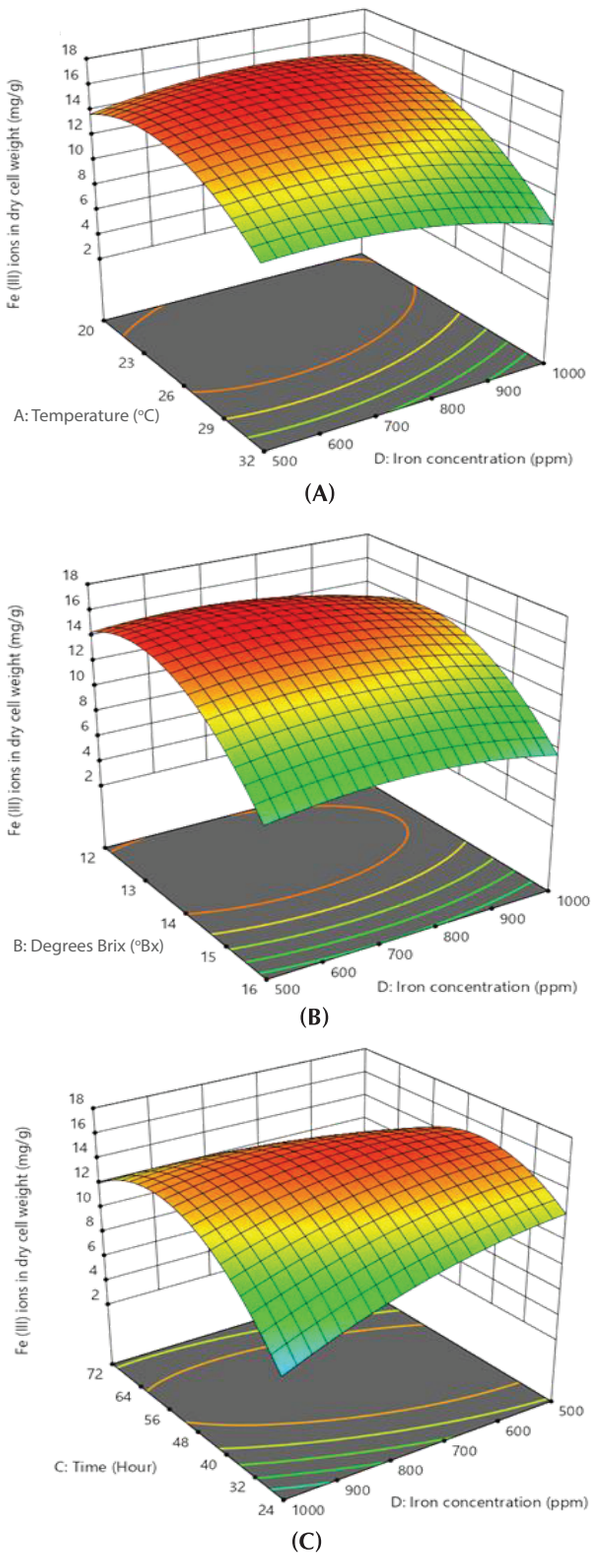


**Fig. 4. Response surface plot indicating the effect of (A) temperature (°C) and initial iron concentration (ppm), (B) degrees brix (°Bx) and initial iron concentration (ppm), (C) incubated time (hour) and initial iron concentration (ppm) interaction on Fe (III) ions amount per dry cell weight of *S. pastorianus*.**

(III) ion accumulation elongates the fermentation time. The ability to adjust the amount of iron intake helps yeast to control nutrient concentration, including metal levels, in its cells. Increasing the concentration of $C_6H_5FeO_7.5H_2O$ in the medium up to 1000 ppm (500, 750, 1000 ppm) resulted in a rising trend of iron accumulation in the biomass of the yeast *S. pastorianus*. The highest quantity, about 16 mg Fe $g^{-1}$ dry wt., was obtained at 750 ppm Fe. *S. pastorianus* is proven in this study to be a promising replacement of *S. cerevisiae* based on the advantages of its fermentation process, which could be more appropriate for use in animal feed. Since *S. pastorianus* is a yeast in the GRAS group, its use in functional food for human is another aspect worth further study [12].

One of the most efficient tools in the analysis of interactions is using graphical plots, especially three-dimensional response surface plots. In Fig. 4, the relationship between the temperature, degrees brix, and time investigated while the initial iron concentration was constant at the median value. This plot indicates that the quadratic coefficients of temperature, degrees brix, and time are significant. As a result, the lower the degree brix, incubation time, and temperature, the higher the impact on the bioaccumulation and biomass production. By raising degree brix, incubation time, and temperature, the enriched cells of *S. cerevisiae* increased to an optimum point and then decreased afterward.

### *Determination of optimum conditions*

The optimal conditions used for the accumulation test for Fe (III) citrate were determined using the maximum desirability to verify the predictive capacity of the model. Results of the optimal conditions to obtain the highest accumulation yield of Fe (III) ions from Fe (III) citrate were a temperature of 24°C, degrees brix of 13°Bx, time of 49 h, and initial iron concentration of 656 ppm. After the performance of triplicate experiments under optimum conditions, the experimental value was 16.82±0.65 mg Fe/g dry cells weight for Fe (III) ion absorption. These experimental results are in good agreement with the predicted value for Fe (III) ion accumulation (16.91±0.58 mg Fe/g dry cells weight).

## Conclusions

In this study, the optimum condition leads to high iron absorption efficiency into *S. pastorianus,* which is

demonstrated by using BBD. The bioaccumulation of ferric ions is influenced by all four factors in which the incubation temperature and degrees brix have significant effects on the iron absorption ability of the yeast as well as the biomass formation. A decrease of iron absorption at high degree brix and high temperature was observed in this study. An optimum condition for bioaccumulation of ferric ions of 16.8 mg/g biomass was achieved with BBD using RSM at 656 ppm initial iron concentration in 13°Bx medium and with *S. pastorianus* incubated at 24°C for 49 h. Furthermore, the result verified that the ability of iron absorption of *S. pastorianus* is limited based on the limited number of active sites for absorbing ferric ions inside the cells, so it is not effective to supply a larger amount of initial iron concentration to the growth medium. It is concluded that iron-enriched *S. pastorianus* has the potential for mass production with a low-cost natural source with the recommended optimum conditions found in this study.

The authors declare that there is no conflict of interest regarding the publication of this article.

## REFERENCES

[1] W. Bahafid, et al. (2017), "Yeast biomass: an alternative for bioremediation of heavy metals", *Yeast-Industrial Applications*, DOI: 10.5772/intechopen.70559.

[2] F. Gaensly, et al. (2014), "The uptake of different iron salts by the yeast Saccharomyces cerevisiae", *Brazilian Journal of Microbiology*, **45(2)**, pp.491-494.

[3] A. Poreda, and T. Tuszyński (2007), "Influence of magnesium and zincions on trehalose synthesis and fermentation activity in brewing yeast Saccharomyces carlsbergensis", *Chemia i Inżynieria Ekologiczna*, **14(2)**, pp.197-207.

[4] I. Schröder, E. Johnson, S. De Vries (2003) "Microbial ferric iron reductases", *FEMS Microbiology Reviews*, **27(2-3)**, pp.427-447.

[5] Y. Yuan, et al. (2004), "Construction of a high-biomass, iron-enriched yeast strain and study on distribution of iron in the cells of Saccharomycescerevisiae", *Biotechnology Letters*, **26(4)**, pp.311-315.

[6] G. Fan, et al. (2008), "Optimizing conditions for anthocyanins extraction from purple sweet potato using response surface methodology (RSM)", *LWT-Food Science and Technology*, **41(1)**, pp.155-160.

[7] Y. Azila, M. Mashitah, S. Bhatia (2008), "Process optimization studies of lead (Pb (II)) biosorption onto immobilized cells of Pycnoporus sanguineus using response surface methodology", *Bioresource Technology*, **99(18)**, pp.8549-8552.

[8] B. Szulc-Musioł, B. Dolińka, F. Ryszka (2016), "Influence of incubation conditions on baker's yeast enrichment in selenium", *Journal of Elementology*, **21(4)**, pp.1253-1261.

[9] R. Singh, et al. (2010), "Biosorption optimization of lead (II), cadmium (II) and copper (II) using response surface methodology and applicability in isotherms and thermodynamics modeling", *Journal of Hazardous Materials*, **174(1-3)**, pp.623-634.

[10] Y. He, et al. (2014), "Wort composition and its impact on the flavour-active higher alcohol and ester formation of beer-a review", *Journal of the Institute of Brewing*, **120(3)**, pp.157-163.

[11] T. Satyanarayana, G. Kunze (2009), *Yeast Biotechnology: Diversity and Applications*, Springer, pp.744.

[12] M. Amiri, et al. (2017), "Optimization of culture conditions for enrichment of saccharomyces cerevisiae with Dl-α-Tocopherol by response surface methodology", *Iranian Journal of Pharmaceutical Research (IJPR)*, **16(4)**, pp.1546-1554.

DOI: 10.31276/VJSTE.62(2).56-64

# The efficiency of solar water heating system with heat pump software application designed for resorts in Vietnam

**Duy Tue Nguyen, Tri Nhut Do***

*Faculty of Engineering, Van Lang University*

Received 6 March 2020; accepted 26 May 2020

***Abstract:***

**Solar energy is a free and nearly endless source of energy. Vietnam has the advantage of harnessing solar energy for many essential purposes because of its geographic location in the tropics. This allows electricity usage to be minimized in solar chemistry and energy conversion from solar energy into electricity; or to completely replace electricity usage in applications such as heating, cooling, ventilation, water treatment, cooking processes, and heating processes. In this paper, three solar water heating systems with a heat pump are designed for resorts located at three famous tourist destinations in Vietnam: Phu Quoc island and the towns of Bao Loc, and Sa Pa. These places represent the Southern, Central, and Northern regions of Vietnam, respectively. Ecotect and Grasshopper software applications are employed with the latest weather, heat, and radiation data and was obtained from *climate.onebuilding.org*. Data analysis is based on Ecotect software and the computational design is done in Grasshopper software. These software applications show that Phu Quoc island is the most efficient place to exploit solar energy, followed by Bao Loc, which is lower due to the fog, and Sa Pa, where solar radiation is low. In order to increase the water heating efficiency in places with very low solar radiation, a heat pump is considered along with a conventional solar water heating system and optimum azimuth angle of 180° South for the solar collector. This method is an efficient solution that can be applied in Sa Pa as well as in other places in Vietnam where there is a lack of solar radiation. The solar energy factor (SEF) is significantly increased from 14.37 to 57.47 and the solar fraction (SF) per year is increased from 93.5 to 98.3% using this method.**

***Keywords:*** **heat pump, solar energy collector, solar water heating system.**

***Classification number:*** **2.3**

## Introduction

In recent years, increasing tourist visits to Vietnam have resulted in a significant increase in the demand for infrastructure and energy consumption. The territory of Vietnam stretches from 8.42° to 23.39° N, thus, Vietnam is a country of enormous sunshine with an average annual solar radiation of about 1675 kWh/m$^2$ and receives nearly 1854 hours/year of sunlight [1]. Solar power is a clean and valuable source of energy to be exploited for heating water. Presently, however, hot water is produced by standard types of energy such as electricity, coal, diesel, gas, and others. These methods are costly and negatively impact the environment. Therefore, solar energy is a better choice to replace these conventional energy sources [2].

Moreover, software modelling is considered to be quite an effective tool for the simulation of energy in many countries around the world. In this work, powerful software is applied to the calculation of heat radiation in Vietnam. This novel software application facilitates design, architecture, and engineering fields to realize a new view of building information modelling (BIM) in regard to the design and construction related to solar radiation, heated water, and energy analysis. Further, this software meets the BIM development roadmap of construction activities and management led by the Vietnamese Prime Minister.

Solar radiation is unevenly distributed across the regions and seasons of Vietnam. This fact is clarified by Ecotect software, which contains weather data from the Climate.

*Corresponding author: Email: trinhutdo@gmail.com

OneBuilding website [3]. A model of a solar collector is established in Grasshopper software with variable dimensions such as the area of the solar collector, its tilt, and the actual azimuth angle. In this work, we gradually change these parameters until optimal parameters are achieved.

The results show that the coldest day at Phu Quoc island, which is located at 10.2° N, 104° E, and 4 m altitude is on the 7th of February, while the coldest day at Bao Loc, located at 11.5° N, 108° E, and 850 m altitude is on the 26th January, and finally the coldest day at Sa Pa, located at 22.4° N, 103.8° E, at 1581 m altitude, is on the 10th of January. The lowest temperatures for each month, which are depicted in Fig. 1, are 2.1°C, 2.2°C and 15.5°C at Sa Pa, Bao Loc and Phu Quoc island, respectively.

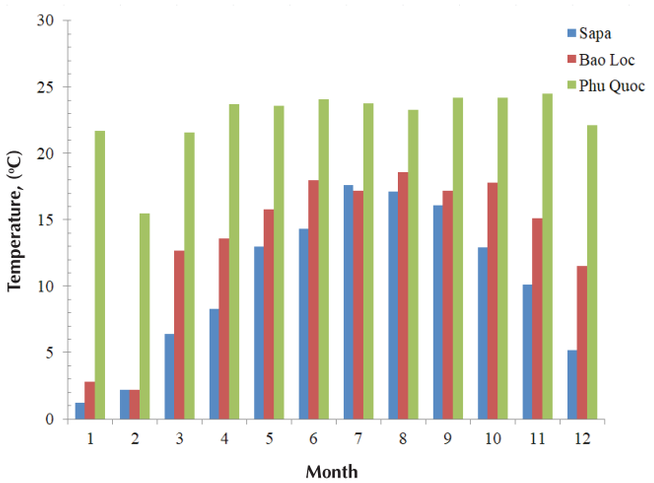


**Fig. 1. The whole year lowest temperature in a month at 3 places in Vietnam.**

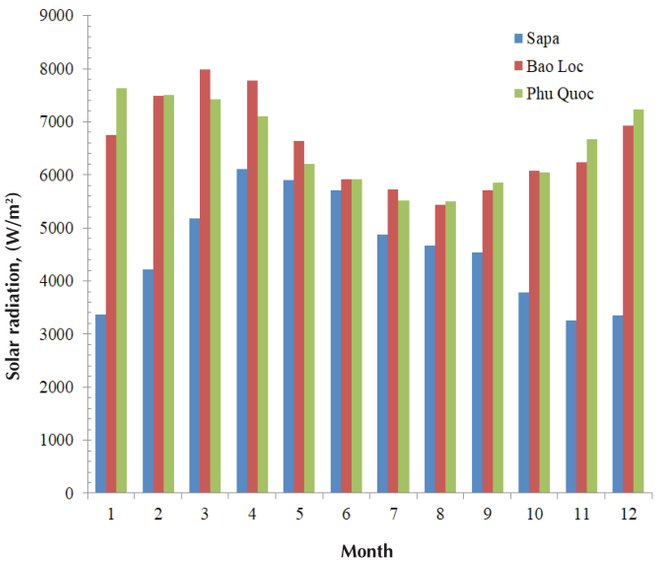


**Fig. 2. The whole year solar radiation at 3 towns in Vietnam.**

As depicted in Fig. 2, the solar radiation in Bao Loc and Phu Quoc island are similar with their smallest difference of 1% in June and highest difference of 13% in January. In particular, the solar radiation at Sa Pa is much lower than the other two locations. The smallest difference between Sa Pa and the other two locations is 50% in January. In order to compensate for this lack of solar radiation, a heat pump is added into the conventional water heating system. As a result, the SEF significantly increased from 14.37 to 57.47 and the SF per year increased from 93.5 to 98.3%.

Lamnatou, et al. (2015) [4] showed that solar energy remains unstable and unpredictable due to its strong dependency on climatic conditions even though it has high efficiency. In order to solve this problem, thermal energy storage equipment and an auxiliary heat supply device are installed in solar water heating systems to satisfy the fluctuating heating load [5]. Mehrpooya, et al. (2015) [6] integrated a heat pump into a solar heating system and declared that such a combined system will ensure a sufficient hot water supply and save energy. Jordan, et al. (2019) [7] carried out an experiment comparing conventional supplementary heating and the solar water heating system with heat pump and their results showed that the energy consumption of the solar system combined with heat pump was 54.9% lower than that of conventional solar water heating combined with electrical resistance. Ta Van Chuong (2017) [8] proved that the use of a heat pump is very efficient to supply 40-50°C hot water in Vietnam. Moreover, he utilized some simulation software to analyse the solar water heating system combined with heat pump and then declared that solar energy can meet 83.7% and 66% of the water heating system energy in Nha Trang and Hanoi city, respectively. In addition, their results also showed that electricity consumption is only 5% of what a conventional electrical water heating system requires when a solar water heating system is combined with a heat pump. Nguyen Van An (2015) [9] and his colleagues designed a solar water heating system combined with a heat pump whose capacity was 30000 litres at The Gioi Xanh hotel in Nha Trang; and the result showed that electricity consumption was only 7-8% of that of a conventional electrical water heating system. However, solar water heating systems in areas such as Phu Quoc island, Bao Loc, and Sa Pa have not yet been studied. Therefore, this paper will address studies in those areas.

In this paper, several solar water heating systems with heat pumps are analysed in terms of their components and operation principle. In particular, the authors calculate the hot water flowrate for a 90-room hotel in each area and all relevant parameters are analysed. The optimization of the solar collector direction was carried out by computational

design in Grasshopper software. This is a new, powerful program used to analyse solar radiation as well as solar water heating systems. Finally, the optimized solar water heating system with heat pump is compared to a conventional one in order to prove its economic efficiency.

The rest of this paper is organized as follows. The fundamental concepts of a solar water heating system combined with heat pump are described in the following section. After that is an evaluation of the economic efficiency of a solar water heating system combined with heat pump is presented. The final section concludes the paper.

## Fundamental concepts of solar water heating system combined with heat pump

From Refs. [10, 11], a heat pump is a device that transfers heat energy from a heat source to a heat storage tank. With a heat pump, heat energy is moved in the opposite direction of spontaneous heat transfer, which means that heat is absorbed from the cold space and released to warmer places. A heat pump uses external energy to complete the task of energy transfer from the heat source to the radiator. The most common design of a heat pump consists of four main components: condensers, expansion valves, evaporators, and compressors. Heat pumps can usually be used either in heating mode or cooling mode, as required by the user. When a heat pump is used for heating, it employs the same basic refrigeration-type cycle used by an air conditioner or a refrigerator but in the opposite direction i.e. the heat pump releases heat into the conditioned space rather than the surrounding environment. In this use, heat pumps generally draw heat from the cooler external air or from the ground.

According to Refs. [12, 13], in order to assess the heat pump efficiency, the $COP_{heatpump}$ must be used as follows:

$$COP_{heatpump} = Q_c/W \quad (1)$$

where $Q_c$ (kW) is the heat rejected from the condenser to increase water's temperature and W (kW) is the power of the compressor used to run the heat pump.

Then, we have

$$Q_c = Q_e + W \quad (2)$$

where $Q_e$ (kW) is the surrounding heat that is transmitted to the evaporator.

Thus,

$$COP_{heatpump} = (Q_e + W)/W \quad (3)$$

According to the 1st thermodynamic law, 1 kW of electrical energy will be theoretically transferred into 1 kW thermal energy when an electrical heater is utilized for hot water producing. However, 1 kW of electrical energy running a compressor when hot water heat pump is utilized will produce $(1 + Q_e)$ kW of thermal energy in practice. The heat consumption $Q_{hotwater}$ (kW) for a water heating system from the initial temperature $t_1$(°C) to the final one $t_2$(°C) is the following:

$$Q_{hotwater} = G.C_p\,(t_2\text{-}t_1) \quad (4)$$

where G and $C_p$ are the mass water flowrate (kg/s) and water heat capacity (4.18 kJ/kg.K), respectively. $G = V \times \delta$ is calculated with a flowrate volume V ($m^3/s$) and water density $\delta$ (1000 $kg/m^3$).

However, an auxiliary heater, such as electrical heater or heat pump, must be used where there is a lack of solar radiation. Thus, the efficiency of a solar water heating system combined with the heat pump must be analysed. The efficiency is evaluated by two parameters, SEF and SF, defined as the following:

$$\text{Solar Energy Factor (SEF)} = \text{SWH/AHE} \quad (5)$$

where SEF is the ratio of the total energy provided by the solar water heating system (SWH) to the auxiliary heater energy (AHE) and

$$\text{Solar Fraction per year (SF)} = \text{SWH/(SWH + AHE)} \quad (6)$$

where SF is the percentage of the total heat requirement that is provided by solar water heating system (SWH) for whole a year.

## Evaluation of efficiency for solar hot water combined with heat pump

In this section, solar water heating systems are analysed in order to evaluate the potential for solar application. The systems are applied to a 90-room hotel in the areas of Phu Quoc island, Bao Loc, and Sa Pa. Additionally, the efficiency of a solar water heating system combined with a heat pump will be compared to the non-heat pump system in the case of a lack of sufficient solar radiation.

Following the standard in Ref. [14], a hot water flowrate of 53.1 litres per room per day and 60°C hot water temperature were chosen for the 90 rooms. As a result, during 8 h of working time that starts at 7:00 AM every day, the maximum hot water flowrate is 4779 litres per day.

The authors design the solar water heating system with the above initial conditions. In addition, other parameters are obtained by the Grasshopper simulation software such as the initial water supply temperature, water heating system energy, and solar collector area.

***Schematic diagram of system*** (Fig. 3)

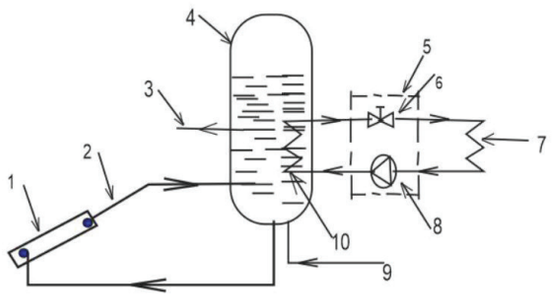


**Fig. 3. The schematic diagram of system.**
1: solar collector; 2: piping system; 3: hot water supply to the resort; 4: hot water tank; 5: heat pump system; 6: expansion valve; 7: evaporator; 8: compressor; 9: cold water supply; 10: condenser.

***The initial water supply temperature***

This parameter is significant because it affects the water heating system energy and depends on environmental temperature, soil thermal diffusivity, and buried depth. In order to obtain the initial water supply temperature, three initial conditions are required for the simulation process: the hourly surrounding temperature of each area, a 3-m buried depth, and dry clay soil. The input and output parameters for the initial water temperature simulation in Fig. 4 are shown in Table 1.

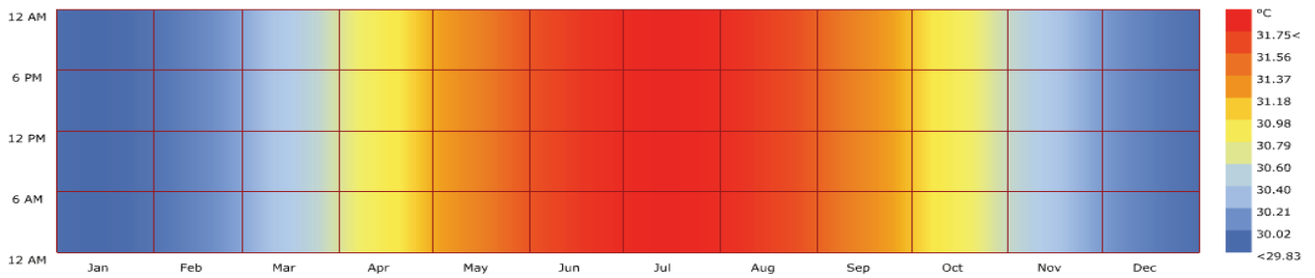


**(A)**

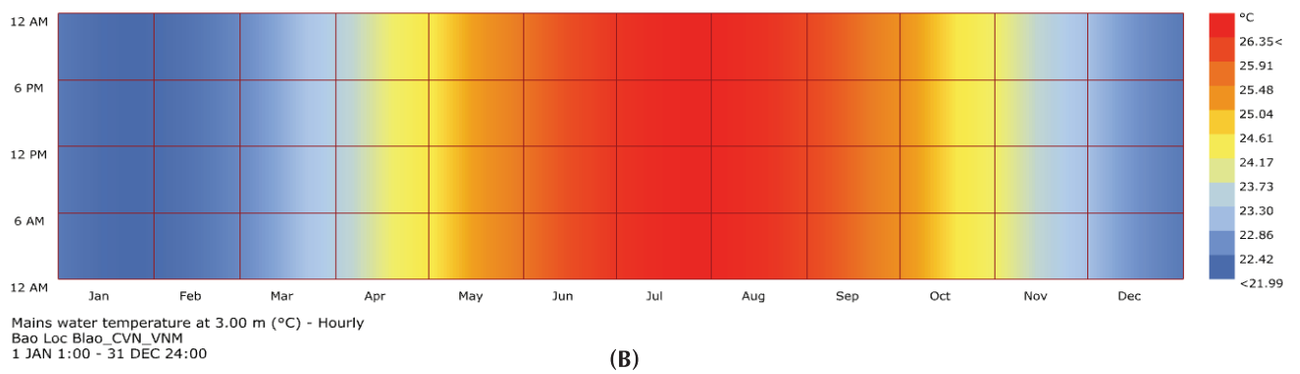


**(B)**

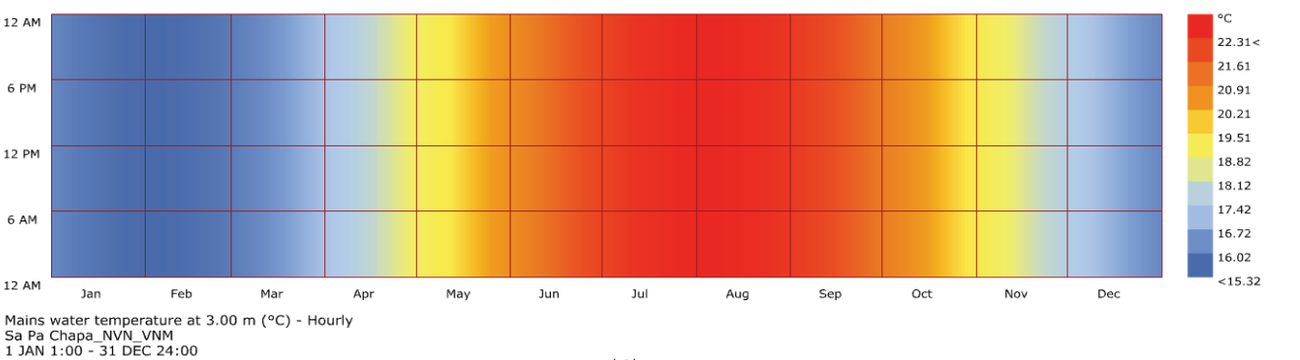


**(C)**

**Fig. 4. The initial water supply temperature during a year in: (A) Phu Quoc island, (B) Bao Loc town, (C) Sa Pa town.**

**Table 1. The input and output parameters for the initial water temperature.**

| Input parameters | Output parameter |
|---|---|
| Weather data | The initial water supply temperature during a year |
| Soil thermal diffusity for dry cray: $2.5.10^{-7}(m^2/s)$ | |
| Pipe depth : 3 meters | |

**Table 2. The average and lowest intitial water supply temperature of each area.**

| Location | Average temperature a year (°C) | The lowest temperature (°C) |
|---|---|---|
| Phu Quoc island | 30.79 | 29.8 |
| Bao Loc town | 24.17 | 22 |
| Sa Pa town | 18.8 | 15.32 |

*Water heating system energy*

Using Eq. (4) with the water flowrate of 597.38 litres/h, the lowest initial water temperature supplied from Table 2 and the final hot water temperature of 60°C produce a maximum water heating system energy of 20.93 kW, 26.35 kW, and 30.85 kW for Phu Quoc island, Bao Loc, Sa Pa, respectively.

In addition, with the water flowrate of the hourly initial water supply temperature analysed in an earlier section, the final hot water temperature and water heating energy for a year are displayed in Fig. 5. The input and output parameters for the simulation are shown in Table 3.

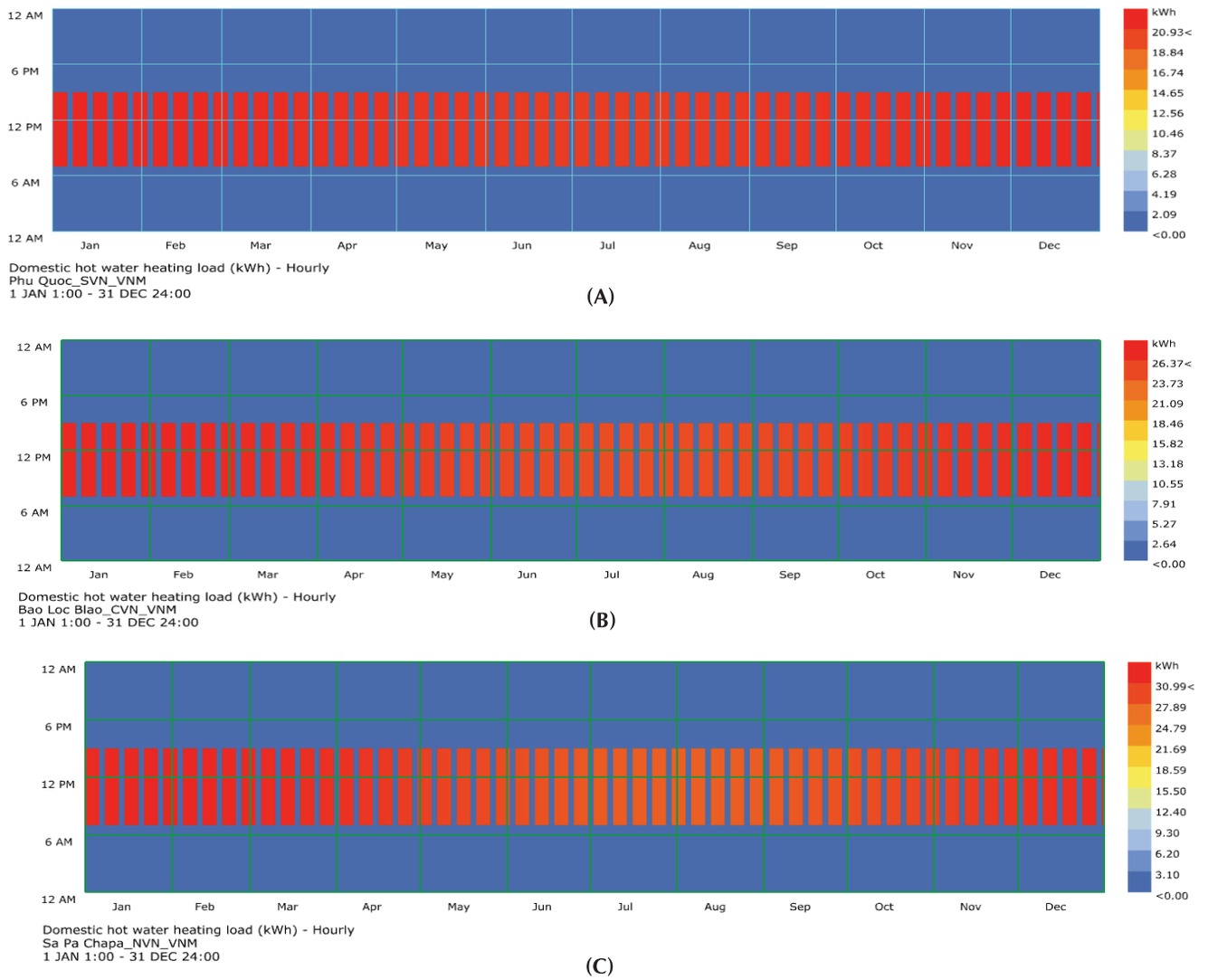


**Fig. 5. The water heating energy during a year in: (A) Phu Quoc island, (B) Bao Loc town, (C) Sa Pa town.**

**Table 3. The input and output parameters for the water heating energy during a year.**

| Input parameters | Output parameter |
|---|---|
| Weather data | The water heating energy during a year |
| Chosing : type "Hotel from 61 to 99 rooms" | |
| 90 rooms | |
| 53.1 liters per room per day | |
| Delivery water temperature: 60°C | |
| The initial water supply temperature during a year | |

Obviously, the water heating energy in Sa Pa is the largest as a result of the cold initial water supply temperature. Therefore, its solar collector area for that location will be the largest. In the following section, the solar collector area and its optimum direction will be chosen.

***Solar collector area***

The solar collector area will be chosen to meet the water heating system energy requirements in each area. Thus, the authors optimized the solar collector area until the final energy that is collected by solar energy meets the calculated water heating system energy. Apart from the solar collector area, another parameter that strongly affects solar energy is azimuth angle of the solar collector. When this angle is changed, the efficiency of solar energy also changes, which is represented by the tilt and orientation factor (TOF). TOF is the solar radiation at the actual tilt and azimuth divided by solar radiation at the optimum tilt and azimuth. In this paper, authors chose the tilt of the solar collector to be 30° with respect to the horizon plane and changed its direction from North (azimuth angle = 0°) to West (azimuth angle = 270°). The results obtained after simulation are presented in Table 4. The input and output parameters for the simulation are shown in Table 5.

**Table 4. TOF of Solar collector.**

| Location | East | West | South | North |
|---|---|---|---|---|
| Phu Quoc island | 86.7% | 92.4% | 100% | 80.3% |
| Bao Loc town | 85.8% | 92.8% | 100% | 80.3% |
| Sa Pa town | 87% | 93.9% | 100% | 81% |

**Table 5. The input and output parameters for TOF.**

| Input parameters | Output parameter |
|---|---|
| Weather data | TOF |
| The actual collector's tilt : 30° | Optimal tilt |
| The actual collector's Azimuth: from 0° to 270° | Optimal Azimuth |
| Annual shading: 0% | |

From Table 4, the optimum azimuth angle of the solar collector is 180° (South) because it creates the largest amount of solar energy during a year. In order to generate enough water heating energy, the sufficient solar collector area is also chosen. Moreover, the collected solar energy for each solar collector area, is shown in Fig. 6. In this simulation, a vacuum solar collector is chosen. In addition, its surface area is changed to match the water heating energy demand found from Fig. 5. In these results, the surface areas are 120 $m^2$, 138 $m^2$, and 314.5 $m^2$ for the locations of Phu Quoc island, Bao Loc, and Sa Pa, respectively.

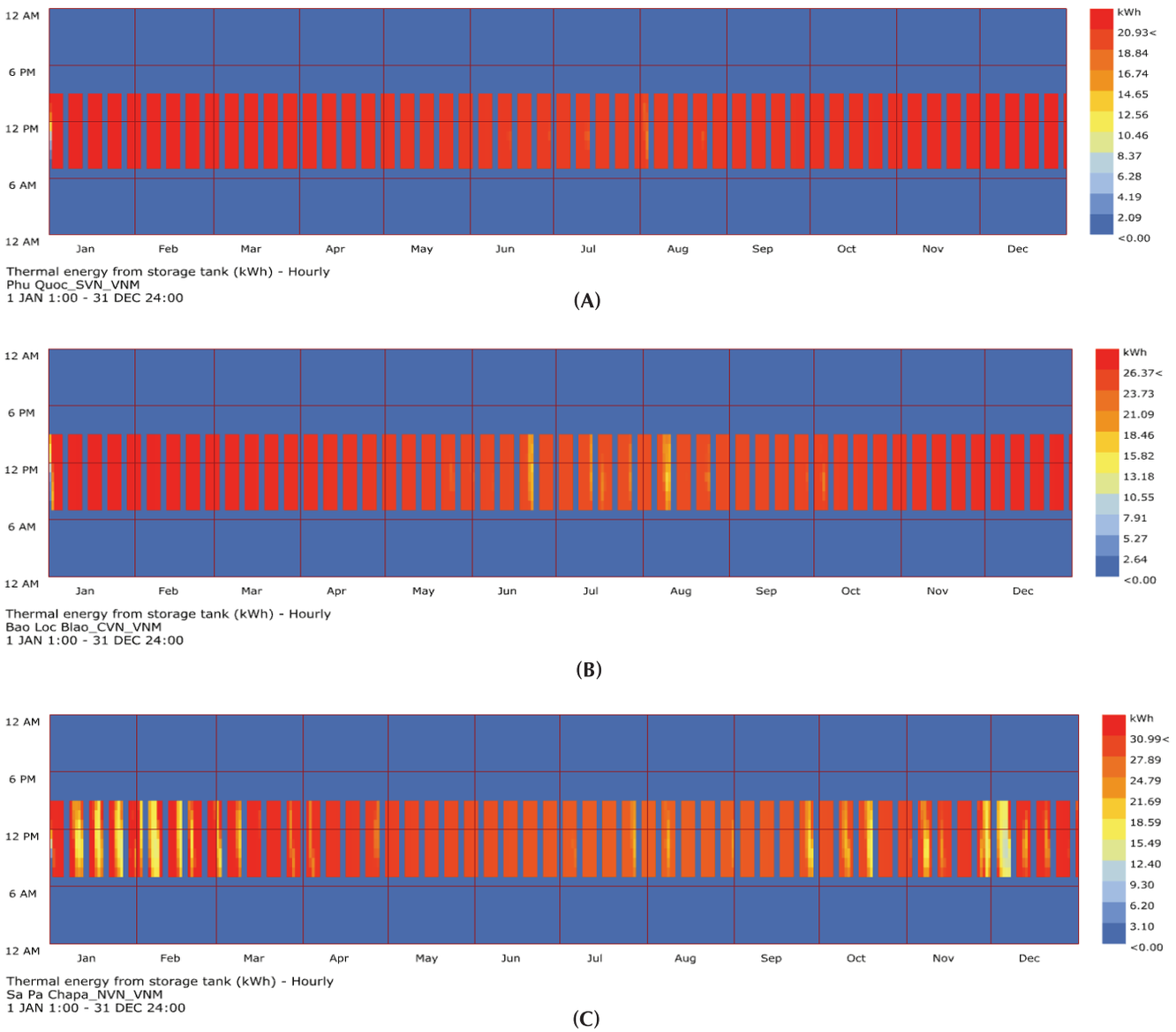


**Fig. 6. The obtained solar energy correspondence with its collector area: (A) Phu Quoc island, (B) Bao Loc town, (C) Sa Pa town.**

The daily solar water heating (DSWH) energy and the whole year solar water heating (SWH) energy which are collected by solar collector in each area are displayed in Table 6.

**Table 6. The DSWH energy and the whole year SWH energy.**

| Location | DSWH (kWh) | SWH (kWh) |
|---|---|---|
| Phu Quoc island | 115.56 | 42180 |
| Bao Loc town | 140.8 | 51401 |
| Sa Pa town | 157.79 | 55769 |

The input and output parameters for the simulations in Figs. 6, 7 and in Table 6 are shown in detail in Table 7.

**Table 7. The input and output parameters for the obtained solar energy with its collector; the auxiliary heater energy and the daily solar water heating energy and the whole year solar water energy.**

| Input parameters | Output parameter |
|---|---|
| Weather data | Solar energy for water heating per hour |
| The water heating energy during a year | The Auxilary heater energy |
| SWH area | DSWH |
| SWH surface percent: 100% | The whole year SWH |
| "Direct " hot water loop | |
| Collector type: "Evacuated collector tube" | |
| The tilt and direction of solar collector | |
| Sky Exposure Factor: choosing 1 | |

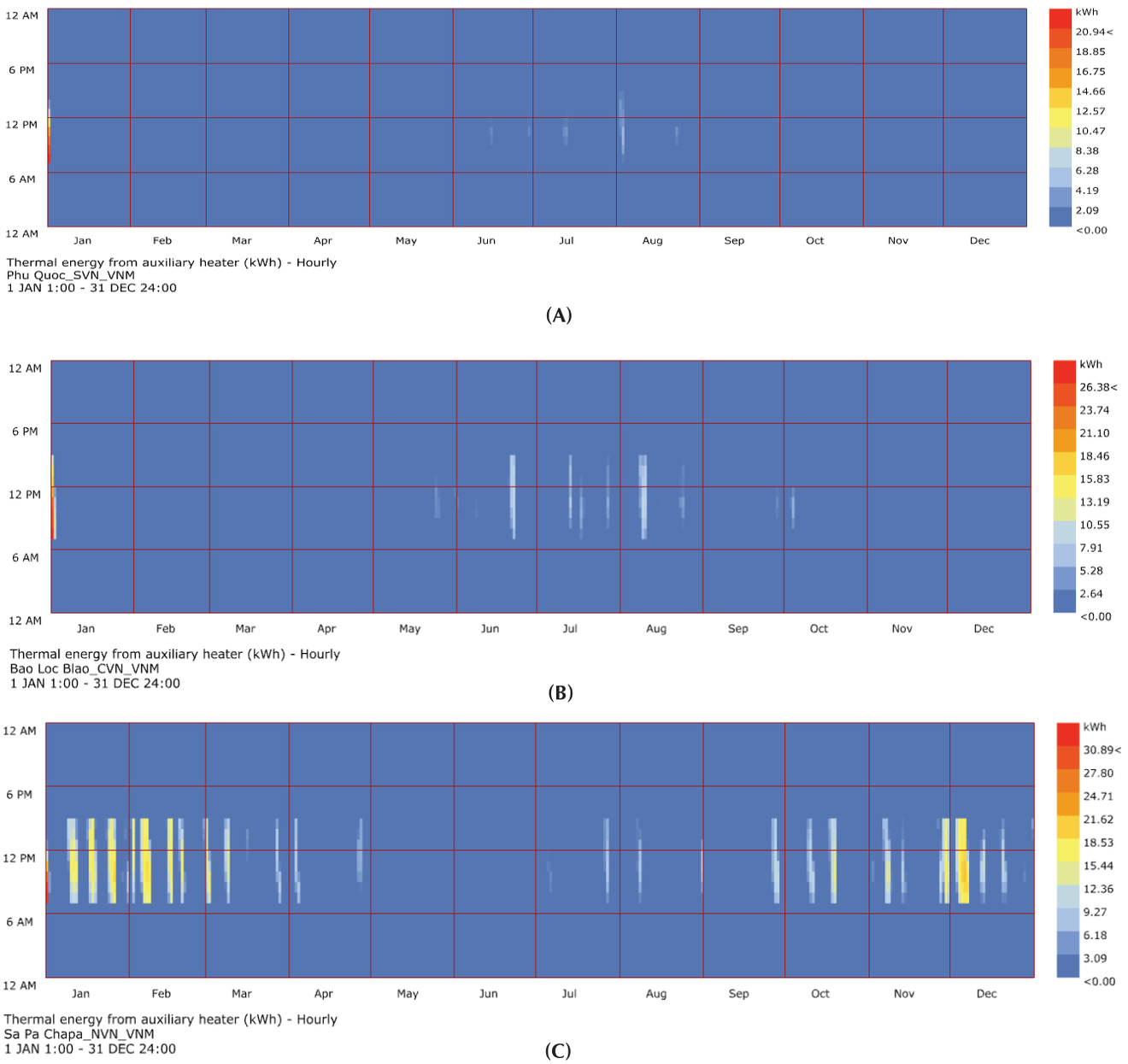


**Fig. 7. Auxiliary heater energy in: (A) Phu Quoc island, (B) Bao Loc town, (C) Sa Pa town.**

In general, solar energy can satisfy water heating energy. However, it cannot supply enough energy to the water heating system over some time periods. This phenomenon is displayed in Fig. 7. As a result, the auxiliary heater is used for supplementary energy.

### *Auxiliary heater*

The supplementary energy from auxiliary heater during a year is displayed in Fig. 7.

In Fig. 7, the lack of solar radiation can be recognized in some period times and auxiliary heater is used to satisfy system's demand. Hence, the whole year auxiliary heater energy (AHE) is obtained from the simulation and it is generated by electricity, gas, oil or heat pump.

### *Economic efficiency of solar water heating combined with heat pump*

In order to calculate the efficiency of the solar water heating system, Eqs. (5) and (6) are used. The results are shown in Table 8.

**Table 8. Efficiency of solar water heating evaluation.**

| Location | SWH (kWh) | AHE (kWh) | SEF | SF(%) |
|---|---|---|---|---|
| Phu Quoc island | 42180 | 124.36 | 340 | 99.7 |
| Bao Loc town | 51401 | 493.38 | 104.18 | 99.04 |
| Sa Pa town | 55769 | 3881.48 | 14.37 | 93.5 |

The input and output parameters for Table 8 are shown in details in Table 9.

**Table 9. The input and output parameters for Efficiency of solar water heating evaluation.**

| Input parameters | Output parameter |
|---|---|
| Solar energy for water heating per hour | SEF |
| The Auxiliary heater energy | SF per year |
| SWH surface percent: 100% | |
| The water heating energy during a year | |
| Solar water system settings | |
| Pump energy: 0 kWh | |

The greater the increase of SEF, the more economic efficiency from the solar water system. In this table, the SEF of the solar water heating system in Sa Pa is the smallest because it must use the auxiliary heater more than in the other locations. In order to increase the SEF, the use of a heat pump is a solution that must be considered. If using heat pump with a $COP_{heatpump} = 4$, following Eq. (3), the new AHE = 3881.48/4 = 970.37 kWh. Therefore, the new SEF and SF in Sa Pa are 57.47 and 98.3%, respectively.

## Conclusions

This paper has briefly presented the fundamentals of a solar water heating system combined with a heat pump. The solar water heating system is designed by Ecotect and Grasshopper software applications in three famous tourist areas in Vietnam. The optimum azimuth angle for the solar collector is chosen. A comparison of the efficiency between solar heating system with and without heat pump is presented. The main ideas of this work can be summarized as follows:

- The solar radiation in Bao Loc is nearly equal to Phu Quoc island. However, as a result of the low initial water supply temperature, solar water heating energy must be about 26% higher in Bao Loc than Phu Quoc island and the solar collector surface area is also 15% higher than that of Phu Quoc island.

- The solar radiation and initial water temperature supply in Sa Pa are the lowest and, thus, greater than 2.62 times collector surface area is required for Sa Pa than that of Phu Quoc island.

Over some periods of time, obviously, solar energy is not able to meet the hot water energy demand to heat water, so an auxiliary heater is needed. However, this leads to more electric energy usage, therefore a heat pump is the best solution to cope with this unavoidable problem.

The authors declare that there is no conflict of interest regarding the publication of this article.

## REFERENCES

[1] Hoang Dinh Tin, Hoang Thi Nam Huong (2012), *Solar Energy Harvesting Applied for Hot Water and Distilled Water from Sea Water*, Vietnam National University Publishing House, 312pp.

[2] Nguyen The Bao (2016), *Renewable Energy and Sustainable Development*, Vietnam National University Publishing House, 536pp.

[3] Climate.OneBuilding: Repository of free climate data for building performance simulation. c2014-2020, http://climate.onebuilding.org/WMO_Region_2_Asia/VNM_Vietnam/index.html, [accessed 2020 Jan 02]

[4] C. Lamnatou, J.D. Mondol, D. Chemisana, C. Maurer (2015), "Modelling and simulation of building-integrated solar thermal systems: behavior of the coupled building/system configuration", *Renew. Sustain. Energ. Rev.*, **48**, pp.178-191.

[5] M. Benghanem (2011), "Optimization of tilt angle for solar panel: case study for Madinah, Saudi Arabia", *Appl. Energ.*, **88**, pp.1427-1433.

[6] M. Mehrpooya, H. Hemmatabady, M.H. Ahmadi (2015), "Optimization of performance of combined solar collector-geothermal heat pump systems to supply thermal load needed for heating greenhouses", *Energ. Convers. Manag.*, **97**, pp.382-392.

[7] R.A. Jordan, J.T. Yamasaki, V.S. Júnior, E.C.B. Dória (2019), "Hybrid solar heat pump system for water", *Engenharia Agrícola, Jaboticabal*, **39(4)**, pp.419-425.

[8] Ta Van Chuong (2017), *Simulation study of Thermal Processes in Hot Water Production Systems Using Solar Collectors Combined with Heat Pumps*, PhD thesis, Hanoi University of Science and Technology, 150pp.

[9] Nguyen Van An (2015), *VNEEP: National Program on Economical and Efficient Use of Energy*, http://tietkiemnangluong.com.vn/tin-tuc/khoa-hoc-cong-nghe/t23124/ket-hop-bom-nhiet-voi-bo-thu-nang-luong-mat-troi.html.

[10] Nguyen The Bao (2015), *Preserving and Managing Energy in Industry and Buildings*, Science and Technology Publishing House, 496pp.

[11] Le Chi Hiep (2010), *Textbook of Air-conditioning Technique*, Vietnam National University Publishing House, 559pp.

[12] Hoang Dinh Tin, Le Chi Hiep (2011), *Thermodynamics Technique*, Vietnam National University Publishing House, 446pp.

[13] Le Nguyen Minh (2009), *Exercises in Thermodynamics Technique*, Vietnam Education Publishing House, 145pp.

[14] The American Society of Heating, Refrigerating and Air-Conditioning Engineers, *ASHARE 2003 application handbook, Chapter 49 (Service water heating)*.

DOI: 10.31276/VJSTE.62(2).65-70



# Surface charge characteristics of a variable charge soil (Rhodic Ferralsols) in the Central Highlands

**Quang Chon Nguyen[1*], Van Cuong Dinh[1], Minh Ngoc Truong[2]**

*[1]Institute of Agricultural Sciences for Southern Vietnam*

*[2]Branch of National Center for Technological Progress in Ho Chi Minh city*

Received 25 February 2020; accepted 4 May 2020

***Abstract:***

**Variable charge soils (VCS) predominantly contain minerals with variable surface charge density, such as kaolinite, gibbsite, goethite, hematite and amorphous minerals. The charge characteristics differ between profile horizons, the topsoil normally possesses net negative surface charge whereas the subsoil may have net positive surface charge and are largely dependent on soil pH. The soils pose a particular challenge to sustainable management in terms of low cation exchange capacity (CEC) at soil low pH and may develop appreciable anion exchange capacity (AEC) under acidic conditions. A full understanding of the variation of charge with soil pH, before establishing strategies for sustainable management of these soils, is essential. This study has found that the VCS from the Central Highlands are extremely acidic (pH<4.5) and very low in CEC (<1.0 $cmol_c\ kg^{-1}$), these problems are more pronounced in the subsoil with exhibiting higher $pH_0$ (4.63) than the existing soil pH (4.26) and higher point of zero net charge (PZNC) (4.88) than point of zero charge ($pH_0$), and developing net positive surface charge (-0.62 $cmol_c\ kg^{-1}$). These properties are attributed to low total organic carbon (TOC) and Fe/Al hydrous oxides in the clay fraction that significantly affect pH buffering capacity and delta CEC. In addition, organic matter (OM) has a great influence on the $pH_0$ of variable charge components, and thus on CEC.**

***Keywords:*** **cation exchange capacity, point of zero charge, surface charge, variable charge soil.**

***Classification number:*** **3.1**

## Introduction

VCS are the soils that have developed under intensive weathering and leaching conditions in tropical and subtropical regions that contain minerals with variable surface charge density, such as kaolinite, gibbsite, goethite, hematite, and amorphous minerals [1, 2]. The charge characteristics of VCS can differ between profile horizons, even within a single soil type. In general, it is found that the surface charge of the topsoil possesses a net negative charge whereas the subsoil may have a net positive surface charge, which is so-called the 'geric property' [3].

Point of zero charge (PZC), or $pH_0$, is the pH value at which the variable net surface charge, resulting from the adsorption of potential determining ions $H^+$ and $OH^-$, is zero. This value is of fundamental significance to the characterization of VCS [4]. For instance, if the soil pH is below $pH_0$, the variable charge sites will carry net positive charge. In contrast, if a soil pH is above $pH_0$, they will carry a net negative charge. Because the charge characteristics of VCS are largely dependent on soil pH, soil acidification often has severe consequences on the fertility of these soils. For example, the decrease in CEC, as a consequence of acidification, results in lower retention capacity for base cations which leads to the possibility of Al and/or Mn toxicities. Thus, it is essential to identify a soil's sensitivity to pH changes to establish appropriate soil pH management schemes.

Although VCS in its natural state maintain highly productive and diverse ecosystems, they pose a particular challenge to sustainable management in terms of low values of CEC at soil pH and rapid reduction in CEC, particularly base $CEC_B$, as soil acidity increases [5]. On the other hand, these soils (particularly in the subsoil or B horizon) develop appreciable AEC under acidic conditions and can retain leachable anions such as nitrate and sulphate [2]. Due to these intrinsic characteristics, surface charge properties are of central importance to the management of VCS. Therefore, it is essential to determine the *in situ* CEC and obtain a full

*Corresponding author: Email: chon.nq@iasvn.org

understanding of the variation of charge with pH before establishing strategies for sustainable management of these soils.

## Materials and methods

### *Soil collection and preparation*

Red soil derived from basalt rock (Rhodic Ferralsols, according to FAO/UNESCO soil classification) under maize cultivation was collected from the Chu Pah district, Gia Lai province, Vietnam, and used in this study. Two soil samples were taken from depths between 0-20 and 20-40 cm. Each soil sample at a particular depth was collected from three similar maize-cultivated fields with five different subsamples per field and was well mixed. The soil samples were air-dried and passed through a 2 mm-sieve before determining their charge characteristics and analysing the physicochemical properties of the soils. The study was conducted in the laboratory of the Institute of Agricultural Sciences of Southern Vietnam from March to August 2018. The clay contents and selected chemical characteristics of the soil are given in Table 1.

**Table 1. Clay contents and selected chemical characteristics of the studied soil.**

| Depths (cm) | Clay (%) | [1]TOC (%) | [2]$Al_{Ox}$ (%) | [3]$Fe_{Ox}$ (%) | [4]$Si_{Ox}$ (%) | [5]$Al_{Cryst.}$ (%) | [6]$Fe_{Cryst.}$ (%) |
|---|---|---|---|---|---|---|---|
| 0-20 | 62 | 2.50 | 0.31 | 0.28 | 0.01 | 1.8 | 14.1 |
| 20-40 | 65 | 1.55 | 0.38 | 0.34 | 0.01 | 2.6 | 16.6 |

[1]Total organic carbon; [2]Oxalate extractable Al; [3]Oxalate extractable Fe; [4]Oxalate extractable Si; [5]Crystalline Al; and [6]Crystalline Fe.

### *Analytical determinations*

The following methodologies were used to determine the properties of the soils: particle size analysis on dispersed samples as described by [6]; TOC by the 6B2B method [7]; oxalate extractable Fe, Al and Si ($Fe_{Ox}$, $Al_{Ox}$, and $Si_{Ox}$, respectively) by the 13A1 method [7]; and citrate bicarbonate dithionite Fe and Al ($Fe_{CBD}$ and $Al_{CBD}$, respectively) by the 13C1 method [7].

Charge fingerprints, which are the curves describing the charge characteristics of soil such as the total $CEC_T$, $CEC_B$, and AEC, were determined using methodology described by Gillman (2007) [8]. The charge characteristics of the soils were ascertained at a solution ionic strength (IS) similar to field conditions (IS=0.006; this is considered to be the typical IS of weathered tropical soils). As shown in Fig. 1, the pH values of the six suspensions of each soil sample were adjusted over the pH range of 4.0 to 7.0, i.e. 4.0, 4.6, 5.2, 5.8, 6.4, and 7.0, using 0.1 M HCl and 0.02 M $Ca(OH)_2$. The charge fingerprints can also determine the soil pH, the pH buffering capacity (pHBC), the point of zero charge ($pH_0$), and the PZNC [8].

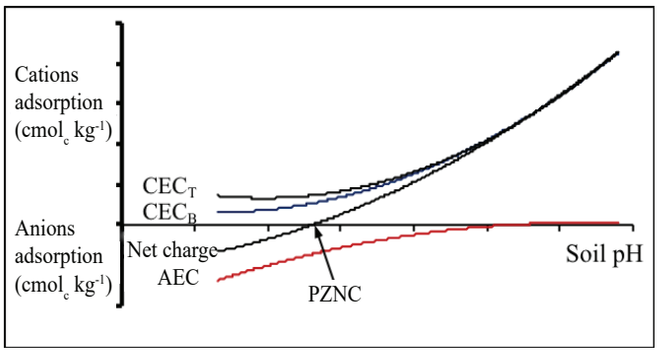


**Fig. 1. The charge fingerprints of the charge characteristics, consisting of the total cation exchange capacity ($CEC_T$), the base cation exchange capacity ($CEC_B$) and anion exchange capacity (AEC).**

### *Data analysis*

Charge fingerprint curves were plotted using Microsoft Office Excel. Charge characteristic values were calculated using the regression equations derived from the charge fingerprint curves. The general analysis of variance (ANOVA) and standard error of means were used to compare differences between the means of the charge fingerprint curves of the soil layers. Linear correlation coefficient (r) matrices were also computed for the various analyses of the soils to express the relationships of surface charge characteristics with soil properties. All analyses were undertaken by GenStat Discovery Edition 3 (7th edition).

## Results

The average pH of the soil was very low, being pH 4.40 and 4.26 in the topsoil (0-20 cm) and subsoil (20-40 cm), respectively (Table 2). The buffering capacity was high in the topsoil, 5.81 cmol$_c$ kg$^{-1}$ pH unit$^{-1}$, and reduced to 4.21 cmol$_c$ kg$^{-1}$pH unit$^{-1}$ in the subsoil. The $pH_0$ and PZNC in the top layer of the soil were not captured by the titration curve (Fig. 2A) or the net charge curve (Fig. 3A) within the pH range of 4.0 to 7.0. Therefore, the $pH_0$ value of the topsoil (3.81), shown in Table 1, was estimated by extrapolation of the regression equation of the curve (Fig. 2A). The $pH_0$ in the subsoil was 4.63 and markedly higher than that in the topsoil (3.81). This value was also higher than the existing soil pH (4.26) at this depth. In addition, the PZNC was identified in this layer as 4.88 which is higher than the $pH_0$ (Table 2).

**Table 2. Means and standard error of means (in brackets) for soil pH, $pH_0$, PZNC, and pHBC of the soil at different soil depths.**

| Soil depth (cm) | Soil pH (1:5) | $pH_0$ | PZNC | pHBC ($cmol_c\ kg^{-1}$ pH $unit^{-1}$) |
|---|---|---|---|---|
| 0-20 | 4.40 (±0.18) | 3.81 (±0.07) | [1]n.e. | 5.81 (±0.27) |
| 20-40 | 4.26 (±0.21) | 4.63 (±0.05) | 4.88 | 4.21 (±0.19) |

[1]Not estimated; ± values are standard errors of the average calculated from six subsamples within the pH range of 4.0 to 7.0.

**Table 3. Means and standard error of means (in brackets) for $CEC_B$, $CEC_T$ and AEC at soil pH of the soil at different soil depths.**

| Soil depth (cm) | $CEC_B$ ($cmol_c\ kg^{-1}$) | $CEC_T$ ($cmol_c\ kg^{-1}$) | AEC ($cmol_c\ kg^{-1}$) |
|---|---|---|---|
| 0-20 | 0.49 (±0.03) | 0.54 (±0.03) | -0.08 (±0.02) |
| 20-40 | 0.23 (±0.01) | 0.24 (±0.01) | -0.62 (±0.05) |

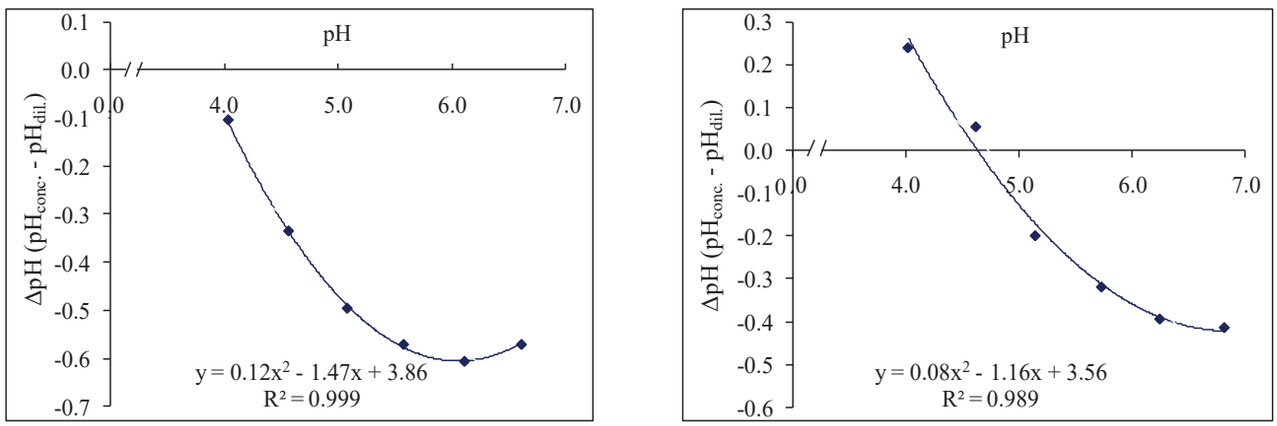


**Fig. 2. Point of zero charge ($pH_0$) of the soil (A) 0-20 cm, and (B) 20-40 cm.**
$pH_{conc.}$: pH concentrated suspension measured by 2 M $CaCl_2$ solution; $pH_{dil.}$: pH diluted suspension measured by 0.002 M $CaCl_2$ solution.

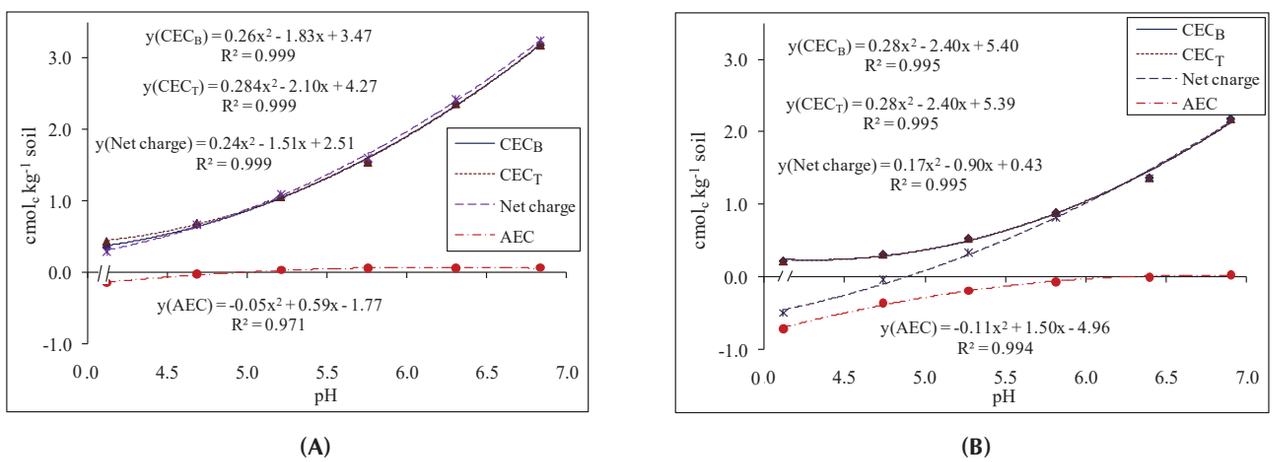


**Fig. 3. Charge characteristics of the soil (A) 0-20 and (B) 20-40 cm.**

Both $CEC_B$ and $CEC_T$ were extremely low at the pH of the existing soil; approximately 0.50 $cmol_c\ kg^{-1}$ for the topsoil and 0.25 $cmol_c\ kg^{-1}$ for the subsoil (Table 3). Over the entire pH range, the $CEC_B$ and $CEC_T$ were nearly identical, particularly in the case of the subsoil (Fig. 2B). The soil had positive charges (AEC) in both layers (Table 3). At soil pH, the AEC is -0.62 $cmol_c\ kg^{-1}$ in the subsoil, which was higher than that of the topsoil (-0.08 $cmol_c\ kg^{-1}$).

Surface charge characteristics of the soil are presented in Table 4. The total net charge had a very low value of <0.5 $cmol_c\ kg^{-1}$ in the topsoil. Although a net negative charge was found in the topsoil, the subsoil exhibited a net positive charge, i.e., a net AEC. The soil is dominated by variable charge surfaces in both soil layers, with variable charge accounting for more than 50% of the total net charge (Table 4).

**Table 4. Means and standard error of means (in brackets) for total net charge, net permanent and net variable charge of the soil at different soil depths.**

| Soil depth (cm) | Total net charge ($cmol_c\ kg^{-1}$) | Net permanent charge ($cmol_c\ kg^{-1}$) | Net variable charge ($cmol_c\ kg^{-1}$) | Percentage of variable charge (%) |
|---|---|---|---|---|
| 0-20 | 0.46 (±0.02) | 0.20 (±0.09) | 0.26 (±0.11) | 56.5 |
| 20-40 | -0.39 (±0.05) | -0.18 (±0.03) | -0.21 (±0.02) | 53.8 |

## Discussion

### *Variations in soil pH and pH buffering capacity*

Soil pH is the most important factor influencing the surface charge of VCS. The quantity of variable charge on a surface is determined by both the dissociation of $H^+$ ions from the surfaces and the adsorption of $H^+$ ions by the hydroxylated surface as a function of pH of the medium. Therefore, in order to determine the surface charge of a given soil; the existing pH of that soil should be taken into account.

The average pH of the soil in this study ranged from 4.26 to 4.40, classifying the soil as very acidic, which is within the typical pH range of highly weathered soils in tropical regions [9, 10]. Perhaps because of the lower pHBC of the subsoil relative to the surface layers, we find the pH value of the subsoil to be lower than that of the topsoil (Table 2). One reason for this is the response of the subsoil to a given proton sink from weathering processes and land use [11, 12].

Many researchers have found that OM and clay content are the two most important factors influencing pHBC [1, 13, 14]. Buffering capacity is also associated with oxide content [1] and the amount of variable charge [1, 5, 15]. All these authors indicated that pHBC increased with increasing content of OM, clay, and sesquioxide, and with greater amounts of variable charge. Our pHBC results are interpreted in the light of these findings. Table 5 indicates that pHBC is highly correlated ($p<0.01$) with TOC and $Fe_{Ox}$. The pHBC values of the soil decreased with increasing soil depth (Table 2) and this is attributed to the smaller amounts of TOC contained in the subsoil (Table 1). Additionally, in studies on 40 acidic surface soils from Queensland, Aitken, et al. (1990) [16] found that the buffering capacity was significantly ($p<0.001$) correlated with TOC and clay content ($R^2=0.88$), with TOC being the most important factor. Thus, from the results of the present study, it can be concluded that OM is an important factor responsible for pHBC.

**Table 5. Linear correlation coefficient (r) for the relationships between selected soil properties and pH buffering capacity and surface charge characteristics.**

| | [1]TOC | Clay | [2]$Al_{Ox}$ | [3]$Fe_{Ox}$ | [4]$Si_{Ox}$ | [5]$Al_{Cryst.}$ | [6]$Fe_{Cryst.}$ |
|---|---|---|---|---|---|---|---|
| $pH_0$ | 0.09 | 0.81* | 0.32 | -0.03 | -0.30 | 0.54 | 0.60 |
| $\Delta CEC_{4.5\text{-}5.5}$ | 0.69 | 0.09 | 0.73* | 0.84** | -0.20 | 0.11 | -0.01 |
| pHBC | 0.96*** | 0.23 | 0.75* | 0.95*** | -0.62 | 0.57 | 0.39 |

*: $p<0.05$; **: $p<0.01$; ***: $p<0.001$; [1]Total organic carbon; [2]Oxalate extractable Al; [3]Oxalate extractable Fe; [4]Oxalate extractable Si; [5]Crystalline Al, and [6]Crystalline Fe.

### *Variations in surface charge characteristics*

The $pH_0$ of VCS is considered to be of essential significance because its position relative to the existing soil pH determines the CEC and AEC of the soil. In addition, $pH_0$ can be used to estimate the net permanent charge of a soil if it is located within the pH range of the charge fingerprint curves [8, 17].

Generally, $pH_0$ decreases with increasing OM and increasing amounts of minerals having substantial isomorphous substitution (i.e. negatively charged materials). $pH_0$ also tends to increase with increasing amounts of Fe and Al hydrous oxides [18] as these materials carry some positive charge at low pH [19]. In the present study, the subsoil was very low in TOC content (1.55%) and very high in Fe hydrous oxides (16.6%) (Table 1). Consequently, the subsoil exhibited a high value for $pH_0$ (4.63) and it was higher than the soil pH (4.26) (Table 2), leading to the net positive charge surface at soil pH as indicated by high AEC (-0.62 $cmol_c\ kg^{-1}$) and very low CEC (0.23 $cmol_c\ kg^{-1}$) (Table 3). This result is consistent with the work of Gillman (1985) [4] for oxidic soils from north Queensland and Anda, et al. (2008) [10] for Malaysian Oxisols, which suggested that OM together with iron oxides influenced $pH_0$ by masking mineral surfaces. All these authors concluded that $pH_0$ was reduced by about one unit for each one percent increase in organic carbon. These results are also strongly supported by the finding of Gillman (1984) [20] on another VCS from the wet tropical coast of north Queensland under sugarcane cultivation. This author found that the increase in $pH_0$ values with soil depth reflected the rapid decrease in OM and dominance of oxidic minerals such as goethite and hematite in the clay fraction.

The greater amount of AEC in the subsoil reflects the influence of Fe and Al hydrous oxides, which are positively charged below their points of zero charge [5]. Thus, even though soil pH values did not alter appreciably with soil

depth, $pH_0$ values well above soil pH indicated that the variable charge components of the soil would be positively charged. In consequence, the negative charge was very low, and the loss of CEC with an associated increase in acidity resulted in the loss of basic cations such as calcium, magnesium, and potassium from the exchange complex [1, 20, 21]. On the other hand, an appreciable amount of positive charge (AEC) would be beneficial to the prevention of the leaching of anion nutrients such as sulphate and nitrate, thus mitigating contamination of groundwater [20, 22].

The interesting result observed in this study is that the subsoil layer exhibited a PZNC of 4.88 (Table 2), higher than the $pH_0$ value (4.63), reflecting that the soil generated a permanent positive charge that accounted for -0.18 $cmol_c$ $kg^{-1}$ out of -0.39 $cmol_c$ $kg^{-1}$ of the total net positive charge (Table 4). This result usually occurs in highly weathered soil, particularly oxide-rich Oxisols/Ferralsols, and is in agreement with the theory of charge characteristics of soils with variable and permanent charge minerals [17]. Permanent positive charge was also found in the lower subsoils from north Queensland [23], and also in the B horizon (35-45 cm) of a Dystrandept (a volcanic ash soil) in Papua New Guinea [24].

Delta $CEC_{4.5\text{-}5.5}$ (ΔCEC, expressed as the change of $CEC_T$ with one unit pH change) was significantly ($p<0.05$) positively correlated with TOC, $Al_{Ox}$, and $Fe_{Ox}$ (Table 5). This indicates that the main sites for variable negative charge generation with pH increases are mainly associated with the soil OM and amorphous Fe and Al hydrous oxides. Aitken, et al. (1990) [16] also found a significant correlation of ΔCEC with TOC and clay content in a diverse suite of acidic soils. These authors suggested that the extent of deprotonation of functional organic groups and variable charge minerals (such as hydrous oxides of Fe and Al) as pH increases determines the increase in net negative charge on surfaces, and this increase is reflected in the magnitude of ΔCEC.

## Conclusions

Variable charge soil (Rhodic Ferralsols) from the Central Highlands poses several constraints to crop production, such as extreme acidity and very low CEC, and these problems are more pronounced in the subsoil. In particular, the subsoil exhibits higher $pH_0$ than the existing soil pH and higher PZNC than $pH_0$. Therefore, the soil has developed a net positive surface charge due to its AEC exceeding its CEC. These properties are attributed to TOC and Fe/Al hydrous oxides in the clay fraction, which significantly affect pHBC and delta CEC. In addition, OM has a great influence on the $pH_0$ of variable charge components, and thus on CEC. Consequently, OM addition to the soil will be an important management strategy to improve soil fertility.

The authors declare that there is no conflict of interest regarding the publication of this article.

## REFERENCES

[1] G. Uehara, J. Keng (1975), "Management implications of soil mineralogy in Lantin America", *Soil Management in Latin America*, New York.

[2] N.P. Qafoku, E.V. Ranst, A. Noble, G. Baert (2004), "Variable charge soils: Their mineralogy, chemistry and management", *Advances in Agronomy*, **84**, pp.159-215.

[3] P.W. Moody, P.T. Cong (2008), *Soil Constraints and Managament Package (SCAMP): Guidelines for Sustainable Management of Tropical Upland Soil*, Australian Centre for International Agricultural Research.

[4] G.P. Gillman (1985), "Influence of organic matter and phosphate content on the point of zero charge of variable charge components in oxidic soils", *Australian Journal of Soil Research*, **23(4)**, pp.643-646.

[5] G.P. Gillman, E.A. Sumpter (1986), "Surface charge characteristics and lime requirements of soils derived from basaltic, granitic, and metamorphic rocks in high-rainfall tropical Queensland", *Australian Journal of Soil Research*, **24(2)**, pp.173-192.

[6] P. Thorburn, R. Shaw (1987), "Effects of different dispersion and fine fraction determination methods on results of routine particle size analysis", *Australian Journal of Soil Research*, **25(4)**, pp.347-360.

[7] G. Rayment, D. Lyons (2011), *Soil Chemical Methods-Australasia*, CSIRO Publishing, Collingwood, Victoria.

[8] G.P. Gillman (2007), "An analytical tool for understanding the properties and behaviour of variable charge soils", *Australian Journal of Soil Research*, **45**, pp.83-90.

[9] G. Uehara, G.P. Gillman (1981), "The mineralogy, chemistry, and physics of tropical soils with variable charge clays", *Westview Press Inc.*, Boulder, Colorado.

[10] M. Anda, J. Shamshuddin, C.I. Fauziah, S. Syed Omar (2008), "Mineralogy and factors controlling charge development of three Oxisols developed from different parent materials", *Geoderma*, **143(1-2)**, pp.153-167.

[11] D. Rowell, A. Wild (1985), "Causes of soil acidification: a summary", *Soil Use and Management*, **1(1)**, pp.32-33.

[12] A. Aweto, O. Obe, O. Ayanniyi (1992), "Effects of shifting and continuous cultivation of cassava (*Manihot esculenta*) intercropped with maize (*Zea mays*) on a forest alfisol in south-western Nigeria", *Agricultural Science*, **118(2)**, pp.195-198.

[13] B. Bache (1988), "Measurements and mechanisms in acid soils", *Communications in Soil Science and Plant Analysis*, **19(7-12)**, pp.775-792.

[14] T. Dickson, R.L. Aitken, P.W. Moody (1998), "Field amelioration of acidic soils in south-east Queensland. II. Effect of amendments on soil properties", *Australian Journal of Agriculture Research*, **49(4)**, pp.627-637.

[15] K. Oorts, B. Vanlauwe, J. Pleysier, R. Merckx (2004), "A new method for the simultaneous measurement of pH-dependent cation exchange capacity and pH buffering capacity", *Soil Science Society of America Journal*, **68(5)**, pp.1578-1585.

[16] R.L. Aitken, P.W. Moody, P.G. McKinley (1990), "Lime requirement of acidic Queensland soils. I. Relationship between soil properties and pH buffer capacity", *Australian Journal of Soil Research*, **28(5)**, pp.695-701.

[17] G. Uehara, G.P. Gillman (1980), "Charge characteristics of soils with variable and permanent charge minerals: I. Theory", *Soil Science Society of America Journal*, **44(2)**, pp.250-252.

[18] R.L. Parfitt (1980), *Chemical Properties of Variable Charge Soils*, *Soils with variable charge*, New Zealand Society of Soil Science, Lower Hutt, pp.167-193.

[19] M.E. Sumner (1963), "Effect of iron oxides on positive and negative charges in clays and soils", *Clay Minerals Bulletin*, **5(29)**, pp.218-226.

[20] G.P. Gillman (1984), "Using variable charge characteristics to understand the exchangeable cation status of oxic soils", *Australian Journal of Soil Research*, **22(1)**, pp.71-80.

[21] A. Noble, G.P. Gillman, S. Nath, R. Srivastava (2001), "Changes in the surface charge characteristics of degraded soils in the wet tropics through the addition of beneficiated bentonite", *Australian Journal of Soil Research*, **39(5)**, pp.991-1001.

[22] M.J. Eick, W.D. Brady, C.K. Lynch (1999), "Charge properties and nitrate adsorption of some acid Southeastern soils", *Environmental Quality*, **28(1)**, pp.138-144.

[23] G.P. Gillman, G. Uehara (1980), "Charge characteristics of soils with variable and permanent charge minerals: II. Experimental", *Soil Science Society of America Journal*, **44(2)**, pp.252-255.

[24] P. Bleeker, R. Sageman (1990), "Surface charge characteristics and clay mineralogy of some variable charge soils in Papua New Guinea", *Australian Journal of Soil Research*, **28(6)**, pp.901-917.

DOI: 10.31276/VJSTE.62(2).71-76



# Comparison of the SSSperm testing kit with the Halosperm testing kit in an analysis of sperm DNA fragmentation

**Le Thi Quyen, Nguyen Thi Minh Thu, Le Thi Minh Phuong, Nguyen Thi Trang***

*Hanoi Medical University*

Received 18 April 2020; accepted 21 May 2020

***Abstract:***

**The objectives of this work were to accurately evaluate testing kits that analyse sperm DNA fragmentation in infertile men and to provide a comparison of an improved testing kit (SSSperm testing kit) to the existing Halosperm testing kit in an analysis of sperm DNA fragmentation. A cross-sectional study was conducted on 300 semen samples from infertile men with a sperm concentration ≥1 million/ml using the Bland-Altman, T-test, and Pearson test for statistical study. The SSSperm testing kit had a coefficient of variation of CV%=2.26%<5% and $t_{tn}$=0.97<$t_c$=2. The two methods have similar DNA fragmentation index (DFI) results (r=0.995; p<0.001). The difference between the results of the two kits was not statistically significant (p=0.236>0.05). In conclusion, the SSSperm testing kit for the analysis of sperm DNA fragmentation is qualified as determined from quantitative tests, and the SSSperm testing kit is equivalent to the Halosperm testing kit.**

***Keywords:*** **comparison, DFI, improved test kit, infertile, sperm DNA fragmentation.**

***Classification number:*** **3.2**

## Introduction

Infertility is defined as the inability to achieve a clinical pregnancy after at least 12 months of regular unprotected intercourse [1]. Recently, infertility cases have quickly increased and has become a global health problem [2]. Globally, there are an estimated 15% of married couples affected by infertility and male infertility accounts for 30-40% of these cases [3, 4]. Male infertility can be initiated by testicular injury, sperm deficiency, or hormone problems [5], while one of the most prominent causes is sperm DNA fragmentation, which affects sperm function and male reproductive health [6].

Today, several methods of testing sperm DNA fragmentation exist such as COMET, TUNEL, SCSA, and SCD, but these methods require high-tech equipment, complex techniques, and high cost [7, 8].

In 2003, Fernández and partners proposed the sperm chromatin dispersion (SCD) test to determine sperm DNA fragmentation. This method is based on the principle that sperm without DNA fragmentation will form large halos around their nucleus, while sperm with DNA fragmentation will not produce halos or will produce very small halos around its nucleus when it is denatured in acidic environment and the nuclear protein is removed [9]. Based on this principle, Fernández and partners created the Halosperm testing kit in 2005 [10]. Since then, many studies of sperm DNA fragmentation using the SCD method or the Halosperm testing kit have been published and contributed significantly to the diagnosis and treatment of male infertility.

In Vietnam, some hospitals and research institutes have used the Halosperm kit to diagnose sperm DNA fragmentation, but the import cost of Halosperm is still high and thus not suitable for many patients. For this reason, our research team has built the SSSperm testing kit and evaluated the accuracy of the kit to determine the degree of sperm DNA fragmentation by the SCD method with the goal

*Corresponding author: Email: trangnguyen@hmu.edu.vn

of completing the process and cutting the costs while still ensuring quality assessment of the degree of sperm DNA fragmentation in Vietnamese men. However, presently in Vietnam there does not exist a homemade kit that can both ensure the completeness as well as the accuracy of the level of sperm DNA fragmentation. Therefore, we conducted this research with the aim of evaluating the equivalency of the SSSperm testing kit and the Halosperm testing kit using the Bland-Altman, T-test, and Pearson tests.

## Subjects and research method

### *Subjects*

Three hundred semen samples from male patients who were diagnosed with infertility at the Hanoi Medical University Hospital were tested and assessed for sperm DNA fragmentation at the Genetic Counselling Centre, Hanoi Medical University Hospital.

The selection criteria for this study consisted of male patients aged from 18 years old whose semen analysis had a sperm density ≥1 million/ml and agreed to participate in the research.

The exclusion criteria for this study was male patients who do not meet the above criteria, have genital cancer, are infected with HIV, syphilis, or gonorrhoea, have an acute disease or mental illness, or did not agree to participate in the research.

### *Research methods*

*Sample size:* to complete the procedure and determine the accuracy of this study, the following formula was used to calculate sample size for a descriptive research according to Lwanga and Lemeshow (1991) [11]:

$$n = Z^2_{1-\alpha/2}\,\frac{1-p}{\epsilon^2 p}$$

in which $Z_{(1-\alpha/2)}$: reliability coefficient (with 95% confidence, $Z_{(1-\alpha/2)}$=1.96); ε=0.10; p=95% (accuracy of reference procedure); n: number of required experiments, which was calculated to be 21 and was rounded up to 50.

To compare the SSSperm testing kit with the Halosperm testing kit, we used the following formula to calculate sample size:

$$n = Z^2_{\left(1-\frac{\alpha}{2}\right)} x\,\frac{p(1-p)}{(\varepsilon p)^2}$$

in which $Z_{(1-\alpha/2)}$: reliability coefficient (with 95% confidence, $Z_{(1-\alpha/2)}$=1.96); p=25% according to the research of Duran, et al. (2002) [12], where the rate of high sperm DNA fragmentation was >30% and had p=25%. For ε, we selected 0.2. Therefore, $n=1.96^2\times0.25\times(1-0.25)/(0.2\times0.25)^2=288.12$, which was rounded to 300. Thus, a sample size of 300 was used.

*Research design:* a cross-sectional study.

*Method of making templates:* the test (using the SSSperm testing kit) was an improvement of Fernandez, et al.'s SCD procedure (2005) [10] using the Halosperm kit from Halotech as follows:

Step 1. Preparation of agar: an agarose Eppendorf tube was placed into the float and melt using a water bath at 95-100°C for 5 min or in microwave for 3 min, until it was completely melted. The semen samples were diluted with a PBS solution such that the concentration of sperm was approximately <15 million/ml. The agarose tube was kept at 37°C for 5 min until the temperature of the Eppendorf-containing agar and of the incubator was balanced.

Step 2. Preparation of cell suspension: 25 µl of semen was added to an agarose tube and mixed well with a pipette. The tube was kept at 37°C while quickly moving on to the next step, in order to avoid solidification of the agarose. A drop of 25 µl of cell suspension was dripped on the circular position of the microscope slide, the slide was covered and gently pressed in order to prevent air bubbles from appearing. The slide was held horizontally throughout the entire process. The slide was placed in a refrigerator at 4°C for 10 min to allow the agarose to solidify.

Step 3. After the cell suspension was solidified, the slide was removed from the refrigerator and the microscope slide cover was removed by gently sliding it off of the slide. The denaturation of the sperm DNA was prepared by placing 80 µl of denaturing solution into a tube containing 10 ml of distilled water and shaking well. The slide with the sperm DNA was placed on the tray containing the denaturing solution for 7 min.

Step 4. Cell lysis: the slide was removed from the denaturing solution and placed in a tray containing 10 ml of lysis solution for 5 min.

Step 5. Wash the lysis solution: after finishing the lysis, the slide was placed in a tray containing distilled water for 5 min to wash off the lysis solution.

Step 6. Dehydration: the sample was dehydrated by adding the slide to an alcohol solution for 6 min, then allowing it to air dry.

Step 7. Dye the slide: the slide was placed horizontally and a Giemsa solution 5-30% was added dropwise to the surface of the slide. Then, it was left at room temperature for 10 min and washed with water from the tap. Excessively washing was avoided, which can lighten the halo colour.

***Data processing***

*Evaluation of results:* the microscope slide was observed under an optical microscope and at least 500 sperms were counted on the slide to determine the degree of sperm DNA fragmentation. Sperm DNA fragmentation was determined by sperm halo according to Fernandez, et al.

The rate of DNA fragmentation or DNA fragmentation index (DFI) was determined by the following formula:

$$\frac{sperms\ having\ small\ halo + sperms\ having\ no\ halo + degenerative\ sperms}{Total\ counted\ sperms} \times 100\%$$

*Data analysis:* to evaluate the accuracy of the SSSperm testing kit, two indicators were used: trueness and precision [13] (see Fig. 1).

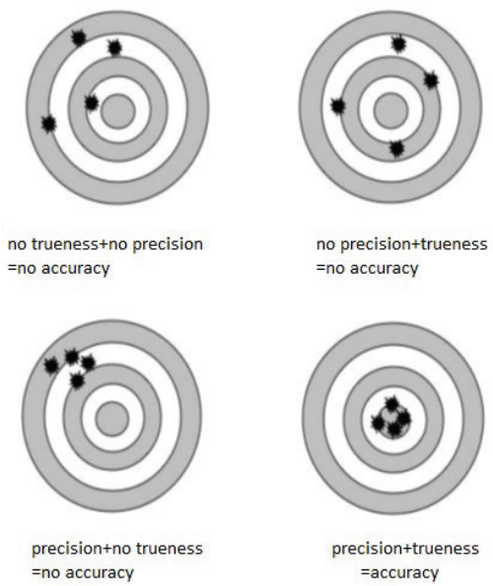


**Fig. 1. Illustration of accuracy** [13].

Precision is the degree of variation of independent test results around the mean. Precision is a qualitative concept and is expressed quantitatively by standard deviation or coefficient of variation. The lower the precision is, the larger the standard deviation or coefficient of variation. The formulae for standard deviation and coefficient of variation are, respectively,

$$SD=\sqrt{\frac{\sum(X_i-\overline{x})^2}{n-1}}$$

$$RSD\%=CV\%=\frac{SD}{\overline{X}}X100$$

in which SD: standard deviation; n: number of experiments; $x_i$: calculated value of the $i^{th}$ experiment; $\overline{X}$: the mean value of the experiments; RSD%: relative standard deviation; and CV%: coefficient of variation.

Precision can be classified into four cases:

- Repeatability: repeatability expresses the degree of accuracy or repeatability, the degree of variation among experiment results which are done in the same laboratory with the same sample homogeneity, and by the same inspector over the same period of time. Repeatability is determined by the following method: on a patient's semen sample, an improved kit (SSSperm kit) is used to determine the degree of sperm DNA fragmentation and this is repeated 10 times. The standard deviation and coefficient of variation is calculated with a CV requirement ≤5%.

- Intermediate precision: the accuracy of the method is expressed according to the variables of laboratory. For several days, with different inspectors, and with different tools, the intermediate precision was found.

- Reproducibility: the accuracy of many laboratories conducting studies on the same homogeneous sample is expressed by reproducibility. Similar to repeatability, reproducibility is necessary provided that the laboratory or method is changed.

- Trueness: this indicates the degree of proximity between the mean of the experimental results and the real value, or accepted value.

Method to determine accuracy: on a patient's semen sample, from which the degree of sperm DNA fragmentation was determined with the Halosperm kit, the same experiment was conducted by using the SSSperm testing kit and repeated 10 times. The mean value and standard deviation were calculated, from which the standard, $t_{tn}$, was calculated using the following formula and then compared with Halosperm kit:

Công thức tính $t_{tn}$:

$$t_{tn}=\frac{|\mu-\overline{x}|}{\sqrt{\frac{s^2}{n}}}$$

in which: $t_{tn}$: experimental t value; μ: real value or accepted value (reference); $\overline{x}$: mean of experimental method; $S^2$: variance of experimental method; n: number of experimental times.

To compare the SSSperm testing kit with the Halosperm testing kit, the difference between the two tests was investigated based on Pearson correlation analysis, T-test, and a Bland-Altman plot using Epidata and SPSS.20 software.

### *Ethical research*

All the patients' information was kept confidential and only analysed for fertility counselling for the patients and for this study, and not for any other purpose.

## Results and discussion

### *Results*

Accuracy evaluation of testing kit analysis of sperm DNA fragmentation in infertile men: a semen sample that had its DFI identified previously by using Halosperm kit, an improved kit (SSSperm kit) was used to determine the degree of sperm DNA fragmentation, and this was repeated 10 times. The results are in Table 1.

**Table 1. Results of the test to determine the accuracy of the SSSperm kit.**

| Experiment | DFI (%) |
|---|---|
| 1st | 15.4 |
| 2nd | 15.0 |
| 3rd | 14.4 |
| 4th | 14.2 |
| 5th | 15.2 |
| 6th | 15.2 |
| 7th | 15.2 |
| 8th | 15.0 |
| 9th | 14.6 |
| 10th | 15.0 |
| Proof (made of Halo kit) | 14.8 |

*Precision:* because the tests were conducted in the laboratory, we calculated the precision through repeatability. From the above results, Table 2 presents the results of the precision evaluation.

**Table 2. Results of precision evaluation.**

| The mean of DFI (%) | 14.92 |
|---|---|
| SD | 0.391 |
| CV% | 2.62% |

In the experiments, especially during the quantitative tests, there are many errors that can affect the test and lead to inaccuracy of the results. Therefore, to control these confounding factors, it is necessary to use the concept of precision. The precision described in these results only depends on random errors and does not relate to the actual results of the sample. The lower the precision, the larger the standard deviation or coefficient of variation, otherwise, the greater the precision, the smaller the coefficient of variation is [13]. In this study, the SSSperm kit showed repeatability with a coefficient of variation CV%=2.62%. Therefore, the coefficient of variation had a value less than 5%, which, according to the Vietnam Standards [13] indicates that repeatability of this procedure meets requirements. Thus, when there are influences of random error factors for the same sample, the degree of sperm DNA fragmentation determined under different conditions has errors within the acceptable range.

Compared with the commercial Halosperm kit created by Fernandez, which has an actual coefficient of variation of 5.3% [14], the SSSperm kit has a lower coefficient of variation. This proves that the SSSperm kit meets the standards of a testing kit.

*Trueness:* the trueness indicates the degree of proximity between the mean values of the experimental results and the real values or accepted values. In the experiment to test trueness, we calculated $t_{tn}$=0.97. Besides, through searching tables, $t_c$=2.262 [13]. Thus $t_{tn}<t_c$. This means that the sperm DNA fragmentation index determined by the SSSperm kit has the same results as the commercial Halosperm kit and the process achieves the accuracy requirements of the analysis. Thus, the precision and trueness of the SSSperm kit completely meet the requirements of a testing kit according to Vietnamese Standards. This was the first step of the project.

Comparison of the SSSperm kit with the Halosperm kit: we have developed an improved procedure for determining the level of sperm DNA fragmentation, which is different from the Halosperm testing kit at the following key points (see Table 3).

**Table 3. Improvements in techniques for testing sperm DNA fragmentation.**

| | **Fernandez, et al. (2003)** [9] | **SSSperm testing kit** |
|---|---|---|
| Denaturing solution | Denaturing solution of kit | HCl 0.29% |
| Lysis solution | Lysis solution 1: 0.4 M Tris-HCl; 0.8 M DTT; 50 mM EDTA; 1% SDS, pH 7.5.<br>Lysis solution 2: 0.4 M Tris -HCl; 2 M NaCl; 1% SDS, pH 7.5 | 0.2 M Tris; 0.1 M DTT 2 M NaCl; 1% Triton, pH 7.5 |
| Dehydration | 3 steps with alcohol 70%, 90% and 100% | 1 step with alcohol 100% |
| Dyes | Wright | Giemsa |

After completing the SSSperm testing kit, we took 300 semen samples to make templates and assessed the degree of sperm DNA fragmentation by using the Halosperm testing kit and the SSSperm testing kit. The results are shown in the following chart (Fig. 2):

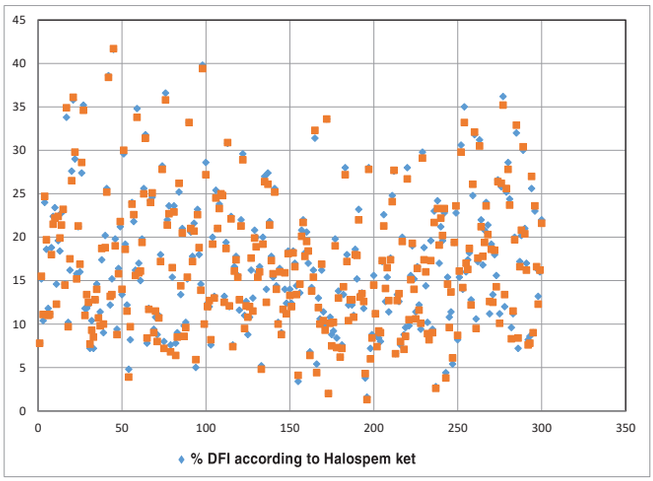


**Fig. 2. Comparison of sperm DNA fragmentation rate determined by using Halosperm kit with SSSperm kit.**

The value of the sperm DNA fragmentation index (DFI) measured by the Halosperm commercial kit and the SSSperm testing kit are almost similar. To compare the two kits quantitatively, we use the Pearson test, T-test, and Bland - Altman plot (Tables 4 and 5).

**Table 4. Testing correlation coefficient between two kits.**

| | | |
|---|---|---|
| **N** | | **300** |
| Pearson correlation coefficient | | 0.995 |
| **P** | | **<0.001** |
| Confidence interval 95% | Upper limit | 0.996 |
| | Lower limit | 0.994 |

The Pearson test shows a strong and significant correlation between the sperm DNA fragmentation index measured by the SSSperm testing kit and commercial Halosperm kit with r=0.995 and p<0.001.

**Table 5. T-test table.**

| t | P | The mean of the difference | Confidence interval 95% | |
|---|---|---|---|---|
| | | | *Lower limit* | *Upper limit* |
| 1.187 | 0.236 | -0.010 | -0.003 | 0.011 |

The results of the level of sperm DNA fragmentation assessment by the SSSperm kit and by the commercial Halosperm kit do not have statistically significant differences within a 95% confidence level (p=0.236>0.05).

The Bland-Altman plot is used to quantify the compatibility between two different measurements or to compare a new test with a standard recognized test. From the above tests, we have built a Bland-Altman plot showing the compatibility between measurement results of two tests (Fig. 3).

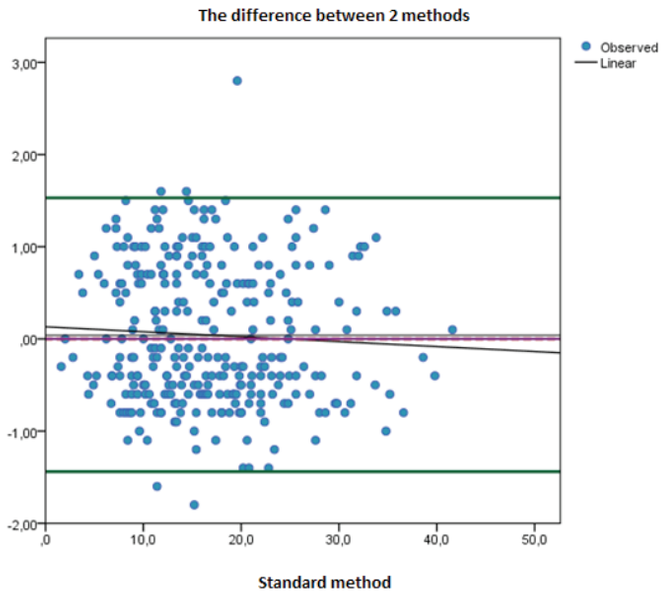


**Fig. 3. Bland-Altman plot showing the compatibility of the two measurement methods.**

The difference between the mean of the two kits is very small (0.042). Most cases have errors within the limit of ±1.96 standard deviations. Therefore, the SSSperm kit and commercial Halosperm kit have the same value in determining the degree of sperm DNA fragmentation.

### *Discussion*

Sperms with fragmented DNA are unable to produce a halo of dispersed DNA loops while normal sperms succeed in producing the halo after treatment with a denaturing agent and removal of the nuclear proteins. Based on this principle, we created an improved test (using the SSSperm kit) to determine sperm DNA fragmentation.

There are advantages of the SSSperm kit and notable differences between the improved test and other existing tests. For example, the improved test is a quantitative test. Unlike semi-quantitative tests like COMET and TUNEL, which determine sperm DNA fragmentation by colour and fluorescence intensity, the improved test determines sperm DNA fragmentation by measuring the percentage of sperms with non-dispersed (have no halo or small halos) or dispersed DNA loops (have large halos), which can be observed with the naked eye.

The Halosperm testing kit is also based on the principle that sperm with fragmented DNA fail to produce halos while normal sperm produce large halos, which was published by Fernandez, et al. in 2003. There have been some studies conducted to evaluate the value of this kit [9]. The results obtained from these studies indicated that this testing kit meets the accuracy requirement to

determine sperm DNA fragmentation and thus it has been widely used in diagnosing male infertility, especially in Vietnam. However, the price of this kit is still high, which is not suitable for many Vietnamese citizens. Therefore, we created an improved testing kit (SSSperm testing kit) which is simpler and cheaper than the Halosperm testing kit but still ensures quality results. When the Pearson test, T-test, and Bland-Altman plot was used to compare the SSSperm testing kit with the Halosperm testing kit, the results indicated that there were significant correlations between the two kits ($r=0.995$, $p<0.001$) and the mean of difference was -0.01, $p=0.236>0.05$, therefore the difference was not statically significant.

In conclusion, the improved test is accurate, fast, inexpensive, and simple. Therefore, the SSSperm testing kit should be used as a routine kit in Vietnam to determine sperm DNA fragmentation in infertile men.

## Conclusions

The SSSperm testing kit has the required accuracy of a quantitative testing kit (with CV%=2.62%<5% and $t_{tn}=0.97<t_c$).

The results obtained from the improved kit is equivalent to the commercial Halosperm kit. Differences in the results obtained from the two methods are not statistically significant and are completely random.

## ACKNOWLEDGEMENTS

Our research team would like to thank our colleagues at the Genetic Counselling Centre, Hanoi Medical University Hospital.

The authors declare that there is no conflict of interest regarding the publication of this article.

## REFERENCES

[1] WHO (2020a), *Revised Glossary on Assisted Reproductive Terminology (ART)*, https://www.who.int/reproductivehealth/publications/infertility/art_terminology2/en/, [cited 2020 Jan 19].

[2] WHO (2020b), *Infertility is A Global Public Health Issue*, http://www.who.int/reproductivehealth/topics/infertility/perspective/en/, [cited 2020 Jan 19].

[3] A. Agarwal, A. Mulgund, A. Hamada, M.R. Chyatte (2015), "A unique view on male infertility around the globe", *Reprod. Biol. Endocrinol.*, **13**, DOI: 10.1186/s12958-015-0032-1.

[4] A. Zeqiraj, S. Beadini, N. Beadini, H. Aliu, Z. Gashi, S. Elezaj, et al. (2018), "Male infertility and sperm DNA fragmentation", *Open Access Maced. J. Med. Sci.*, **6(8)**, pp.1342-1345.

[5] NIH (2020), *What are Some Possible Causes of Male Infertility?* https://www.nichd.nih.gov/health/topics/infertility/conditioninfo/causes/causes-male, [cited 2020 Jan 19].

[6] A. Agarwal, M.K.P. Selvam, S. Baskaran, C-L. Cho (2019), "Sperm DNA damage and its impact on male reproductive health: a critical review for clinicians, reproductive professionals and researchers", *Expert Rev. Mol. Diagn.*, **19(6)**, pp.443-457.

[7] J. Ribas-Maynou, A. García-Peiró, A. Fernández-Encinas, C. Abad, M.J. Amengual, E. Prada, et al. (2013), "Comprehensive analysis of sperm DNA fragmentation by five different assays: TUNEL assay, SCSA, SCD test and alkaline and neutral comet assay", *J. Andrology*, **1(5)**, pp.715-722.

[8] D. Sakkas, J.G. Alvarez (2010), "Sperm DNA fragmentation: mechanisms of origin, impact on reproductive outcome, and analysis", *Fertil. Steril.*, **93(4)**, pp.1027-1036.

[9] J.L. Fernández, L. Muriel, M.T. Rivero, V. Goyanes, R. Vazquez, J.G. Alvarez (2003), "The sperm chromatin dispersion test: a simple method for the determination of sperm DNA fragmentation", *J. Androl.*, **24(1)**, pp.59-66.

[10] J.L. Fernandez, L. Muriel, V. Goyanes, et al. (2005a), "Simple determination of human sperm DNA fragmentation with an improved sperm chromatin dispersion test", *Fertil. Steril.*, **84(4)**, pp.833-842.

[11] S.K. Lwanga, S. Lemeshow (1991), *Sample Size Determination in Health Studies, A Practical Manual*, WHO, Geneva.

[12] E.H. Duran, M. Morshedi, S. Taylor, et al. (2002), "Sperm DNA quality predicts intrauterine insemination outcome: a prospective cohort study", *Hum. Reprod.*, **17(12)**, pp.3122-3128.

[13] Vietnam Ministry of Science and Technology (2015), *Vietnam Standard -TCVN 10863:2015, ISO/TS 22971:2005 of the Accuracy (Trueness and Precision) of Measurement Method and Measurement Result - Pracrical Guidance for Use TCVN 6910-2:2001 (ISO 5725-2:1994) in Designing, Implementing and Statistically Analysing Interlaboratory Repeatability and Reproducubility Results.*

[14] J.L. Fernandez, L. Muriel, V. Goyanes, et al. (2005b), "Halosperm® is an easy, available, and cost-effective alternative for determining sperm DNA fragmentation", *Fertil. Steril.*, **84(4)**, p.860.

DOI: 10.31276/VJSTE.62(2).77-82



# Angiotensin-converting enzyme inhibitory activity of some Vietnamese medicinal plants

**Xoan Thi Le[1*], Xuyen Thi Phi[1], Duong Thi Thuy Nguyen[1], Hang Thi Nguyet Pham[1], Tai Nguyen Van[1], Olapoju Samuel O.[1], Kinzo Matsumoto[2]**

*[1]National Institute of Medicinal Materials, Vietnam*
*[2]Department of Kampo Pharmacology, Daiichi University of Pharmacy, Japan*

Received 25 March 2020; accepted 29 May 2020

***Abstract:***

**This study investigated the angiotensin 1-converting enzyme (ACE) inhibitory activity of certain medicinal plants that have been traditionally used as an anti-hypertensive, diuretic, or related diseases treatment in Vietnam. Ten different medicinal plants were selected and screened for *in vitro* ACE inhibitory activity. A spectrophotometric assay was developed for the determination of ACE activity in the presence of ACE inhibitors using hippuryl-L-histidyl-L-leucine as the ACE-specific substrate. When the *in vitro* activities of ACE were assessed in the presence and absence of aqueous or ethanol extracts from each medicinal plant, 2 out of the 22 medicinal plant extracts inhibited the ACE activity by more than 90% at a concentration of 50 µg/ml. The estimated $IC_{50}$ value of the *L. rubra* and *U. sessilifructus* were 1.31±0.44 and 12.86 µg/ml, respectively. These results suggest that the *L. rubra* rhizome and *U. sessilifructus* extract are potential anti-hypertensive drug-like candidates with ACE inhibitory activity.**

***Keywords:*** **angiotensin 1-converting enzyme, antihypertensive, *Leea rubra*, *Uncaria sessilifructus*.**

***Classification number:*** **3.3**

## Introduction

Hypertension is a leading cause of death worldwide. About 7.6 million mortalities are annually recorded due to hypertension and this number accounts for approximately 13.5% of total mortality [1]. Currently, many types of synthetic anti-hypertension drugs have been used for the treatment of patients with hypertension. Unfortunately, the proportion of treated and managed cases with such antihypertensive drugs is relatively low in developing countries, probably because of high medical care costs combined with low annual incomes [2]. Therefore, the development of alternative therapeutics for hypertension remains a critical issue in those countries [3].

Various medicinal plants have been investigated to explore natural resources with therapeutic potentials for the patients with hypertension by focusing on calcium channels, β-receptors, diuretic activity, and the renin-angiotensin system (RAS). Particularly, the angiotensin-converting enzyme (ACE) in the RAS has been targeted to develop anti-hypertensive drugs since ACE plays a vital role in blood pressure regulation. This enzyme catalyses the conversion of angiotensin I to angiotensin II and thereby causes vasoconstriction. At the moment, ACE inhibitors such as captopril and lisinopril are clinically used as first-line drugs for the treatment of patients with hypertension. However, the use of these drugs is, in some cases, limited because of their various side effects such as cough, numbness, and mild skin itching, etc. Therefore, the natural source-based development of ACE inhibitors with fewer side effects has been attracting much interest.

**Corresponding author: Email: xoanle@gmail.com*

These backgrounds have prompted us to investigate the ACE inhibitory of certain medicinal plants that are traditionally used as anti-hypertensives, diuretics, and as treatments of related diseases in Vietnam by using an *in vitro* screening system of ACE inhibitors. Numerous methods for the measurement of ACE activity have been developed and reported, including ultraviolet spectrophotometric (USP), visible spectrophotometric (VSP), fluorometric, radiochemical, high-performance liquid chromatography (HPLC), and capillary electrophoresis [4-6]. In this study, using the spectrophotometric method based on the detection of the production of Hippuric acid (HA) from Hip-His-Leu (HHL) by the action of ACE in the presence of ACE inhibitors, we determine the ACE inhibitory activities of 22 different extracts from 10 medicinal plants. This study suggests that the *L. rubra* rhizome and *U. sessilifructus* extract are potential anti-hypertensive drug-like candidates with ACE inhibitory activity.

## Materials and methods

### *Plant materials*

Ten medicinal plants were used for the *in vitro* screening study: *Eucommi aulmoides*, *Apium graveolens*, *Calliasia fragrans*, *Catharanthus roseus*, *Artocarpus altilis*, *Diospyros kaki*, *Annona muricata*, *Uncaria sessilifructus*, *Leea rubra*, and *Hibiscus sabdariffa*. The plants were collected from several locations in Vietnam in 2019, identified by Dr. Pham Thanh Huyen [Department of Medicinal Plant Resources, National Institute of Medicinal Materials (NIMM), Vietnam] and deposited at NIMM with voucher specimen numbers as shown in Table 1.

### *Extract preparation*

The plant materials were cleaned, dried at 60°C in a hot air oven, and then cut into small pieces. For the *in vitro* study, each plant material (20 g) was extracted with water or ethanol 50% (1:7 w/v) at reflux for 2 h and filtered using a filter paper (Whatnam® qualitative filter paper, Grade 93, 580×580 cm, Merck, Darmstadt, Germany). This step was repeated 3 times. The filtered samples were combined and then concentrated under reduced pressure at 60°C. The obtained extract was then dried in a vacuum oven at 60°C until the moisture content of the extract was below 5%. The yield of the extraction from each plant is described in Table 1. These plant extracts samples were stored at 4°C and deposited at NIMM.

### *ACE inhibition assay*

The plant extracts were dissolved in DMSO to make a stock solution with a concentration of 100 mg/ml and stored at -20°C until use. For the *in vitro* ACE inhibition assay, the stock solutions were diluted by a borate buffer of pH 8.3. The concentration of each plant extract in the ACE enzyme reaction was 50 µg/ml. To estimate the $IC_{50}$ values of the herbal extracts, a dilution of the stock solutions were made with the borate buffer to achieve test concentrations of 0.156, 0.3125, 0.625, 1.25, and 2.5 µg/ml. Captopril (Across organics, Belgium), an ACE inhibitor, was used as a positive control, which was diluted in water at a concentration of 1 mM, then the stock was diluted in the borate buffer to reach the test concentration range.

The ACE inhibitory activity was assayed according to the previous method [5] with minor modifications. The composition and reaction procedure are as follows: 12.5 µl of the inhibitor samples (plant extracts or captopril), 27.5 µl borate buffer, and 10 µl ACE 0.02 U/ml were mixed. After incubation for 5 min at 37°C, the mixture was gently blended with 75 µl HHL solution (N-Hippuryl-His-Leu hydrate powder, Sigma, Germany) by using a vortex and subsequently incubated at 37°C for 30 min. The reaction was terminated by adding 100 µl HCl 1 M and mixing. The control sample was prepared by replacing the inhibitor solution with the borate buffer. The blank sample (of both control sample and tested samples) was prepared by replacing the ACE solution by the borate buffer. Each sample was mixed with 150 µl quinoline (Across organics, Belgium). Subsequently, 75 µl of benzene sulfonyl chloride (Sigma, Germany) was added into mixture. After 45 min incubation in dark at 25°C, 300 µl of ethanol was introduced into the mixture. The absorbance of 200 µl of the mixture was determined at 490 nm using an ELISA system 96 well - EL x808 Biotek. Each reaction was done in replicas of two. In parallel with each reaction, the samples and controls had a blank to draw a comparison. The controls were similar to the test tubes but the samples were replaced with buffer.

ACE inhibitory activity was determined using the formula:

$$I\ (\%) = \frac{(OD\text{control} - OD\text{test})}{OD\text{control}} \times 100\ (\%)$$

where OD control is the absorbance value (optical density)

of the control tubes, OD test is the absorbance (optical density) value of test tubes, and the $IC_{50}$ value is the concentration of herbal extract or captopril that inhibited 50% of ACE activity under experimental conditions using regression analysis.

***Total phenolic content of aqueous L. rubra rhizome extract***

Total phenolic content of the *L. rubra* rhizome extract was performed using the Folin-Ciocalteau method as previous described [7, 8]. Briefly, 20 µl of the sample (5 mg/ml) and 930 µl of 2% $Na_2CO_3$ were seeded in a tube to which 50 µl of Folin-Ciocalteau reagent was added. The reaction mixture was incubated at 40º C for 60 min and the absorption of the mixtures was read at 760 nm. The sample was tested at a final concentration of 100 µg/ml in triplicate and a calibration graph with four data points for gallic acid was obtained. The total phenolic content of the sample was expressed as mg of gallic acid equivalents (GAE) per gram of extract. On the basis of this analysis, the total phenolic content of the aqueous *L. rubra* rhizome extract amounts to 65.1 mg GAE/g.

## Results

Ten medicinal plants were obtained from different locations in Vietnam. Aqueous and ethanolic extract from these medicinal materials were screened for their *in vitro* activities to inhibit ACE. As shown in Table 1, the plant extracts showed more than 70% ACE inhibition at a concentration of 50 µg/ml, including the *L. rubra* rhizome (aqueous extract) and *U. sessilifructus* (ethanol extracts), *C. fragran* (aqueous and ethanolic extract), *C. roseus* (ethanolic extract), *A. graveolens* (aqueous extract), and *A. muricata* (aqueous extract). Especially, the *L. rubra* rhizome aqueous and *U. sessilifructus* ethanol extracts showed more than 90% inhibition at a concentration of 50 µg/ml.

The ACE inhibition effects of the aqueous *L. rubra* rhizome and *U. sessilifructus* ethanol extracts were further analysed. As shown in Fig. 1, the inhibitory effect of the *L. rubra* rhizome aqueous extract and *U. sessilifructus* ethanol extracts on the *in vitro* ACE activity were concentration dependent. The estimated $IC_{50}$ values of the *L. rubra* rhizome aqueous extract and *U. sessilifructus* ethanol extract on the *in vitro* ACE activity were 1.3±0.5 µg/ml and 12.86±3.08 µg/ml, respectively. On the other hand, captopril, an ACE inhibitor used as a positive control had an $IC_{50}$ value of 18.0±2.0 nM.

**Table 1. Plant materials used for ACE inhibition in vitro assay, part of plant, extraction solvent and the percentage of ACE inhibition.**

| Plants | Family name | Collection data | | | Plant parts | Extraction solvent | Yield of extraction (%) | % ACE inhibition (50 µg/ml) |
|---|---|---|---|---|---|---|---|---|
| | | *Date* | *Site* | *Voucher no.* | | | | |
| *Callisia fragran* (Lindl.) Woodson | Commelinaceae | 3/2019 | Thai Nguyen province | DL-260219 | Leaves | Water | 29.2 | 82.8±1.7 |
| | | | | | | Ethanol | 36.2 | 71.9±6.4 |
| *Leea rubra* Blume | Leeaceae | 4/2019 | Yen Bai province | DL-230219 | Rhizome | Water | 20.9 | 100±0.0 |
| | | | | | | Ethanol | 23.9 | 63.5±9.8 |
| | | | | | Aerial part | Water | 8.2 | 50.0±7.1 |
| | | | | | | Ethanol | 9.8 | 12.0±6.8 |
| *Eucommia ulmoides* Oliv. | Eucommiaceae | 6/2018 | Lao Cai province | DL-240219 | Stem bark | Water | 17.7 | 67.5±14.2 |
| | | | | | | Ethanol | 18.3 | 16.0±14.2 |
| *Catharanthus roseus* G. Don | Apocynaeae | 4/2018 | Thai Binh province | DL-220219 | Aerialpart | Water | 31.1 | 58.6±12.2 |
| | | | | | | Ethanol | 29.9 | 79.7±4.2 |
| *Apium graveolens* Linn. | Apiaceae | 4/2018 | Thai Binh province | DL-210219 | Aerialpart | Water | 34.2 | 79.5±7.6 |
| | | | | | | Ethanol | 35.1 | 37.5±2.1 |
| *Artocarpus altilis* Fosberg | Moraceae | 4/2018 | Ho Chi Minh city | DL-200219 | Leaves | Water | 15.0 | 48.6±6.6 |
| | | | | | | Ethanol | 14.7 | 67.8±10.7 |
| *Diospyros kaki* Thunb. | Ebenaceae | 8/2018 | Lang Son province | DL-250219 | Leaves | Water | 15.9 | 22.5±7.5 |
| | | | | | | Ethanol | 16.90 | 25.6±9.38 |
| *Annona muricata* Linn. | Annonaceae | 3/2019 | Thai Nguyen province | DL-270219 | Leaves | Water | 30.7 | 73.1±18.8 |
| | | | | | | Ethanol | 32.7 | 19.4±4.3 |
| *Uncaria sessilifructus* Roxb. | Rubiaceae | 3/2018 | Bac Can province | DL-190219 | Stem with hook | Water | 18.3 | 67.0±7.0 |
| | | | | | | Ethanol | 12.1 | 93.5±4.0 |
| *Hibiscus sabdariffa* Linn. | Malvaeae | 4/2019 | Phu Yen province | DL-280219 | Calyxes | Water | 35.1 | 65.8±4.5 |
| | | | | | | Ethanol | 45.1 | 39.1±7.4 |

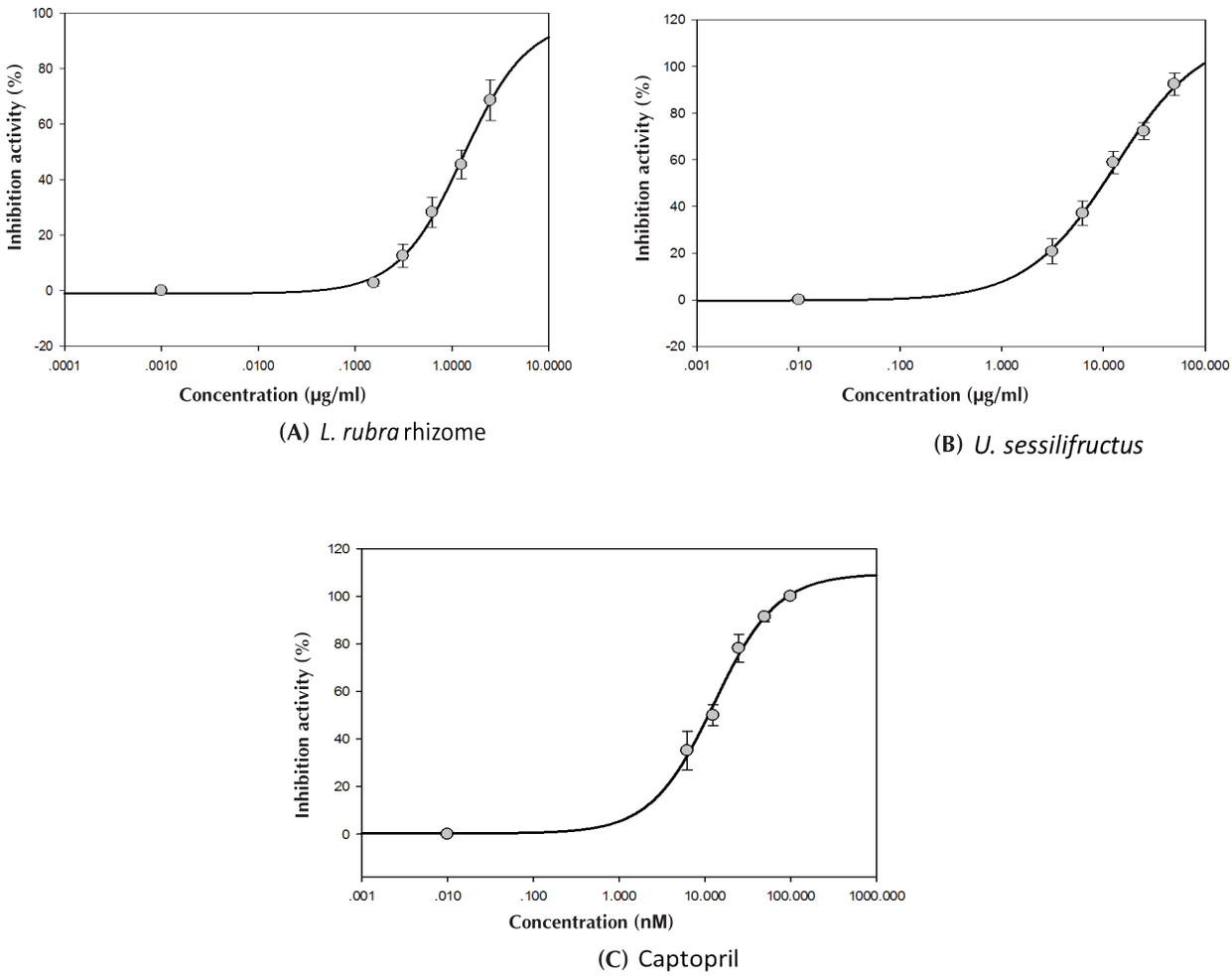


**Fig 1. Inhibition activity of *L. rubra* rhizome extract (A), *U. sessilifructus* ethanol extract (B) and captopril (C) on ACE *in vitro*.**

## Discussion

In this study, we used the VSP method to screen 22 extracts from 10 traditional herbs for their *in vitro* ACE inhibitory potentials using captoptil as the positive control. The $IC_{50}$ values of captopril determined in this study using this VSP method (18.0 nM) are in agreement with the range of 5-23 nM reported previously [4, 5, 9]. USP/VSP and HPLC are commonly used in the assay for determining ACE activity and inhibition *in vitro*. The USP method was developed by Cushman and Cheung in 1970 based on the hydrolysis of hippuryl -L-histidy where Hip-His-Leu converts into Hippuric acid (HA) and His-Leu (HL) by ACE. HA then was extracted by ethyl acetate and measured by USP at a wavelength 228 nm. However, this method has weak points such as a complicated process, wasted time, and instability during separation of HHL from HA because both absorb wavelengths of 228 nm. Therefore, HA may be overestimated [5]. The VSP method was developed by modifying the USP method by using spectrophotometry in the visible light wavelength range. For the modified VSP methods, the ethyl acetate extraction step was replaced by adding a colorimetric agent that binds with HA such as benzene sulfonyl chloride in the presence of quinoline. The VSP method process has the advantages of simplicity, high sensitivity, and cost effectiveness because of the absence of the procedure that separates HA from the reaction mixture [5, 6]. The HPLC method was employed to assay ACE activity with reaction principles similar to the USP method. Although the HPLC method exhibits higher precision and reproducibility than VSP method, the use of HPLC requires costly instrumentation requiring proper preventative

maintenance, the highest grade of purity solvents, and a complex and time consuming procedure. In contrast, the VSP provides a simple and rapid means for chemical analysis [5] that is suitable for screening proposes with a large number of samples.

The present study demonstrated that the *L. rubra* rhizome aqueous extract exhibited the highest *in vitro* ACE inhibitory potency of all the plant materials screened with an $IC_{50}$ of 1.31±0.44 µg/ml. *L. rubra* belongs to the family Vitaceae. *L. rubra*, which is widely distributed in Vietnam, Thailand, and Cambodia. *L. rubra* is an herb with dusty red fruits that ripens to a black, purple red stem with an average height of about 2.5 m. Traditionally, this plant is used for the treatment of inflammation and pain [10]. Surprisingly, there is another species of *Leea* genus that is often used in traditional remedies for hypertension [11]. According to the previous study demonstrating the *in vitro* ACE inhibitory effect of some Brazilian medicinal herbs, the ethanolic extract of aerial part of *L. rubra* inhibited the activity of ACE by 57.0±12.5% at a concentration of 100 µg/ml [11]. Consistent with Braga's study, our *in vitro* results show that aqueous and ethanolic extracts of *L. rubra's* aerial part inhibited ACE activity by 50.0 and 12.0%, respectively, at a concentration 50 µg/ml. Moreover, we found that aqueous and ethanolic *L. rubra* rhizome extracts inhibited the ACE activity by 100 and 63.5%, respectively. This finding demonstrates that the *L. rubra* rhizome aqueous extract exhibits a higher ACE inhibitory activity than the aerial part. Moreover, with an $IC_{50}$ as low as 1.31±0.44 µg/ml, the *L. rubra* rhizome extract is considered as a crude plant extract that possesses potent ACE inhibition. In our dedication to discover effective anti-hypertension therapies from natural products, the effect of this plant extract in hypertensive rat models is under investigation in our laboratory.

The main chemical compositions of the *L. rubra* rhizome extract that causes the angiotensin-converting enzyme inhibitory activity are unclear. As far as we know, no specific work on *L. rubra* rhizome isolate has been reported to date. However, based on a chemical analysis, we demonstrated that this crude extract consists of high phenolic content with the total phenolic content was estimated as 65.1 mg GAE/g. Moreover, Phuong, et al. (2015) [12] isolated and identified 5 phenolic compounds including gallic acid, proto-catechuic acid, 4-hydroxybenzoic acid, arctiin, and kaempferol-3-O-α-L-rhamnopyranosyl(1→2)-α-L-arabinofuranoside from *L. rubra* leaves. From the *L. rubra* leaves, this group also isolated and identified 4 flavonoids including myricitrin, 7-methoxymyricitrin, rhamnetin-3-O-a-L-rhamnopyranoside, and juglanin [13]. In addition, there was a study demonstrating the hypotensive effect of gallic acid suspected by acting on the renin-angiotensin system [14]. Thus, there is a possibility that gallic acid as well as flavonoids constituents of *L. rubra* may be the active ingredients contributing to the ACE inhibition effect of the *L. rubra* rhizome extract, however, further study is needed to demonstrate this possibility.

Besides the *L. rubra* rhizome extract, we found that *U. sessilifructus* extracts exhibit significant ACE inhibition activity. As far as we know, the ACE inhibition effect of *U. sessilifructus* has not been reported previously. However, Hansen, et al. (1995) [15] reported that *U. rhynchophylla* is one of 7 species that inhibit ACE by more than 50% among the 31 species investigated. Notably, five *Uncaria* species, namely *U. rhynchophylla*, *U. macrophylla*, *U. hirsuta*, *U. sinensis*, and *U. sessilifructus* are documented in Chinese Pharmacopoeia as the raw materials of Uncariae Ramulus Cum Uncis. This *Uncaria* species has been traditionally used for the treatment of hypertension, headache, and fever. The indole alkaloid content of *U. sessilifructus* is considered as the antihypertensive active ingredient [16, 17]. Feng, et al. (2019) [18] reported that the *Uncaria* species including *U. sessilifructus* reduced the systolic blood pressure in spontaneously hypertensive rats (SHRs). Thus, these results allow us to speculate the ACE inhibition activity contributing to the anti-hypertensive action of this plant.

A negative result of the ACE inhibition screening does not always mean that this plant species does not work as an anti-hypertensive drug as compounds may influence other hypotensive mechanisms. It also should be noted that the presence of potent ACE inhibition does not mean that the species are potent anti-hypertensive drugs. Therefore, further studies on pure compounds isolated from the active extracts are necessary. Also, the effect of a potential candidate should be evaluated using an animal model of hypertension.

## Conclusions

In conclusion, our results showed that the *L. rubra* rhizome and *U. sessilifructus* extracts exhibit significant ACE inhibitory activity. This study suggests that the *L. rubra* rhizome and *U. sessilifructus* may be beneficial for the treatment of hypertension.

## ACKNOWLEDGEMENTS

This work was in part supported by National Institute of Medicinal Materials, Vietnam.

The authors declare that there is no conflict of interest regarding the publication of this article.

## REFERENCES

[1] H. Arima, F. Barzi, J. Chalmers (2011), "Mortality patterns in hypertension", *J. Hypertens.*, **29**, pp.S3-S7.

[2] H.A. Hien, N.M. Tam, V. Tam, A. Derese, D. Devroey (2018), "Prevalence, awareness, treatment, and control of hypertension and its risk factors in (Central) Vietnam", *Int. J. Hypertens.*, **2018(29)**, pp.1-12, DOI: 10.1155/2018/6326984.

[3] R.V. Picon, F.D. Fuchs, L.B. Moreira, S.C. Fuchs (2013), "Prevalence of hypertension among elderly persons in urban Brazil: a systematic review with meta-analysis", *Am. J. Hypertens.*, **26(4)**, pp.541-548.

[4] G.H. Li, H. Liu, Y.H. Shi, G.W. Le (2005), "Direct spectrophotometric measurement of angiotensin I-converting enzyme inhibitory activity for screening bioactive peptides", *J. Pharm. Biomed. Anal.*, **37(2)**, pp.219-224.

[5] J. Chen, Y. Wang, R. Ye, Y. Wu, W. Xia (2013), "Comparison of analytical methods to assay inhibitors of angiotensin I-converting enzyme", *Food Chem.*, **141(4)**, pp.3329-3334.

[6] I. Ahmad, A. Yanuar, K. Mulia, A. Mun'im (2017), "Review of angiotensin-converting enzyme inhibitory assay: rapid method in drug discovery of herbal plants", *Pharmacogn. Rev.*, **11(21)**, pp.1-7.

[7 Y. Cai, Q. Luo, M. Sun, H. Corke (2004), "Antioxidant activity and phenolic compounds of 112 traditional Chinese medicinal plants associated with anticancer", *Life Sci.*, **74(17)**, pp.2157-2184.

[8] P.T. Thuong, N.D. Su, T.M. Ngoc, T.M. Hung, N.H. Dang, N.D. Thuan, K. Bae, W.K. Oh (2009), "Antioxidant activity and principles of Vietnam bitter tea *Ilex kudingcha*", *Food Chem.*, **113(1)**, pp.139-145.

[9] B.A. Murray, D.J. Walsh, R.J. FitzGerald (2004), "Modification of the furanacryloyl-L-phenylalanylglycylglycine assay for determination of angiotensin-I-converting enzyme inhibitory activity", *J. Biochem. Biophys. Methods*, **59(2)**, pp.127-137.

[10] T.L. Do (1999), *Vietnamese Medicinal Plants and Remedies*, Hanoi, Medical Publishing House.

[11] F.C. Braga, C.P. Serra, N.S. Viana Júnior, A.B. Oliveira, S.F. Cortes, J.A. Lombardi (2007), "Angiotensin-converting enzyme inhibition by Brazilian plants", *Fitoterapia*, **78(5)**, pp.353-358.

[12] N. Phuong, V. Tuan, P. Thuong, P. Nam, H. Hung, N. Khoi (2015), "Phenolic compounds isolated from the leaf of *Leea rubra* Blume ex Spreng", *Journal of Medicinal Materials*, **20**, pp.353-358.

[13] N. Phuong, V. Tuan, P. Thuong, N. Khoi (2014), "Flavonoids from the leaves of *Leea rubra* Blume ex Spreng", *Journal of Medicinal Materials*, **19**, pp.110-116.

[14] L. Jin, Z.H. Piao, S. Sun, B. Liu, G.R. Kim, Y.M. Seok, M.Q. Lin, Y. Ryu, S.Y. Choi, H.J. Kee, M.H. Jeong (2017), "Gallic acid reduces blood pressure and attenuates oxidative stress and cardiac hypertrophy in spontaneously hypertensive rats", *Sci. Rep.*, **7(1)**, DOI: 10.1038/s41598-017-15925-1.

[15] K. Hansen, U. Nyman, U.W. Smitt, A. Adsersen, L. Gudiksen, S. Rajasekharan, P. Pushpangadan (1995), "In vitro screening of traditional medicines for anti-hypertensive effect based on inhibition of the angiotensin converting enzyme (ACE)", *J. Ethnopharmacol.*, **48(1)**, pp.43-51.

[16] J.G. Zhang, J.J. Chen, C.A. Geng (2019), "Advances in indole alkaloids from traditional Chinese medicine of *Uncariae Ramulus Cum Uncis* documented in Chinese Pharmacopoeia", *Zhongguo Zhong Yao Za Zhi = Zhongguo Zhongyao Zazhi = China Journal of Chinese Materia Medica*, **44(4)**, pp.685-695.

[17] M.E. Heitzman, C.C. Neto, E. Winiarz, A.J. Vaisberg, G.B. Hammond (2005), "Ethnobotany, phytochemistry and pharmacology of *Uncaria* (Rubiaceae)", *Phytochemistry*, **66(1)**, pp.5-29.

[18] Z. Feng, J. Hou, Y. Yu, W. Wu, Y. Deng, X. Wang, H. Zhi, L. Zhang, W. Wu, D.A. Guo (2019), "Dissecting the metabolic phenotype of the antihypertensive effects of five *Uncaria* species on spontaneously hypertensive rats", *Front. Pharmacol.*, **10**, pp.845.

DOI: 10.31276/VJSTE.62(2).83-88



# Phleomycin resistance gene as a reliable selection marker for *Agrobacterium tumefaciens*-mediated transformation of the citrus postharvest pathogen *Penicillium digitatum*

**Van-Tuan Tran[1, 2*], Tao Xuan Vu[2, 3]**

[1]*Faculty of Biology, University of Science, Vietnam National University, Hanoi*
[2]*National Key Laboratory of Enzyme and Protein Technology, University of Science, Vietnam National University*
[3]*Center of Experimental Biology, National Center for Technological Progress, Ministry of Science and Technology of Vietnam*

Received 15 April 2020; accepted 2 June 2020

***Abstract:***

***Penicillium digitatum* exists in nature as a causative agent of green mould disease in citrus fruits at the postharvest stages. Inspections of the molecular mechanism of the host invasion by *P. digitatum* usually require suitable selection markers for genetic manipulation. In this study, we recruited the phleomycin resistance gene as a selection marker for the genetic transformation of *P. digitatum* using *Agrobacterium tumefaciens*. The results showed that the growth of the wild strain *P. digitatum* PdVN1 from fungal spores is quite sensitive to phleomycin and is inhibited at a concentration of 50 µg/ml, whereas growth from fungal mycelium is more tolerant and completely suppressed at a concentration of 200 µg/ml. Under optimised conditions, the *A. tumefaciens*-mediated transformation (ATMT) efficiency of *P. digitatum* with the phleomycin resistance marker could reach over 1000 transformants per $10^6$ spores. All the tested transformants presented the integration of T-DNA in their genomes and were mitotically stable for the phleomycin resistance. Furthermore, the results also revealed the success for heterologous expression of the *DsRed* fluorescent gene in the fungus, in which the strong red fluorescent signal could be observed over the whole fungal mycelium and spores. Our work demonstrates for the first time that the phleomycin resistance gene can serve as a reliable selection marker for *A. tumefaciens*-mediated transformation of the postharvest pathogen *P. digitatum*. This selection marker can be exploited for T-DNA insertional mutagenesis and for functional investigations of target genes involved in citrus decay by *P. digitatum*.**

***Keywords:*** ***Agrobacterium*-mediated transformation, citrus postharvest pathogen, *DsRed* fluorescent reporter gene, *Penicillium digitatum*, phleomycin resistance marker.**

***Classification number:*** **3.5**

## Introduction

*Penicillium digitatum* causes green mould disease on citrus fruits and has been reported to be the most destructive pathogen during the postharvest stages. This pathogen can infect fruits through wounded points on the citrus peel prior to the colonization of the whole fruits for severe decay. *P. digitatum* grows on an infected citrus peel and can be seen as white mycelium, which later turns olive colour due to fungal sporulation [1-3]. The molecular mechanism of citrus infection by *P. digitatum* is still unclarified. Up to date, only a few genes required for pathogenicity of *P. digitatum* have been characterized [4-6]. The development of new genetic tools with reliable selection markers is essential and can help to dissect more about the infection process of this pathogenic fungus.

*Agrobacterium tumefaciens* is a soil-borne bacterium, which has the capability of transferring the T-DNA from the tumour-inducing (Ti) plasmid into plants and fungi [7]. The *Agrobacterium tumefaciens*-mediated transformation (ATMT) was reported for the first time in filamentous fungi by de Groot, et al. in 1998 [8]. At the time, this transformation method became popular and useful for fungal research community. Currently, the ATMT methods have been demonstrated to be highly efficient for genetic transformation of a large number of filamentous fungi [8-10]. ATMT represents a simple method for genetic

*Corresponding author: Email: tuantran@vnu.edu.vn

transformation with high efficiency and fungal spores can be used directly as the transformation material [10, 11]. The common antifungal agents, including hygromycin, nourseothricin, and phleomycin, have been broadly exploited for genetic transformation of filamentous fungi [3, 8, 10-12]. Although phleomycin was employed for the transformation of different fungi and plants [13-16], so far it has not been tested on the citrus postharvest pathogen *P. digitatum*. Recently, ATMT has been demonstrated to be an effective transformation method in *P. digitatum* using two dominant selection markers conferring the resistance to hygromycin and nourseothricin. The ATMT efficiencies with these two selection markers reached the yields of 60-1240 transformants for $10^6$ spores depending on the examined strains of *P. digitatum* [3, 17]. In addition, the *DsRed* fluorescent gene originated from the reef coral *Discosoma* sp. has been commonly used as a model reporter gene for genetic transformation of numerous filamentous fungi including *P. digitatum* [3, 11, 18-21]. In this study, we report for the first time that the phleomycin resistance gene can be employed as a selectable marker for genetic transformation of *P. digitatum* using *A. tumefaciens*. Our work shows that the transformation efficiency with the phleomycin resistance marker could achieve over 1000 transformants for $10^6$ spores.

## Materials and methods

### *Microbial strains and cultivation media*

*Escherichia coli* DH5α and *Agrobacterium tumefaciens* AGL1 were used for plasmid propagation and fungal transformation, respectively. These bacteria were grown in Luria-Bertani medium. The fungal strain *P. digitatum* PdVN1, isolated in Vietnam [3], was grown on the potato dextrose agar (PDA) medium.

### *Preparation of fungal spore suspensions*

The wild strain *P. digitatum* PdVN1 and transgenic strains were grown on the PDA plates at 25°C for 4-5 days. Fungal spores were collected as mentioned earlier [3]. The spore suspensions were adjusted to the concentration of $10^6$ spores/ml for later use. The spore concentration was monitored with a hemocytometer under microscopy.

### *Extraction of fungal genomic DNA*

Fungal strains were grown in the potato dextrose broth (PDB) medium at the temperature of 25°C at 200 rpm for 3 days and fungal mycelia from the cultures were collected by filtration through Miracloth (Calbiochem, Darmstadt, Germany). Genomic DNA was extracted from the fungal biomass as previously described [22].

### *Examination of the susceptibility of P. digitatum to phleomycin*

A PDA agar plug with the diameter of 4 mm containing fungal mycelium or 10 µl of spore suspension ($10^6$ spores/ml) of the wild strain PdVN1 was placed on the PDA medium supplemented with phleomycin (50-200 µg/ml). The plates were incubated at a temperature of 25°C for 3-4 days to examine growth of the fungus.

### *PCR amplification*

PCR amplifications of the phleomycin resistance marker and the *DsRed* reporter gene were performed with specific primer pairs (Table 1). GoTaq® Green Master Mix (Promega, Madison, USA) was used for PCR screening. PCR procedure includes 94°C (3 min); 30 cycles of 94°C (30 s), 58-60°C (30 s), 72°C (1-2 min); 72°C (7 min). PCR products were analysed on 0.7% agarose gels.

**Table 1. The primers used in this study.**

| Primer name | Sequence (5'-3') | Product size (bp) | Source |
|---|---|---|---|
| DsRed-F | AACTCGAGCACGTGCTTAAGGATATCATGGCCTCCTCCGAGG | 729 | [19] |
| DsRed-R | AAGGATCCCCGCGGGAGCTCGATATCCTACAGGAACAGGTGGTGGC | | |
| Phleo-F | GGGCTCGAGAGGCCTCCGGTGACTCTTTCTGGC | 1250 | [11] |
| Phleo-R | TCGGTCAGTCCTGCTCCT | | |

### *Agrobacterium tumefaciens-mediated transformation of P. digitatum*

The binary vector pPK2-Red2 was transformed into the bacterium *A. tumefaciens* AGL1 by electroporation using the Gene Pulse Xcell™ Electroporation System (Bio-Rad, California, USA). *A. tumefaciens* AGL1 carrying the binary vector was used for genetic transformation of *P. digitatum* as previously described [3]. PDA plates supplemented with phleomycin (200 µg/ml) and cefotaxime (300 µg/ml) were used for selection of fungal transformants and for suppression of the *A. tumefaciens* cells, respectively. The plates were kept at the temperature of 25°C for 4-5 days to collect transformants.

### *Examination of transgenic strains*

Fungal transformants as transgenic strains were cultivated on PDA containing phleomycin at the concentration of 200 µg/ml to confirm the ability of phleomycin resistance. Afterwards, these transformants were examined for mitotic stability with several mitotic generations on PDA. The transformants were then grown in PDB for 3 days at 25°C and their mycelia were collected for genomic DNA extraction. T-DNA integrations into the genome of the pathogenic fungus were verified by PCR with two independent primer pairs listed in Table 1. The selected transformants were grown directly on microscopic slides containing droplets of PDA as reported by Vu, et al. (2018) [3] and the expression of the *DsRed* fluorescent gene in these transformants was analysed under Axioplan fluorescence microscope (Carl Zeiss, Jena, Germany).

## Results and discussion

### *Penicillium digitatum PdVN1 is highly susceptible to phleomycin*

We examined the susceptibility of the wild strain *P. digitatum* PdVN1 to phleomycin by growing the fungus on the medium containing this antifungal agent at different concentrations. The results showed that fungal spores were more susceptible and totally suppressed by phleomycin at a concentration of 200 µg/ml. In contrast, fungal mycelium was more resistant to low concentrations of this agent. At a concentration of 200 µg/ml, phleomycin could completely inhibit growth of the fungus with both the inoculation materials as spores and mycelium (Fig. 1A). Therefore, this concentration of phleomycin was used for transformation of *P. digitatum* PdVN1 in order to inhibit the growth of untransformed fungal cells. For transformation of *P. digitatum*, the binary vector pPK2-Red2 was employed. This vector contains a transfer DNA (T-DNA) region, which harbours two different cassettes for expression of the phleomycin resistance gene and the *DsRed* gene under the regulation of the constitutive *gpdA* promoter from the model filamentous fungus *Aspergillus nidulans* (Fig. 1B). Recently, pPK2-Red2 has also been successfully exploited for genetic transformation of the penicillin-producing fungus *Penicillium chrysogenum* using phleomycin as the selection agent [11].

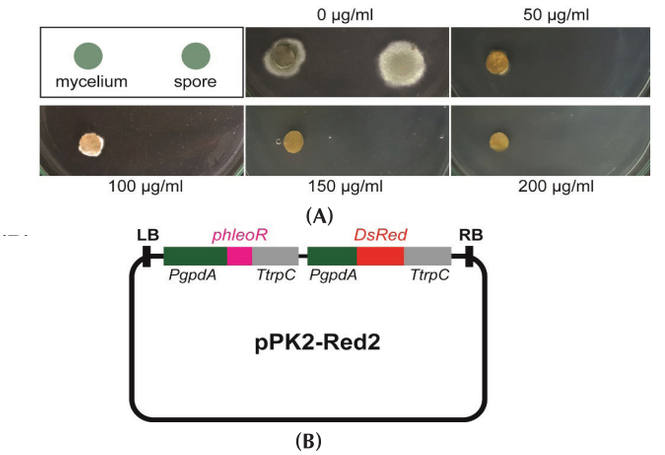


**Fig. 1. The susceptibility of *P. digitatum* PdVN1 to phleomycin and the map of the binary vector pPK2-Red2. (A)** The wild strain PdVN1 (mycelium, spores) was grown on the PDA medium supplemented with different concentrations of phleomycin (50-200 µg/ml). **(B)** The map of the binary vector pPK2-Red2 showing the T-DNA structure containing the expression cassettes for the phleomycin resistance gene *(phleoR)* and the *DsRed* fluorescent reporter gene. This T-DNA region is restricted by the left border (LB) and right border (RB).

### *Phleomycin resistance gene represents a reliable selection marker for transformation of the citrus postharvest pathogen P. digitatum*

In this study, we employed the binary vector pPK2-Red2 [11] for evaluating the genetic transformation of *P. digitatum* PdVN1. This vector harbours the phleomycin resistance marker, in which the *Sh ble* gene conferring phleomycin resistance is regulated by the constitutive *gpdA* promoter from the filamentous fungus *A. nidulans* (Fig. 1B). The *Sh ble* gene isolated from *Streptoalloteichus hindustanus* encodes a protein binding to phleomycin and subsequently inhibits its DNA cleavage activity [14, 16]. Our results showed that the ATMT method using the phleomycin resistance marker is efficient for genetic transformation of *P. digitatum* PdVN1. With the transformation conditions optimized for the ATMT including a temperature of 25°C, time of 72 h for the co-cultivation step, acetosyringone (AS) concentration of 200 µM for induction, and spore concentration of $10^6$ spores/ml, the efficiency for transformation of *P. digitatum* PdVN1 could reach over 1000 transformants per $10^6$ spores (Fig. 2). The transformation efficiency with the phleomycin resistance marker in this study is similar to the ones with two other selection markers conferring the resistance to hygromycin and nourseothricin (approximately 1240 transformants per $10^6$ spores) that we previously reported for the ATMT method in *P. digitatum* [3].

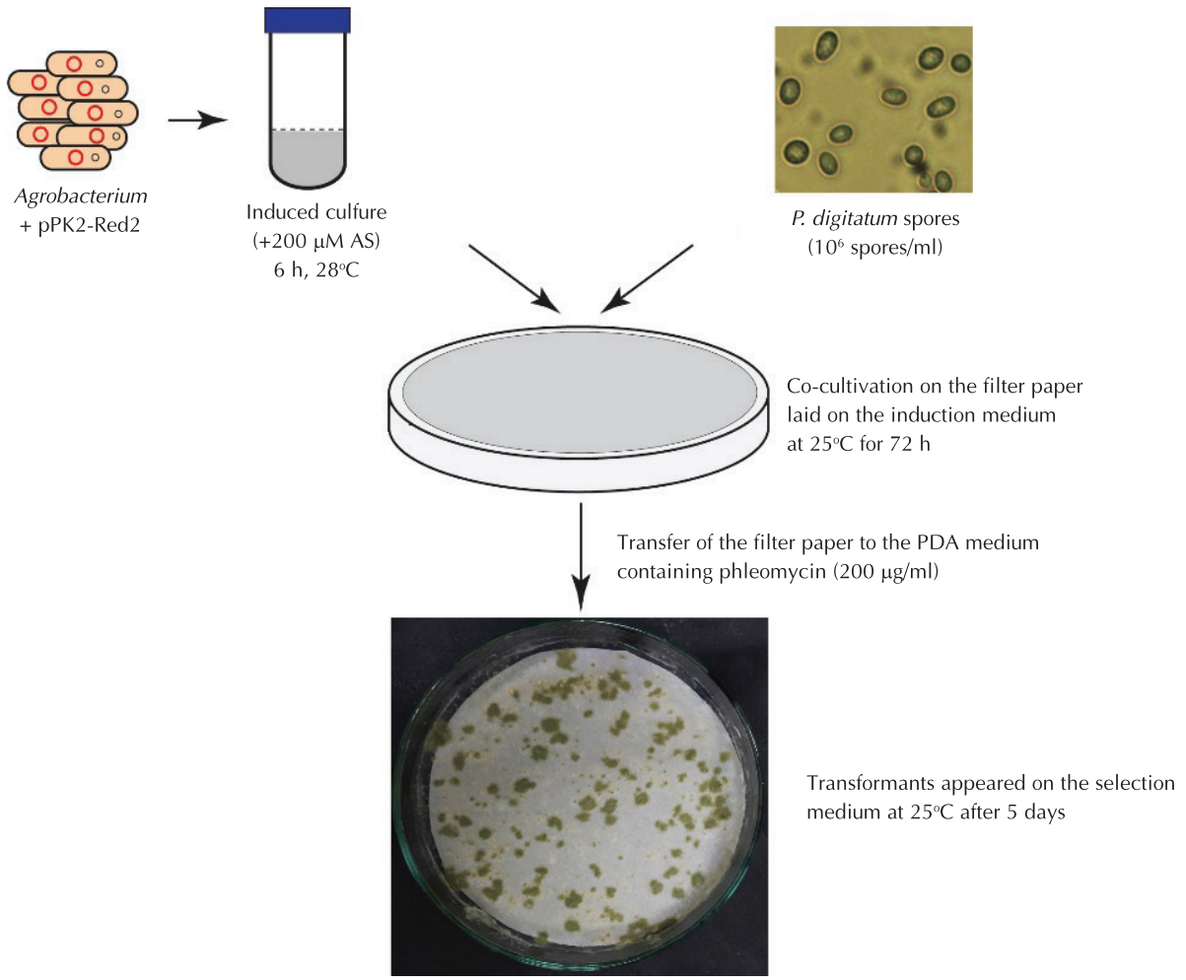


**Fig. 2. The optimized procedure for *A. tumefaciens*-mediated transformation of *P. digitatum* PdVN1 using the phleomycin resistance marker.** The induced *Agrobacterium* cells containing the binary vector pPK2-Red2 were mixed with fungal spores for co-cultivation on the cellulose membrane covered on the induction medium (IM). This step promoted the transfer of T-DNA fragment from *Agrobacterium* into the fungal genome. The membrane was then shifted to the PDA medium supplemented with a suitable concentration of phleomycin for selection of transformants.

***The transgenic strains are mitotically stable for maintaining the T-DNA structure***

Five transformants as transgenic strains named Pd-R1, Pd-R2, Pd-R3, Pd-R4, and Pd-R5 were randomly selected and cultivated on the PDA medium containing phleomycin. The young mycelia of these strains were cut and transferred to new plates containing the PDA medium without phleomycin for three successive mitotic generations prior to re-growing on the PDA medium supplemented with the selection agent as phleomycin. Our results indicated that all five tested transformants still grew well on the selection medium supplemented with phleomycin in comparison to the wild strain PdVN1 (WT), which was not able to survive on this medium (Fig. 3A). These transgenic strains were then analysed by PCR with two different primer pairs, which amplify specifically the phleomycin resistance cassette and the *DsRed* fluorescent gene (Table 1). The results showed that the T-DNA structure carrying the cassettes for expression of the *Sh ble* gene conferring phleomycin resistance and the *DsRed* reporter gene was integrated in the genomes of all five strains (Fig. 3B). Interestingly, these results were also similar to the transformation data obtained from *P. chrysogenum* when the binary vector pPK2-Red2 and phleomycin as the selection agent were used for genetic transformation of this penicillin-producing fungus [11]. In fact, the mitotic stability of T-DNA structures in fungal genomes had been reported in several filamentous fungi [7-9, 19].

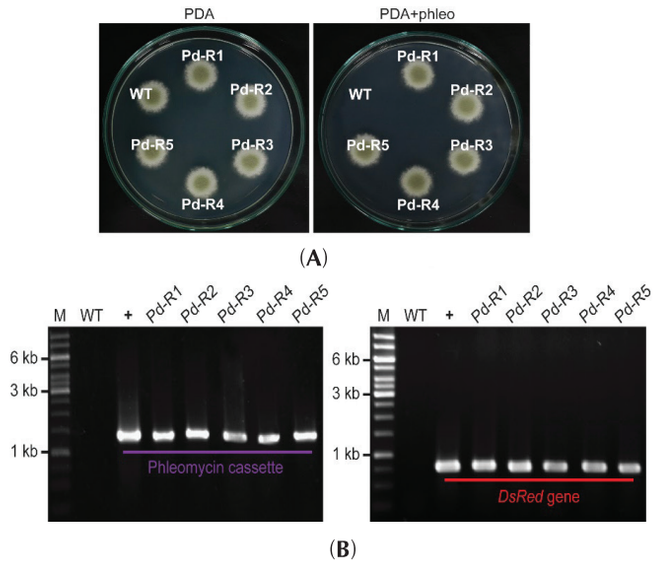


**Fig. 3. Confirmation of the phleomycin resistant transformants.** (**A**) Five randomly selected transformants (Pd-R1, Pd-R2, Pd-R3, Pd-R4, Pd-R5) were grown simultaneously on PDA and PDA containing 200 µg/ml of phleomycin (PDA+phleo). The *P. digitatum* PdVN1 strain (WT) was used as reference control. (**B**) The examined transformants were verified by PCR using the primer pair amplifying the phleomycin resistance marker or the *DsRed* fluorescent reporter gene. Total DNA isolated from *P. digitatum* PdVN1 (WT) and the purified plasmid pPK2-Red2 were used as DNA templates for controls, respectively.

***Successful expression of the DsRed fluorescent reporter gene in P. digitatum using the phleomycin resistance marker***

We cultivated all five transgenic strains together with the wild strain PdVN1 directly on the sterile microscopic slides containing droplets of the PDA medium. After 3 days of incubation at 25°C, the slides were checked under the fluorescence microscope using the filter set with the excitation/emission of 558/583 nm for detection of the DsRed signal. The results showed that the expression of the *DsRed* reporter gene in all five strains was very strong and the red fluorescent signal was observed in both fungal hyphae and spores (Fig. 4).

The random integration of T-DNA from a binary vector into fungal genome could create insertion mutants, which resulted in a large collection of the mutants for further identifications of potential genes involved in metabolism, differentiation and pathogenicity in fungi [9, 10, 14]. Therefore, the transfer of the T-DNA structure containing the phleomycin resistance marker from the binary vector pPK2-Red2 into the citrus postharvest pathogen *P. digitatum* PdVN1 may be a good approach for the construction of insertion mutant libraries. Furthermore, the *DsRed* reporter gene in the binary vector can also be replaced with a gene of interest for overexpression in this pathogenic fungus.

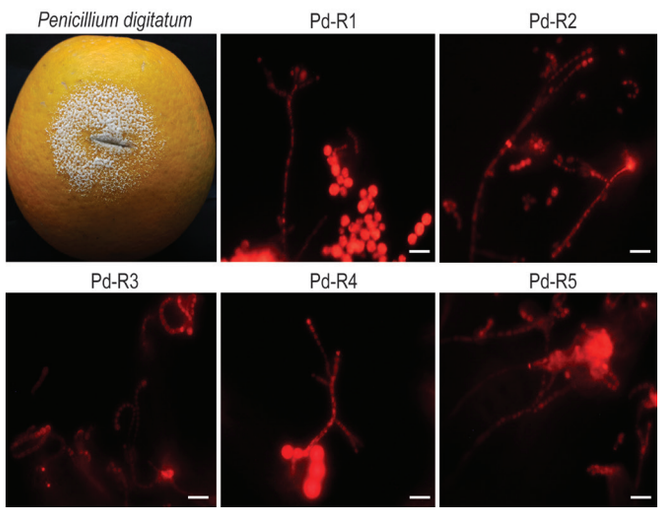


**Fig. 4. Examination of the DsRed expression in the transgenic strains.** All five transgenic strains (Pd-R1 to Pd-R5) generated from the wild strain *Penicillium digitatum* PdVN1 were grown directly on microscopic slides containing the PDA medium. Fungal mycelia were observed under the Axioplan fluorescence microscope. The scale bars indicate the same sizes of the images.

## Conclusions

In this study, we have successfully employed the phleomycin resistance gene as a reliable selection marker for the genetic transformation of the citrus postharvest pathogen *P. digitatum* using the bacterium *A. tumefaciens*. The transformation efficiency of *P. digitatum* PdVN1 under the optimized conditions could reach over 1000 transformants per $10^6$ spores. The transformants could maintain the ability for phleomycin resistance after several mitotic generations. We further succeeded in heterologous expression of the *DsRed* reporter gene in *P. digitatum* using a binary vector carrying the phleomycin resistance marker. This selection marker in combination with the optimized ATMT method for *P. digitatum* can be exploited for gene targeting or for the generation of insertion mutants by T-DNA integration events for screening the potential genes required for fungal pathogenicity on citrus.

## ACKNOWLEDGEMENTS

This research is funded by Vietnam National Foundation for Science and Technology Development (NAFOSTED) under grant number 106.04-2018.36.

The authors declare that there is no conflict of interest regarding the publication of this article.

## REFERENCES

[1] M. Lopez-Perez, A.R. Ballester, L. Gonzalez-Candelas (2015), "Identification and functional analysis of *Penicillium digitatum* genes putatively involved in virulence towards citrus fruit", *Mol. Plant Pathol.*, **16(3)**, pp.262-275.

[2] M. Marcet-Houben, A.R. Ballester, B. de la Fuente, E. Harries, J.F. Marcos, L. Gonzalez-Candelas, T. Gabaldon (2012), "Genome sequence of the necrotrophic fungus *Penicillium digitatum*, the main postharvest pathogen of citrus", *BMC Genomics*, **13(1)**, pp.646-662.

[3] T.X. Vu, T.T. Ngo, L.T.D. Mai, T.T. Bui, D.H. Le, H.T.V. Bui, H.Q. Nguyen, B.X. Ngo, V.T. Tran (2018), "A highly efficient *Agrobacterium tumefaciens*-mediated transformation system for the postharvest pathogen *Penicillium digitatum* using DsRed and GFP to visualize citrus host colonization", *J. Microbiol. Methods*, **144**, pp.134-144.

[4] J.H. Costa, J.M. Bazioli, J.G. de Moraes Pontes, T.P. Fill (2019), "*Penicillium digitatum* infection mechanisms in citrus: What do we know so far?", *Fungal Biol.*, **123(8)**, pp.584-593.

[5] M. Wang, X. Sun, C. Zhu, Q. Xu, R. Ruan, D. Yu, H. Li (2015), "PdbrlA, PdabaA and PdwetA control distinct stages of conidiogenesis in *Penicillium digitatum*", *Res. Microbiol.*, **166(1)**, pp.56-65.

[6] L. Vilanova, N. Teixido, R. Torres, J. Usall, I. Vinas, P. Sanchez-Torres (2016), "Relevance of the transcription factor PdSte12 in *Penicillium digitatum* conidiation and virulence during citrus fruit infection", *Int. J. Food Microbiol.*, **235**, pp.93-102.

[7] D. Li, Y. Tang, J. Lin, W. Cai (2017), "Methods for genetic transformation of filamentous fungi", *Microb. Cell Fact.*, **16(1)**, pp.168-180.

[8] M.J. de Groot, P. Bundock, P.J. Hooykaas, A.G. Beijersbergen (1998), "*Agrobacterium tumefaciens*-mediated transformation of filamentous fungi", *Nat. Biotechnol.*, **16(9)**, pp.839-842.

[9] A. Idnurm, A.M. Bailey, T.C. Cairns, C.E. Elliott, G.D. Foster, G. Ianiri, J. Jeon (2017), "A silver bullet in a golden age of functional genomics: the impact of *Agrobacterium*-mediated transformation of fungi", *Fungal Biol. Biotechnol.*, **4(1)**, pp.6-33.

[10] C.B. Michielse, P.J. Hooykaas, C.A. van den Hondel, A.F. Ram (2005), "*Agrobacterium*-mediated transformation as a tool for functional genomics in fungi", *Curr. Genet.*, **48(1)**, pp.1-17.

[11] T.X. Vu, H.H. Vu, G.T. Nguyen, H.T. Vu, L.T.D. Mai, D.N. Pham, D.H. Le, H.Q. Nguyen, V.T. Tran (2019), "A newly constructed *Agrobacterium*-mediated transformation system revealed the influence of nitrogen sources on the function of the LaeA regulator in *Penicillium chrysogenum*", *Fungal Biol.*, **123(11)**, pp.830-842.

[12] E.D. Mullins, X. Chen, P. Romaine, R. Raina, D.M. Geiser, S. Kang (2001), "*Agrobacterium*-mediated transformation of *Fusarium oxysporum*: an efficient tool for insertional mutagenesis and gene transfer", *Phytopathology*, **91(2)**, pp.173-180.

[13] Z.-M. He, M.S. Price, G.R. Obrian, D.R. Georgianna, G.A. Payne (2007), "Improved protocols for functional analysis in the pathogenic fungus *Aspergillus flavus*", *BMC Microbiol.*, **7(1)**, pp.104-114.

[14] A. Gatignol, M. Baron, G. Tiraby (1987), "Phleomycin resistance encoded by the *ble* gene from transposon Tn 5 as a dominant selectable marker in *Saccharomyces cerevisiae*", *Mol. Gen. Genet.*, **207(2-3)**, pp.342-348.

[15] I.E. Mattern, P.J. Punt, C.A.M.J.J. Van den Hondel (1988), "A vector for *Aspergillus* transformation conferring phleomycin resistance", *Fungal Genet. Rep.*, **35(1)**, pp.25-27.

[16] P. Perez, G. Tiraby, J. Kallerhoff, J. Perret (1989), "Phleomycin resistance as a dominant selectable marker for plant cell transformation", *Plant Mol. Biol.*, **13(4)**, pp.365-373.

[17] J.-y. Wang, H.-y. Li (2008), "*Agrobacterium tumefaciens*-mediated genetic transformation of the phytopathogenic fungus *Penicillium digitatum*", *J. Zhejiang Univ. Sci. B*, **9(10)**, pp.823-828.

[18] L. Mikkelsen, S. Sarrocco, M. Lubeck, D.F. Jensen (2003), "Expression of the red fluorescent protein DsRed-Express in filamentous ascomycete fungi", *FEMS Microbiol. Lett.*, **223(1)**, pp.135-139.

[19] K.T. Nguyen, Q.N. Ho, T.H. Pham, T.-N. Phan, V.-T. Tran (2016), "The construction and use of versatile binary vectors carrying *pyrG* auxotrophic marker and fluorescent reporter genes for *Agrobacterium*-mediated transformation of *Aspergillus oryzae*", *World J. Microbiol. Biotechnol.*, **32(12)**, pp.204-212.

[20] M.N. Islam, S. Nizam, P.K. Verma (2012), "A highly efficient *Agrobacterium* mediated transformation system for chickpea wilt pathogen *Fusarium oxysporum* f. sp. *ciceri* using DsRed-Express to follow root colonisation", *Microbiol. Res.*, **167(6)**, pp.332-338.

[21] M. Eckert, K. Maguire, M. Urban, S. Foster, B. Fitt, J. Lucas, K. Hammond-Kosack (2005), "*Agrobacterium tumefaciens*-mediated transformation of *Leptosphaeria* spp. and *Oculimacula* spp. with the reef coral gene *DsRed* and the jellyfish gene *GFP*", *FEMS Microbiol. Lett.*, **253(1)**, pp.67-74.

[22] V.T. Tran, T.B.X.L. Do, T.K. Nguyen, X.T. Vu, B.N. Dao, H.H. Nguyen (2017), "A simple, efficient and universal method for the extraction of genomic DNA from bacteria, yeasts, molds and microalgae suitable for PCR-based applications", *Vietnam Journal of Science, Technology and Engineering*, **59(4)**, pp.66-74.

DOI: 10.31276/VJSTE.62(2).89-96



# Application of constructed wetland for advanced treatment of industrial wastewater

**Nguyen Phuoc Dan[1], Le Thi Minh Tam[1*], Vu Le Quyen[2], Do Hong Lan Chi[2]**

*[1]Centre Asiatique de Recherche sur l''Eau (CARE), University of Technology, Vietnam National University, Ho Chi Minh city*

*[2]Institute for Environment and Natural Resources, Vietnam National University, Ho Chi Minh city*

Received 5 August 2019; accepted 29 November 2019

***Abstract:***

**An experimental study to use a pilot vegetated submerged bed (VSB) wetland for the advanced treatment of effluent from the central wastewater treatment plant (CWWTP) of an industrial zone was carried out. The pilot VSB wetland included reeds (*Phragmites australis*), cattail (*Typha orientalis*), and blank cells in parallel. The constructed wetland was observed to be a suitable measure for wastewater reuse via the high performance of organic matter, turbidity removal, and detoxification. At loading rates of up to 250 kg chemical oxygen demand (COD) $ha^{-1}d^{-1}$, both cells with emergent plants obtained high efficiency of contaminant removal. Suspended solids (SS) and turbidity removal reached 67-86% and 69-82%, respectively. The COD removal efficiencies of the reed and cattail cells at a loading rate of 130 kg COD $ha^{-1}d^{-1}$ were 47 and 55%, respectively. At a high loading of 400 kg COD $ha^{-1}d^{-1}$, the toxicity unit (TU) reduced from 32-42 to 4.9 and 4.2 in the effluent of the cattail and reed cells, respectively. Especially at loadings of 70, 130, and 185 kg COD $ha^{-1}d^{-1}$, the effluent TU was less than 3.0, corresponding to a non-toxic level to the ecosystem. The effluent quality met industrial or landscaped wastewater reuse at these loading rates.**

***Keywords:*** **constructed wetland, wastewater polishing, wastewater reclamation and detoxification.**

***Classification number:*** **5.1**

## Introduction

Until 2009, there were 16 industrial zones in Ho Chi Minh city, Vietnam. All of them are located in the suburbs of Ho Chi Minh city. Now, all industrial zones have a CWWTP with capacities ranging from 2,000 to 6,000 $m^3d^{-1}$ [1]. Preliminary treatment, followed by secondary treatment with activated sludge, was used widely in these CWWTPs. However, degradation of the quality of receiving water canals in the suburbs has led the Ministry of Natural Resources and Environment [1] to report poor operation and control of effluent discharge in CWWTPs .

On the other hand, industrial zones have also been faced with the challenge of freshwater scarcity due to factors contributing to the degradation of groundwater quality such as high salinity, high iron, and manganese concentration, resulting in a decrease of groundwater supply and increase of the price of piped water by the Water Supply Company. Therefore, wastewater reclamation is a good option to solve these problems. In order to use polished and reclaimed effluent from the CWWTPs in for industrial applications or as irrigation for landscaped areas in the industrial zones, advanced treatment is necessary to remove any remaining SS, biochemical oxygen demand (BOD), and nutrients.

Constructed wetlands are an environmentally friendly technology for wastewater treatment or polishing of effluent, and it is becoming increasingly popular in many countries all over the world [2-4]. The mechanism of pollutant removal by a constructed wetland is well known. It is based on biological filtration processes that occur in the medium layer dense with aquatic plants [5]. In developing countries, the application of constructed wetlands for decentralized

*Corresponding author: Email: minhtamnt2006@hcmut.edu.vn

wastewater treatment is being promoted because of low construction requirements and low operation costs compared with other conventional wastewater treatment systems [6-8].

Therefore, this study aims to (1) investigate the treatment efficiency of a VSB wetland for advanced industrial wastewater treatment and (2) assess the detoxification of the VSB wetland in terms of the reduction of acute toxicity.

## Materials and methods

### *The pilot VSB wetland*

The pilot horizontal VSB wetland was located on the campus of the CWWTP of Le Minh Xuan industrial zone located in the Binh Chanh district, a sub-urban area of Ho Chi Minh city. The Le Minh Xuan industrial zone generates 4,000 $m^3d^{-1}$ of wastewater. The Le Minh Xuan industrial zone contains polluting industries such as chemical manufacturing, tanning, pesticide, textile, and dyeing companies, which were required to relocate from the inner city by the city government. Therefore, the wastewater of the industrial zone may contain toxic compounds. The pilot VSB wetland included three cells, each with the size of 12×3.5×1.2 m, and the empty working volume of each cell was 42 $m^3$ (Fig. 1). *Phragmites australis* and *Typha orientalis* were transplanted at a density of 20 plants $m^{-2}$ and 25 plants $m^{-2}$, respectively. These emergent plants were taken from natural low-lying land next to the Le Minh Xuan industrial zone. Both of these plants were studied because they could tolerate high loading of industrial wastewater [9, 10]. All of the selected plants that were over 2.0 m in height were cut from the top part into a stem section of 0.3 m height with the root. The pilot size and structure of the media are presented in Table 1.

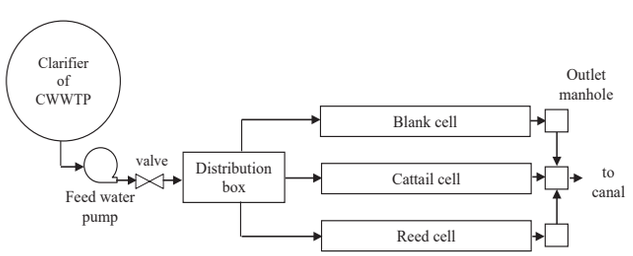


**Fig. 1. Layout of the pilot VSB wetland.**

**Table 1. Size and structure of the pilot VSB wetland cell.**

| No | Parameter | Unit | Size |
|---|---|---|---|
| 1 | Length | m | 12 |
| 2 | Width | m | 3.5 |
| 3 | Bottom slope | % | 0.01 |
| 4 | The number of layers: | - | 3 |
| | Height of gravel (20×4 mm) layer | mm | 250 |
| | Height of gravel (10×20 mm) layer | mm | 100 |
| | Height of sand layer (0.1-0.5 mm) | mm | 250 |

### *Feed wastewater*

The feed wastewater was the effluent from a secondary clarifier of the CWWTP in the Le Minh Xuan industrial zone. Table 2 shows the characteristics of the effluent during the experiment of the pilot VSB wetland, which started from January in 2008 and ended on August 2009.

**Table 2. Quality of effluent from the CWWTP during the run of the pilot VSB wetland.**

| Parameter | Unit | Range | Average value (n=40) | Effluent quality standards (*) |
|---|---|---|---|---|
| pH | - | 6.91-7.69 | 7.4±0.3 | 6-9 |
| Turbidity | FAU | 14-140 | 35±29 | NA |
| Colour | Pt-Co | 132-500 | 259±198 | 70 |
| TSS | $mgl^{-1}$ | 10-34 | 39±31 | 100 |
| COD | $mgl^{-1}$ | 62-540 | 189±141 | 100 |
| N-ammonia | $mgl^{-1}$ | 0.4-1.2 | 0.68±0.2 | 10 |
| N-nitrite | $mgl^{-1}$ | 0.02-0.04 | 0.03±0.01 | NA |
| N-nitrate | $mgl^{-1}$ | 27-72 | 55±14.6 | 30 |
| $BOD_5$ | $mgl^{-1}$ | 36-250 | 61±13 | 50 |

Note: (*) Vietnamese industrial effluent quality standards for secondary treatment (QCVN40:2011/BTNMT); NA: non-available.

Table 2 shows that the effluent of the CWWTP had much variation during the experimental run of the pilot VSB wetland. The high variation of the effluent quality was due to (i) poor control of discharge from industries inside the industrial zone and (ii) poor operation of the CWWTP. Therefore, the quality of the CWWTP effluent used did not

to meet the Vietnamese industrial effluent standards in terms of COD, $BOD_5$ and colour.

### *Operation conditions*

The pilot VSB wetland was run at loading rates of 70, 130, 185, 250, and 400 kg COD $ha^{-1}d^{-1}$. The COD loading rates were controlled by the adjustment of the feed wastewater flowrate using a pump discharge valve and weirs in the distribution box. The adjusted flow rate of the fed wastewater was in the range of 2.7 to 12 $m^3d^{-1}$. The influent COD to the VSB wetland was the real COD effluent of the CWWTP. The influent COD values at loading rates greater than and equal to 185 kg COD $ha^{-1}d^{-1}$ occurred during poor operation or overload of the CWWTP (Table 3).

**Table 3. The operation conditions of pilot VSB wetland.**

| Loading rate (kg COD $ha^{-1}d^{-1}$) | Duration (days) | HRT(*) (day) | Influent COD to VSB wetland ($mgl^{-1}$) |
|---|---|---|---|
| 70 | 12 | 9.0 | 72±11 (n=5) |
| 130 | 22 | 5.4 | 90±10 (n=12) |
| 185 | 14 | 4.0 | 129±60 (n=7) |
| 250 | 31 | 2.0 | 250±90 (n=8) |
| 400 | 31 | 2.0 | 416±75 (n=8) |

Note: (*) HRT = $V_bQ^{-1}$. Where: $V_b$ - the empty bed volume (24 $m^3$ of material bed), and Q - flow rate ($m^3d^{-1}$).

### *Analysis methods*

All parameters including COD, SS, turbidity, colour, ammonia, nitrite, and nitrate were analysed according to the Standard Methods for the Examination of Water and Wastewater [11].

The acute toxicity tests of *Vibrio fischeri* and *Daphnia magna* were used in this study to assess the detoxification of the VSB wetland. The freeze-dried marine bacteria *V. fischeri* was obtained from AZUR Environmental (standardized protocols from US EPA) using the Microtox analyzer 500 ISO, 1998 [12]. The concentration causing 50% inhibition of light emitted by the bacteria (EC50) was determined after 5, 15, and 30 min. The maximum dimethyl sulfoxide (DMSO) concentration used for testing was 2%.

*D. magna* or waterflea is a common microcrustacean found in fresh water. The culture of the *D. magna* Straus clone 1829 was maintained in an M4 medium [13]. The immobilization of the *D. magna* was recorded after 24 h and 48 h. An ISO medium [14] was used for the dilution of the sample and as the control. The maximum DMSO concentration used for testing was 0.1%.

## Results and discussion

### *Turbidity and SS removal*

Turbidity is an aesthetic parameter widely used in regulations of reclaimed water quality. Limits on turbidity for agricultural or for industrial reuse range from 2 to 5 FAU [15]. Fig. 2 shows the variation of influent and effluent turbidity during the operation time.

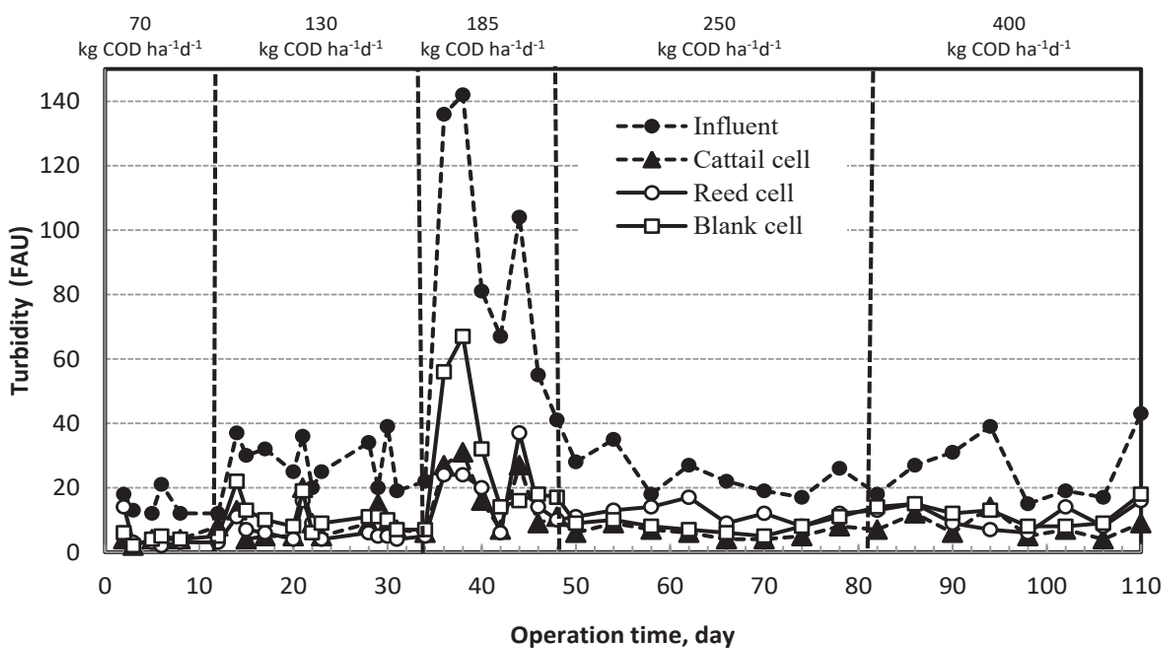


**Fig. 2. Course of influent and effluent turbidity versus operation time.**

Turbidity is used as a surrogate measure of suspended solids [15]. A high performance of turbidity removal was observed. The VSB wetland with dense root zone may provide a transport-attachment trap for turbidity that escaped the CWWTP. At all the tested COD loading rates, the removal efficiencies of the reed and cattail cells were higher than that of the blank cell. In the cattail and reed cell, 68 and 73% of influent turbidity were removed, respectively, while a turbidity removal of 64% was found in the blank cell at loading rates of 70 and 130 kg COD $ha^{-1}d^{-1}$.

The average removal efficiencies were 65 and 68% in the cattail and reed cell, respectively, at loading rates equal to and greater than 185 kg COD $ha^{-1}d^{-1}$. The performance of the reed cell was a little higher than that of the cattail cell at most of the loading rates. This trend may be attributed to the superior growth of the local reed to that of the cattail in terms of density of roots, rhizomes, and leaves.

It is noteworthy the mean of the effluent turbidity of the cattail and reed cells at loading rates less than 185 kg COD $ha^{-1}d^{-1}$ were 7.4±4.6 FAU and 6.1±4.0 FAU, respectively, which meets the limit on turbidity for agricultural reuse (10 FAU). However, in order to satisfy the allowable turbidity for industrial reuse (3 FAU), additional treatment such as adsorption, flocculation, or filtration for VSB wetland effluent is needed.

The effluent suspended solids of the cattail and reed cells at low COD loading rates were 5.9±2.5 and 4.5±1.8 $mgl^{-1}$, respectively. These values met the SS threshold for industrial reuse (20 $mgl^{-1}$). The average effluent suspended solids of all cells at the high loading rate of 400 kg COD $ha^{-1}d^{-1}$ were less than 26 $mgl^{-1}$. Thus, a wash-out of the bio-solids of the VSB wetland had not occurred after 110 days of runs at short hydraulic retention times (HRTs).

### *Colour removal*

The influent for the VSB wetland was the effluent of secondary treatment at the CWWTP. Then, the colour was mainly caused by non-biodegradable soluble organic matter. This resulted in low colour removal by the VSB wetland at low COD loading rates (70 and 130 kg COD $ha^{-1}d^{-1}$). The average colour removal of the reed, cattail, and blank cells at low COD loading rates were 16, 21, and 12%, respectively. The average effluent colour values were 145, 155, and 160 Pt-Co for the reed, cattail, and blank cells, respectively (Fig. 3).

At higher loading rates, in which overload of the CWWTP occurred, higher colour removal of all cells were obtained. Discharge to the CWWTP comes mainly from 16 textile and dyeing companies in the industrial zones that lead to high influent colour values into the pilot VSB wetland [16]. At the loading rate of 185 kg COD $ha^{-1}d^{-1}$, the average colour removal efficiency of the reed, cattail, and blank cells were 51, 48 and 45%, respectively. High colour removal at this loading rate was significantly attributed to the attached bacteria living in the bed media and rhizomes. The bacteria living in the wetland continuously degraded the organic dyes, which could not be completely removed by the CWWTP.

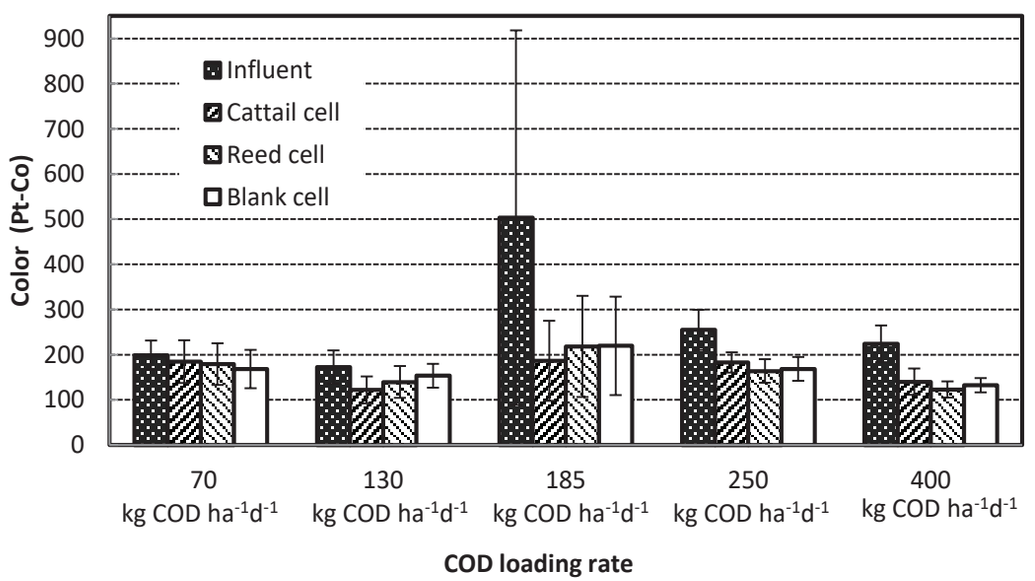


**Fig. 3. Colour profile versus COD loading rates.**

### *COD removal*

At COD loading rates of 70 kg COD $ha^{-1}d^{-1}$ (HRT of 5 d) and 130 kg COD $ha^{-1}d^{-1}$ (HRT of 3 d) when the mean influent COD to the VSB wetland was 84±14 $mgl^{-1}$ (n=18), the average COD removal of the reed, cattail, and blank cells were 48, 41, and 31%, respectively. The remaining COD after the secondary treatment of the CWWTP was mainly non-biodegradable and slow-degradable organic matter that resulted in low COD removal efficiencies at low COD loading rates. The average effluent COD concentration of the reed, cattail, and blank cells were 49, 43, and 57 $mgl^{-1}$, respectively, while the average effluent $BOD_5$ concentration of all cells were less than 15 $mgl^{-1}$, which met allowable $BOD_5$ concentrations for agricultural, industrial, or environmental reuses (20 $mgl^{-1}$).

Figure 4 shows that at higher loading rates, namely 185 kg COD $ha^{-1}d^{-1}$ (HRT of 2 d) and 250 kg COD $ha^{-1}d^{-1}$ (HRT of 1 d), the average effluent COD removal of the reed, cattail, and blank cells were 51, 51, and 41%, respectively. The average effluent COD values of both the reed and cattail cells were 78 $mgl^{-1}$, which was lower than the allowable COD value set by the Vietnamese industrial effluent quality standards (100 $mgl^{-1}$). This indicates that the application of a VSB wetland can be a suitable measure to mitigate organic

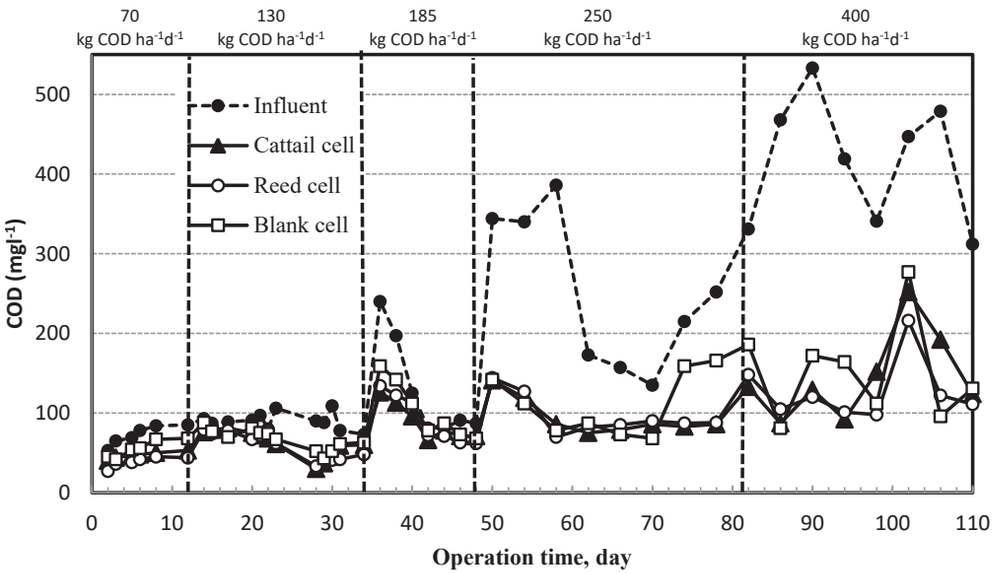


**Fig. 4. Course of influent and effluent COD concentrations versus operation time.**

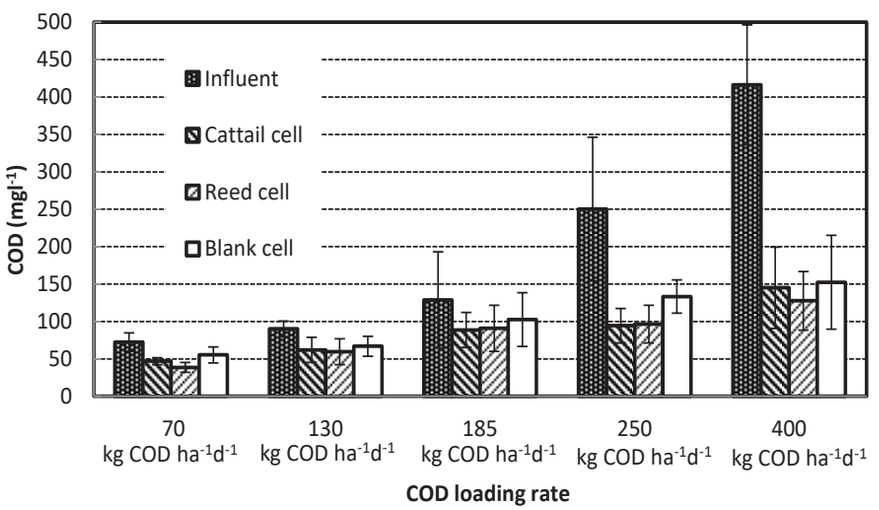


**Fig. 5. COD concentration profile versus COD loading rates.**

loading shock or overload of wastewater from a treatment plant.

Figure 5 presents high influent COD values at the loading rate of 400 kg COD $ha^{-1}d^{-1}$ (HRT of 1 d) due to the overload of the CWWTP. High performance of both the cattail and reed cells in terms of COD removal was observed. The COD removals of the reed and cattail cells were about 69 and 64%, respectively. These results were similar to those of previous studies [17, 18]. The biodegradable organic matter that remained in the effluent from the secondary treatment of the CWWTP were broken down completely by attached bacteria in the VSB wetland. However, the average effluent COD concentration did not meet the COD threshold given by the Vietnamese industrial effluent quality standards.

***Nitrogen removal***

The feed wastewater quality of the pilot VSB was characterized by low ammonia concentration and high nitrate concentration (Table 2). The average total nitrogen removal of the reed, cattail, and blank cells at a COD loading rate of 70 kg COD $ha^{-1}d^{-1}$ (HRT of 5 days) were 40, 37, and 29%, respectively. Fig. 6 shows that a lower total nitrogen removal was obtained at short HRTs.

There was no remarkable difference between the cattail and reed cells in terms of total nitrogen removal. The performance of the emergent plant cells was higher by 10% of the total nitrogen than that of the blank cell, which had the same support media but without the emergent plant. The uptake of nitrates by the emergent plants may have led to this difference [19]. Because of low ammonia concentration in the influent, attached denitrifying bacteria living in the bed media, along with rhizomes, played the main role in total nitrogen removal. However, the average effluent nitrate-N concentration at low loading rates and high loading rates (higher than 130 kg COD $ha^{-1}d^{-1}$) were 35 and 45 $mgl^{-1}$, respectively. Those values were higher than the allowable nitrate concentration set by the Vietnamese industrial effluent quality standards. In order to meet the standards, an anaerobic-aerobic (A-O) process should be done in the CWWTP.

***Toxicity assessment***

L.C.D. Hong, et al. (2000) [12] reported that wastewater with a $TU_a$ higher than 10 could cause a medium toxic effect on the ecological system, and a $TU_a$ higher than 50 is considered very toxic. The effluent of the CWWTP at low COD loading rates when the average COD concentration was around 78 $mgl^{-1}$ had an average TU of 32, corresponding to medium toxicity level.

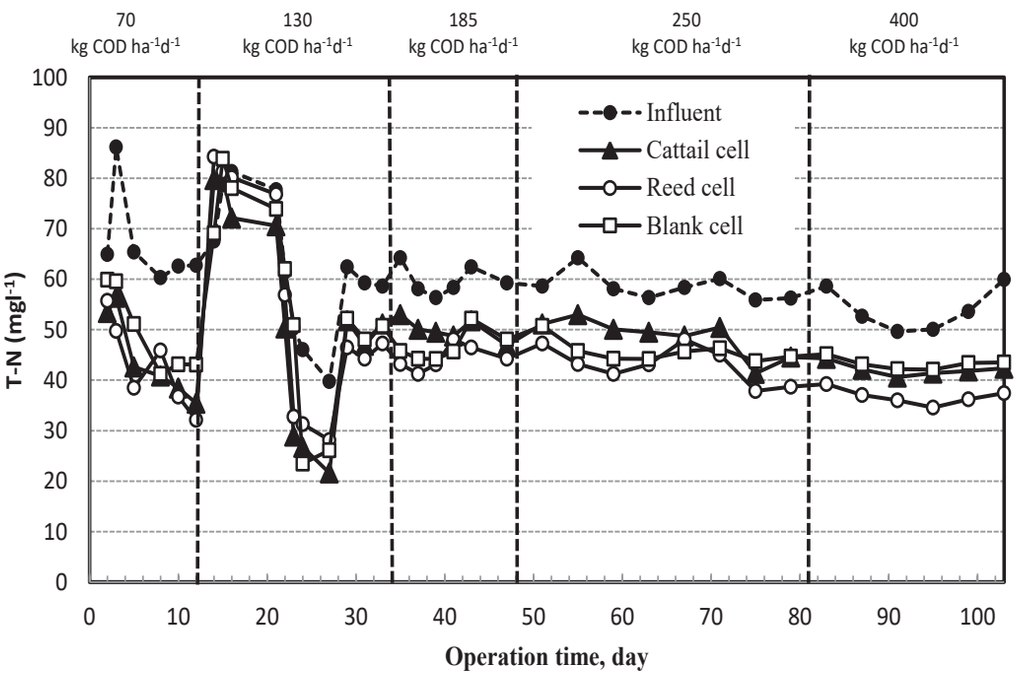


**Fig. 6. Course of influent and effluent total nitrogen concentrations versus operation time.**

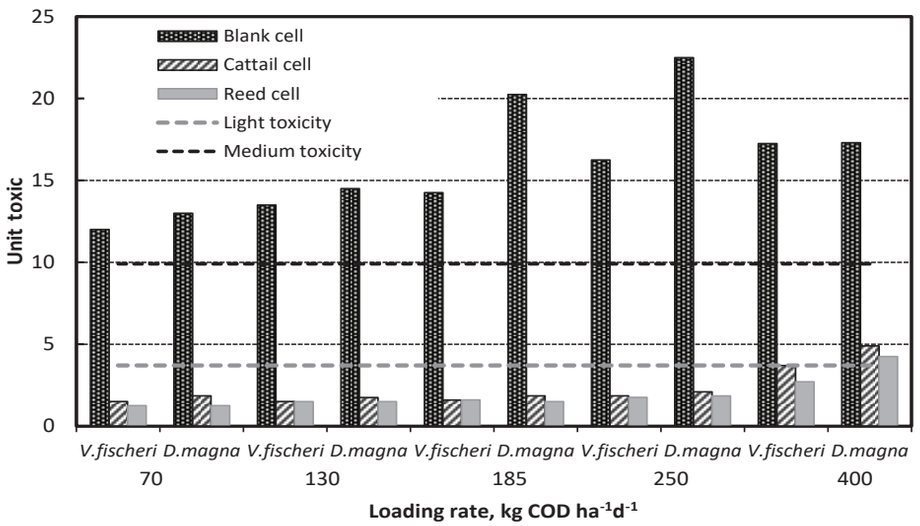


**Fig. 7. The reduction of acute toxicity at various COD loading rates.**

It was noticeable that the VSB wetland remarkably reduced $TU_a$ of at all COD loading rates (Fig. 7). A high TU reduction efficiency was observed for both reed and cattail cells. At loading rates equal to and less than 250 kg COD $ha^{-1}d^{-1}$, the TUs of the effluent of the emergent plant cells were less than 3.0, while those of the blank cell was around 12. At a COD loading rate of 400 kg COD $ha^{-1}d^{-1}$, the TUs of the VSB wetland was approximately 5.0, corresponding to a light toxicity level. A significant difference in $TU_a$ between the emergent plant cells and the blank one may be attributed to plant uptake of toxicants remaining in the influent. The effluent from the CWWTP may contain metals such as zinc, cadmium, and chromium and pesticide/herbicide residuals that originated from the 24 plating industries and a few pesticide industries in the industrial zone. Dan and Thanh (2010) [16] reported that the effluent from the CWWTP of the Le Minh Xuan industrial zone contained heavy metals, such as 0.5-2.7 $mgl^{-1}$ of zinc, 0.27-0.45 $mgl^{-1}$ of nickel, and 0.02-0.90 $mgl^{-1}$ of chromium. Compared to the soil media, the plants do not take up as much metal or organic toxicants, but they are involved in oxygenation and microbiological processes that contribute to the ability of the wetland to remove metals and organic toxicants [19].

## Conclusions

The VSB wetland was a good option for wastewater reuse and to enhance the performance of the industrial wastewater treatment plant. The pilot VSB wetland obtained high turbidity, SS, and COD removal at loading rates equal to and less than 250 kg COD $ha^{-1}d^{-1}$. The colour removal performance of the VSB wetland was low, even at low COD loading rates, due to the nonbiodegradable soluble substances contributing to the colour of the IZ wastewater treatment plant effluent. The highest total nitrogen removal efficiency, 40%, was obtained with the reed cell. The effluent quality at these loading rates met the limits for agricultural and industrial reuses.

The VSB wetland was a proper measure to mitigate overload or loading shock from industrial wastewater treatment plants. The results of this study show that the VSB wetland obtained a high efficiency of acute toxicity reduction due to the contributions of plant uptake of toxicants, biodegradation by attached bacteria, and other related physical-chemical processes.

## ACKNOWLEDGEMENTS

The authors were grateful to the financial support of Vietnam National University, Ho Chi Minh city.

The authors declare that there is no conflict of interest regarding the publication of this article.

## REFERENCES


[1] Ministry of Natural Resource and Environment (2010), *Annual Report on National Environment*.

[2] J. Vymazal (2009), "The use constructed wetlands with horizontal sub-surface flow for various types of wastewater", *Ecological Engineering*, **35**, pp.1-17.

[3] H. Wu, J. Zhang, H.H. Ngo, W. Guo, Z. Hu, S. Liang, et al. (2015), "A review on the sustainability of constructed wetlands for wastewater treatment: design and operation", *Bioresource Technology*, **175**, pp.594-601.

[4] X. Wang, Y. Tian, X. Zhao, S. Peng, Q. Wu, and L. Yan (2015), "Effects of aeration position on organics, nitrogen and phosphorus removal in combined oxidation pond-constructed wetland systems", *Bioresource Technology*, **198**, pp.7-15.

[5] R. Kadlec, R. Knight, J. Vymazal, H. Brix, P. Cooper, and R. Haberl (2000), *Constructed Wetlands for Pollution Control: Processes, Performance, Design and Operation*, IWA Publishing.

[6] J. Lloyd, D. Klessa, D. Parry, P. Buck, and N. Brown (2004), "Stimulation of microbial sulphate reduction in a constructed wetland: microbiological and geochemical analysis", *Water Research*, **38**, pp.1822-1830.

[7] A. Machado, M. Beretta, R. Fragoso, and E. Duarte (2017), "Overview of the state of the art of constructed wetlands for decentralized wastewater management in Brazil", *Journal of Environmental Management*, **187**, pp.560-570.

[8] W. Park (2009), "Integrated constructed wetland systems employing alum sludge and oyster shells as filter media for P removal", *Ecological Engineering*, **35**, pp.1275-1282.

[9] C.S. Calheiros, A.O. Rangel, and P.M. Castro (2008), "The effects of tannery wastewater on the development of different plant species and chromium accumulation in Phragmites australis", *Archives of Environmental Contamination and Toxicology*, **55**, pp.404-414.

[10] C.S. Calheiros, A.O. Rangel, and P.M. Castro (2009), "Treatment of industrial wastewater with two-stage constructed wetlands planted with *Typha latifolia* and *Phragmites australis"*, *Bioresource Technology*, **100**, pp.3205-3213.

[11] American Public Health Association, American Water Works Association, Water Environment Federation (2005), *Standard Methods for the Examination of Water and Wastewater, 21st*, USA.

[12] L.C.D. Hong, K. Becker-van Slooten, J.J. Sauvain, T.L. Minh, and J. Tarradellas (2000), "Toxicity of sediments from the Ho Chi Minh city canals and Saigon river, Viet Nam", *Environmental Toxicology: An International Journal*, **15**, pp.469-475.

[13] B.P. Elendt (1990), "Selenium deficiency in Crustacea", *Protoplasma*, **154**, pp.25-33.

[14] E. ISO (2012), "Water quality-determination of the inhibition of the mobility of Daphnia magna Straus (Cladocera, Crustacea) - acute toxicity test", *EN ISO*, **6341**, p.1996.

[15] Metcalf & Eddy, Inc. an AECOM Company, T. Asano, F.L. Burton, H. Leverenz, R. Tsuchihashi, et al. (2007), *Water Reuse: Issues, Technologies, and Applications*, McGraw-Hill Education.

[16] N.P. Dan and B.X. Thanh (2010), *Surveying wastewater system of Le Minh Xuan Industrial Zone and proposing the improvement measures*.

[17] T. Chen, C. Kao, T. Yeh, H. Chien, and A. Chao (2006), "Application of a constructed wetland for industrial wastewater treatment: a pilot-scale study", *Chemosphere*, **64**, pp.497-502.

[18] H. Hadad, M. Maine, and C. Bonetto (2006), "Macrophyte growth in a pilot-scale constructed wetland for industrial wastewater treatment", *Chemosphere*, **63**, pp.1744-1753.

[19] R. Lorion (2001), *Constructed Wetlands: Passive Systems for Wastewater Treatment*, US EPA Technology Innovation Office.

# Vietnam Journal of Science, Technology and Engineering (VJSTE): Manuscript Template

**General Instructions on using this template and submitting a manuscript to VJSTE:** Thank you for preparing a manuscript for submission to VJSTE. Using this template, or following the guidelines below, will help us in processing your paper. Our goal is to be able to identify each section of your manuscript so that we can accurately record the title, authors, abstract, etc. and also be able to enrich it by including reference links and an accurate layout.

You can submit your paper at http://vietnamscience.vn

So that we can identify the parts of your paper, and even if you do not use our template, please begin each section with the specific key words listed below. Please do not use paragraph breaks in the title, author list, or abstract.

**Title**

**Authors**

**Affiliations**

**Abstract**

**One Sentence Summary**

**Main Text**

**Acknowledgements**

**References**

Several of these headings are optional, for example, not all papers will include a one-sentence summary, figures or tables.

Please use the .docx format (all version after Word 2007).

More specific formatting instructions are provided in the actual template, which follows.

**Title: How to Format a Science Paper (replace with your real title)**

**Authors:** The author list should be one single paragraph (no breaks). Authors should be listed by first name or initial followed by last name and separated by commas. Use superscript numbers to link affiliations, and symbols *†‡ for author notes. For example, X. Jones[1]*, P. Smith[1,2]

**Affiliations:**

[1]Affiliations should be preceded by superscript numbers corresponding to the author list, and each affiliation should end with a period.

[2]Each affiliation should be a separate paragraph.

*Correspondence to: include the email addresses or telephone number of the corresponding author(s). Please use the asterisk (*) symbol for the corresponding author information.

**Abstract**: The abstract should be about 100-150 words, and organized in this structure: An opening sentence that sets the question that you address and is comprehensible to the general reader, background content specific to this study, results, and a concluding sentence. It should be one paragraph only.

**One Sentence Summary:** A brief summary of the main result of your paper, without excessive jargon and less than 150 characters.

**Main Text:** In general, this should include a brief (1-2 paragraph) introduction, followed by a statement of the specific scope of the study, followed by results and then interpretations. Please avoid statements of future work or claims of priority, and avoid repeating the conclusions at the end.

All of the Figures and Tables should be cited in order (which should be cited as, for example, figure S1, and table S1). You can include page breaks if you would like to place the figures within the text.

**Subheads:** These can be included in Research Articles or Reviews and should be brief.

**Equations** can be included. We do not recommend using the native Word 2007, 2008, 2010 or 2011 equation editor. This can in some cases produce less reliable MathML, the online markup language we use, which may result in display errors. Instead, use the legacy equation editor in word (Insert menu; select insert object; select word equation) or use Mathtype (recommended). If you enter equations in simple LaTeX, check that they will convert accurately (Word 2007 and higher can convert simple LaTeX equations).

**Fig. #:** (Begin each figure caption with a label, "**Fig. 1.**" for example, as a new paragraph.).

**Fig. 1.** The figure caption should begin with an overall descriptive statement of the figure followed by additional text. They should be immediately after each figure. Figure parts are indicated with capital letters (**A**). If you prefer, you can place both the actual figures and captions logically through the text near where they are cited rather than at the end of the file (but not both). If a paragraph in the main text begins with the name of a figure, write out "Figure" in full (e.g., <para>"Figure 1 shows….").

**Fig. 2.** You can place graphics above each equation as part of this file.

**Table #:** (Begin each table caption with a label "**Table 1.**", etc.) as a new paragraph.

**Table 1.** Start this caption with a short description of your table. Format tables using the Word Table commands and structures. Do not create tables using spaces or tabs characters.

**Acknowledgments:** The acknowledgments should include a statement about where the data reported in the paper are presented, archived, or available. If in an archive, include the accession number or a placeholder for it. Please also include relevant funding information such as grant numbers and funding agencies. You can also include a statement of author contributions here. The acknowledgements can be multiple paragraphs.

**References:**

References should be cited in bracket with a number [1]. Multiple reference citations are separated by commas [2, 3] or if a series, dashes [4-6].

References are listed in numerical order, and in the same order in which they are cited in text. The reference list should include all and only those references you have cited in the text. The reference list appears at the end of the paper.

Please include the above heading "References".

Please do not mix in references with explanatory notes.

The reference consist of: Family name(s) and initials of all authors (year of publication), "Titles of journal articles" (optional), *Title of journal, book or other publication*, **volume(number)**, page numbers.

Example of a reference list:

[1] T. Binzoni, T.S. Leung, D. Boggett, D.T. Delpy (2002), "A new near infrared laser-Doppler flowmeter for deep tissue perfusion monitoring", *MAGMA*, **14,** pp.74-75.

[2] T. Binzoni, T.S. Leung, D. Boggett, D.T. Delpy (2003), "Non-invasive laser Doppler perfusion measurements of large tissue volumes and human skeletal muscle blood RMS velocity", *Phys. Med. Biol.*, **48(1)**, pp.2527-2549.

ISSN 2525-2461

# Vietnam Journal of Science, Technology and Engineering

JUNE 2020 • VOLUME 62 NUMBER 2



**EDITORIAL OFFICE**

113 Tran Duy Hung Str., Cau Giay Dist., Hanoi

Tel: (84.24) 39436793; Fax: (84.24) 39436794

Email: khcnvn@most.gov.vn

Website: vietnamscience.vn

**PUBLICATION LICENCE**

No.1153/GP-BTTTT 26th July 2011

No.2528/GP-BTTTT 26th December 2012

No.592/GP-BTTTT 28th December 2016